Co-optimizing Engine Hardware and Fuel Chemistry for Improving Thermal Efficiency and Reducing Pollutant Emissions of Gasoline Fueled Direct Injection Internal Combustion Engines

by

Kaustav Bhadra

A dissertation submitted in partial fulfillment
of the requirements for the degree of
Doctor of Philosophy
(Mechanical Engineering)
in the University of Michigan
2023

Doctoral Committee:

Professor Andre L. Boehman, Chair.
Dr. Robert Middleton
Professor Shelie Miller
Professor Margaret Wooldridge

Kaustav Bhadra

kaustav@umich.edu

ORCID iD: 0000-0002-6989-6672

Dedication

This dissertation is dedicated to my parents, Ma and Baba and my brother, Arjun.

Acknowledgements

The past 5 and a half years in grad school have been quite a journey. As I am typing out my dissertation, there are several people whom I would like to thank for being a part of this journey. The culmination of this journey resulting in this dissertation would not have been possible without the people acknowledged below.

Firstly, I would like to thank my thesis advisor, Professor Boehman for taking a chance on me as a young 22-year-old recent graduate out of India who had no prior automotive experience. My doctoral degree pursuit would not have been made possible had he not given me the opportunity. He was patient with me and let me learn from senior graduate students who were a part of our research group. He provided immense support throughout my stay, which allowed me to pursue different research ideas as part of this dissertation. I cannot thank him enough for his support especially during the Covid-19 pandemic. I will forever be grateful to him for the opportunity.

A huge thanks to my colleague and good friend for life, Charles Solbrig for his continuous support, help and guidance. This entire body of work would not have been possible without his help. Chuck, I feel so lucky to have had the opportunity to work with you on this project and got to learn from the best because of it. You truly are a magician.

I would like to thank the rest of my doctoral committee, Professor Wooldridge, Professor Miller and Dr. Robert Middleton for their guidance and feedback on all the experimental work that was done as a part of this thesis. Thank you Rob, for mentoring and guiding me throughout. Your help with the GT Power work allowed me to pursue some simulation work as a part of this thesis. The one on one sessions helped me immensely.

I would like to thank the Auto Lab technicians, William Kirkpatrick and Kent Pruss for their continuous support. Bill, thank you for all the help over the years whether it be in the test cell, in the machine shop or the fuel shed. I will remember the stories you have shared with me fondly. I would like to thank ME staff member Karen Brown and ME grad-coordinator Adam Mael for their continuous support. I would also like to thank our previous grad-coordinator Lisa Rogers for her help when I first got enrolled at the University of Michigan.

I would like to thank all the members of Dr. Boehman's group that I have had the pleasure of sharing my time at U of M with. Their help and friendship over the years have made the whole experience memorable. Thanks to Dr. Erick Garcia for showing me the ropes when I first got here fresh out of undergrad. I often reminisce about my first day at the Auto Lab when you asked me to hand you the ratchet and I had no idea what that was. Cleaning up oil spills and coolant spills were always a blast. Thanks to Dr. Vasilleos Triantapoulos for mentoring me on how to conduct data analysis and lending a hand with the ExxonMobil fuels study. Thanks to previous group members Dr. Jonathan Martin, Dr. Taehoon Han, Dr. Kwang Hee Yoo, Justin Koczak, Dr. Jordan Easter, Dr. Shuqi Cheng, Dr. Taemin Kim and recently graduated Dr. Andrew Di Mauro for their mentorship. Thanks to Taehoon for providing valuable insight and feedback. Your experience with SI engines helped me get up to speed when I moved to gasoline testing from diesel. I would also like to thank the current members of our lab group: Courtney

Videchak, Mohammed Abdullah and Joseph Trzaska. Sharing my journey with you people has been super fun. You have always provided a helping hand whenever I needed one. Joe, it has been awesome hanging out these past couple of years and doing MEGC stuff as well. Thanks to all the people that have been a part of the Auto lab over the years: Dr. Subramaniam Balakrishna, Vansh Sharma, Ravee Bakshi, Thanush Rajendran, Minato Tomuro, Jason Hebert, Kevin Pabst, Ryan Sebastian, Jeremy Babinet, Stephen Holmquist, Ryan Jenkins, Stephen Mundy, Ivan Carrasco, Gaurav Handa, Kevin Hui, Varun Chakrapani, Michael Wadas, Dr. Juan Hernandez and Dr. Lian Soto. I have really enjoyed your company. I would also like to thank my friend and fellow graduate student Sanat Modak for all the good times that we have had. From taking the same classes when we first got here to converting to the doctorate program and eventually graduating, our paths were so similar. Thanks for all your help.

A significant part of my thesis was made possible due to my internship at Aramco Americas, Detroit Research Center. I would like to thank my mentor Dr. Alexander Voice for his continuous mentorship. Your feedback on experiment design and data analysis helped me immensely. I would also like to thank Dr. Yu Zhang and David Cleary for the opportunity to conduct impactful research at their facility. I would like to thank Josiah Davis for his efforts throughout the project. His experience with all things test cell related was priceless. I would like to thank all the friends that I have made during my internship.

My basketball buddies, Hadi, Justin, Narek, Ravee and Ryan you guys have made these last few years super fun. Basketball allowed me to focus on something other than research. Sharing the court with you guys allowed me to escape from grad school life when it got stressful. Hoops with you guys is always the best.

I would like to thank the number of sponsors that I have had over the years. Thanks to ExxonMobil for funding fuels research as a part of DOE's SuperTruck 2 program. Thanks Dr. Gregory Lilik and Dr. Abhijeet Chausalkar for the opportunity and feedback. Thanks to BMTS Gmbh for their financial support on the turbocharger project. Thanks to Dr. Alexander Taylor for helping us acquire the engine and parts needed for engine installation. It was unfortunate that the project ended prematurely. My thesis would perhaps have looked a whole lot different if Covid 19 had not happened and we had got to work on the electric turbocharger. I am glad to have had the experience of working with BMTS. I appreciated the feedback I received from their researchers in Germany especially Dr. Nisar Al Hasan. Huge thanks to Aramco Americas for the internship opportunity and allowing me to conduct research at their Detroit facility.

Finally, I would like to thank my parents who told me to go ahead and chase my dreams of achieving a doctoral degree from one the most premier engineering schools in the world. They provided constant support even during the tough times when I was not sure how my grad school experience would look like especially during the Covid pandemic which directly resulted in delays in my research progress. Their involvement in proofreading my thesis drafts and feedback during mock presentations were invaluable. I would also like to thank my brother for his constant support and all the fun that we have had over the past couple of years as roommates. I would like to thank my family in India especially my aunt and my cousins for their kind words of support and their enthusiasm in my doctoral thesis work.

Table of Contents

List of Tables

List of Figures

List of Appendices

List of Abbreviations

AHRR ..... Apparent Heat Release Rate

AKI ..... Anti-Knock Index

BCT ..... Bulk Cylinder Temperature

BDC ..... Bottom Dead Center

BMEP ..... Brake Mean Effective Pressure

BSCO ..... Brake Specific Carbon Monoxide

$BSCO_2$ ..... Brake Specific Carbon Dioxide

BSFC ..... Brake Specific Fuel Consumption

$BSNO_X$ ..... Brake Specific Nitrogen Oxides

BSTHC ..... Brake Specific Total Unburnt Hydrocarbons

BTE ..... Brake Thermal Efficiency

CD ..... Combustion Delay

CEG ..... Cetane Enhanced Gasoline

CHP ..... Cumene Hydroperoxide

CI ..... Compression Ignition

CID ..... Cetane Ignition Delay

DCN ..... Derived Cetane Number

DI ..... Direct Injection

DI SOI ..... Direct Injection Start of Injection

DI% ..... Fraction of fuel injected directly as a percentage of total fuel

DPF ..... Diesel Particulate Filter

DTBP ..... Di-tert-butyl-peroxide

ECU ..... Engine Control Unit

EGR ..... Exhaust Gas Recirculation

EHN ..... Ethyl-hexyl-nitrate

EIVC ..... Early Intake Valve Closing

EVC ..... Exhaust Valve Closing

EVO ..... Exhaust Valve Opening

EVP ..... Exhaust Valve Phase

FGT ..... Fixed Geometry Turbocharger

FID ..... Flame Ionization Detector

FNT ..... Floating Nozzle Turbocharger

FTIR ..... Fourier Transform Infrared Spectroscopy

FTP75 ..... Federal Test Procedure 75

GCI ..... Gasoline Compression Ignition

GDI ..... Gasoline Direct Injection

GPF ..... Gasoline Particulate Filter

GT ..... Gamma Technologies

HACA ..... Hydrogen Abstraction Acetylene Addition

HCCI ..... Homogeneous Charge Compression Ignition

HFS ..... Heavy Fuel Stratification

HWFET ..... Highway Fuel Economy Test

ID ..... Ignition Delay

IMEP ..... Indicated Mean Effective Pressure

IVC ..... Intake Valve Closing

IVO ..... Intake Valve Opening

IVP ..... Intake Valve Phase

KI20 ..... Knock Intensity 20

KIp2p ..... Knock Intensity peak-to-peak

LFE ..... Laminar Flow Element

LIVC ..... Late Intake Valve Closing

LTC ..... Low Temperature Combustion

LTFT ..... Low Temperature Fischer Tropsch

LTHR ..... Low Temperature Heat Release

MBT ..... Maximum Brake Torque

MFS ..... Medium Fuel Stratification

MON ..... Motor Octane Number

NDIR ..... Non-dispersive Infrared Sensor

NHPI ..... n-Hydroxyphthalimide

NMEP ..... Net Mean Effective Pressure

NO_X ..... Nitrogen Oxides

NTC ..... Negative Temperature Coefficient

NTE ..... Net Thermal Efficiency

PACE ..... Partnership of Advanced Combustion Engines

PAH..... Polycyclic Aromatic Hydrocarbons

PCCI..... Premixed Charge Compression Ignition

PCP ..... Peak Cylinder Pressure

PECC..... Paraffin Enhanced Clean Combustion

PFI..... Port Fuel Injection

PFS..... Partial Fuel Stratification

PM..... Particulate Mass

PMEP ..... Pumping Mean Effective Pressure

PN ..... Particulate Number

PN23 ..... Particulate Number > 23 nm

PPCI ..... Partially Premixed Charge Compression Ignition

PSD ..... Particle Size Distribution

RCCI ..... Reactivity Controlled Compression Ignition

RON ..... Research Octane Number

RPECS ..... Rapid Prototyping Electronic Control System

SI..... Spark Ignition

SWRI..... Southwest Research Institute

TBHP ..... Tert-butyl-hydroperoxide

TDC..... Top Dead Center

THC..... Total Unburnt Hydrocarbons

UHC ..... Unburnt Hydrocarbons

US06 ..... United States 06 supplemental federal test procedure

VAT ..... Variable throat Area Turbocharger

VCT..... Variable Camshaft timing

VFT ..... Variable Flow Turbocharger

VGT ..... Variable Geometry Turbocharger

VNT ..... Variable Nozzle Turbocharger

WLTP..... Worldwide Light vehicles harmonized Test Procedure

Abstract

This thesis addresses the drawbacks of current generation downsized boosted gasoline powered engines through experiments that were designed to push the limits of thermal efficiency. Experiments were conducted on both spark ignited and compression ignited engine platforms to demonstrate potential solutions.

The drawbacks of light-duty downsized gasoline spark ignited engines that are addressed in this thesis are the limited thermal efficiency, high knock propensity and high particulate matter emissions. All the experiments on the spark-ignited platform were conducted on a production, multi-cylinder spark ignited engine that was equipped with both port and direct injectors as well as a twin independent variable camshaft timing. The drawbacks of light-duty downsized gasoline compression ignited engines that are addressed in this thesis are the limited combustion efficiency and limited combustion stability at low loads and low temperatures. All the experiments on the compression-ignited platform were conducted on single cylinder research engine.

The first part of the dissertation addresses the limited thermal efficiency of downsized spark ignited GDI (gasoline direct injection) engines by implementing Miller cycle operation with the assistance of a prototype floating nozzle turbocharger. Valve timing tables were generated using a GT-Power model which predicts the camshaft phasor positions for lowest fuel

consumption. The results of the simulation study indicate that the engine can operate with higher thermal efficiency than the baseline strategy by adopting a Miller valve timing. The excess boost pressure required to implement the changes to the valve timing was provided by the prototype turbocharger. Implementation of Miller cycle resulted in a 4% improvement in fuel economy and a 30% reduction in NO_x emissions over the FTP75 (Federal Test Procedure) standard drive cycle.

The second part of the dissertation addresses the knock propensity and particulate matter emissions from spark ignited GDI engines. Three independent studies are conducted to investigate the knock-soot correlation first discovered by Han. The results show that Miller timing, direct injection and high-octane rated fuels lower knock propensity and improve thermal efficiency. The results also indicate that there is a significant increase in accumulation mode particles generated in the engine during knocking and the concentrations of the particles are proportional to knock intensity. This correlation is confirmed to exist on a multi-cylinder platform across hardware changes, injection strategy changes and changes in fuel chemistry.

The last part of the dissertation delves into the issue of reduced combustion robustness of gasoline compression ignition at low loads and low temperatures. High cetane rated gasoline fuel was formulated using small percentages of peroxide compounds. Cetane enhanced gasoline was shown to reduce manifold pressure requirements up to 60 kPa and increase combustion efficiency up to 8% compared to the baseline gasoline. The implementation of a prototype dual fuel injector presented an opportunity for optimizing the consumption of cetane enhanced gasoline by switching to regular gasoline when combustion stability is high. This combination of CEG (cetane enhanced gasoline) and a dual fuel injector can potentially overcome the challenge of GCI (gasoline compression ignition) operation at engine-idle conditions and cold starts.

The studies presented in this thesis provide potential pathways for enhancing thermal efficiency and reducing emissions of future production light-duty gasoline engines. The observations made from the experiments in this thesis can directly impact the decision making of future light-duty downsized gasoline engine manufacturers.

Chapter 1
Introduction

1.1 Motivation

Carbon-based fuels are the world's largest sources of energy across different sectors whether that be for industry, electricity or transportation (Figure 1-1). Transportation accounts for 26% of total energy used [1,2] (Figure 1-1) and 29% of all greenhouse gas emissions from the US [1,2]. Currently, internal combustion engines that use petroleum derivatives power the majority of the world's vehicles. Approximately 56% of the transportation sector in the US uses motor gasoline as a primary source of fuel [1,2] (Figure 1-2). Light duty vehicle sales numbers show that gasoline fueled internal combustion engine vehicles make up about 80% of vehicles sold in the US in 2020 [1,2] (Figure 1-2). Petroleum and liquid fuels are predicted to continue to be the largest energy sources for transportation even as late as 2050 (Figure 1-2).

Battery electric vehicles, fuel cell vehicles and plug-in hybrid vehicles are alternate powertrain architectures that involve electrification that can lead to lower vehicular emissions. However, current vehicle electrification technology is limited by cost, performance degradation, charging time and energy density. Energy Information Administration annual energy outlook reports predict that gasoline fueled spark ignited engines will still make up the majority of sales among light duty vehicles for the foreseeable future [1,2]. While electrification continues to

make strides in terms of progress to overcome its drawbacks, engine research to improve efficiency is paramount for an immediate solution for sustainable transportation. Considering the fact that a majority of the world's vehicles are predicted to still have an internal combustion engine in some capacity even as late as 2050, it is necessary that we attempt to operate them in the most efficient way possible [3–7]. In the longer term, these engines may be powered increasingly by lower-carbon but costlier bio-based and synthetic fuels. Improving combustion engine efficiency can reduce both the cost and the emissions associated with transportation.

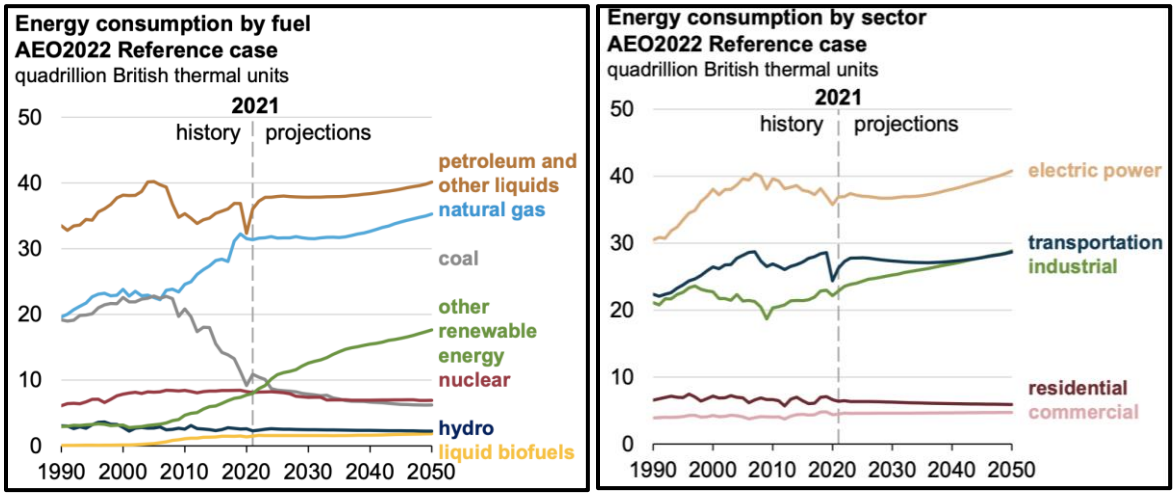

Figure 1-1: Share of energy consumption by fuel and sector [1].

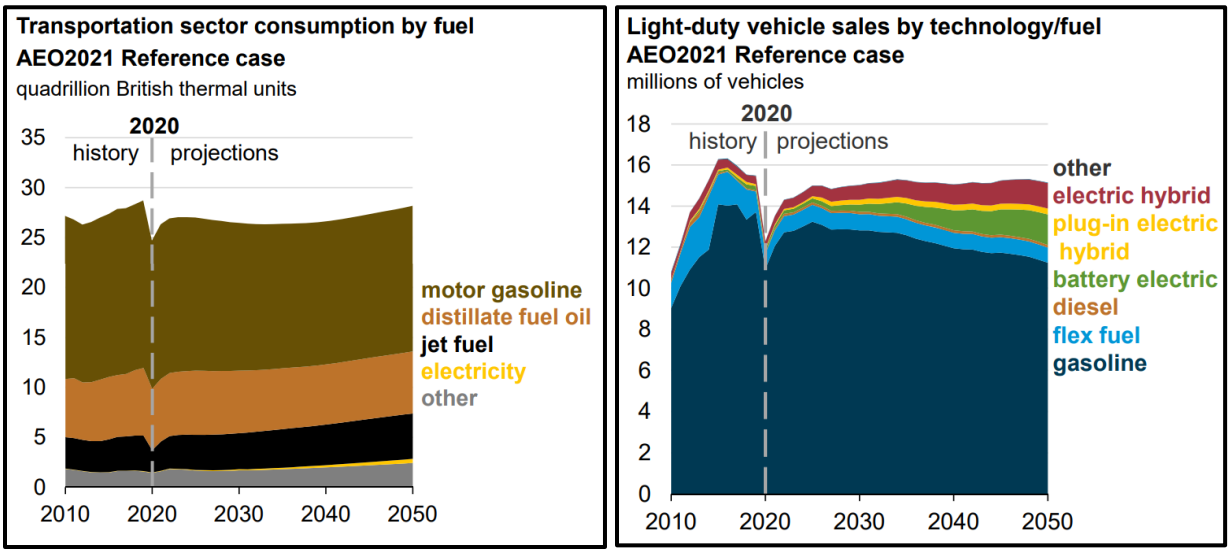

Figure 1-2: Transportation sector fuel consumption and predicted light duty vehicle sales [1].

As is evident from an energy balance diagram of the combustion process in an internal combustion engine, there is scope for improvement since a small fraction of the total chemical energy in the fuel is effectively converted to useful brake work (Figure 1-3). The four strokes of a conventional engine cycle are intake, compression, power and exhaust (Figure 1-4). As the piston is completing the four strokes while turning the crankshaft, a significant fraction of useful energy is lost to heat transfer, friction and exhaust energy combined. At the same time, it is important that chasing efficiency gains does not lead to increased pollutant emissions. The research in this dissertation hopes to provide some insight into possible ways of accomplishing that.

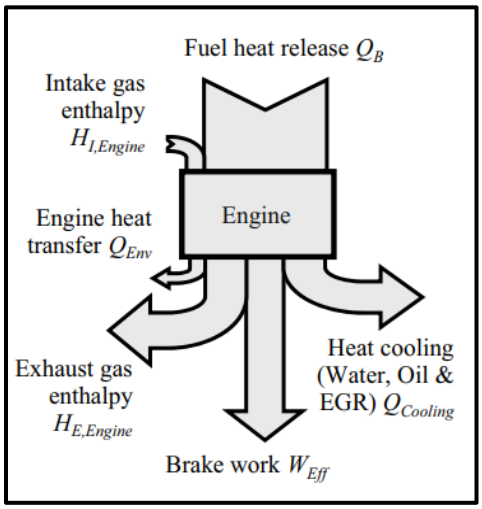

Figure 1-3: Energy balance of an internal combustion engine [8].

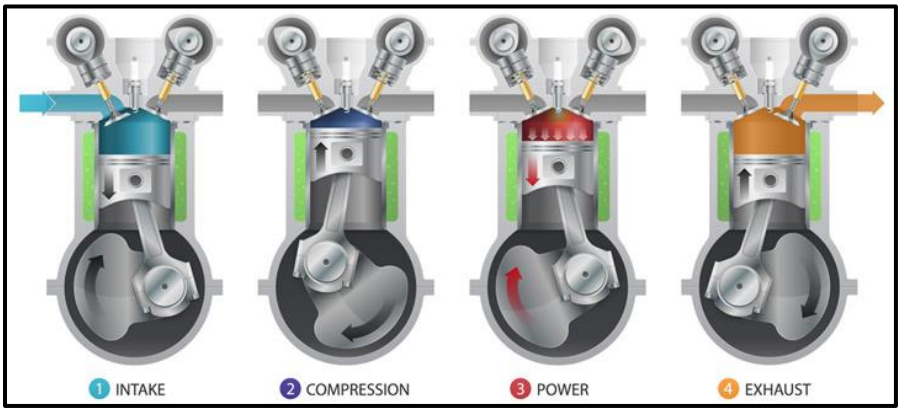

Figure 1-4: Conventional four-stroke cycle of an internal combustion engine [9].

1.2 Objective

The objective of this dissertation is to tackle specific limitations of current generation gasoline fueled engine technology. All the strategies and the respective hypotheses mentioned in the individual chapters of this thesis are experimentally verified. These strategies use a combination of new hardware and different fuel chemistries to achieve higher thermal efficiency, stable combustion and lower engine out emissions.

1.3 Dissertation Overview

This dissertation is split into two parts based on the ignition strategy employed in a gasoline fueled internal combustion engine. Part 1 discusses research that was conducted on an internal combustion engine platform operating with a gasoline spark ignition process. Part 2 discusses research that was conducted on an internal combustion engine platform operating with a gasoline compression ignition process.

Figure 1-5 shows an outline of the current dissertation. Each experimental chapter will address a specific drawback, discuss the literature associated with that drawback and the current state of the art. This is followed by testing out the author's hypotheses through experiments designed to address these issues.

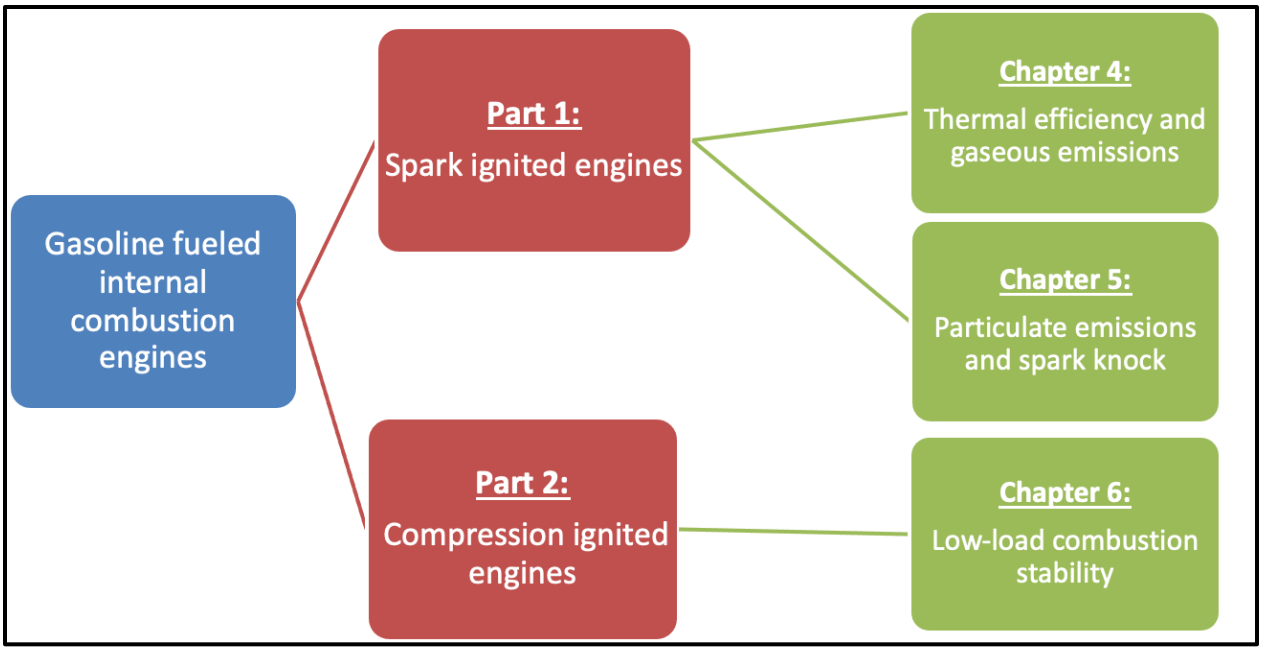

Figure 1-5: Dissertation outline.

The dissertation begins with an introduction and motivation for the thesis, as detailed in chapter 1. This is followed by background concepts as detailed in chapter 2. Chapter 3 explains the evaluation methods and data analyses for both parts of the thesis. The experimental chapters of the thesis are organized as follows.

Chapter 4 discusses the limitations of current generation downsized turbocharged gasoline direct injected spark ignited engines with respect to thermal efficiency. This chapter specifically looks into the thermodynamic benefits of operating with an over-expanded cycle over a large region of engine operation. Miller cycle operation over a large area on the engine speed load map is shown to have thermal efficiency benefits and leads to a reduction in NO_X emissions. Miller cycle operation is made possible using hardware changes which allows for the higher boost levels needed to meet power requirements. Comparisons are made on the basis of steady state engine mapping. This effort is followed by comparisons of standardized transient test cycle data to demonstrate real world applicability of the Miller conceptual engine.

Chapter 5 discusses two other major limitations of current generation GDI engines, which are high particulate emissions and engine knock. Particulate emissions are studied at commonly visited knock limited conditions on a spark ignited GDI engine. A unique relationship between particulate emissions and knock that was observed in earlier research is verified and further explored. The effect of hardware changes and fuel chemistry changes on this relationship is investigated. Both changes led to knock limit extension and it was confirmed that the relationship existed even when the knock limit was extended either through Miller cycle operation or through the high octane index fuel.

Chapter 6 pivots to the research conducted on an engine operating in a gasoline compression ignition mode. The issue with combustion stability at light loads and low temperatures in GCI combustion is addressed. Novel hardware in the shape of a dual fuel injector along with fuels of varying reactivity are explored as potential solutions for improving combustion stability and reducing fuel consumption. The dual fuel injector allows enhancement of reactivity of the fuel air mixture in the engine cylinder on demand, therefore allowing a reactivity-controlled compression ignition combustion.

Finally, chapter 7 summarizes the work and provides conclusions from each of the experimental chapters. Suggestions are provided for future work that could further enhance understanding of certain observations from the research in this dissertation.

Chapter 2
Background

2.1 Gasoline Fueled Engines

Most conventional engines can be classified into two major types based on their combustion strategy. These are spark ignited engines and compression ignition engines. Most engines in the world run on either of two primary petroleum derived products: gasoline or diesel. Spark ignited engines are primarily run on low reactive gasoline fuel while compression ignited engines are primarily run on high reactive diesel fuel. As a result, the engine community often refers to spark ignited engines as “gasoline” engines and compression ignited engines as “diesel” engines [8].

2.2 Gasoline Spark Ignition Engines

Spark ignited engines are equipped with a spark plug which releases an electrical discharge in the cylinder. This electrical discharge initiates the flame by ionizing the air fuel mixture and forming a flame kernel. The flame begins as a laminar flame but quickly transitions to a turbulent flame. The turbulent flame consumes the air fuel mixture in the cylinder as it propagates and quenches as it approaches the cylinder walls which are maintained at relatively colder temperatures [8,10]. Spark ignited engines can be further classified into two types based

on the strategy they employ for the induction of air. These are naturally aspirated engines and forced induction engines.

Naturally aspirated engines induct air into the cylinder at atmospheric pressure. The engine load is controlled only using a throttle valve. As a result, almost the entire engine speed load map is a throttled operation with wide open throttle conditions corresponding to peak load at different engine speeds. On the other hand, forced induction engines or boosted engines make use of additional boosting hardware which compresses air from atmospheric pressure to higher pressures in order to force more air into the cylinder. The ideal gas law suggests that higher pressure is directly proportional to greater mass. Increasing the air pressure increases its density and allows for more air to be packed into the cylinder.

2.2.1 Downsized Boosted Gasoline Direct Injection Engines

The higher intake air pressures associated with boosted engines allow these engines to be sized of smaller displacement which the industry terms as “downsizing”. The late 2000s and early 2010s saw a huge shift in the gasoline engine market. Downsized boosted engines began to displace their larger naturally aspirated counterparts due to a number of benefits that are well documented in literature [11–15].

These benefits include increased torque and power compared to similarly sized naturally aspirated engines [16], lower frictional and heat transfer losses due to the lower surface area of mating surfaces and lower throttling losses [17]. The smaller geometries reduce the overall weight of the engine and thus the overall weight of the vehicle. The difference in sizes of a downsized engine compared to a natural aspirated engine of engines with equally rated power is depicted in Figure 2-1. The higher pressures due to boosting allow the throttle valve to reside in more open positions over a larger range of operation over the engine speed-load map. A

combination of lower pumping losses and lower frictional and heat transfer losses leads to higher thermal efficiency and lower fuel consumption [18]. Wada et al. demonstrated a 10% reduction in brake specific fuel consumption compared to their baseline 1.8 L naturally aspirated engine when developing a new downsized 1.5L turbocharged engine [16]. A comparison of the brake specific fuel consumption of both engines over their respective speed-load maps is shown in Figure 2-1.

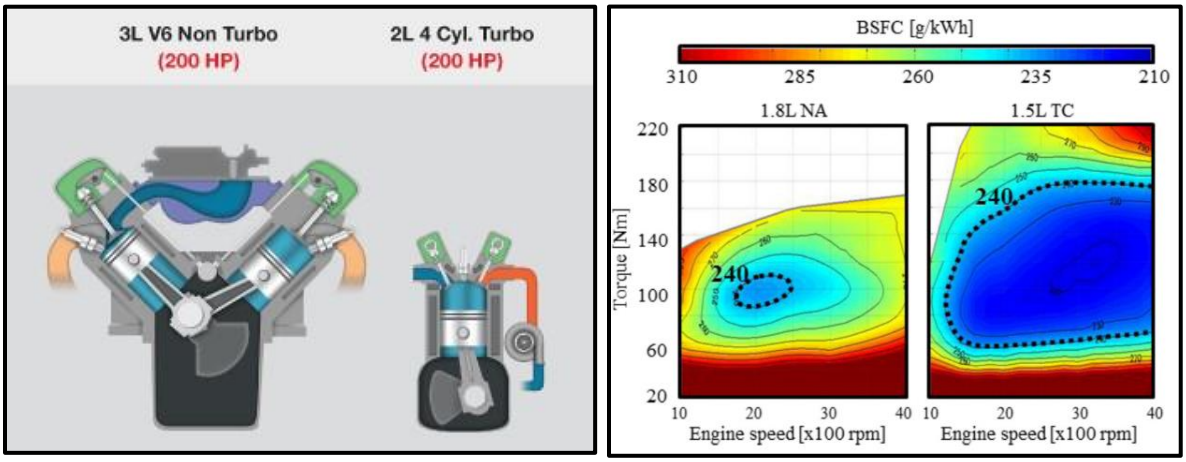

Figure 2-1: Downsizing with boosting allows smaller engine geometries and thus fuel consumption benefits [16,17].

Downsized engines are equipped with additional hardware that allows the air entering the cylinder to be pressurized above atmospheric pressure. This additional hardware is usually either a turbocharger or a supercharger. Superchargers are mechanically driven positive displacement pumps that compress the intake air. Superchargers are usually powered by a belt or chain drive from the engine's crankshaft. As a result, the engine is the energy source for compressing the air. While superchargers have the benefit of faster response to the throttle, they inherently lower the engine efficiency since they draw power from it. Turbochargers are an alternate boosting hardware which uses the exhaust gas enthalpy that would have otherwise been wasted to compress the intake air. A turbocharger consists of a turbine and a compressor mechanically

connected by a shaft. The energy extracted from engine exhaust, which enters the turbine and is expanded to a lower pressure, is used to compress the intake air to the engine. Turbochargers provide the benefit of reducing exhaust gas enthalpy losses. However, they do impose backpressure at all times even during throttled operation when boosting is not required. Manufacturers of turbochargers have employed "wastegate" valves that allow the exhaust gas to bypass the turbine vanes and therefore resolve the issue of higher pumping losses to a certain extent. Figure 2-2 shows the schematic layouts of different non-electric forced induction systems. Figure 2-3 illustrates the working mechanism of a typical single stage turbocharger.

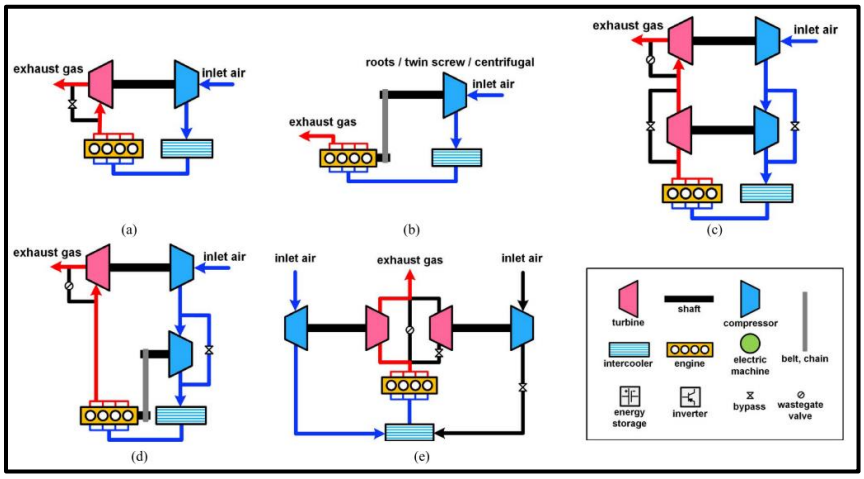

Figure 2-2: Schematic layout of non-electric forced induction systems (a) Single-stage turbocharger (b) Mechanical supercharger (c) Regulated two-stage turbocharger (d) Low-pressure turbocharger with high-pressure mechanically driven supercharger with bypass (e) Parallel sequential turbocharging [19].

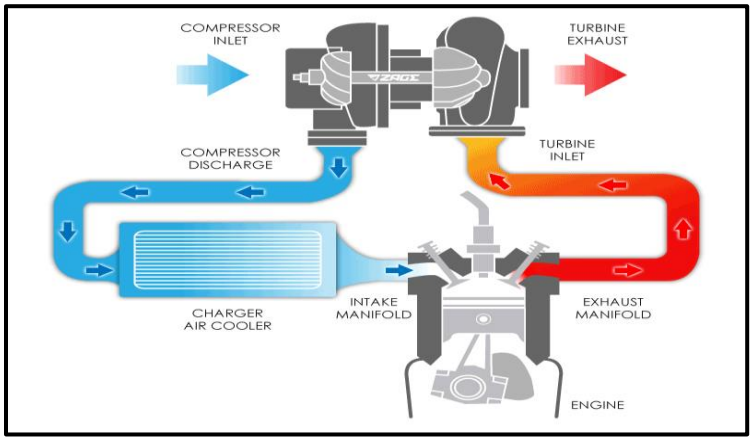

Figure 2-3: Schematic of a turbocharger [Source: https://gomechanic.in/blog/turbocharger-and-its-major-types/].

Turbochargers can be broadly classified into two types based on their turbine vanes. These are “fixed geometry turbos” and “variable geometry turbos”. Fixed geometry turbos as the name suggests are equipped with a fixed set of turbine vanes whose aspect ratio does not change. As a result, the compressor is controlled using the “wastegate” valve as mentioned above which controls the amount of exhaust flow to the turbine vanes. Variable geometry turbos on the other hand use different control strategies to control the aspect ratio of the vanes and thus provide greater degree of freedom of controlling boost as shown in Figure 2-4.

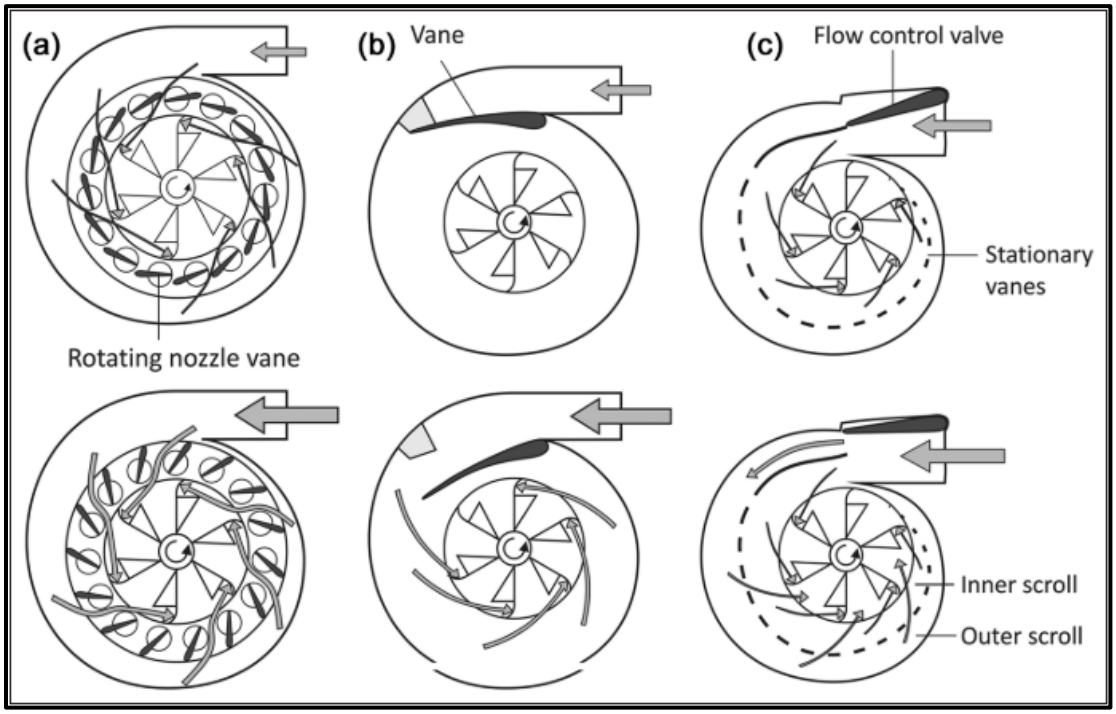

Figure 2-4: Types of variable geometry turbo (VNT;VAT;VFT) (a) VNT: Variable geometry Nozzle Turbine (b) VAT: Variable throat Area Turbine (c) VFT: Variable Flow Turbine [20].

The benefits provided by VGTs compared to their fixed geometry counterpart are improved low speed torque, faster transient response and lower fuel consumption [21–25]. Moreover, they are advantageous compared to fixed geometry turbochargers since they require less specific enthalpy gradient to generate sufficient power to spin the compressor [21]. While

VGTs are very commonplace in diesel engines [26], they are somewhat of a challenge to implement on gasoline engine platforms. Due to stoichiometric operation of gasoline engines, the exhaust gas temperatures encountered by the turbine inlet are usually much higher at full load on a gasoline engine than they would be on a diesel engine [20]. As a result, the turbine vanes and the actuating mechanism must be made of materials that can reliably perform at high temperatures. If they can be implemented on gasoline engines, they allow for more flexibility of valve timings that can be employed using variable valve timing mechanisms to further improve thermal efficiency of the engine [27,28]. The operation of a typical variable geometry turbocharger is shown in the Figure 2-5.

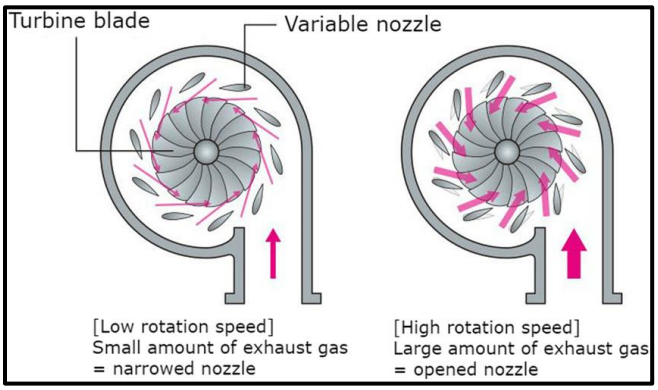

Figure 2-5: Variable geometry turbo operation [29].

Electrically assisted induction systems such as e-turbos and e-compressors have also been drawing interest in the gasoline boosted engine community with the theory suggesting that the additional electrical machine can store excess energy and then use that energy to reduce turbo lag and lead to faster transient response. The schematic of electric forced induction systems is shown in Figure 2-6. While this application has not become mainstream yet for passenger vehicles, it has been extensively used in the racing community, particularly in Formula 1 since the new hybrid turbocharged engine era starting in 2013.

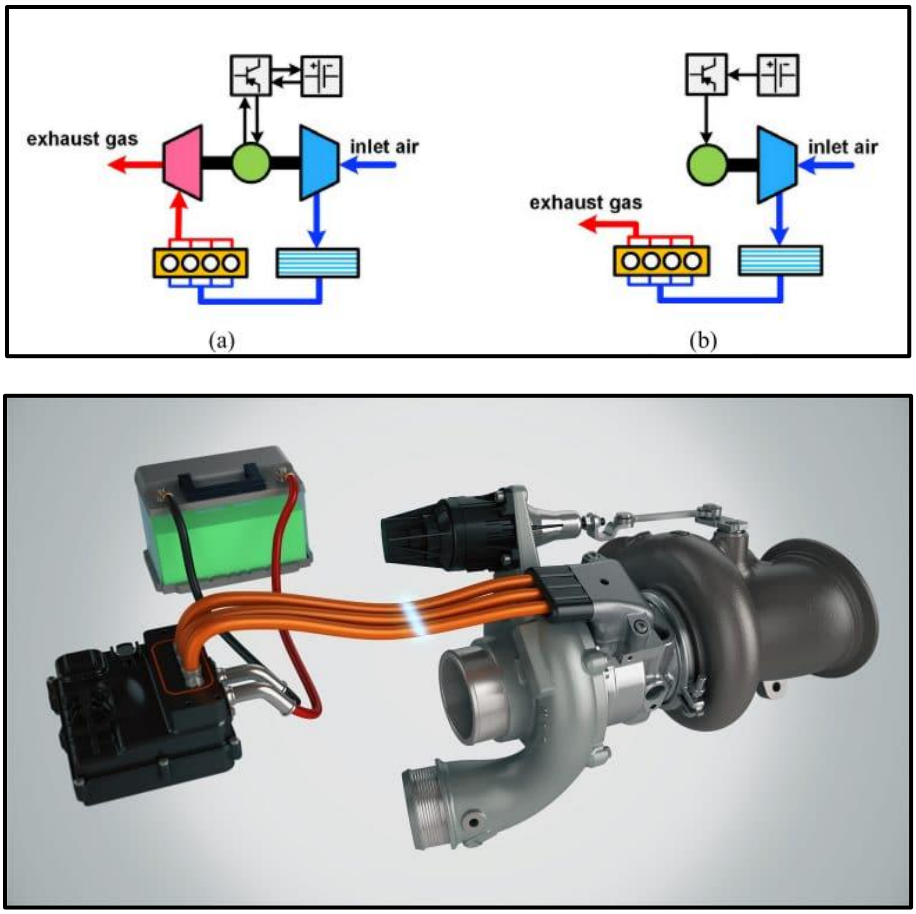

Figure 2-6: Schematic layout of electric forced induction systems [19].

2.2.2 Knocking in Spark Ignition Engines

Engine spark-knock or simply ‘knock’ refers to a phenomenon that occurs in spark ignited gasoline fueled internal combustion engines. It is abnormal combustion that occurs when the unburned charge called ‘end-gas’ auto-ignites due to high temperatures and pressures in the cylinder before a propagating premixed turbulent flame can consume it.

Following the initiation of the flame kernel after the spark discharge, the turbulent flame propagates across the cylinder consuming the air fuel mixture in the cylinder. However, as it does so, it also compresses the unburnt end gas. The degree of compression of the end gas

depends on when the flame was initiated using the spark in the cycle. The earlier the spark is initiated, the higher the propensity of knock to occur as the compression of the end gas is intensified with the rising motion of the piston in the cylinder. The Figure 2-7 shows the sequence of events leading up to engine spark knock with the flame propagation leading to compression of the end gas and eventually autoignition.

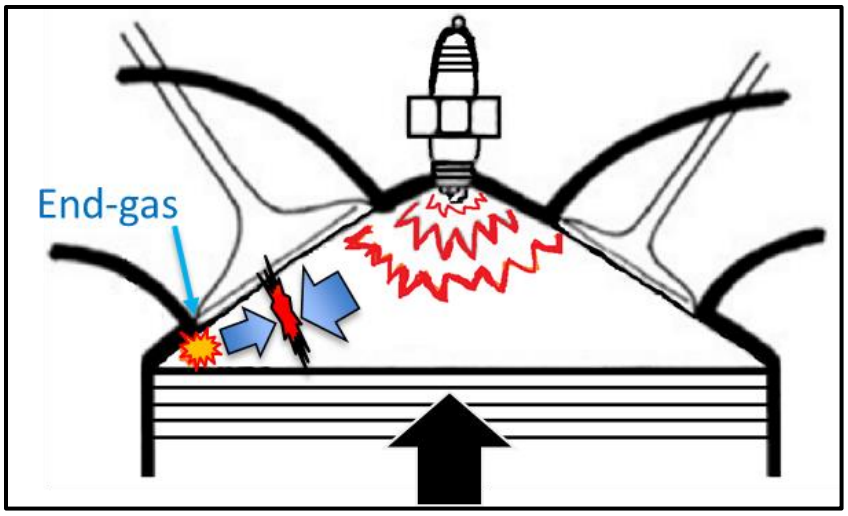

Figure 2-7: Illustration of spark knock in SI engines [30].

Although a constant volume instantaneous combustion is desirable in terms of higher thermal efficiency, there are undesirable consequences of spark knock. These include lack of controlled combustion and high intensity pressure oscillations. These high intensity pressure oscillations propagate as waves across the combustion chamber and result in a high pitch pinging sound and eventually hardware damage. The author of this dissertation had the unfortunate experience of encountering one such event that led to engine hardware damage and to the engine having to be replaced entirely. Some pictures from the incident mentioned showing the aftermath are presented below in Figure 2-8.

Figure 2-8: Damage to Ford Dragon 1.5L engine valves, piston, liner and head due to heavy knock event.

A good rule of thumb is that the more resistant to knock an engine is, the more efficient it can operate [31]. Spark timing determines the combustion phasing in gasoline SI engines. However, at conditions where the engine is prone to knock which is usually at low engine speeds and high engine loads, they are forced to operate inefficiently to avoid spark knock. Engines are more prone to knock at low engine speeds and high loads compared to when the same loads are run at higher engine speeds as the end gas in the combustion chamber has a greater residence time in the cylinder allowing more time and thus a higher chance for it to auto-ignite. The greater residence time is due to the slower burn rate which is a result of lower mean piston speed.

Merola et al. [32] used an optically accessible engine to capture high speed images of premixed turbulent flame propagation across the combustion chamber. While normal combustion

cycles showed a single flame front originating at the spark plug location gradually consuming the air fuel charge in the cylinder, a knocking cycle showed the existence of multiple flame fronts. Hot spots in the combustion chamber as seen in the Figure 2-9 led to multiple sites of autoignition. Schießl et al. [33] obtained laser induced fluorescence (LIF) images knock events from an optically accessible engine which clearly showed regions of end-gas autoignition. One such image is shown in Figure 2-10.

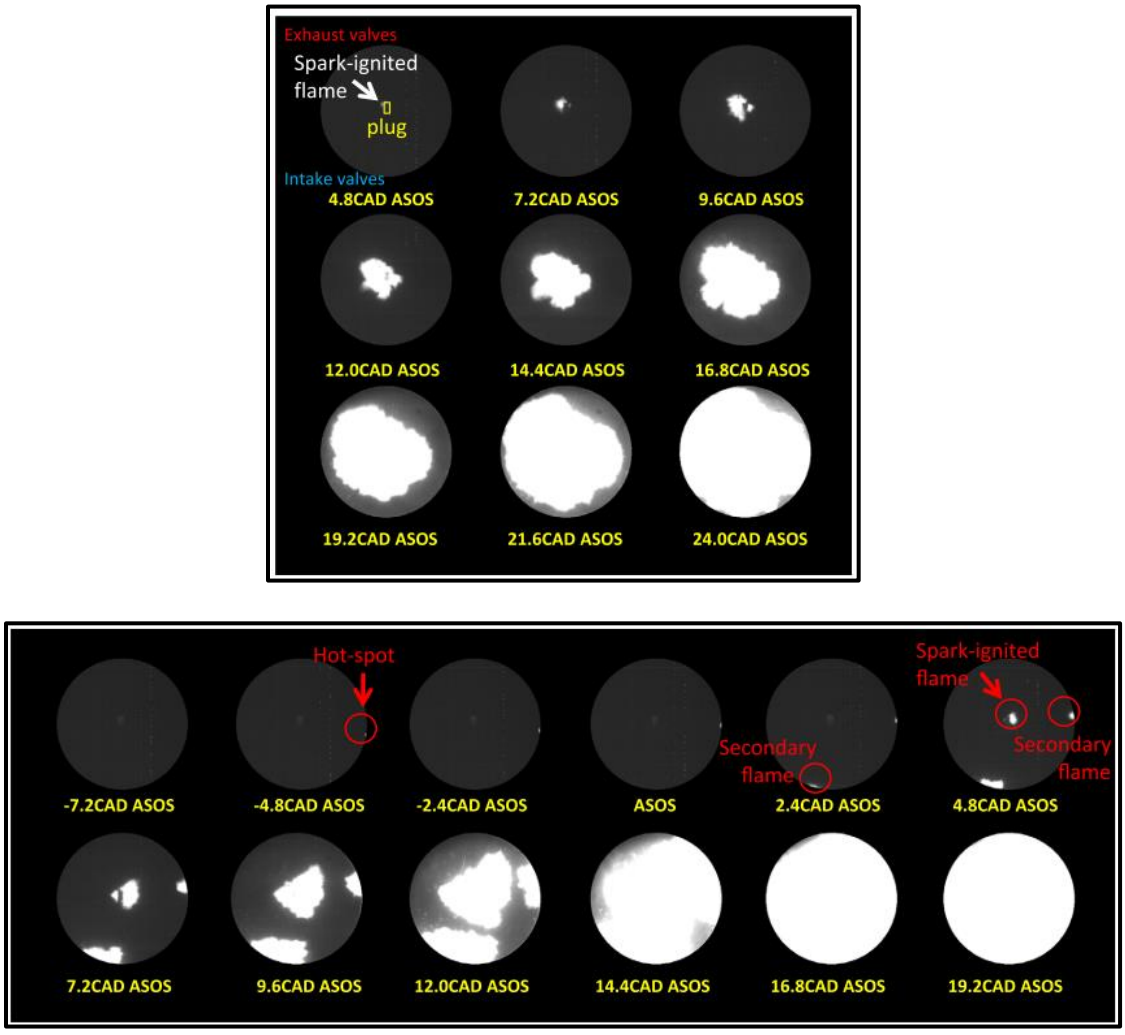

Figure 2-9: Flame propagation during normal combustion vs. during knocking [32].

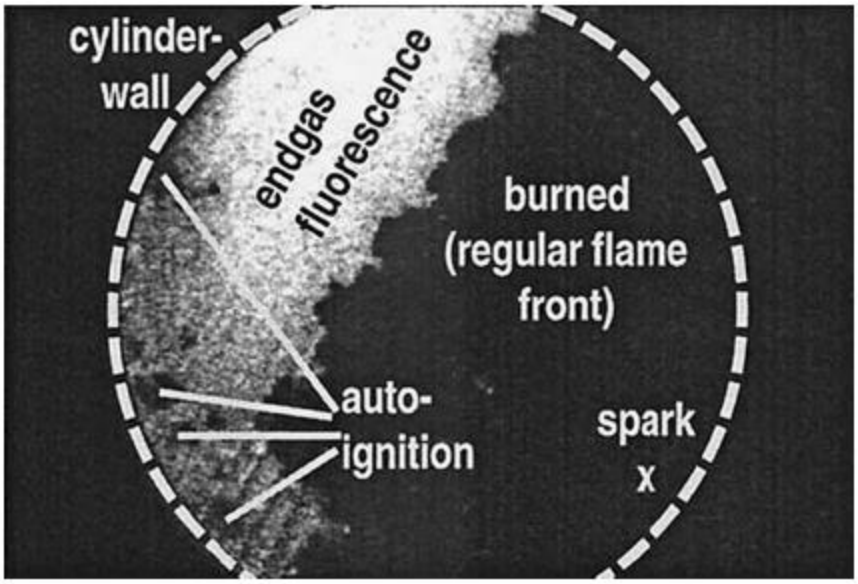

Figure 2-10: Laser Induced Fluorescence (LIF) image of a knocking cycle [33]**.**

Combustion phasing in engines is closely related to thermal efficiency. Phasing the combustion too early can lead to high compression work since cylinder pressure increases after ignition. On the other hand, phasing combustion too late can lead to not enough stroke length available in the expansion stroke to efficiently extract useful work. Engines run most efficiently by phasing combustion in between these two scenarios and this timing is called 'Maximum Brake Torque or 'MBT' timing.

The transition from naturally aspirated engines to downsized boosted engines has led to numerous benefits as detailed in an earlier section. However, in doing so, it has led to the engine be more prone to knock. As a result, a combination of different strategies than those used with naturally aspirated engines have to be used to resolve this issue.

In the industry, it is common for knock to be tackled by retarding spark timing. While this effectively reduces knocking, a consequence is that you light your spark very late in the cycle well after Maximum Brake Torque timing. As a result, the cycle is not run efficiently from

a thermodynamic point of view. Other ways of reducing knock propensity and advancing the knock limited combustion phasing of the engine is by using high octane rated fuels [30,31,34–42] and dilution of the fuel air charge using exhaust gas [43–49] both of which lower the reactivity of the end gas. Figure 2-11 shows the potential for extracting greater indicated work per engine cycle by switching to a high octane rated fuel at knock limited points.

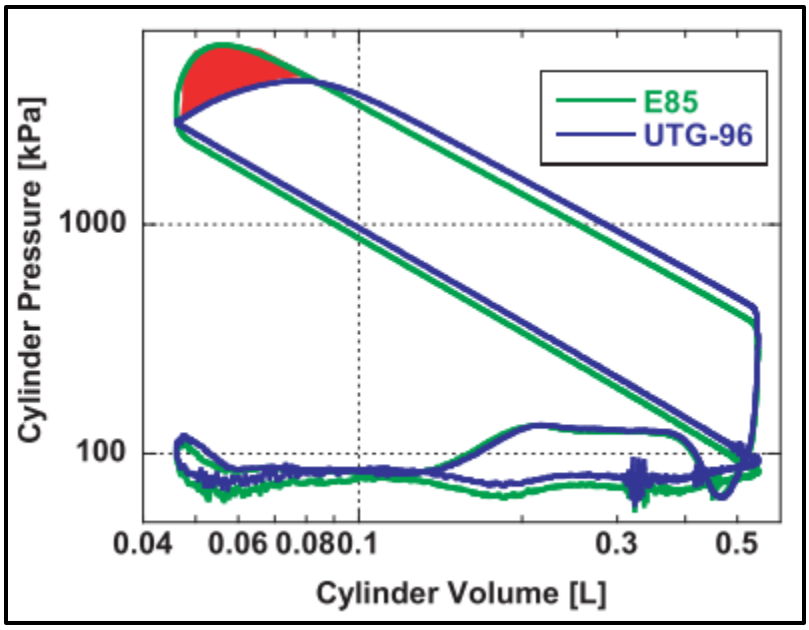

Figure 2-11: Excess work per cycle that can be extracted by advancing the knock limit using high octane fuels [50]**.**

While using high-octane rated fuels that are not as readily available as gasoline seems like an impractical solution, researchers have looked into the possibility of using a combination of gasoline fuels of varying reactivities. Octane-on-demand strategies involve leveraging two sets of injectors, usually one set of port injectors and a second set of direct injectors fueled by two separate fuels. This allows the calibrator to use the low reactivity fuel only at knock limited conditions and use the less refined high reactivity fuel over most of the engine speed load map. Benefits include lower knock propensity and reduced fuel consumption as a consequence of running the engine more efficiently.

2.2.3 Miller Cycle

Gasoline engine combustion is based on the ideal Otto cycle which has equal magnitudes of compression ratio and expansion ratio. As a result, the Otto cycle fails to extract the enthalpy from exhaust gases when the exhaust gas is expelled the combustion chamber at pressures greater than the intake pressure. This is where the modified four stroke over-expanded cycles come in. Unlike the Otto cycle, over-expanded cycles utilize expansion ratios greater than compression ratios to expand combustion products down to lower pressures so as to extract more useful work per cycle [8] as seen in Figure 2-12.

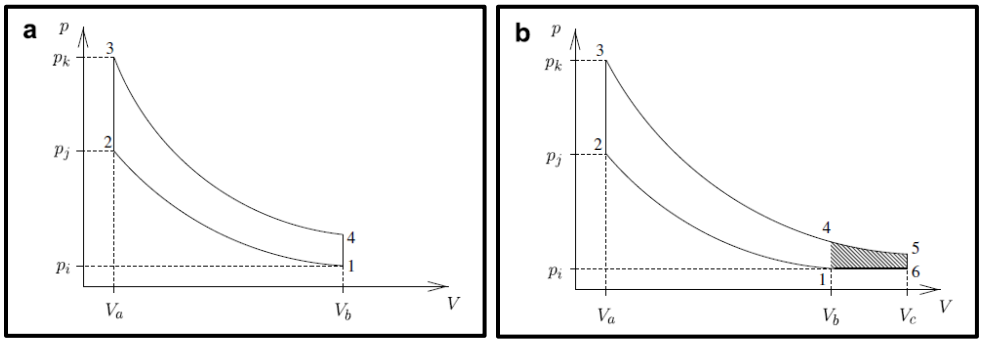

Figure 2-12: Otto and Miller air standard cycles [51].

The two most popular over-expanded cycles are the Atkinson cycle and the Miller cycle. Both cycles share some similar themes with differences in the patents filed for each and frequently both terms are used interchangeably in the literature. Atkinson's original patent for over expanded cycles used a combination of poppet valves, cams and over center arms to mechanically make the expansion stroke greater than the compression stroke. Miller on the other hand leveraged intake valve timings to reduce effective compression ratio to values lower than the geometric compression ratio of the engine. Since Miller filed his patent for boosted engines

with intercoolers, some people also differentiate between the two cycles based on whether they are implemented on a naturally aspirated engine or a boosted engine.

In modern applications, Atkinson and Miller cycles are implemented leveraging intake valve timings. There are two ways of doing this. These are:

1. LIVC: Late Intake Valve Closing
2. EIVC: Early Intake Valve Closing

These are achieved with specially manufactured intake cams that change the lift profile of the intake valves. LIVC holds the intake valve open at peak lift for extended period of time closing the valve well after the cylinder has passed BDC. EIVC on the other hand closes the intake valve earlier than conventional timing by opening the valve up to partial lift which is a fraction of the maximum lift. LIVC reduces the effective compression ratio either by pushing the intake air back into the intake ports. EIVC accomplishes the same by first expanding the air and then recompressing it. Typical lift profiles for LIVC and EIVC cams are shown in Figure 2-13.

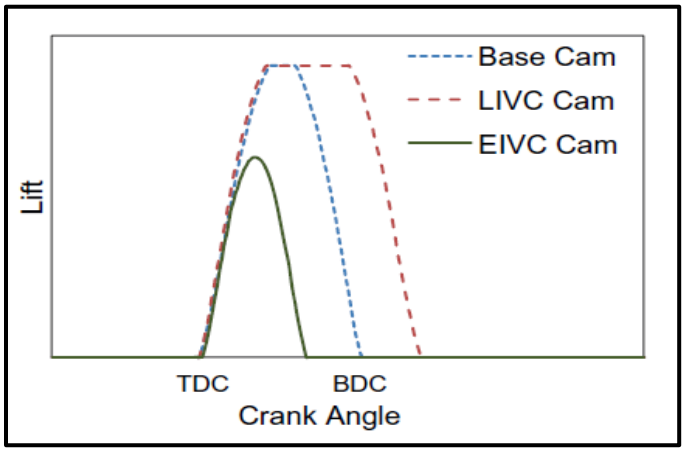

Figure 2-13: Illustration of different cam profiles [52].

While over-expanded cycles provide thermal efficiency benefit, they are limited by reduced volumetric efficiency that limits the maximum power attainable from the engine.

Variable valve timing hardware allows modern engines to switch from Miller/Atkinson cycle operation at low loads to conventional Otto cycle operation at high loads. This allows the engine to meet power requirements with limited turbochargers available in the market. Transitioning to Otto cycle operation increases the effective compression ratios thus letting engine calibrators meet their load targets at various engine speeds. The benefit of implementing Miller cycle operation at throttle conditions is depicted in Figure 2-14. Both EIVC and LIVC implementation results in lower throttling losses.

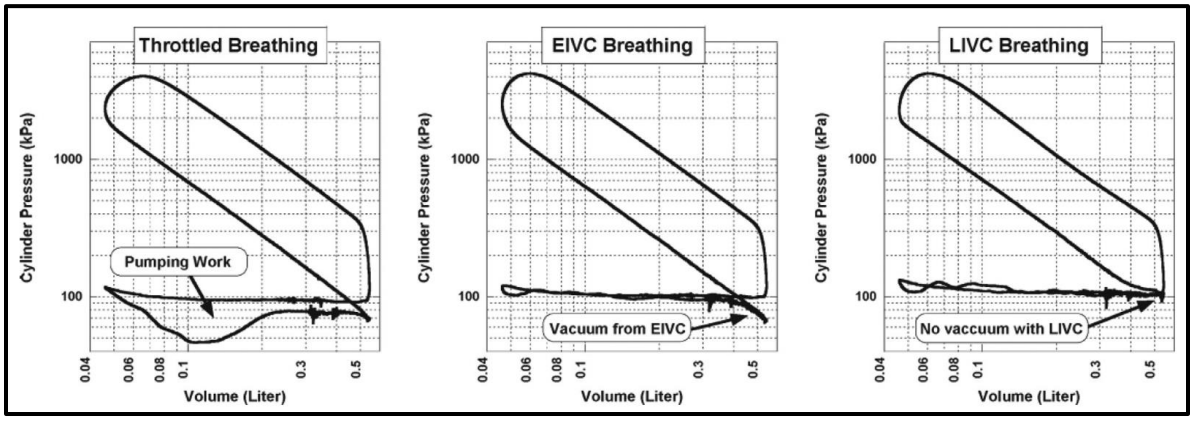

Figure 2-14: Log pressure-log volume diagrams of conventional and over-expanded cycles [40].

2.2.4 Soot emissions from GDI engines

Compression ignition engines running on diesel fuel emit more particulate matter than their spark ignited counterparts largely due to the inherent heterogeneous nature of the diesel spray in the cylinder. As a result, there are regions of locally fuel rich mixture which are ideal for high soot emissions. This has required diesel engine exhaust aftertreatment systems to include a Diesel Particulate Filter (DPF).

Historically spark ignited engines have been mostly port fuel injected to allow sufficient time for the fuel to mix with the air thus creating a more homogeneous mixture. This

homogenous mixture which is locally closer to stoichiometric air fuel ratios leads to less particulate matter emissions. As a result, vehicles powered by gasoline spark ignited engines have not required expensive particulate filters. However, in transitioning from naturally aspirated engines to boosted engines, knock propensity increased and hence the benefits of direct injection in the cylinder at high pressure needed to be leveraged. Injecting the fuel directly into the cylinder resulted in charge cooling effect due to the latent heat of vaporization of the fuel. This reduced temperature of the fuel air mixture allowed extension of the knock limited combustion phasing.

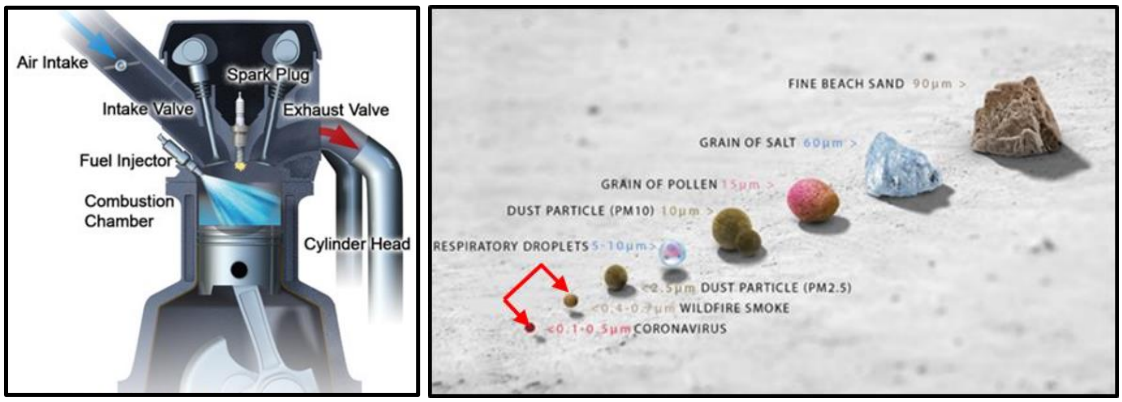

Figure 2-15: Direct fuel injection leading to wall wetting [53] and range of ultrafine particle matter size [54].

A consequence of injecting the fuel directly in the cylinder is that it has less time available for atomization and results in the formation of pool fires through wetting of the combustion chamber surface with fuel as seen in Figure 2-15. While combining direct injection with downsized boosted engines have led to thermal efficiency and fuel economy benefits, it has led to an increase in ultrafine sized particulate matter. Although the ultrafine particles (<100 nm) do not contribute significantly to the particulate mass emissions, they are orders of magnitude higher in number compared to larger sized particles. Moreover, they can be considered a greater

health hazard since they are capable of penetrating deeper in human lungs and eventually make it into the bloodstream [55] as seen in Figure 2-16.

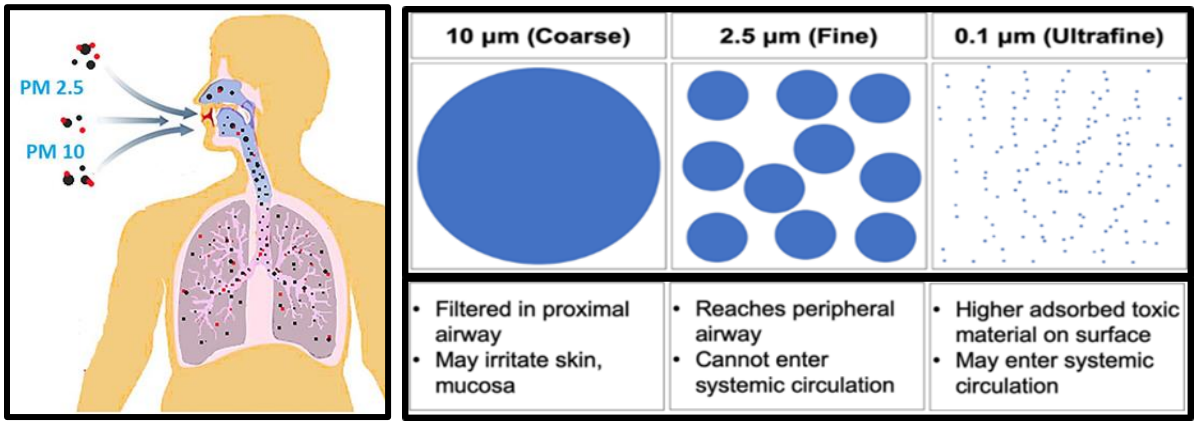

Figure 2-16: Ultrafine particles overview and health concerns [53,56].

Incomplete combustion of fuel and lubricating engine oil can lead to the formation of volatile species [57]. Although a very small fraction of engine oil is consumed in modern engines, oil consumption can lead to a significant fraction of particulate matter emissions [58]. Particulate matter formation is most often a combination of multiple processes as illustrated below. The fuel undergoes pyrolysis in the absence of sufficient oxygen to form the first aromatic ring. The aromatics grow to form polycyclic aromatic hydrocarbons (PAH) through a continuous sequence of H-abstraction and acetylene-addition reactions (HACA). These compounds are precursors for soot particles. After PAH formation, these compounds polymerise to initially form nuclei. The nuclei coagulate to form solid state clusters [59]. Particulate matter emissions from GDI engines can be classified into two major categories based on the diameter of the particle. These are the nucleation mode which refer to smaller sized particles less than 50 nm and accumulation mode which refers to larger particles that are of diameter greater than 50 nm [57].

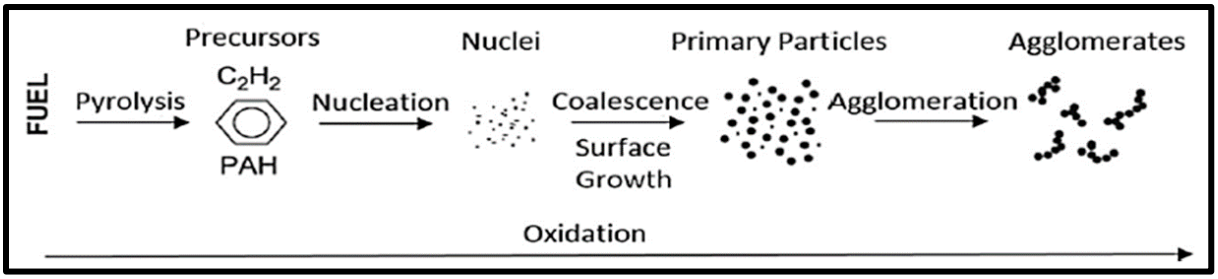

Figure 2-17: Soot formation and evolution mechanism [30].

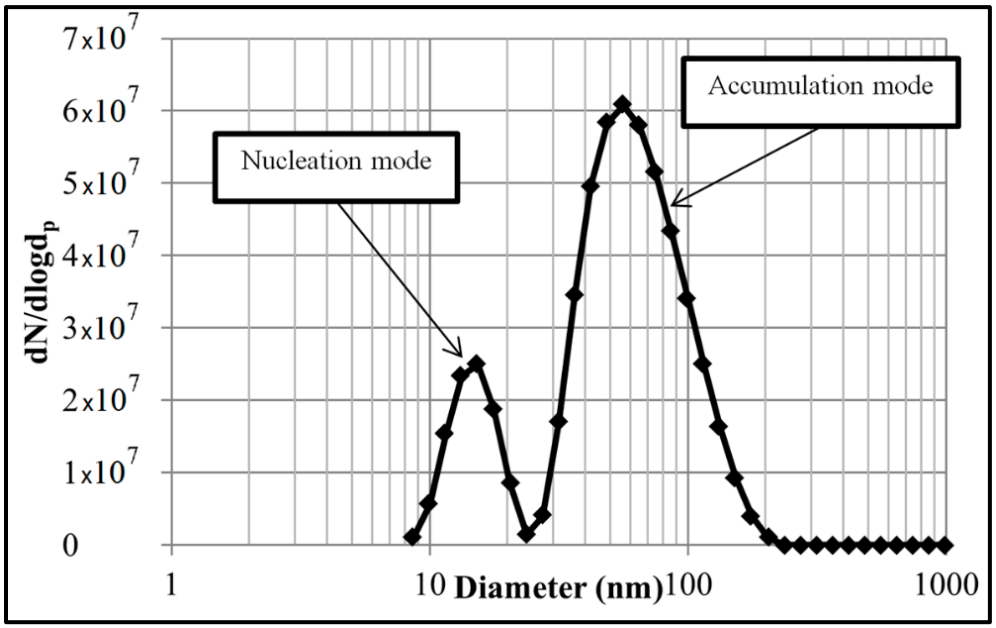

Figure 2-18: Typical Engine Exhaust particle size distribution [57].

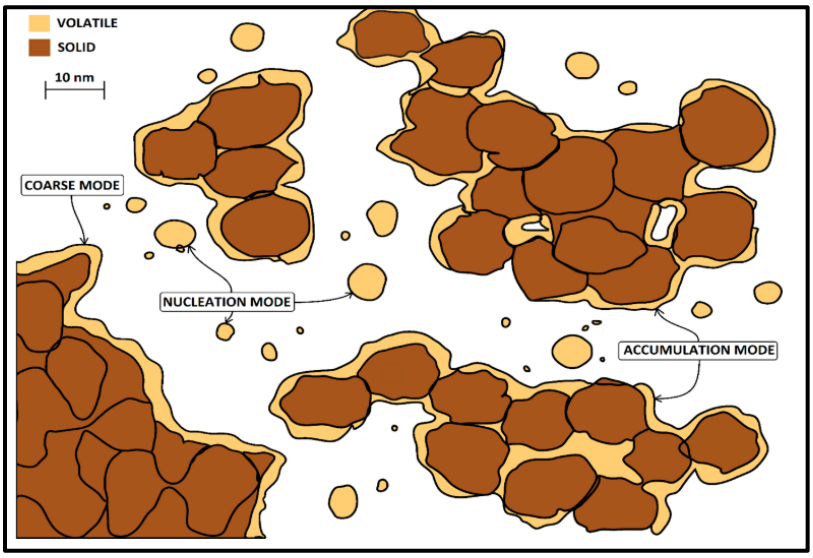

Figure 2-19: Schematic illustration of particles of different sizes [55].

2.3 Gasoline Compression Ignition Engines

As opposed to their spark ignited counterparts, compression ignition internal combustion engines rely on the reactivity of the fuel to promote auto ignition at high temperatures and pressures in the cylinder. Combustion phasing is not controlled by the timing of a spark discharge but rather using the timing of fuel injection in the cylinder. Compression ignition engines operate at lean conditions and higher compression ratios, both of which contribute to their higher thermal efficiencies [8]. Although the term "diesel" engine is often used to refer to compression ignition engines, there is no restriction that prevents gasoline from being used in a compression ignition engine. Hence, it is only natural that this thesis dissertation should explore the realm of gasoline compression ignition as well.

Conventional, compression-ignition engine-powered vehicles face the problem of emitting higher amounts of engine-out soot and tailpipe NO_X compared to their spark ignited counterparts. This can be attributed to the heterogeneous nature of the diesel spray and combustion chemistry associated with it. Dec's [60] popular conceptual model for diesel direct injection diffusion spray displays the various regions of differing local equivalence ratios. The fuel is injected into the combustion chamber where it entraps the surrounding air to create a rich fuel air mixture. The low availability of oxygen in this region leads to low combustion efficiency and formation of soot. The fuel air mixture extends to the outer periphery of the spray where the equivalence ratio approaches stoichiometric values. This results in high local temperatures at the periphery of the spray which contribute to NO_X formation.

As a result, expensive aftertreatment systems must be employed to reduce emissions. Systems to deliver high rates of exhaust gas recirculation (EGR) and turbochargers may be employed to reduce combustion temperature and engine out NO_X emissions. Fuel systems

capable of injecting fuel at up to 2500 bar or higher are used to promote fuel atomization, vaporization, and mixing to reduce soot formation. Particle filters are used in the aftertreatment system to further reduce particulate emissions, and active selective catalytic reduction with urea dosing is used to remove NO_X from the exhaust under lean conditions. The cost of deploying, diagnosing, and operating the systems required for diesel engines to meet future emissions standards may reduce their appeal, despite their high efficiency.

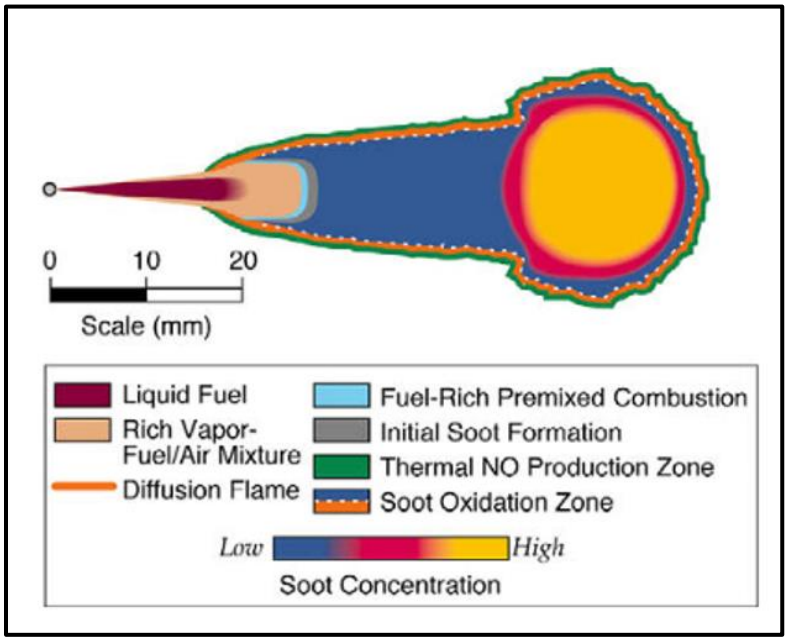

Figure 2-20: Conceptual model for DI diesel compression ignition combustion [60].

2.3.1 Combustion Concepts for Compression Ignition Engines

To address the compression ignition emissions challenge, research has focused on ways of improving mixing to reduce soot emissions, and ways of reducing combustion temperature to improve NO_X emissions. Figure 2-21 illustrates the high soot and high NO_X formation islands on a plot of local equivalence ratio vs local temperature. In conventional diesel engines, increasing EGR to reduce combustion temperatures may lead to a significant increase in soot

emissions. Thus, development of advanced compression ignition engines has focused on suppressing the reactivity of the charge mixture to lengthen the ignition delay resulting in better mixing and lower local equivalence ratio. Longer ignition delay which is the time between the start of injection and significant increase in in-cylinder pressure due to combustion can be achieved using higher rates of EGR, or with a lower reactivity, higher-volatility fuels such as gasoline. In this work, the former will be broadly referred to as low temperature combustion (LTC), whereas the latter will be referred to as gasoline compression ignition (GCI).

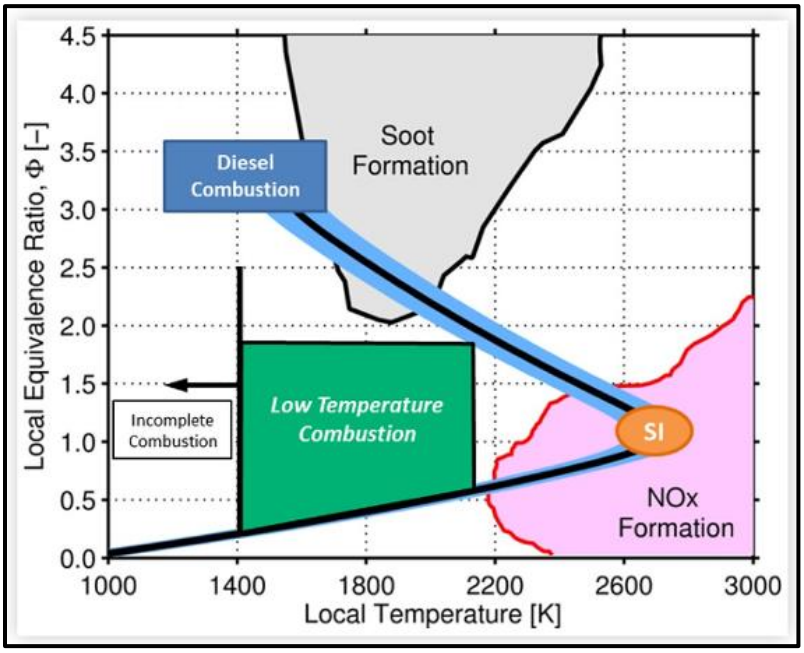

Figure 2-21: Illustration of LTC island avoiding soot and NO_X formation islands [61].

Early research focused on achieving Low Temperature Combustion (LTC) in diesel compression ignition engines through a combination of high levels of EGR and lower compression ratio [62] . Researchers found that this led to low levels of engine out NO_X and soot. Using high levels of EGR, positive ignition delay was maintained, and the diffusion phase of conventional diesel combustion was avoided. High levels of dilution with EGR changed the

thermal and chemical properties of the in- cylinder mixture. Low flame temperatures meant that the coagulation of Polycyclic Aromatic Hydrocarbons (PAH) to form tar and subsequent transformation into soot was not possible. Moreover, the low flame temperatures due to increased dilution and higher heat capacity of the exhaust products in the cylinder led to reduced NO_X formation as explained by the Zeldovich mechanism [63,64].

However, an undesired consequence of achieving LTC using high EGR dilution was the accompanying high levels of carbon monoxide (CO) and unburnt hydrocarbons (UHC) emissions due to the reduced combustion efficiency [65,66]. High levels of boosted intake air are required to overcome this and even then, high EGR LTC can deteriorate combustion stability and lead to misfires. Combustion phasing at high levels of dilution is an added challenge. The low volatility and high reactivity of diesel fuel meant that it was suitable for LTC operation at low loads but could operate only in a narrow region at higher loads [67].

Lilik et al.'s experiments with low temperature Fischer-Tropsch (LTFT) fuel were the exception to this phenomenon. Lilik found that a high cetane rating LTFT fuel enabled low CO and UHC emissions. Also combining large rates of EGR with the high cetane fuel allowed NO_X and PM emissions reduction while preventing large ignition delays. Due to the use of paraffinic fuel, this combustion was termed Paraffin Enhanced Clean Combustion (PECC) [68].

Researchers then began to focus on achieving longer ignition delay using low reactivity, high volatility fuels such as gasoline to promote fuel air mixing. This technology of using gasoline fuel in a compression ignition engine is called Gasoline Compression Ignition (GCI).

Gasoline Compression Ignition strategies have been extensively researched under a variety of different names (HCCI: Homogenous Charge Compression Ignition [69–74]; PCCI: Premixed Charge Compression Ignition [75–77]; PPCI: Partially Premixed Compression Ignition

[76,78–83]; GCI: Gasoline Compression Ignition [61,75,84–91]), but they all essentially represent the same technology.

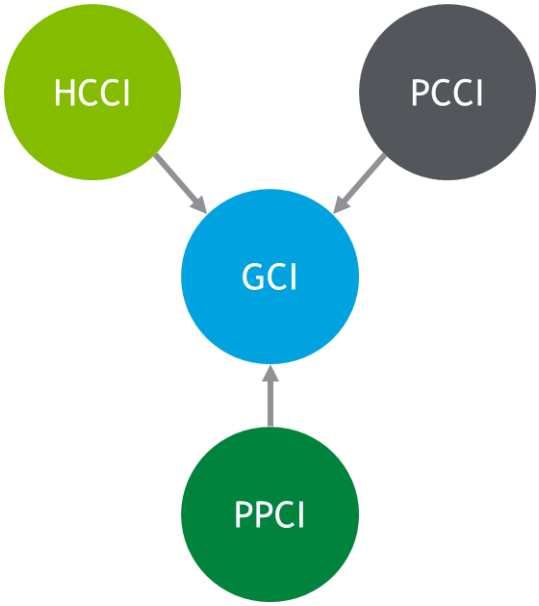

Figure 2-22: Types of gasoline compression ignition.

Kalghatgi and his collaborators have extensively studied different GCI strategies [92,93] to simultaneously reduce NO_X and soot emissions from compression ignition engines. It was observed that high levels of premixing fuel and air can lead to increase in pressure rise rate with increasing engine load. This might even result in high heat release rates before the piston has reached top dead center (TDC). As a result, researchers have explored GCI combustion strategies that operate with a higher degree of premixed combustion at low loads but employ later injection timing at high load to reduce pressure rise rate and emulate diesel-like combustion. Zhang et al. [81,82,90,94] has demonstrated the benefits of running both light duty and heavy duty GCI engines using higher volatility, gasoline-like fuels ranging from low-octane naphtha to regular 87 AKI market gasoline. On the other hand, Cheng et al.'s [95] study with PACE (Partnership of Advanced Combustion Engines) fuel surrogates operating in HCCI mode

reiterated the need to include non-standardized properties in addition to ASTM properties (RON/MON) to fully capture gasoline combustion behavior in HCCI conditions. Sellnau et al. has extensively studied and been involved in the development of gasoline direct injection compression ignition concepts for light duty engines [84,85,87,96–99]. The major challenge with adopting these strategies into production vehicles is due to the limited range of engine operation and lack of control of combustion phasing at certain engine conditions. Multi-mode engines have been explored as an option, but they come with added control complexity [100,101].

GCI continues to be extensively explored due to its ease of implementation using existing hardware and predicted faster market penetration compared to other engine technologies. It offers a relatively cheap and efficient engine and after-treatment system compared to more expensive options. Moreover, these engines could run on lower octane gasolines which means that less energy would need to be spent on refining crude oil [102].

Chapter 3
Experimental Methods and Setup

3.1 Gasoline Spark Ignited Engine System

3.1.1 Engine Setup

The experiments on the spark ignited platform were conducted on a model year 2020 1.5L displacement 3-cylinder Ford EcoBoost Dragon engine. The 2020 Ford Escape and later versions of the vehicle are equipped with this engine. The engine was selected for this project to study the compatibility of boost hardware and Miller valve timings using current commercial engine technology. The engine is equipped with both low-pressure port fuel injectors (PFI) and high pressure direct injectors (DI) allowing flexibility with injection strategy. Dual overhead variable cam timing (VCT) phasors for the intake and exhaust valves allowed a wide range of valve timings for engine mapping. Each set of valves had 60 crank angle degrees of actuation from their respective locked positions. Additional engine details are specified in Table 3-1.

Engine	Ford Dragon
Displacement	1.5 L
Bore	84 mm
Stroke	90 mm
Bore:Stroke Ratio	0.933

Compression Ratio	11:1
Con rod length	143.2 mm
IVO Locked	20 daTDC
IVC Locked	88 dbTDC
EVO Locked	92 daTDC
EVC Locked	0 daTDC
VCT Actuation	60 CAD
Max Power	182 Horsepower
Max Torque	250 N-m

Table 3-1: Model year 2020 1.5L Ford EcoBoost Dragon engine specifications.

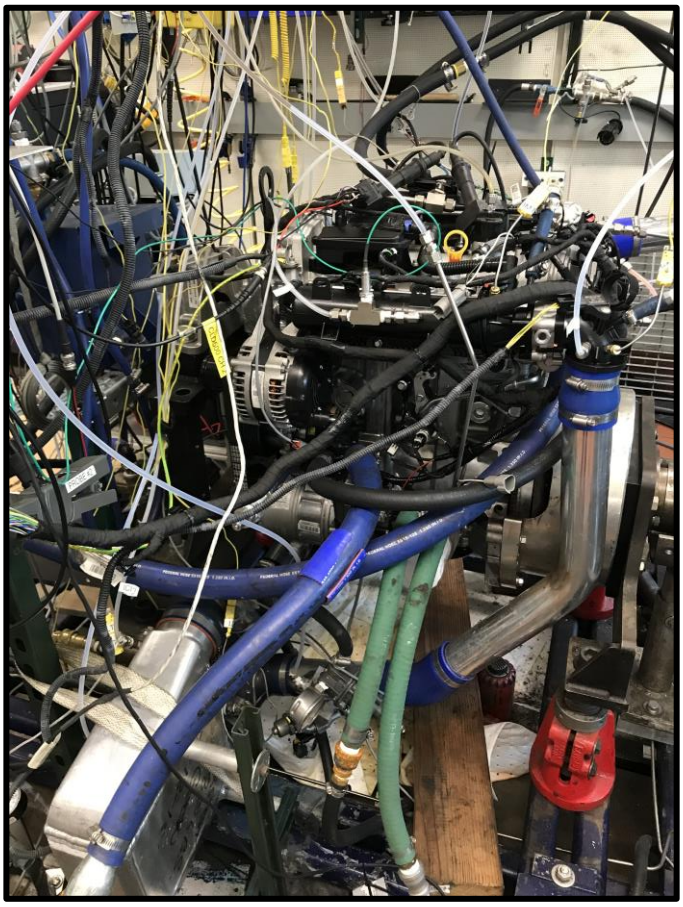

Figure 3-1: Ford 1.5L 3-cylinder EcoBoost Dragon engine at UM Auto Lab.

Baseline engine setup included the stock Continental turbocharger, which is the turbocharger that Ford uses with its production engines. The stock Continental turbocharger is a fixed geometry turbocharger which means that the vanes on the turbine side are always at the same aspect ratio. It is equipped with a wastegate to regulate the amount of boost required at different speed load points on the engine map. The wastegate valve allows the exhaust to bypass the turbine vanes, which prevents the compressor from overboosting especially during throttled operation. Moreover, the wastegate creates less restriction and backpressure than does the turbine vanes allowing for reduced pumping losses.

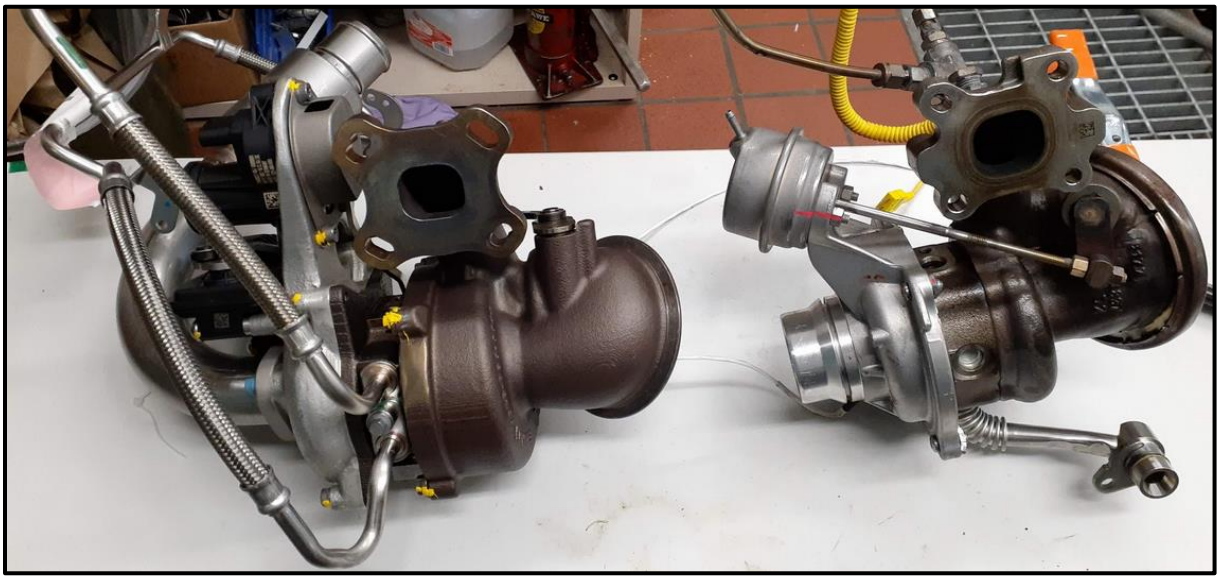

Figure 3-2: BMTS floating nozzle turbocharger (FNT) and stock Continental fixed geometry turbocharger.

Later experiments were conducted by fitting a BMTS prototype floating nozzle turbocharger (FNT) which uses variable turbine vane aspect ratio to control boost. Bulk of this dissertation work on the spark ignited platform was conducted with the engine equipped with the BMTS provided turbocharger. The BMTS turbocharger is a unique prototype since it is also

equipped with a wastegate in addition to the floating nozzle. This is a second degree of freedom for controlling boost and reducing pumping losses.

The production engine is equipped with 11:1 compression ratio pistons. The dual overhead variable cam timing actuators were leveraged to convert the valve timings for the engine map to a representative Miller timing. The high-pressure direct fuel injectors were mounted centrally with the spark plugs mounted next to them. The production spark plugs were replaced with Kistler "6118C" spark plug pressure transducers to measure and record cylinder pressure versus crank angle degree data. Further details about the transducers are provided in the next section.

3.1.2 Remaining Test Cell Setup

The baseline fuel used in this study is premium pump grade E10 (Ethanol 10%vol.) unleaded gasoline supplied by Corrigan Oil Company. The baseline fuel was kept the same throughout the entirety of the project. The fuel was supplied to the test cell from a 250 gallon tank. However, when experimental fuels were tested in chapter 5, the fuel was supplied using 5 gallon containers placed in the test cell. Experimental fuel details are provided in chapter 5. Fuel is conditioned to a temperature of 25^{o}C using an AVL 753C fuel conditioning unit which also vents out any air bubbles that might have entered the fuel to ensure constant temperature and density of fuel entering the fuel rails. Fuel flow is measured using a Coriolis type flow meter present in the AVL 735S system which is used in conjunction with the AVL 753C.

The engine oil used was Ford motorcraft full syntheitc SAE 5W-20. The oil was also kept the same for the duration of the project to eliminate the possibility of differences in friction and engine oil chemistry affecting the particulate emissions. Engine oil was replaced every 1000

hours of operation followed by a break in procedure for consistency. Engine oil temperature was controlled by coolant temperature of the engine. Since continuous high speed, high load testing was not part of this thesis, installation of a separate oil conditioning unit was not warranted.

An AVL conditioned air unit supplies air to the compressor inlet on the engine at a fixed temperature and humidity. To mimic real world ambient air conditions, air temperature was maintained at 25^{o}C and relative humidity at 35%. An LFE (Laminar Flow Element) and a separate air mass flow meter were installed in between the conditioned air unit and the compressor inlet for intake air measurements. The two separate measurements for air flow allow for a daily check to be made on the measurements. An intercooler was installed right after the compressor outlet to keep the compressed intake air entering the intake manifold at a fixed temperature of 25^{o}C. The intercooler heat exchanger is provided with chilled water supply to cool the air down to the demanded temperature.

Coolant temperature and flow were maintained constant with an AVL "ConsysCool" coolant conditioning unit. Coolant temperature was maintained at 85^{o}C for the entirety of testing during this dissertation.

Kistler "6118C" spark plug cylinder pressure piezoelectric transducers were installed for each cylinder to provide in cylinder pressure data that is post processed for heat release analysis. AVL charge amplifiers were used to convert the charge signal to a voltage to read the pressure. An AVL Indimaster and accompanying Indicom indicating system was used as the high-speed data acquisition system for cylinder pressure measurements and high-speed intake pressure measurements. Cylinder pressure was recorded at a resolution of 0.1 Crank angle degrees. An AVL 416 crank angle encoder was bolted to the engine crankshaft to phase the pressure

measurements with the location of the piston. Low speed data was recorded via an AVL PUMA v 1.5.3 data acquisition system.

The exhaust pipe was machined to install multiple probes downstream of the turbine outlet that provide exhaust flow to the emissions bench and particle sizing instruments. Gaseous emissions were measured using an AVL Sesam i60 emissions bench while particulate data was measured using a Cambustion DMS500 fast particulate analyzer.

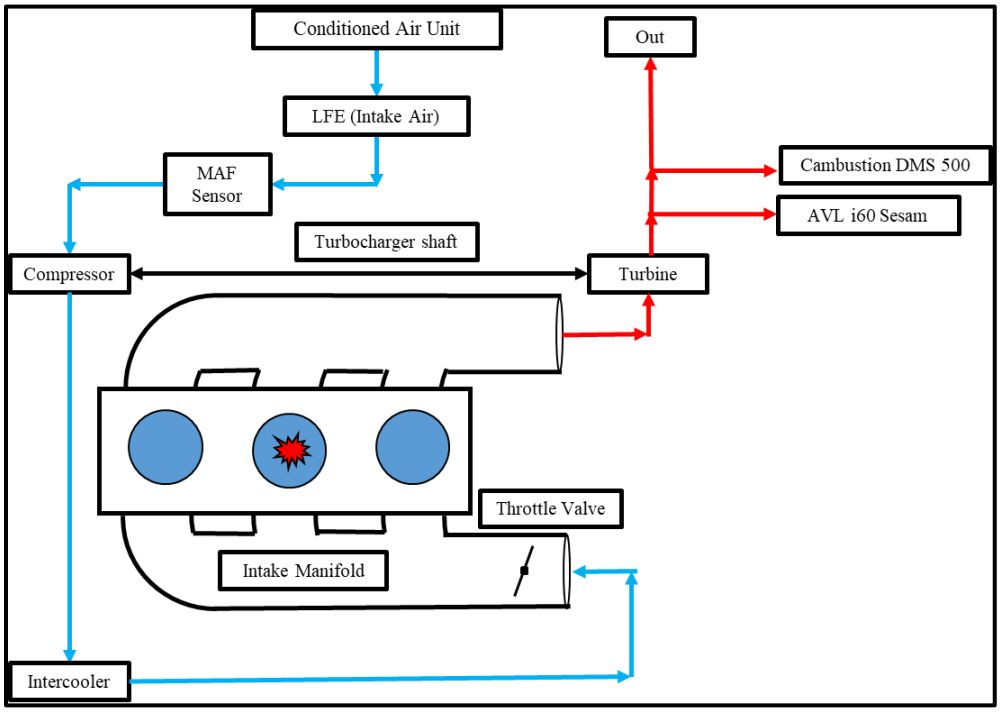

Figure 3-3: Schematic of test cell layout at UM Auto Lab.

3.1.3 Emissions Equipment Setup

A state of the art AVL "Sesam i60" emissions bench is used to collect gaseous emissions data from turbine out exhaust. The emissions bench is equipped with a FID (Flame Ionization Detector) which provides Total Unburnt Hydrocarbon (THC) data as well as methane (CH_4) measurements. It is also equipped with a separate O_2 sensor for detecting oxygen in the exhaust.

Lastly, it also comes with an FTIR (Fourier-transform infrared spectroscopy) that provides concentration of various chemical species that include water (H_2O), nitrogen oxides (NO, NO_2), carbon monoxide (CO), carbon dioxide (CO_2), nitrous oxide (N_2O), ethanol (C_2H_5OH) and ammonia (NH_3). Hydrocarbon speciation data is also provided by the FTIR. The FTIR is an MKS liquid nitrogen cooled detector. Background checks were performed on a daily basis after purging the lines with zero gas to maintain the calibration.

A Cambustion DMS 500 fast particulate analyzer is used for particulate emissions measurements. In addition to providing total particle number on a #/cc basis for particles sizes in the range of 5-1000 nm, it also provides a particle size distribution. This allows the user to measure nucleation and accumulation mode concentration measurements. A conversion matrix installed in the software converts the concentration of particles in various rings to a total particulate mass on a mg/m^3 basis. The DMS500 comes with two stages of dilution: a primary diluter that can go up to dilution ratios of 6:1 and a secondary diluter which allows for much higher dilution ratios like 600:1. For gasoline spark ignited applications, the secondary diluter is usually not required. Filtered exhaust sample flow is passed through a corona discharge which applies a charge to each particle. The particles then enter the classifier where they are attracted to the different classifier rings based on the differences in their charge to drag ratio. The differences in concentration of particles entering the different classifier rings determines the particle size distribution.

3.2 Gasoline Compression Ignited Engine System

3.2.1 Engine Setup

Experiments were conducted on an FEV 0.55 L Compression Ignition Single Cylinder Research Engine (Aramco SCRE) with a modified cylinder head from Aramco. The engine test cell setup is illustrated in Figure 3-4. The engine specifications are listed in Table 3-2.

The bore and stroke of the engine are 86 mm and 94.6 mm respectively. The compression ratio can be varied from 14.6 to 15.85. The highest compression ratio of 15.85 was used for this study and was kept constant throughout the study. The piston bowl geometry is a conventional re-entrant bowl. The exhaust valve is opened during the intake stroke to use the exhaust "rebreathing" strategy to get internal EGR into the combustion chamber. This helps with auto ignition and low load combustion stability. The intake air pressure and temperature are controlled by a Quincy QGV-300 compressor upstream of the engine. The controlled air then makes its way downstream past the sonic nozzle which is used to measure the mass flow rate of the intake air. Downstream of the nozzle, there is a cooled EGR supply if needed. The engine is equipped with both port and direct fuel injectors. Only direct injection was used in these experiments.

Engine	Aramco SCRE
Displacement (L)	0.55
Number of Cylinders	1
Cycle	Four Stroke
Bore	86 mm
Stroke	94.6 mm
Connecting Rod Length	152.1 mm

Number of Intake Valves	2
Number of Exhaust Valves	2
Geometric Compression Ratio	15.85
Fuel Injection	Stock DI/ QuantLogic DI
Air Supply	Quincy QGV-300 Compressor
EGR System	High Pressure Cooled EGR
Piston Design	Conventional Reentrant Bowl
Ignition	Compression Ignition
IVO	7 ^{o}bTDC
IVC	145 ^{o}bTDC
EVO	86 ^{o}aTDC
EVC	245 ^{o}aTDC (rebreathe)

Table 3-2: Aramco single cylinder research engine specifications.

3.2.2 Remaining Test Cell Setup

Fuel was conditioned to 25^{o}C temperature using an AVL 753 fuel conditioning unit and fuel flow was measured using an AVL 733 fuel balance which is equipped with a Coriolis type flow meter. An additional ReSol RS55C conditioning unit and ReSol RS463 flow meter were installed to condition and measure the flow rate of the second fuel. The existing AVL system in the test cell was used for the low fuel consumption measurements of the high reactivity fuel. The newly installed ReSol system was used to supply and measure flow of the lower reactivity fuel. The difference in intake and exhaust pressure that drives the internal EGR during the exhaust rebreathing is controlled using a dual poppet EGR valve downstream of the exhaust manifold.

A Kistler 6052C piezoelectric transient pressure transducer is used to measure cylinder pressure. The charge signal from the transducer is amplified by an AVL Micro iFEM charge amplifier with capability of drift compensation and adjustable time constant. A BEI sensors crank angle encoder is used to encode data at 0.1 CAD resolution between IVC and EVO. An AVL 442 Blowby meter is also equipped to verify that measurements are consistent throughout all experiments of the study. Engine coolant and oil temperatures were maintained by independent AVL conditioning units. An AVL 577 coolant and oil conditioner for supply to the cylinder head and an AVL ConsysLube 25/50 for oil to the engine block.

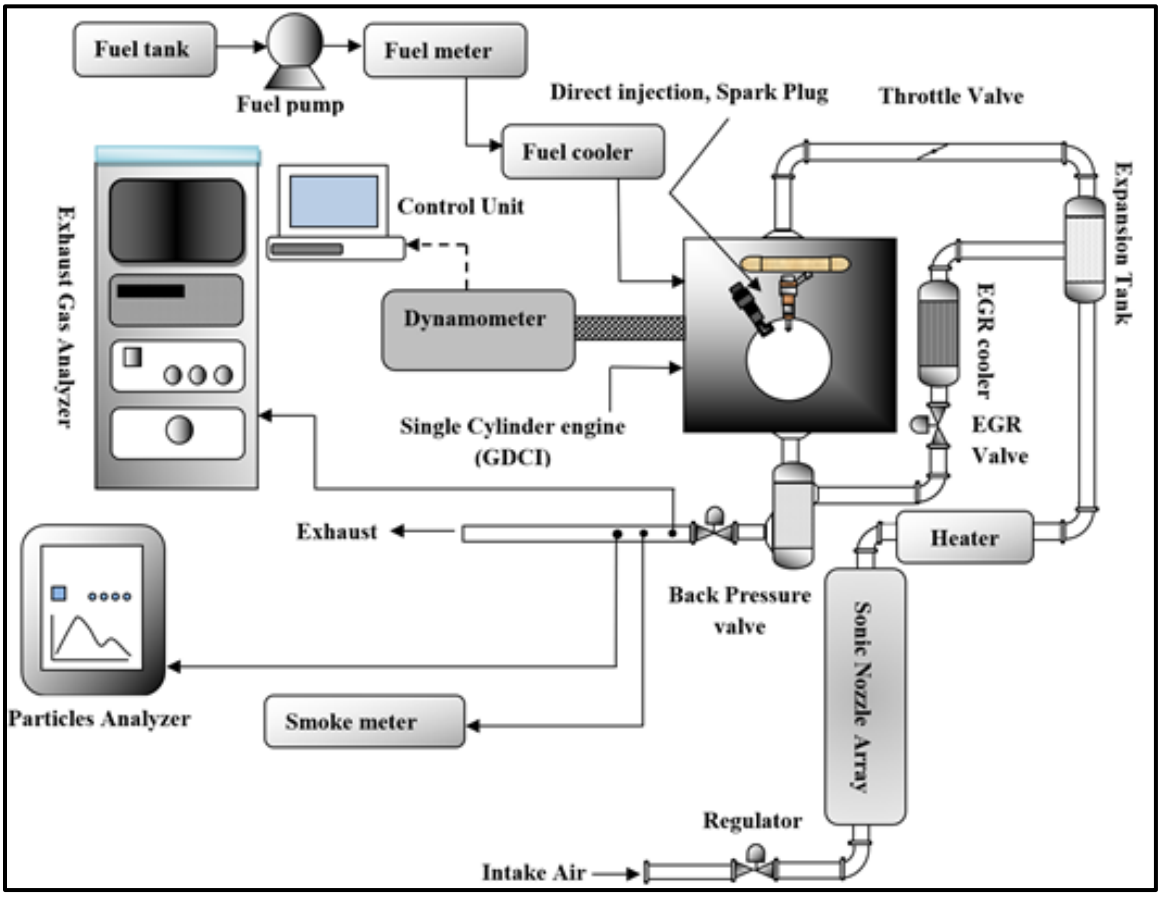

Figure 3-4: Test cell layout for Aramco Single Cylinder Research Engine before the addition of ReSol system.

3.2.3 Emissions Equipment Setup

Engine out gaseous emissions are sampled upstream of the backpressure valve to an AVL i60 emissions bench which measures carbon monoxide (CO), carbon dioxide (CO_2), nitrogen oxides ($NO_X = NO + NO_2$), oxygen (O_2) and total unburnt hydrocarbons (THC) concentrations. THC and CH_4 measurements are provided by a heated Flame Ionization Detector (FID) while the rest of the gaseous emissions are provided by a Non Dispersive Infrared (NDIR) analyzer. Details of the different analyzers that are a part of the i60 emissions bench are provided in the table below. Particulate matter data is recorded using an AVL 483 MicroSoot meter which measures particulate mass and verified with an AVL 415S Smokemeter which provides Filter Smoke Number measurements based on opacity of the filter paper. The filter smoke number is shown to correlate well with the particulate mass data provided by the micro soot meter.

Analyzer	Principle
THC	FID
CH_4	FID
NO_X	NDIR
CO	NDIR
CO_2	NDIR
O_2	NDIR

Table 3-3: Analyzer and their respective principles of operation of i60 emissions bench.

3.3 Engine Data Processing

The following subsections describe the calculations that were made during data post processing in the following chapters.

3.3.1 Volumetric Efficiency Calculations

The actual valve positions were calculated using the locked positions of the valves and phase angles of each of the VCT phasors using the following formulae where EVP and IVP stand for the Exhaust Valve Phase and Intake Valve Phase respectively:

$$EVC_{act} = EVC_{Locked} + EVP \quad \textbf{(3-1)}$$

$$IVO_{act} = IVO_{Locked} + IVP \quad \textbf{(3-2)}$$

$$IVC_{act} = IVC_{Locked} + IVP \quad \textbf{(3-3)}$$

$$EVO_{act} = EVO_{Locked} + EVP \quad \textbf{(3-4)}$$

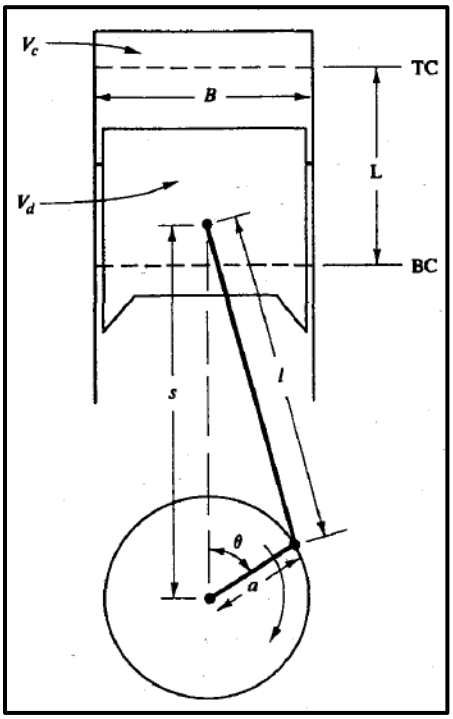

Figure 3-5: Basic geometry of cylinder, piston, connecting rod and crankshaft [8].

From Heywood's book of Internal Combustion Engine fundamentals [8], we can write the following using simple trigonometry (Note all variables are as they are denoted in Figure 3-5):

$$s_{IVC} = \sqrt{(l^2 - (a * \sin(IVC_{act}))^2)} + (a * \cos(IVC_{act})) \quad \textbf{(3-5)}$$

$$s_{EVO} = \sqrt{(l^2 - (a * \sin(EVO_{act}))^2)} + (a * \cos(EVO_{act})) \quad \textbf{(3-6)}$$

The volume of the combustion chamber at any given crank angle can be determined from the position of the piston using the following formulae:

$$V_{IVC} = V_c + \left(\pi * \left(\frac{B^2}{4}\right) * s_{IVC}\right) \quad \textbf{(3-7)}$$

$$V_{EVO} = V_c + \left(\pi * \left(\frac{B^2}{4}\right) * s_{EVO}\right) \quad \textbf{(3-8)}$$

Effective Compression and expansion ratios can then be calculated as:

$$\text{Eff. CR} = \frac{V_{IVC}}{V_c} \quad \textbf{(3-9)}$$

$$\text{Eff. ER} = \frac{V_{EVO}}{V_c} \quad \textbf{(3-10)}$$

The valve overlap is estimated as:

$$\text{Valve Overlap} = EVC_{act} - IVO_{act} \quad \textbf{(3-11)}$$

The volumetric efficiency is then estimated as follows:

$$\eta_{Vol.} = \left(\frac{\dot{m}*2}{\rho*\text{Total } V_d*\text{Engine Speed}}\right) * 100 \quad \textbf{(3-12)}$$

where $\dot{m}$ represents the mass flow rate of air measured experimentally and

ρ represents the density of air calculated according to universal gas law as follows:

$$\rho = \left(\frac{P_{int}}{R_{int} * T_{int}}\right) \quad \textbf{(3-13)}$$

3.3.2 Heat Release Rate Analysis

The apparent heat release rates are calculated from in-cylinder pressure traces using the first law of thermodynamics according to the following equation from Heywood [8] where γ is the ratio of specific heats and is determined from the log P vs log V curve of in-cylinder pressure:

$$\frac{dQ_{net}}{d\theta} = \frac{\gamma}{\gamma - 1} p \frac{dV}{d\theta} + \frac{1}{\gamma - 1} V \frac{dp}{d\theta} \quad (3\text{-}14)$$

3.3.3 Knock Quantification

While there are several knock quantification methods in the literature [103–105], for the sake of consistency with the observations made by Han [30], it was decided that the metric to be used for quantifying knock in Chapter 5 should remain the same as that of Han.

The two metrics used for quantifying knock in this thesis are the KIp2p (Knock Intensity peak to peak) and the KI20 (Knock Intensity 20). Both these metrics involve the filtering of the raw in-cylinder pressure trace. The filtering is done by first converting the pressure traces from the time domain to the frequency domain by applying a fast fourier transformation based on the following equation:

$$\hat{p}(\omega) = \frac{1}{\sqrt{2\pi}} \int_{-\infty}^{+\infty} p(t)\, e^{-i\omega t} dt \quad \textbf{(3-15)}$$

Once converted to the frequency domain, a high-pass filter is used to cut out the frequencies corresponding to normal combustion.

The peak to peak knock intensity is calculated from the difference in the maximum and minimum values of filtered pressure data within the knock window (-20 to 70 ^{o}aTDC). It is calculated as follows:

$$KIp2p = |(max(p(i)) - min(p(i)))| \quad \textbf{(3-16)}$$

where p(i) represents the filtered pressure for the ith crank angle degree.

KI20 on the other hand which is an energy basis calculation is a bit more complicated and sophisticated than the simple amplitude based KIp2p. It is less prone to be affected by external noise such as valve events and is calculated as follows:

$$KI_{20} = \frac{1}{N_{samp}} \sum_{i=1}^{N_{samp}} (p(i) - p_{mean})^2 \quad \textbf{(3-17)}$$

An illustration of this process is reprinted from Han in the Figure 3-6 below.

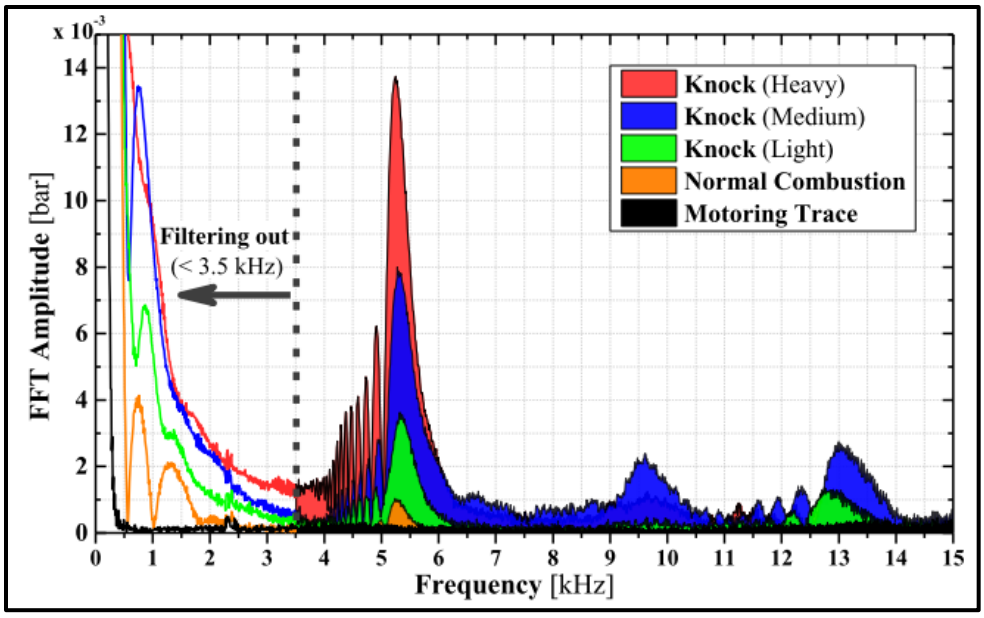

(a)

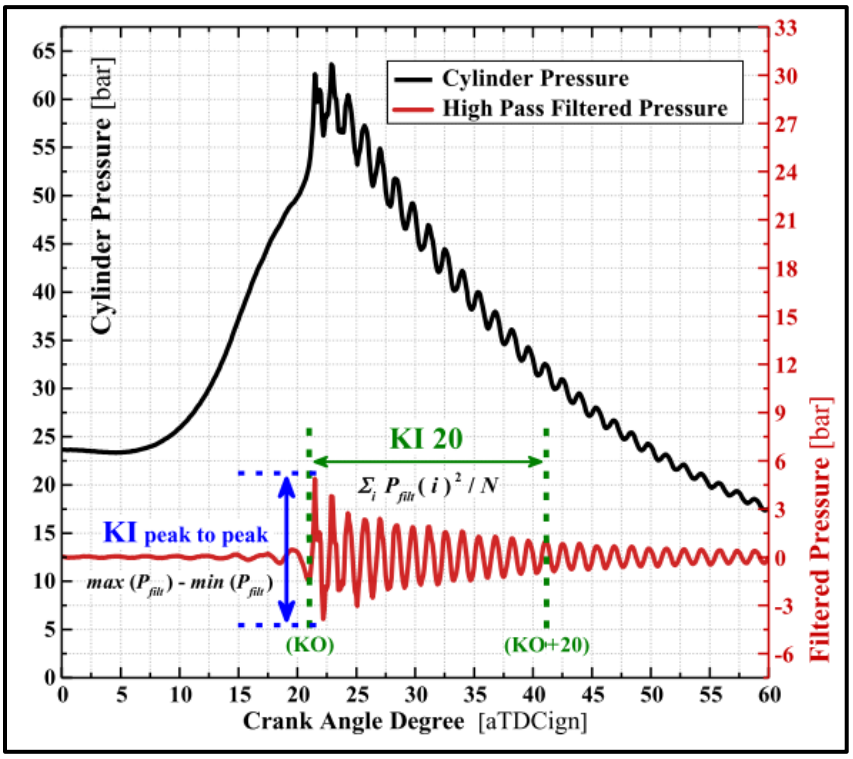

(b)

Figure 3-6: (a) FFT amplitude and cut-off frequency (b) Illustration of raw cylinder pressure trace and filtered cylinder pressure trace of knocking cycle [30].

Part 1: Gasoline Spark Ignition Combustion

Chapters 4 and 5 discuss the research that was conducted on a downsized boosted gasoline spark ignition engine platform at the University of Michigan, Walter E. Lay Automotive Laboratory.

Chapter 4

Expanding the Range of Miller Cycle Operation for a Light-duty Downsized Gasoline Turbocharged Spark Ignition Engine

4.1 Introduction

The benefits of operating an engine on an over-expanded cycle are well documented in the literature from a thermodynamic standpoint [8,106–109]. In addition to thermodynamic benefits which lead to lower fuel consumption, other benefits of operating under Miller or Atkinson cycle include reduced NO_X emissions [110,111] and reduced knock propensity [112].

Szybist et al. [40] observed reduced fuel consumption and engine out NO_X emissions at a mid-load condition of 8 bar BMEP which was a throttled condition on their light duty SI engine setup. Both LIVC and EIVC strategies resulted in higher thermal efficiencies compared to the baseline throttled operation. The thermal efficiencies observed with the LIVC strategy were higher than that observed with the EIVC strategy. An interesting observation from this study was that although the LIVC strategy led to higher engine thermal efficiency, it resulted in higher particulate emissions possibly due to suboptimal fuel air mixing. Another potential reason for the high particulate emissions is the potential fuel impingement on the intake valve due to the variable valve actuation setup which meant that the intake valve closing and opening could not be controlled independently.

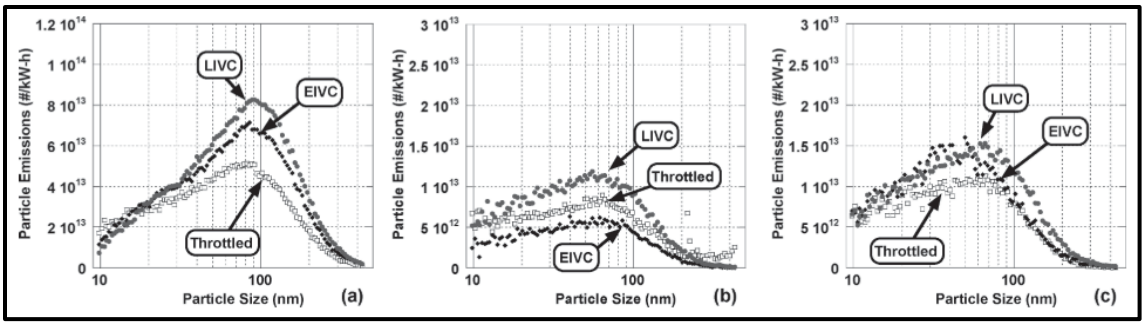

Figure 4-1: Illustration of increased particulate emissions using LIVC strategies at 3 different direct injection timings [40].

Researchers have also compared different Miller timing strategies to quantify which of them is the most beneficial. Bozza et al. [113] conducted a study of different Miller valve timings using a 1D GT Power model and predicted significant reduction in fuel consumption with EIVC operation compared to the baseline Otto cycle operation. Li et al. [52] compared LIVC and EIVC operation to the baseline operation at low and moderate engine loads at two different speeds on their light duty 2.0L 4 cylinder DISI engine. They were able to leverage the anti-knock capabilities of Miller cycle operation to equip their engine with high compression ratio pistons. The increase in compression ratio led to higher thermal efficiency at low loads where the engine was throttled. At the higher load condition, the Miller cycle operation led to lower knock propensity and thus advancement of combustion phasing which led to a higher thermal efficiency.

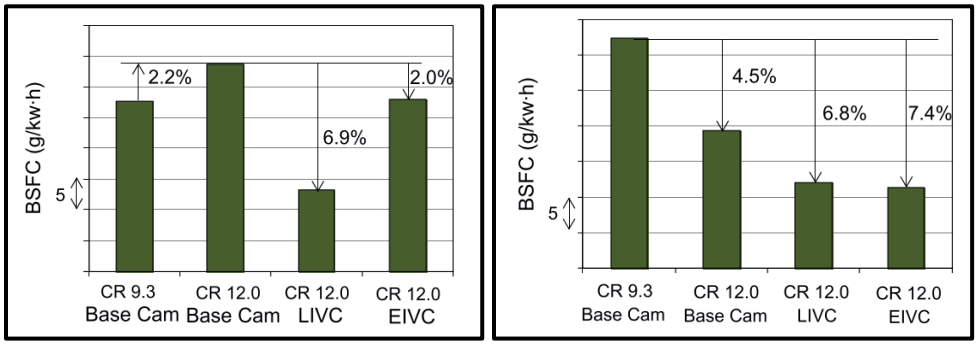

Figure 4-2: Comparison of Otto and Miller cycle operation at a) High load condition b) Low load condition [52].

Luisi et al. [114] used a Fiat MultiAir Variable valve actuation system to test both EIVC and LIVC strategies on a downsized turbocharged engine and found that EIVC strategies led to reduced levels of turbulence in the cylinder. This resulted in slower flame propagation. Also high load engine testing using both strategies showed that LIVC could be run with more advanced combustion phasing compared to EIVC due to its superior capability of mitigating knock. The consensus from a majority of these studies is that the LIVC strategy can lead to lower fuel consumption, higher degree of knock mitigation and enhanced turbulence in the cylinder compared to the EIVC strategy. Hence LIVC is seen more often in production vehicles than is EIVC.

Researchers have also explored the possibility of combining Miller valve timing strategies with other engine technologies to further improve thermal efficiency and reduce emissions. Wei et al. [115] demonstrated that boosted Miller operation combined with a split direct injection strategy led to greater knock resistance. Shen et al. [116] combined Miller operation with low pressure cooled external EGR and demonstrated better fuel economy and reduced knock propensity. They also demonstrated lower engine out NO_X emissions but reduced combustion efficiency, since diluting the charge with exhaust led to higher carbon monoxide and unburnt hydrocarbon emissions.

Al-Hasan et al. [117] discusses the need for more advanced turbomachinery to be used in conjunction with Miller valve timings through engine tests and 1-D simulation. Although Miller timings and increased compression ratio led to fuel consumption benefits over the WLTP cycle, it resulted in slower response time and lower low end torque without the newly adapted turbocharger. An improved compressor design combined with a radial axial turbine led to a 45%

improvement in time to torque response while still maintaining the thermodynamic benefits of Miller operation.

A common theme of all the studies that are in the literature is that they are mostly limited to steady state operation at low to moderate engine loads where the benefits of over-expanded cycles are realized through more open throttle positions. This shows the need for a study where the fuel economy and emissions reduction benefits of Miller cycle operation have to be demonstrated over transient engine operation which more closely resembles real world operation.

Moreover, the Environmental Protection Agency's benchmarking studies of recent production vehicles raises another research question [47,118,119]. These studies show us the extent of Miller/ Atkinson cycle implementation in current generation production vehicles. The EPA uses a metric called the Atkinson ratio to quantify the extent of Millerization at a certain point on the engine speed load map. The Atkinson ratio is defined as the following:

$$\text{Atkinson Ratio} = (\text{Effective Expansion Ratio})/(\text{Effective Compression Ratio})$$

This means that a value greater than 1 indicates overexpanded operation while a value closer to 1 represents a traditional Otto cycle operation. From the maps of Atkinson ratios that were published in these studies, one may notice that the region occupied by Atkinson Ratio >1 is much larger for both the naturally aspirated engines compared to their boosted downsized counterpart. The boosted downsized Honda engine barely registers speed load points where the Atkinson ratio is greater than one and even if it does, it is mostly limited to low engine loads. This strategy is employed in downsized boosted engines due to the inability of boosted Miller operation to be able to meet load and power requirements due to reduced volumetric efficiency coupled with suboptimal boosting hardware. While the larger geometry naturally aspirated engines can still meet their load requirements through Atkinson operation due to their larger

geometric compression ratios, the downsized engines have to switch from Miller operation to traditional operation as engine load demand is increased.

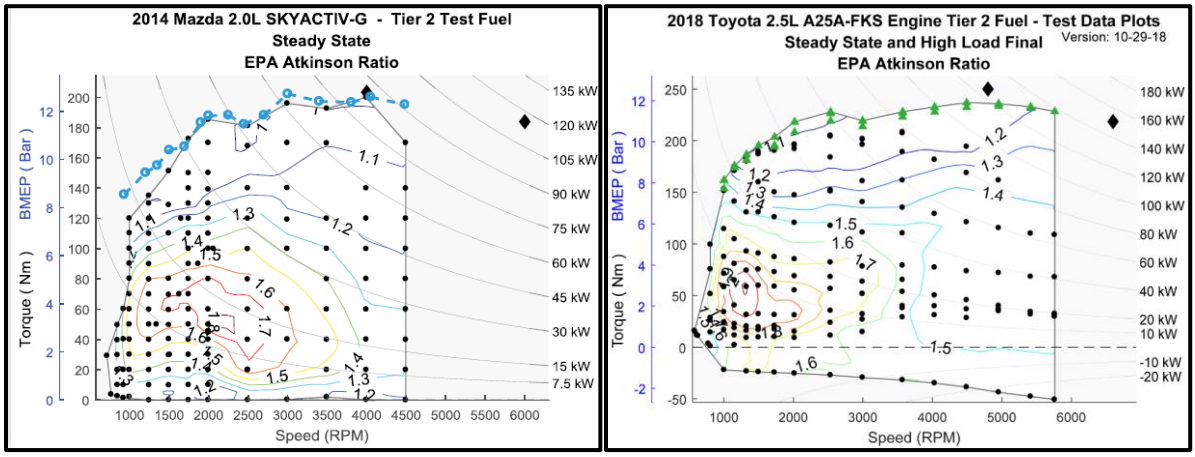

Figure 4-3: Atkinson ratio maps of a 2014 Mazda 2.0L and 2018 Toyota 2.5L (both naturally aspirated) [47,118].

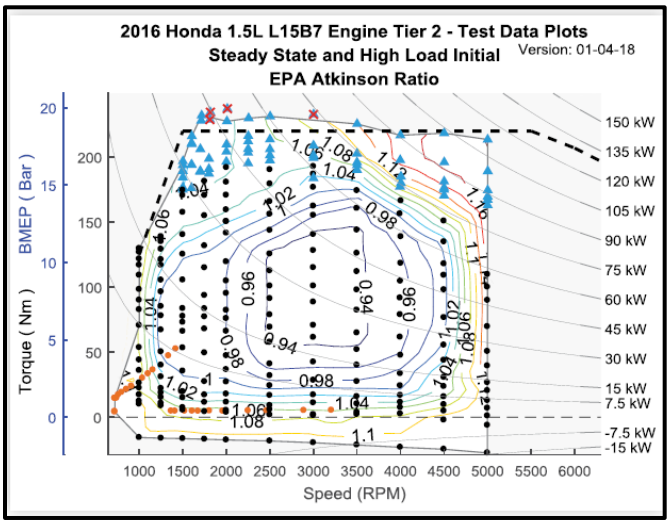

Figure 4-4: Atkinson ratio map of a 2016 Honda 1.5L (downsized turbocharged) [119].

Thus, a study is proposed to convert an existing state of the art downsized turbocharged Ford 1.5L engine to a Miller engine using a prototype BMTS manufactured floating nozzle turbocharger. The prototype turbocharger aims to meet the increased boost demand associated with Miller operation while still maintaining fast time to torque response that is desirable for the driver. Although variable geometry turbochargers are popular in use with diesel engines, they are

not as commonplace on gasoline platforms. This is largely due to high flow rates and high variation in exhaust flow rates associated with gasoline engines. Furthermore, the high turbine inlet temperatures due to stoichiometric operation of gasoline engines can be the cause for mechanical failures of floating nozzle actuators. BMTS prototype turbocharger has undergone numerous design evolutions through simulation and turbocharger bench testing to overcome these issues before it was sent to the University of Michigan for engine testing.

4.2 Experimental Methods

The experiments were conducted in three phases. Figure 4-5 illustrates the three different phases of experiments that were involved in this chapter of the dissertation.

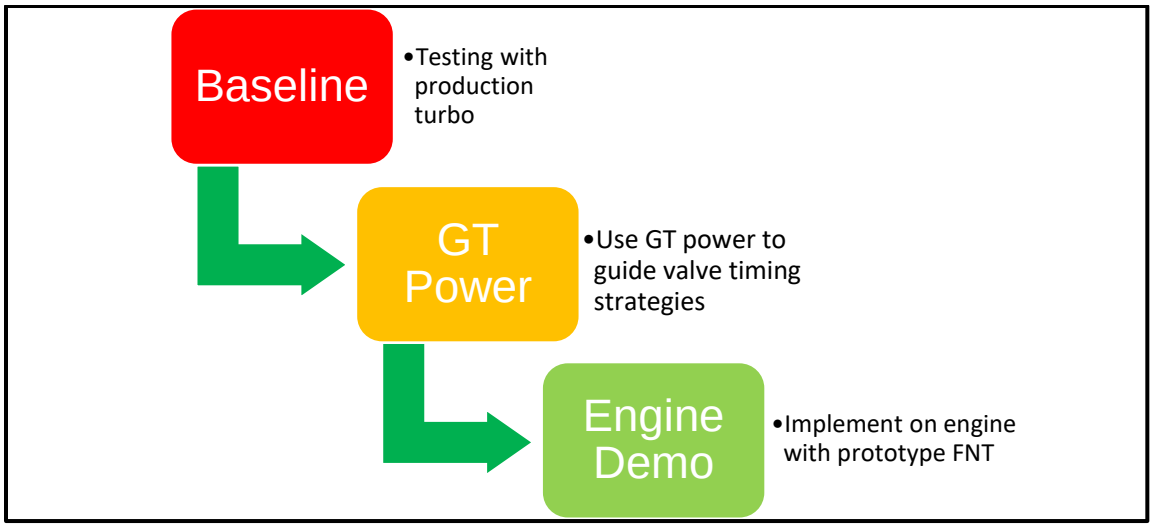

Figure 4-5: Illustration of 3 phases of experiments.

Phase 1 involved generating baseline engine data for comparisons with the Miller engine. Baseline data was generated with the engine equipped with the stock fixed geometry continental turbocharger with wastegate control. No changes were made to the ECU and the engine control was maintained the same as it would have been on the production engine. Baseline data that was generated included steady state engine maps to quantify the fuel consumption and emissions benefits if there were any at different speed load points over the entire operating range of the

engine. In addition to steady state engine maps, a number of different standardized transient tests were run to generate baseline data for the engine under simulated real world driving conditions. These standardized tests are what the different emissions regulatory boards use for rating vehicle emissions and fuel economy for production vehicles. The tests that were conducted as part of this dissertation included the following:

1. Federal Test Procedure 75 (FTP-75)
2. Highway Fuel Economy Test (HWFET)
3. US06 Supplemental Federal Test Procedure (US06)
4. Worldwide Light vehicles harmonized Test Procedure (WLTP)

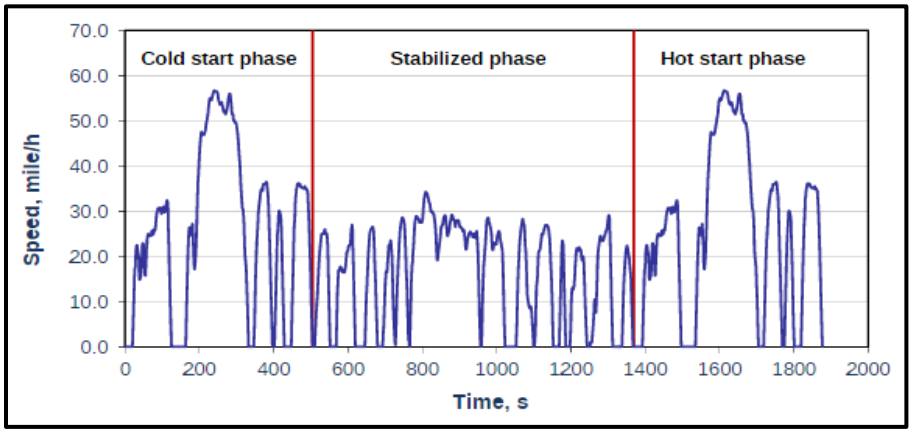

(a)

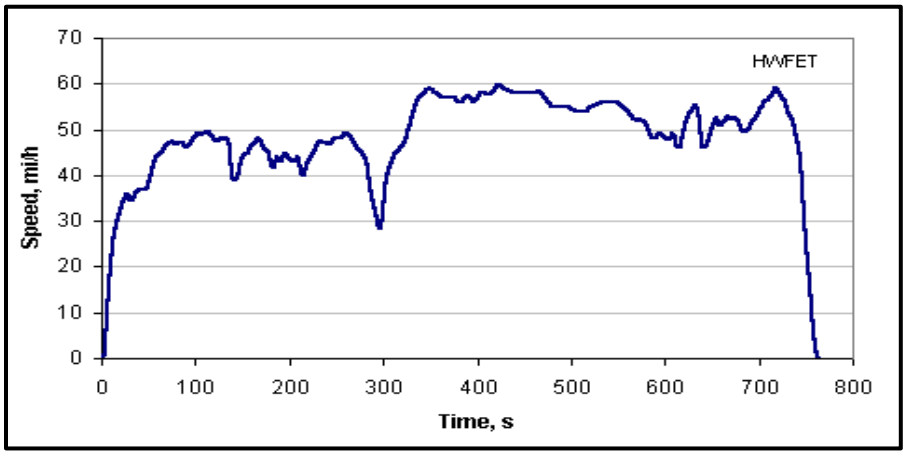

(b)

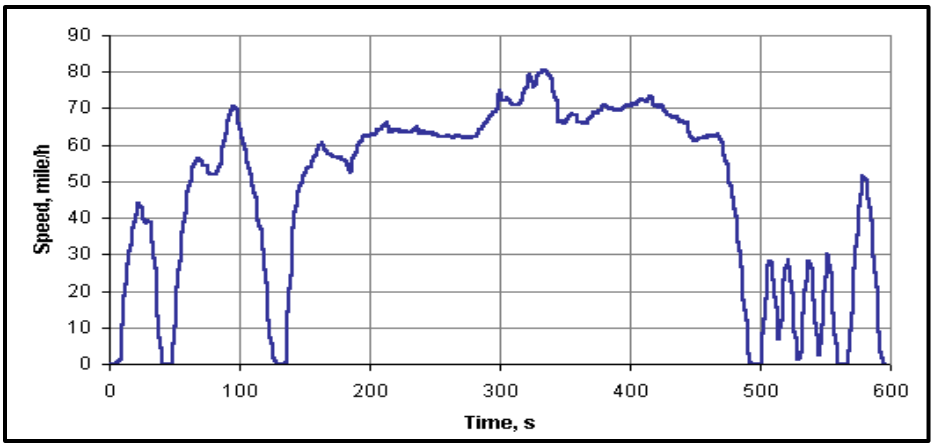

(c)

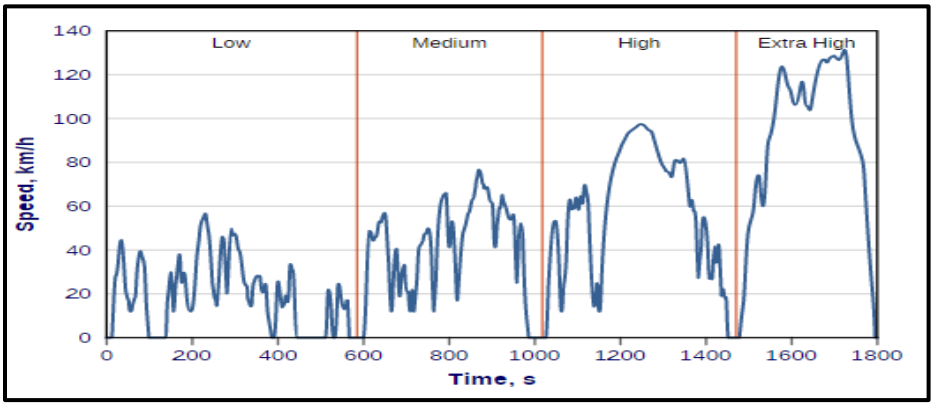

(d)

Figure 4-6: Vehicle speed trajectories for the (a) FTP75 (b) HWFET (c) US06 (d) WLTP test cycles.

Of these, the first three are standardized tests that are conducted by American regulatory boards such as the Environmental Protection Agency (EPA). The WLTP is a test that is used by European regulatory boards. The engine speed load point arrays versus time for the transient tests were provided from a GT Drive transmission model of a 2020 Ford Escape.

Phase 2 involved modifying an existing validated GT Power model for the baseline Ford Dragon engine. The initial GT Power model was provided to the author of this dissertation by Dr. Robert Middleton. The modifications that were made accounted for the change in hardware

to a variable geometry floating nozzle turbocharger which was equipped with a larger capacity compressor. The compressor map and the turbine maps for different nozzle positions were provided to the author by BMTS Gmbh. These maps were imported into the new modified GT Power model. This was followed by some validation efforts matching predicted torque, rack position, turbine inlet pressures and temperatures and brake specific fuel consumption of the engine values from the model to initial engine data. Further details of the GT Power validation efforts are provided in Appendix 'B'. After validation, different combinations of intake and exhaust valve phasing were tested using a factorial design of experiments at different speed load points over the engine map. The intake and exhaust valve phasor positions that resulted in the best fuel consumption were selected to fill out the new the phase angles for the engine map. The phase angles were selected across the map such that effective compression ratio was monotonically increasing with increasing engine load.

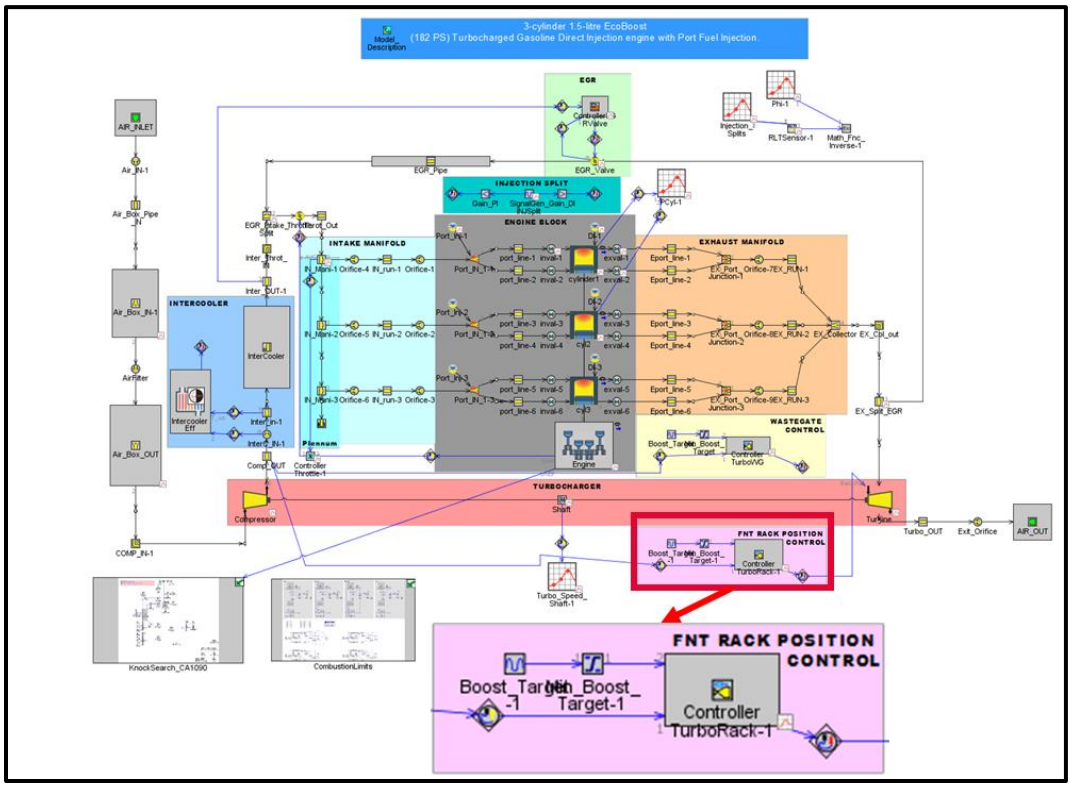

Figure 4-7: Illustration of GT power model of Ford Dragon engine modified with BMTS FNT.

Once new values for VCT phase angles over our engine speed load map were generated with the help of GT Power simulations, phase 3 of experiments involved over-riding existing ECU tables. Engine control rapid prototyping hardware, RPECS (Rapid Prototyping Electronic Control System) from SWRI (SouthWest Research Institute) was used to override the existing ECU controls. Using RPECS, the author was able to create and populate lookup tables for VCT Phase position and the corresponding boost required for meeting load requirements.

An example of these lookup tables in ATI Vision is illustrated in the Figure 4-8 below. Tables that needed to be populated as part of the calibrating efforts with the new turbocharger installed included tables for VCT Intake, VCT Exhaust, boost required (manifold pressure), open loop VGT position for fast response and lambda. The baseline controls would switch the engine to a fuel rich operation at high power conditions to protect the catalyst in the aftertreatment system from thermal degradation. However, with the reduced effective compression ratio and associated lower turbine inlet pressures, it was decided to run the engine at stoichiometric air fuel ratio over then entire engine speed load map. Moreover, stricter emissions regulations have ensured that using more fuel to cool charge temperatures will not be a likely option for future applications.

Steady state engine map data was generated after entering the new calibration tables in ATS Vision software to compare against the baseline map data. Furthermore, the transient tests were repeated with the Miller engine configuration to compare on the basis of a more real-world application.

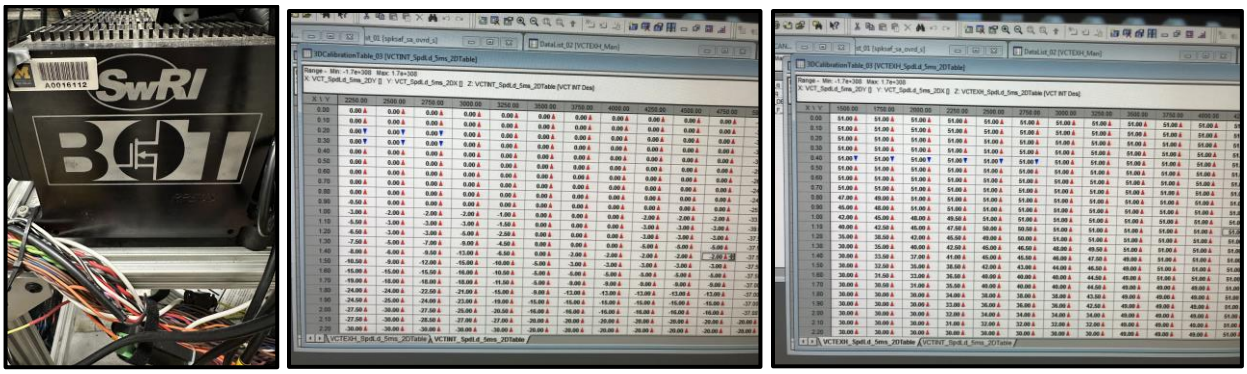

(a) (b) (c)

Figure 4-8: Picture of (a) RPECS box and populated tables in ATI Vision of (b) Intake valve phasing (c) Exhaust valve phasing.

4.3 Results and Discussion

4.3.1 Implementing Miller calibration using predictions from GT Power

The degree of freedom of both the intake and exhaust cam phasors can be realized from Figure 4-9, which shows the phasors at their two extreme positions. This illustrates that different combinations of phasor positions can result in different values of valve overlap ranging from a negative valve overlap of -20 CAD to a positive valve overlap of 100 CAD. The valve overlap and the differences in intake and exhaust pressure depending on the engine speed and load determines the levels of exhaust gas residuals that are left behind in the cylinder from the previous cycle. This residual percentage or internal exhaust gas recirculation can have an effect on the engine out emissions and propensity of knock due to the dilution of fresh air fuel charge with exhaust gas products.

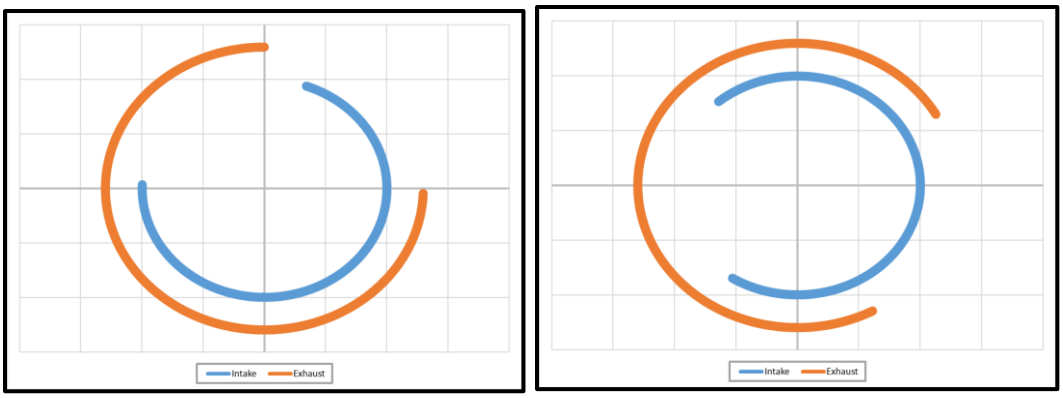

Figure 4-9: Illustration of degree of freedom of intake and exhaust VCT.

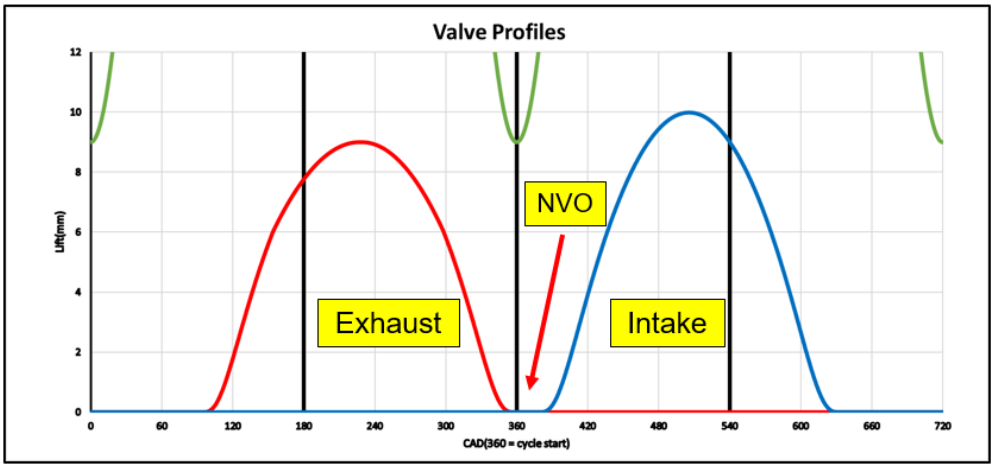

(a)

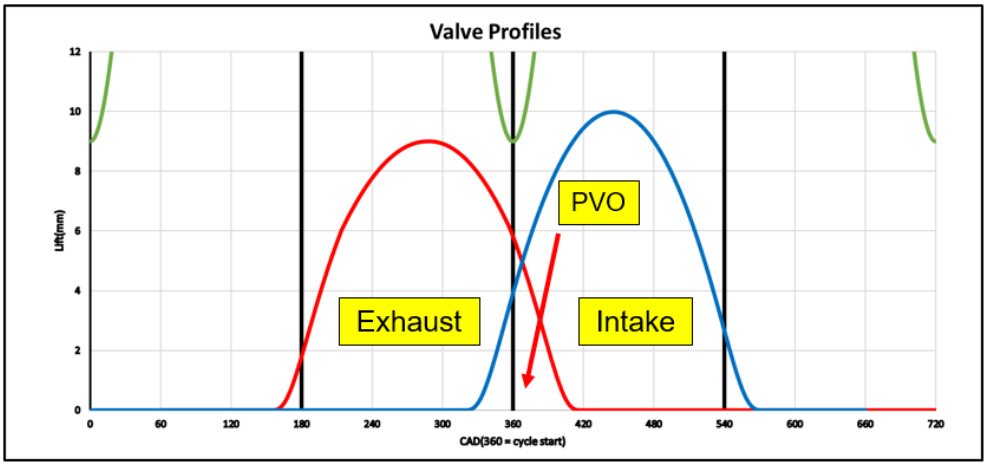

(b)

Figure 4-10: Illustration of (a) negative valve overlap and (b) positive valve overlap that are a consequence of different combinations of intake and exhaust VCT phasing.

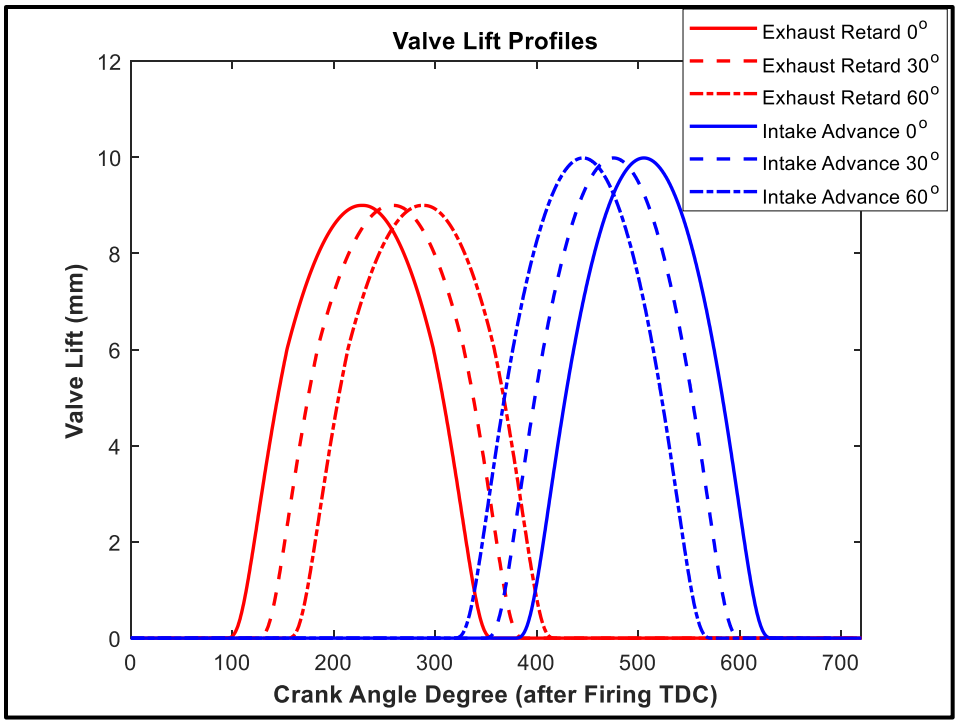

Figure 4-11: Degree of freedom of intake and exhaust cam phasors.

As described in the experimental methods section, a full factorial (7x7) design of experiments was conducted at each speed load point. The GT Power model was set such that spark timing or combustion phasing sweeps were conducted at each combination of intake and exhaust VCT. The combustion phasing sweeps were set to move to the next point if thermal efficiency deteriorated with further advance or if the knock threshold was reached.

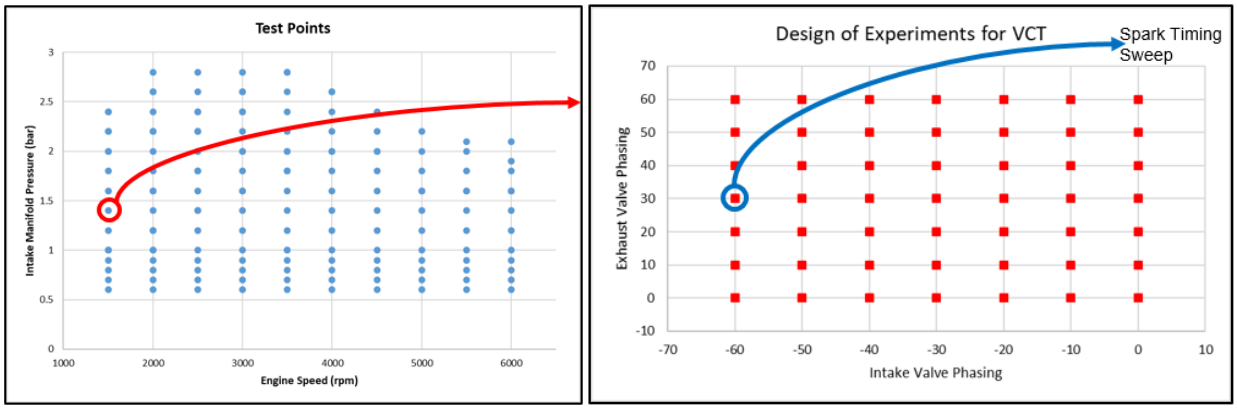

Figure 4-12: Illustration of design of experiments with GT power.

The intake and exhaust VCT positions that led to the best thermal efficiency were compiled for each speed load point over the entire engine map. An example of this is shown in Figure 4-13. The case shown in Figure 4-13 is at two different manifold pressures at an engine speed of 1500 rpm. The red cross shows the point with the maximum torque possible at the given manifold pressure and the green cross shows the point with the lowest fuel consumption. The two manifold pressures considered in this example are 1.2 bar and 1.4 bar. Comparing the maximum torque point at 1.2 bar to the lowest fuel consumption at 1.4 bar, we see that they are at equal torque or load of 150 N-m. This shows that a load of 150 N-m at 1500 rpm can be achieved by the engine in a number of ways. One way would be by combining a manifold pressure of 1.2 bar with VCT intake at -60^{o} and VCT exhaust at 50^{o}. Alternately, this could be achieved by combining a manifold pressure of 1.4 bar with VCT intake at -20^{o} and VCT exhaust at 30^{o}. Comparing the two, the higher manifold pressure with late intake valve closing resulted in a reduction of brake specific fuel consumption by 40 g/kWh. The benefit of running late intake valve closing outweighs the potential increase in pumping losses due to closing the rack position of the variable geometry turbo. This exercise is repeated several times.

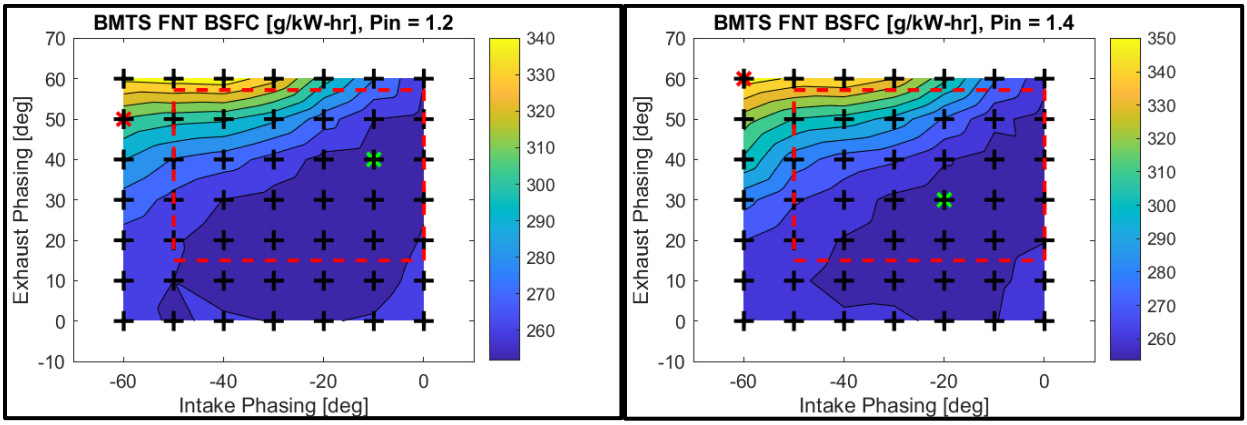

(a) (b)

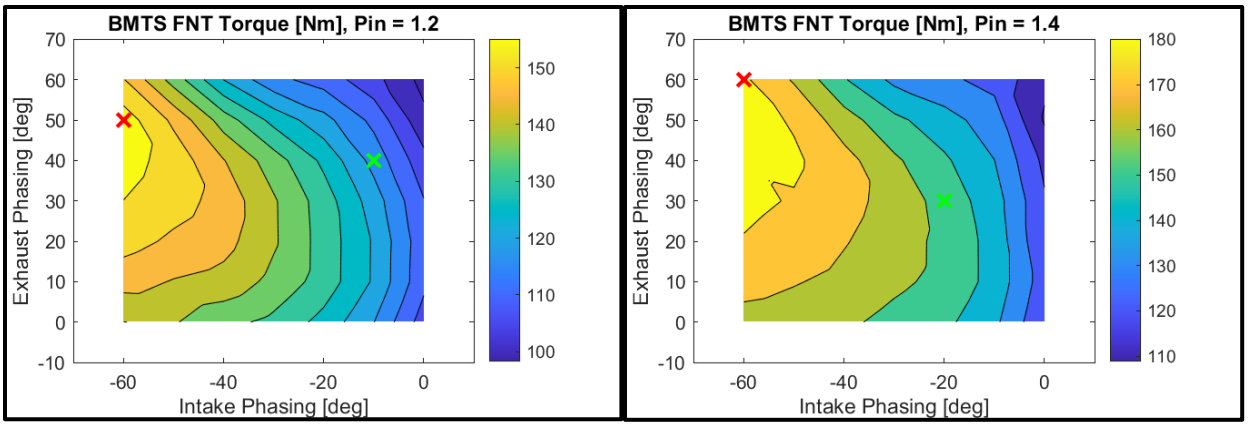

(c) (d)

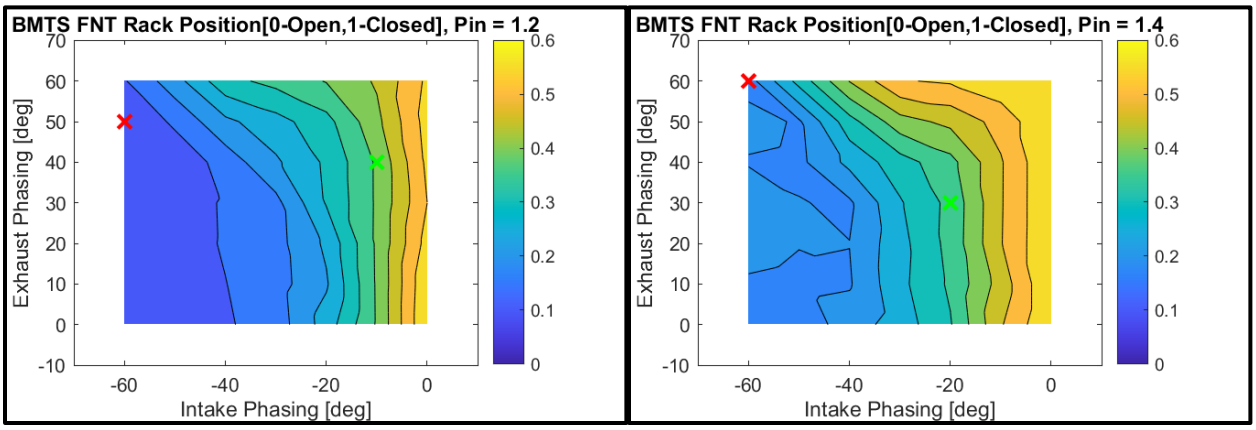

(e) (f)

Figure 4-13: Comparison of same torque at two different intake pressures (1.2 bar vs. 1.4 bar) at 1500 rpm (a) BSFC at 1.2 bar (b) BSFC at 1.4 bar (c) Torque at 1.2 bar (d) Torque at 1.4 bar (e) Rack position at 1.2 bar (f) Rack position at 1.4 bar [Red cross = Max. torque; Green cross = Min. fuel consumption].

Due to certain limits that were installed in the ECU that could not be overridden, some of the values implemented on the actual engine demonstration look different to what was suggested by the simulations. Effective compression and effective expansion ratios calculated from the intake valve closing (IVC) and exhaust valve opening (EVO) timings are shown below.

Ford Dragon Engine with Continental WG Turbo

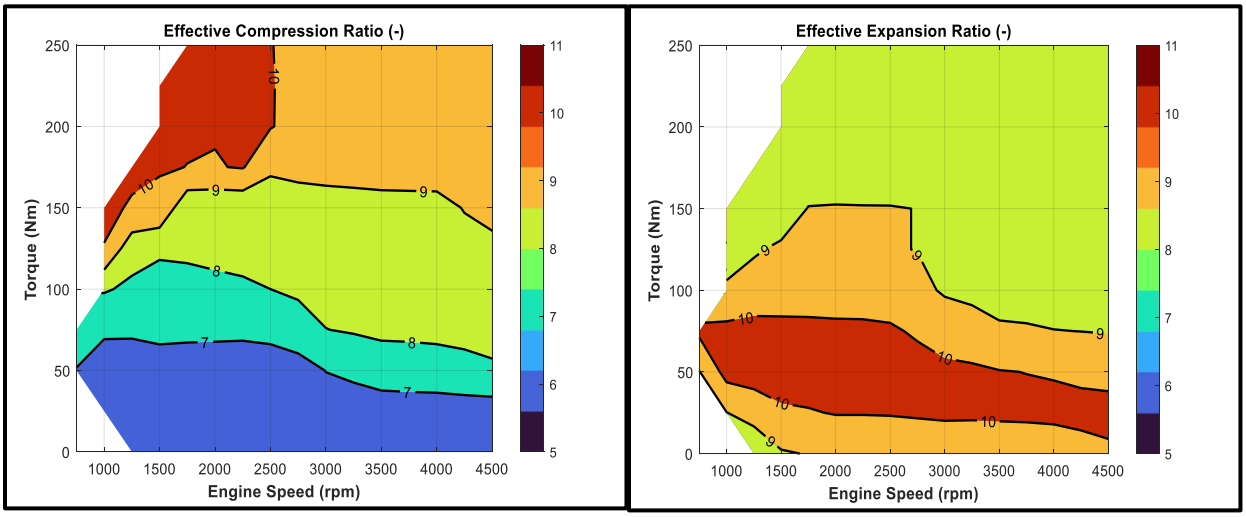

(a) (b)

GT Power Model with BMTS FNT

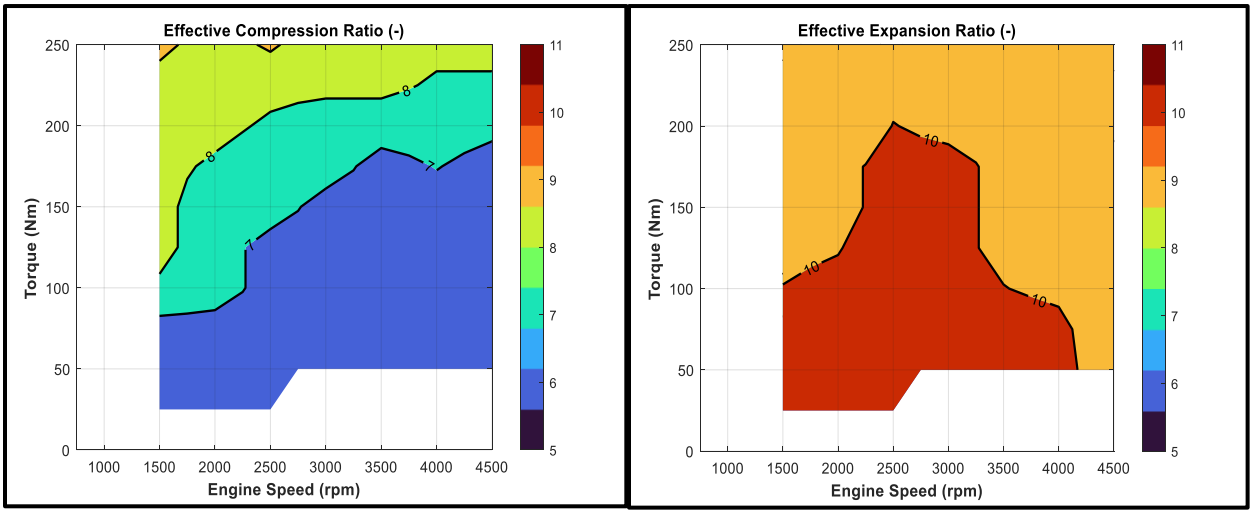

(c) (d)

Ford Dragon Engine with BMTS FNT

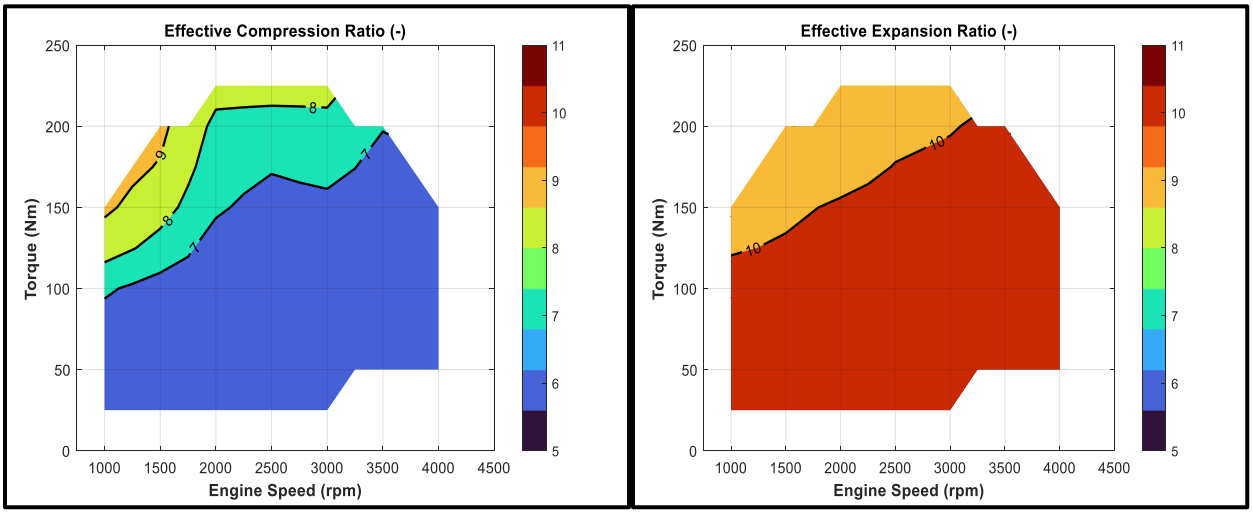

(e) (f)

Figure 4-14: Comparison of effective compression and expansion ratios.

(a) Effective compression ratio of baseline engine (b) Effective expansion ratio of baseline engine (c) Effective compression ratio of Miller engine predicted by GT power (d) Effective expansion ratio of Miller engine predicted by GT power (e) Effective compression ratio of Miller engine (f) Effective expansion ratio of Miller engine.

The GT Power model suggests that with the larger sized compressor of the BMTS FNT turbo, it is possible to meet high power requirements at lower effective compression ratios and run with a higher thermal efficiency. Likewise, the model predicts that the larger compressor size allows the power requirements to be met with less exhaust enthalpy and as a result, more work can be extracted during the expansion stroke. As a consequence of lower effective compression ratio and greater effective expansion ratio, we can run the engine with an over-expanded cycle. This is clearly illustrated using the EPA's definition of Atkinson Ratio. Recall from equation 4-1 that the EPA defines the Atkinson ratio as the follows:

E.P.A. Atkinson Ratio = Effective Expansion Ratio / Effective Compression Ratio

Atkinson Ratios greater than one imply a Miller or Atkinson cycle operation. As can be seen from the mapping of the baseline engine with the production strategies, Atkinson ratios

greater than one are limited to low load operation. Atkinson cycle operation at low loads has the benefit of lower compression work as well as lower throttling losses due to the throttle valve residing in a more open position to compensate for the lower volumetric efficiency. However, the reduced compression ratio and associated low cylinder pressures and temperatures means that power requirements are difficult to meet at high loads. Hence, the intake valve phasors are advanced to increase the effective compression ratios to meet power requirements. At the same time, the exhaust valve phasors are advanced for two reasons. This is done to reduce valve overlap to reduce the amount of hot exhaust gas residuals re-entering the combustion chamber that could potentially result in high propensity of knock. Moreover, opening the exhaust valves early results in less work extracted from the combustion products. The high enthalpy exhaust gas is required to meet high boost requirements at the high load conditions. The combination of increased compression ratio and reduced expansion ratio results in a lower Atkinson ratio.

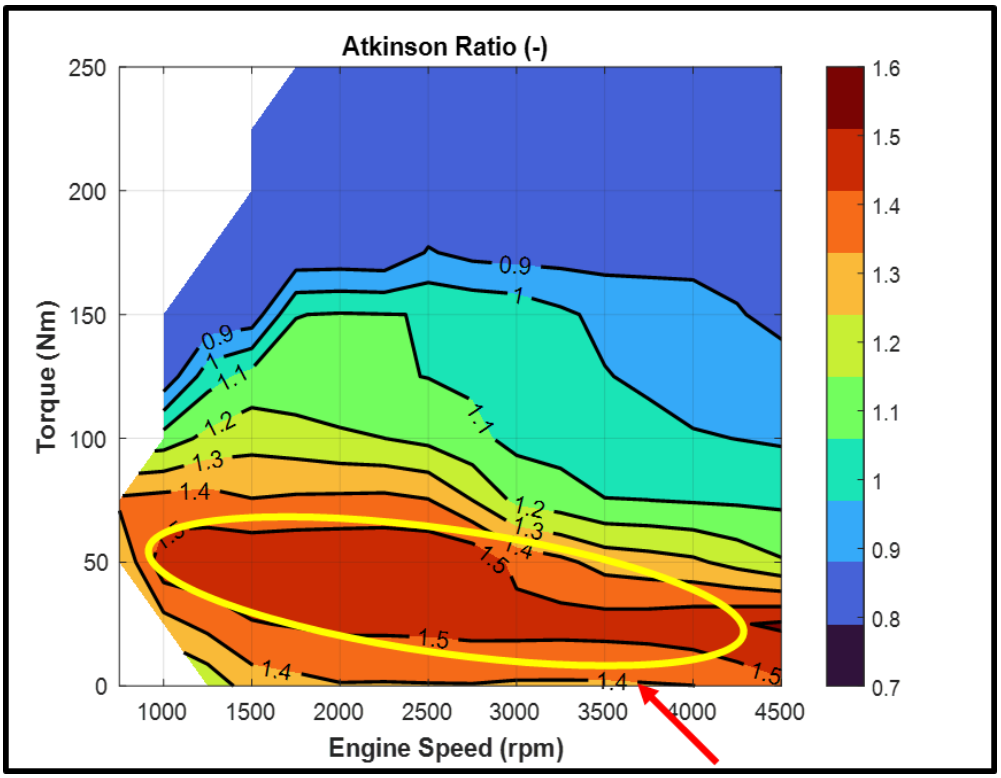

Figure 4-15: Atkinson ratios of baseline engine.

The Atkinson ratios for the engine map as suggested by the GT Power simulations and the actual ratios implemented on the engine are illustrated below (Figure 4-16 and Figure 4-17). Compared to the baseline engine, we see that the islands of larger Atkinson ratios occupy a larger portion of the engine speed load map. As a result, Miller cycle was successfully implemented over a larger portion of the engine speed load map.

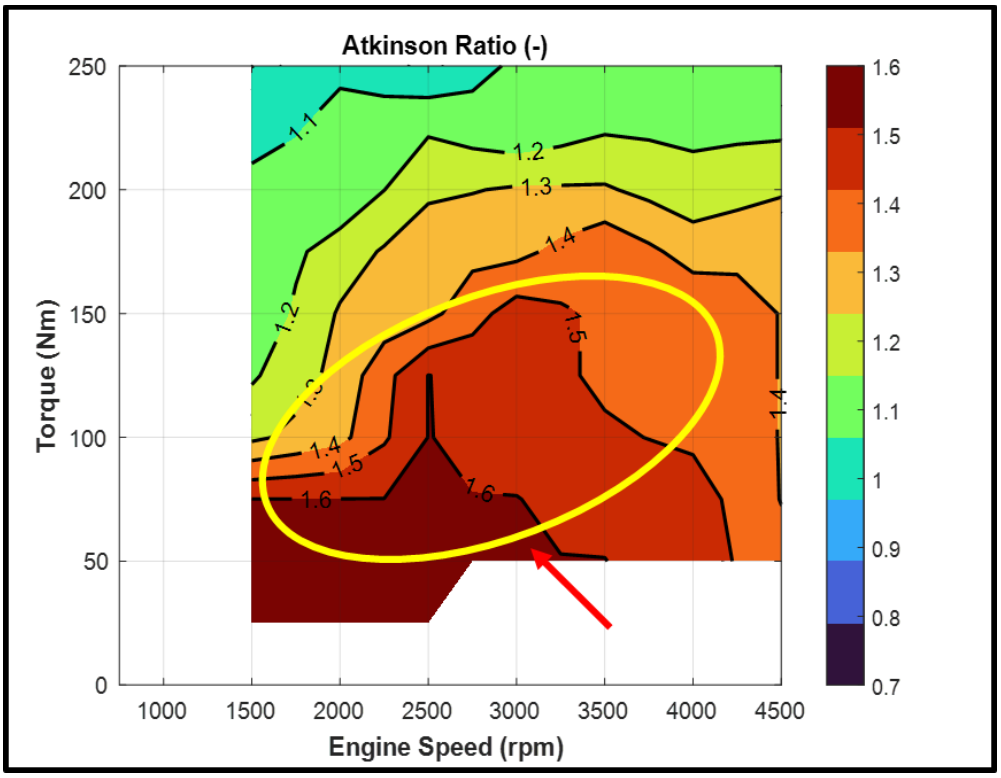

Figure 4-16: Optimum Atkinson ratios for the Miller engine as predicted by the GT Power model.

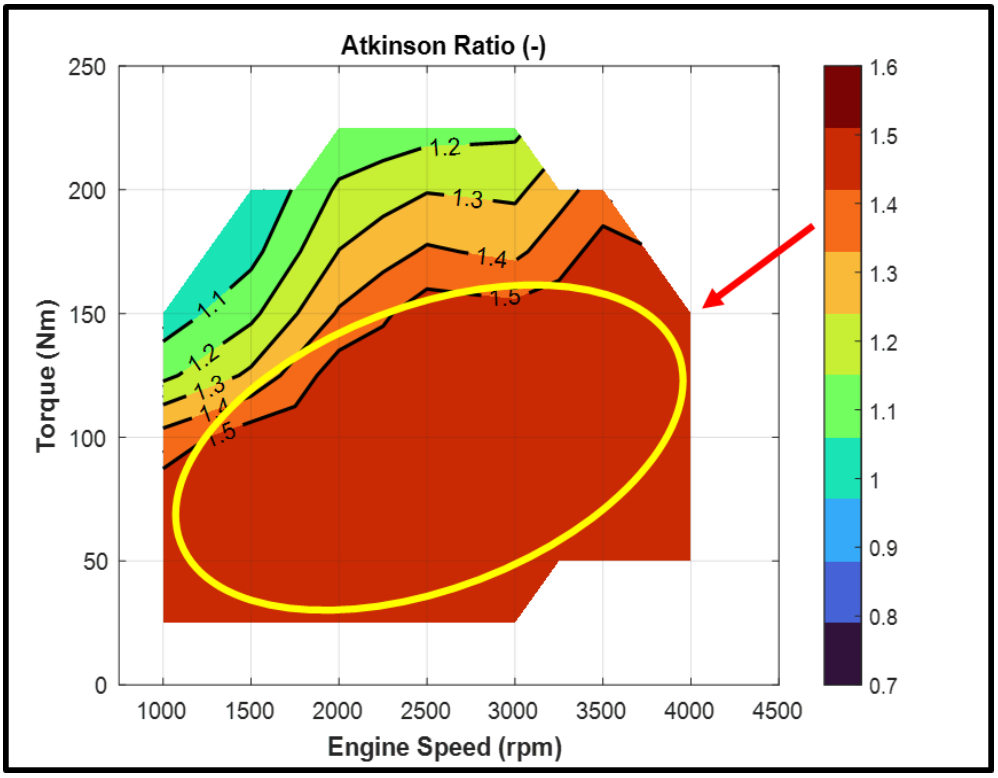

Figure 4-17: Atkinson ratios implemented on Miller engine with prototype BMTS FNT.

4.3.2 Steady State Engine Map comparisons (Fuel Economy and Gaseous Emissions)

This section discusses the result of implementing Miller cycle with the help of a prototype BMTS Gmbh FNT on the Ford Dragon 1.5 L engine. Steady state data was not collected at 4500 rpm and elevated loads for the Miller engine due to the clutch plate and spline failure. The only way around this problem was replacing these parts to resume testing. The failure of clutch plate and dyno shaft is illustrated in the Figure 4-18 below to give the reader an idea of the situation. Moreover, replacing these parts was also an arduous task since it involved putting the engine on a pallet, disassembling the shaft and bell housing and clutch plate and putting all the new parts back on.

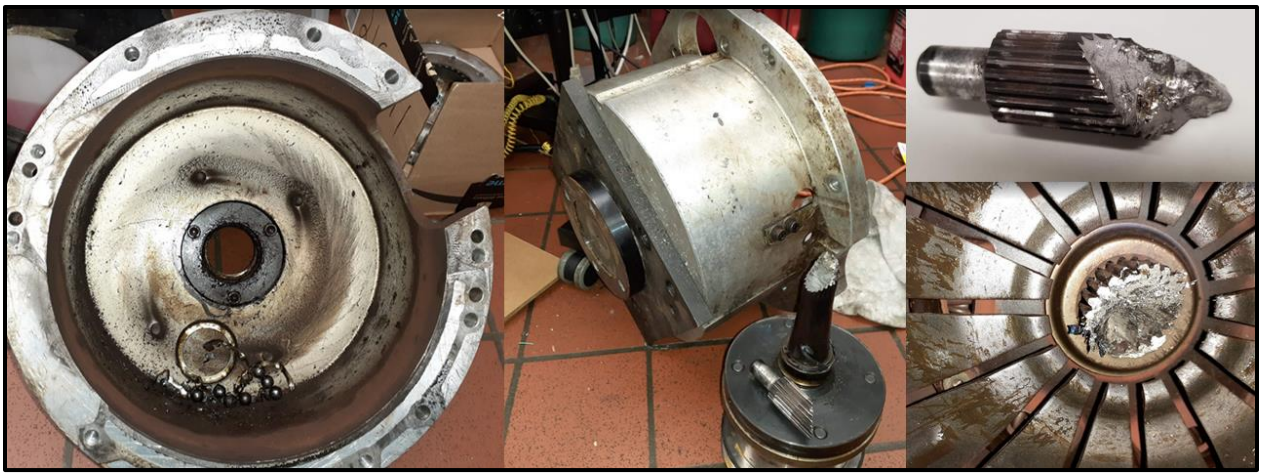

Figure 4-18: Clutch Plate and Dyno Shaft Failure at UM Auto Lab.

Fuel Consumption and Thermal Efficiency:

A comparison of the brake specific fuel consumption numbers shows that lower fuel consumption islands occupy a larger region of the engine speed load map. In addition, the lowest fuel consumption islands have moved to lower engine speeds where the engine tends to reside at for longer durations during real world operation. A more intuitive way of picturing the effect of reduced fuel consumption is looking at the brake thermal efficiency where a higher number indicates higher efficiency. A comparison of the thermal efficiencies depicts the same story as fuel consumption.

Superimposing the points that the engine resides at during the FTP 75 cycle gives an idea of how the engine resides more in higher efficiency islands due to the change to Miller cycle operation especially in urban scenarios where traffic is largely start-stop.

Baseline Engine with FGT **Miller Engine with VGT**

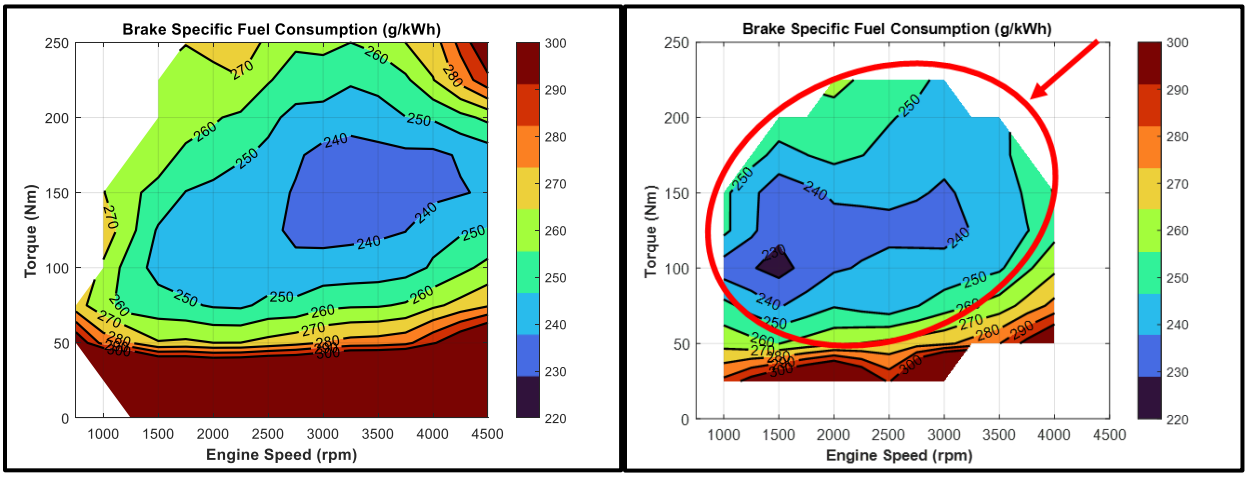

(a) (b)

Figure 4-19: Comparison of brake specific fuel consumption.

(a) BSFC of the baseline engine (b) BSFC of the Miller engine

Baseline Engine with FGT **Miller Engine with VGT**

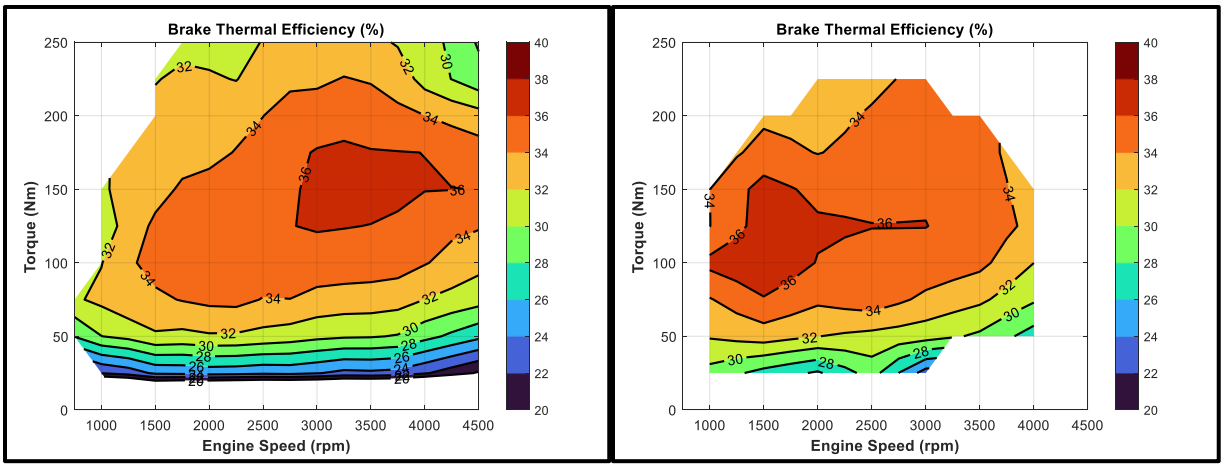

(a) (b)

Figure 4-20: Comparison of brake thermal efficiency.

(a) BTE of the baseline engine (b) BTE of the Miller engine

Baseline Engine with FGT **Miller Engine with VGT**

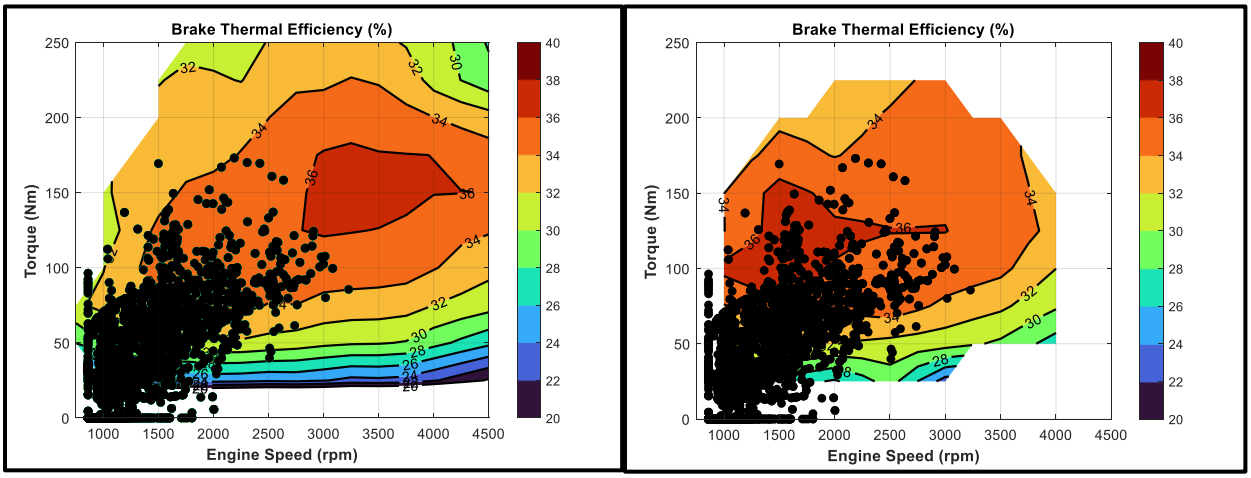

(a) (b)

Figure 4-21: Thermal Efficiency islands superimposed with engine speed load points of FTP 75 cycle.

(a) Baseline engine map shows that engine resides largely in 32%-34% BTE range (b) Miller engine map shows that engine resides largely in 34%-36% BTE range

A comparison of the throttle position shows that the throttle is in an open position for most part of the engine map for the Miller engine. Pressure drop across the throttle gives an idea of how much throttling losses are reduced by employing a Miller strategy. Lower pumping losses are also recorded at points where thermal efficiency is improved.

One thing to note is that at speeds above 3000 rpm at throttled conditions, the throttle is in a more closed position on the Miller engine than it is on the baseline engine (highlighted in red). This is due to the larger sized compressor overboosting compared to the baseline continental turbocharger at these conditions. This results in lower thermal efficiency at these points with the Miller engine as seen in Figure 4-20. The ramifications of this are discussed in the later section with testing done with an open wastegate.

Baseline Engine with FGT **Miller Engine with VGT**

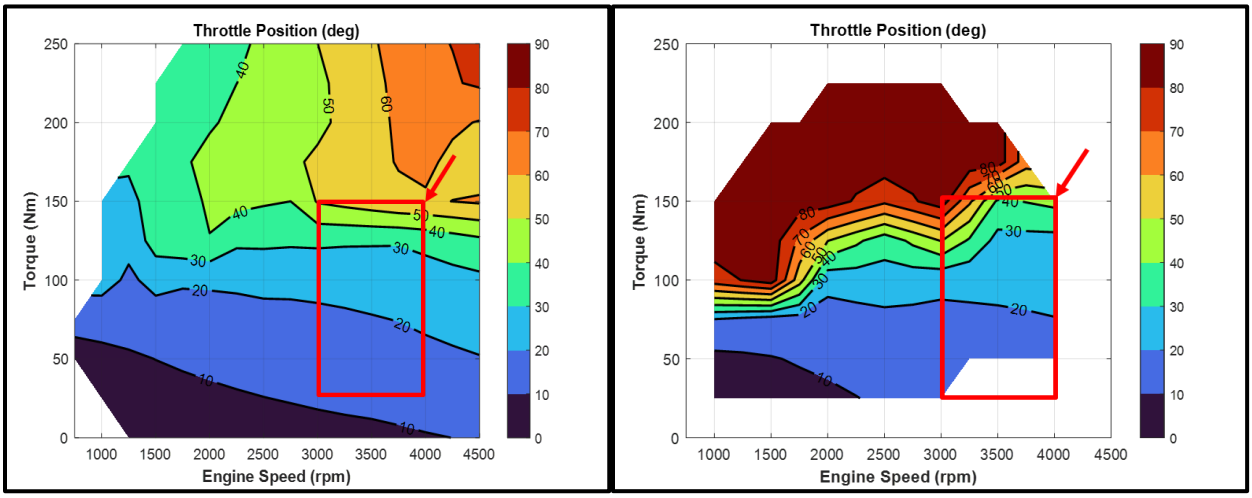

(a) (b)

Figure 4-22: Comparison of throttle valve position (90º = wide open throttle).

(a) Throttle valve position for baseline engine (b) Throttle valve position for Miller engine; Miller engine has a more open valve position except for the region highlighted in red

Baseline Engine with FGT **Miller Engine with VGT**

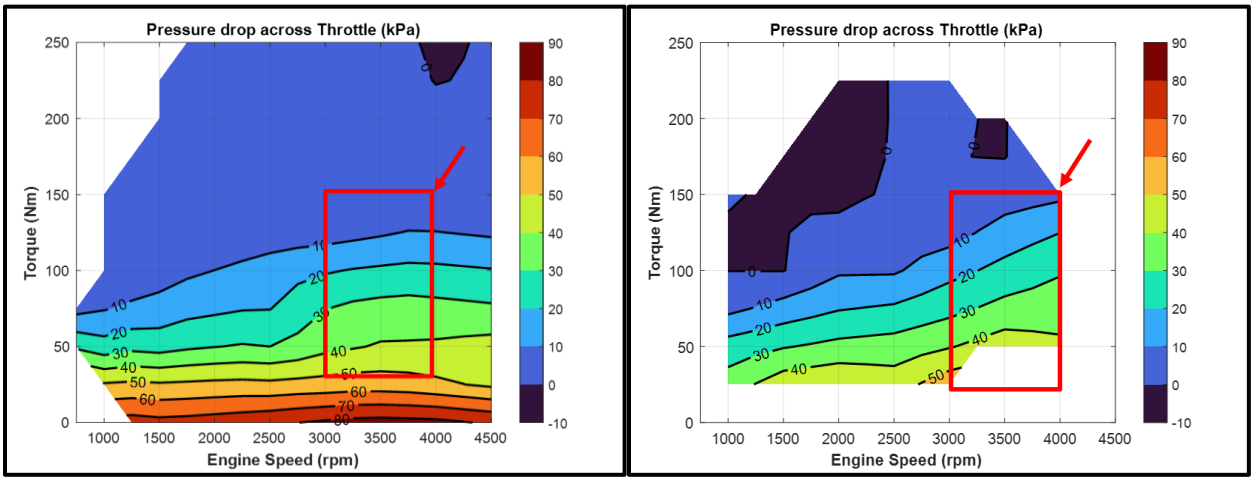

(a) (b)

Figure 4-23: Comparison of pressure drop across throttle body.

(a) Pressure drop across throttle body for baseline engine (b) Pressure drop across throttle body for Miller engine; Once again for the region highlighted in red, the Miller engine operates with a higher pressure drop across the throttle

Baseline Engine with FGT **Miller Engine with VGT**

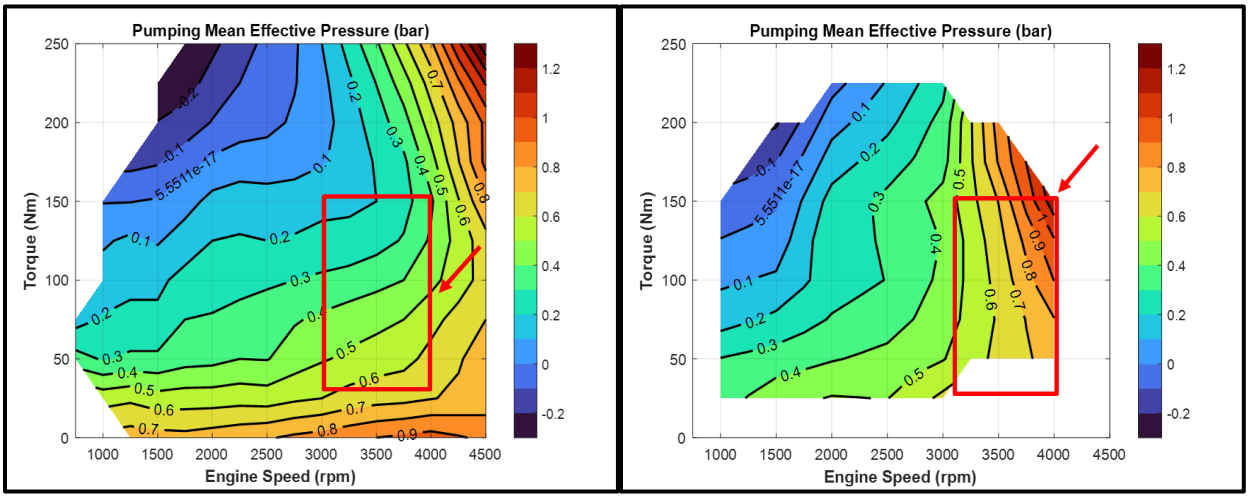

(a) (b)

Figure 4-24: Comparison of pumping mean effective pressure (PMEP).

(a) PMEP of baseline engine (b) PMEP of Miller engine; The comparison shows lower PMEP for the Miller engine at low speeds and low loads but higher PMEP in the region highlighted in red.

NO_X emissions:

A comparison of the engine-out NO_X emissions shows that the NO_X emissions are significantly reduced with the implementation of Miller cycle. NO_X emissions are largely governed by peak in-cylinder temperatures, as described in the Zeldovich mechanism for thermal NO_X production [8]. The reduced peak in cylinder temperatures due to lower effective compression ratios reduces the engine-out NO_X emissions. This is backed up by the comparison of peak in cylinder pressures of the baseline engine versus the Miller engine.

Baseline Engine with FGT **Miller Engine with VGT**

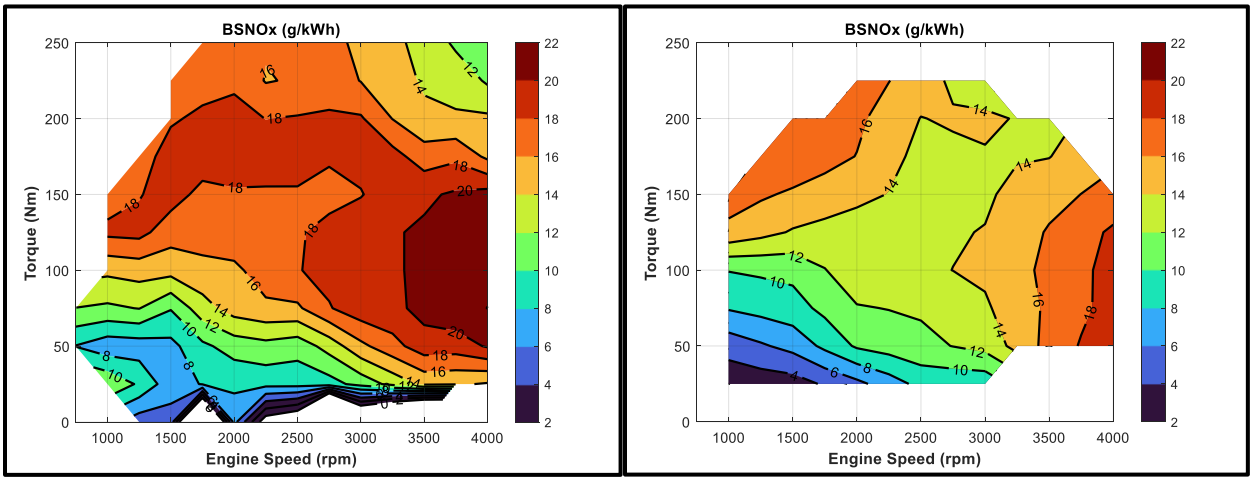

(a) (b)

Figure 4-25: Comparison of engine out brake specific NO_X emissions.

(a) $BSNO_X$ for the baseline engine (b) $BSNO_X$ for the Miller engine; Comparison shows lower NO_X emissions for the Miller engine

Baseline Engine with FGT **Miller Engine with VGT**

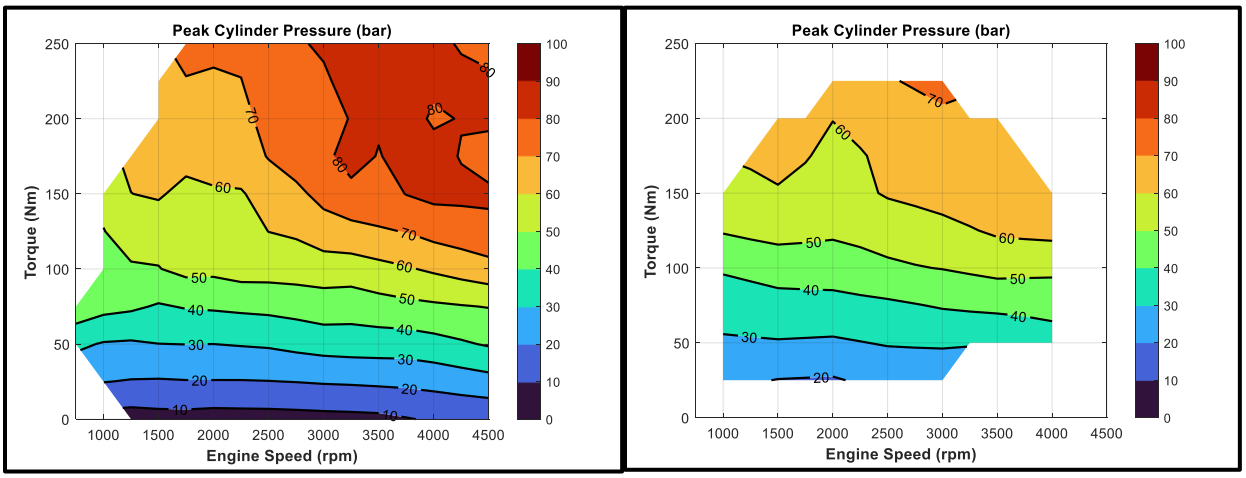

(a) (b)

Figure 4-26: Comparison of peak in-cylinder pressure (PCP).

(a) PCP of baseline engine (b) PCP of Miller engine; A comparison shows that for similar regions on the engine speed load map, the Miller engine has approximately 10 bar lower PCP which correlates well with the in-cylinder temperature

Baseline Engine with FGT **Miller Engine with VGT**

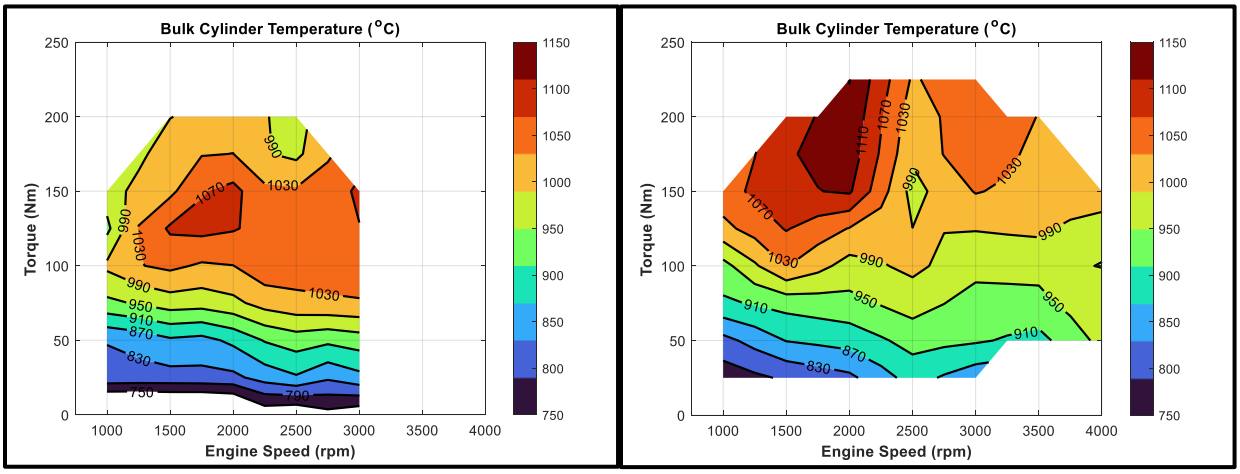

(a) (b)

Figure 4-27: Comparison of bulk cylinder temperature (BCT).

(a) BCT of baseline engine (b) BCT of Miller engine;

Comparison of the BCTs shows good correlation with the PCPs and also verifies that the BCT is lower for the Miller engine over speed load map.

CO emissions:

Miller cycle implementation also led to the reduction in engine out carbon monoxide emissions. The reduction in CO emissions could have been due to the increased boost pressure which could have resulted in enhanced scavenging resulting in lower fractions of residual exhaust from previous cycles. This could have led to higher combustion efficiency and thus lower carbon monoxide [120]. Although a stoichiometric air fuel ratio (λ=1) was maintained using feedback from the ECU lambda sensor, it is possible that the higher boost pressures associated with the Miller engine could have resulted in a greater number of locally lean regions. Even a small change in air fuel ratio ($\Delta\lambda$=0.1) can result in a reduction of CO emissions by 33% [121].

Baseline Engine with FGT **Miller Engine with VGT**

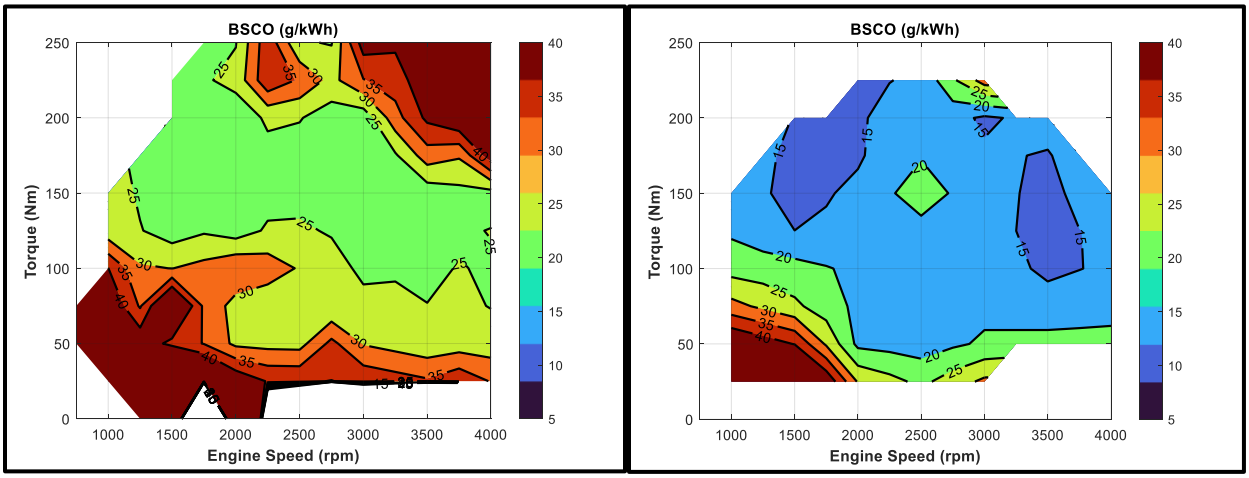

(a) (b)

Figure 4-28: Comparison of engine out brake specific carbon monoxide emissions (BSCO).

(a) BSCO of baseline engine (b) BSCO of Miller engine; Comparison shows reduced CO emissions for the Miller engine

THC emissions:

The unburnt hydrocarbon data paints a similar picture to the reduced carbon monoxide emissions. The higher boost pressure led to lower hydrocarbon emissions at certain regions of the map. However, an interesting observation was the increased hydrocarbon emissions at low-speed high load conditions.

This could be due to the injection strategy that was employed. The injection strategy was not overridden and thus the baseline injection strategy was used. This could have resulted in non-optimal injection strategies for the Miller implementation.

This is not a concern at points where the injection strategy is largely port fuel injection such as at low loads. Since the fuel has enough time to mix in the intake port and the late intake valve opening from our Miller operation resulted in more time available for mixing, there is not a significant change in unburnt hydrocarbon emissions. As seen from the contour plot of direct

injection percentage (Figure 4-30), the high hydrocarbon emissions islands with the Miller engine coincides with large DI%.

Baseline Engine with FGT **Miller Engine with VGT**

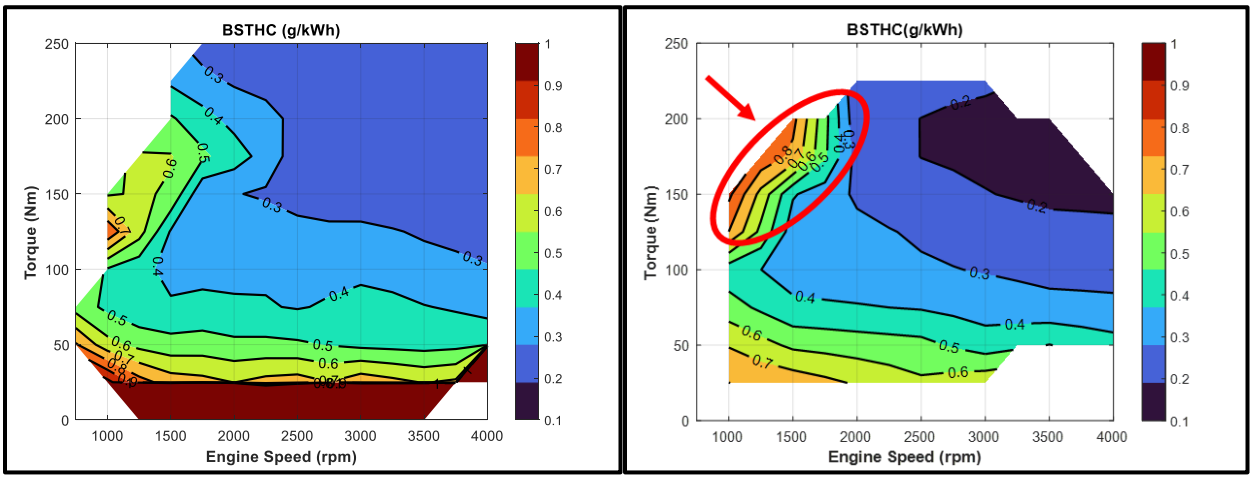

(a) (b)

Figure 4-29: Comparison of engine out brake specific total unburnt hydrocarbons (BSTHC).

(a) BSTHC of baseline engine (b) BSTHC of Miller engine; Comparison shows no significant differences except in the region highlighted in red where the THC emissions are higher for Miller engine.

Baseline Engine with FGT

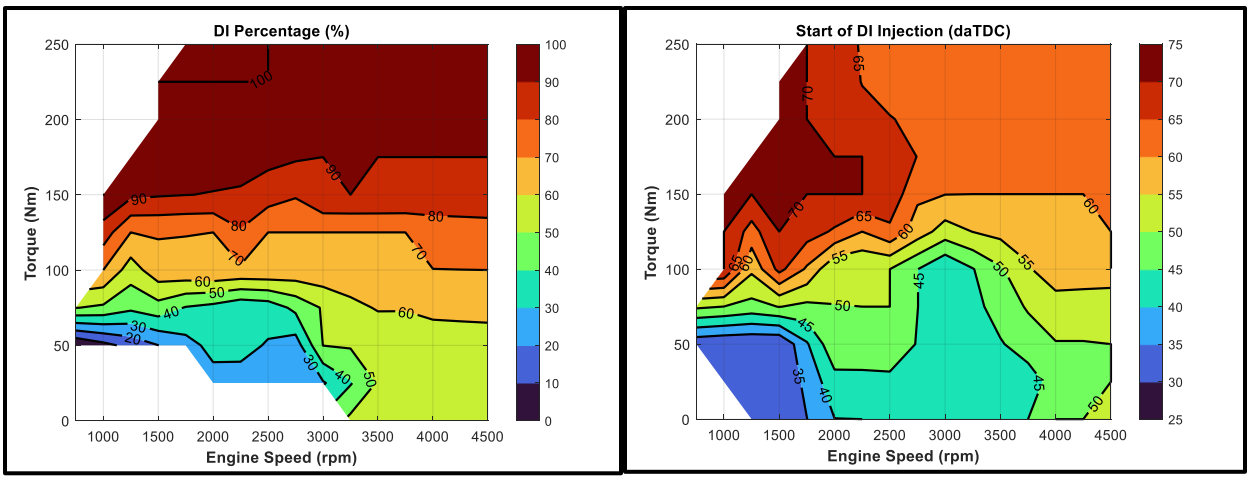

(a) (b)

Miller Engine with VGT

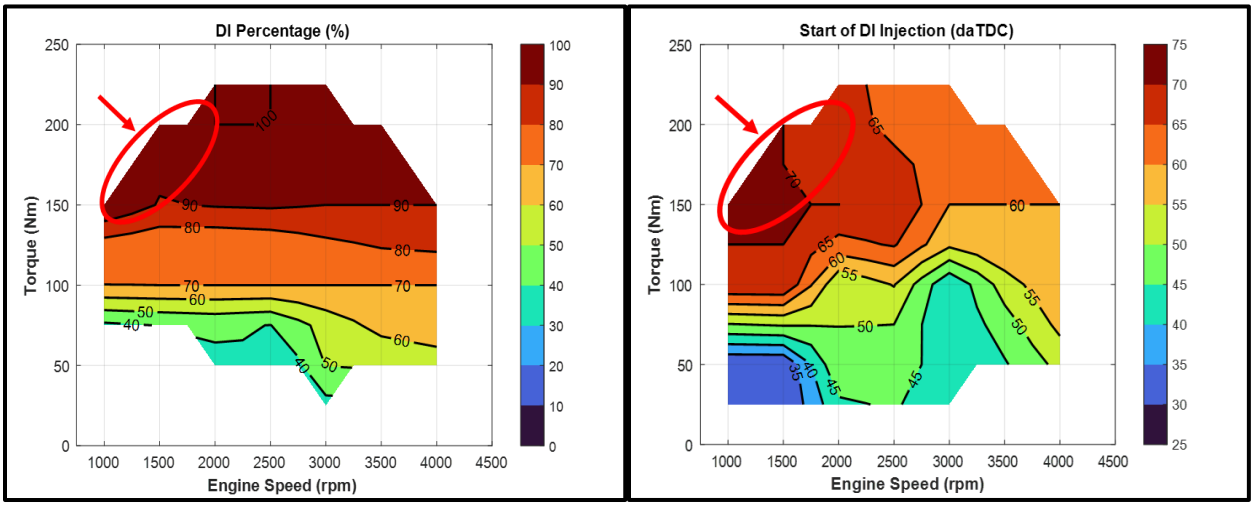

(c) (d)

Figure 4-30: Injection strategy of the baseline and Miller Engine (No changes made).

(a) DI% of baseline engine (b)DISOI of baseline engine (c) DI% of Miller engine (d) DISOI of Miller engine; Comparison of the injection strategies of the 2 engines shows that no were changes were made to the baseline strategy which could have resulted in a sub optimal injection strategy at certain points on the speed load map.

The late intake valve opening at the low-speed high load cases is not ideal since this means that the high-pressure fuel entering the combustion chamber has a larger propensity for cylinder wall impingement due to the lack of high pressure air and reduced time available for mixing. This could result in fuel also getting stuck in the crevices above the top piston ring. The Figure 4-31 below depicts how different the intake valve opening events are for the two calibrations. The difference in DI SOI (Direct Injection Start of Injection) and IVO (Intake Valve Opening) which gives us an idea of the time between the two events of fuel injection and air induction is quite significant in the regions of the map that coincide with high THC emissions.

Moreover, high hydrocarbon emissions are also a precursor to high levels of soot emissions. The very same phenomenon was also seen in the research work of fellow Auto Lab

colleagues who noticed high particulate emissions when fuel was injected before the intake valve opening event or close to the intake valve opening event [30,41] (Figure 4-32).

Baseline Engine with FGT **Miller Engine with VGT**

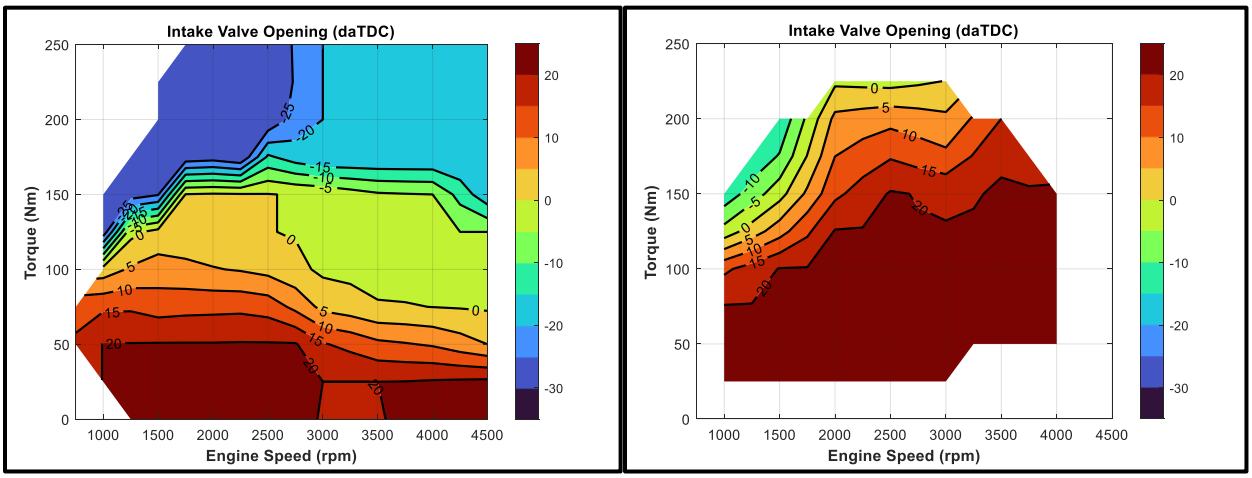

(a) (b)

Baseline Engine with FGT **Miller Engine with VGT**

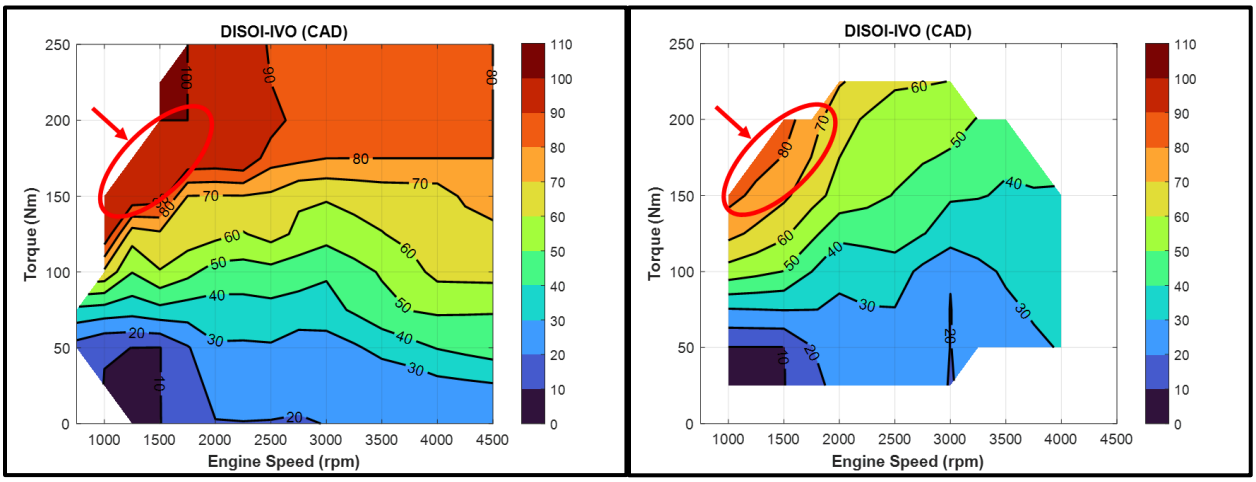

(c) (d)

Figure 4-31: Difference in valve timings and injection timings of the two calibrations.

(a) IVO of baseline engine (b) IVO of Miller engine (c) DI SOI of baseline engine (d) DI SOI of Miller engine; Comparison of valve timings shows there's a considerable difference in valve timings at the low speed high load regions

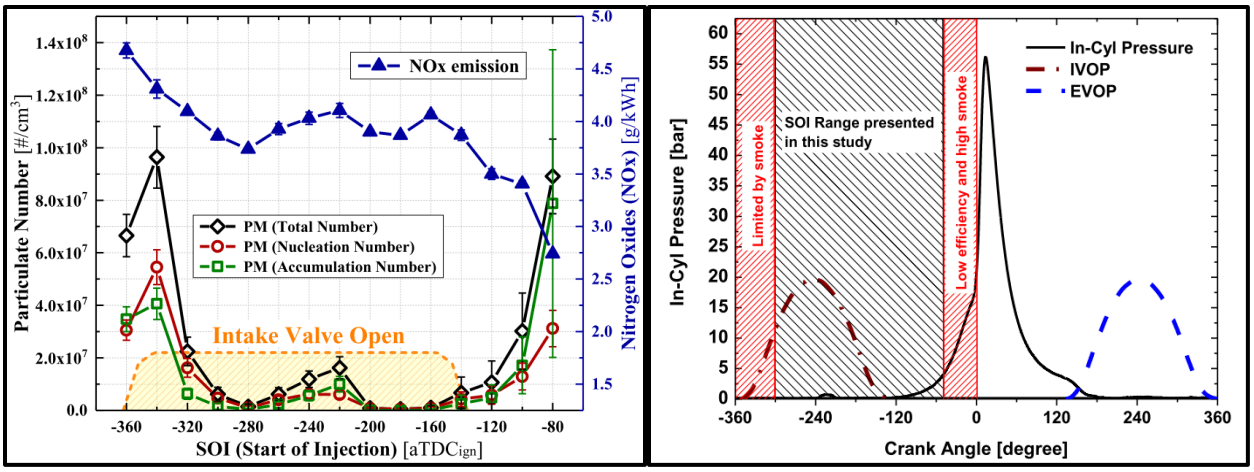

(a) (b)

Figure 4-32: Injection event before intake valve opening leads to high levels of particulate emissions as observed by (a) Han and (b) Singh respectively [30,41].

Lastly, the lower in-cylinder temperatures and pressures due to reduced effective compression ratio combined with the lower volumetric efficiency could be a reason for higher hydrocarbon emissions.

Baseline Engine with FGT **Miller Engine with VGT**

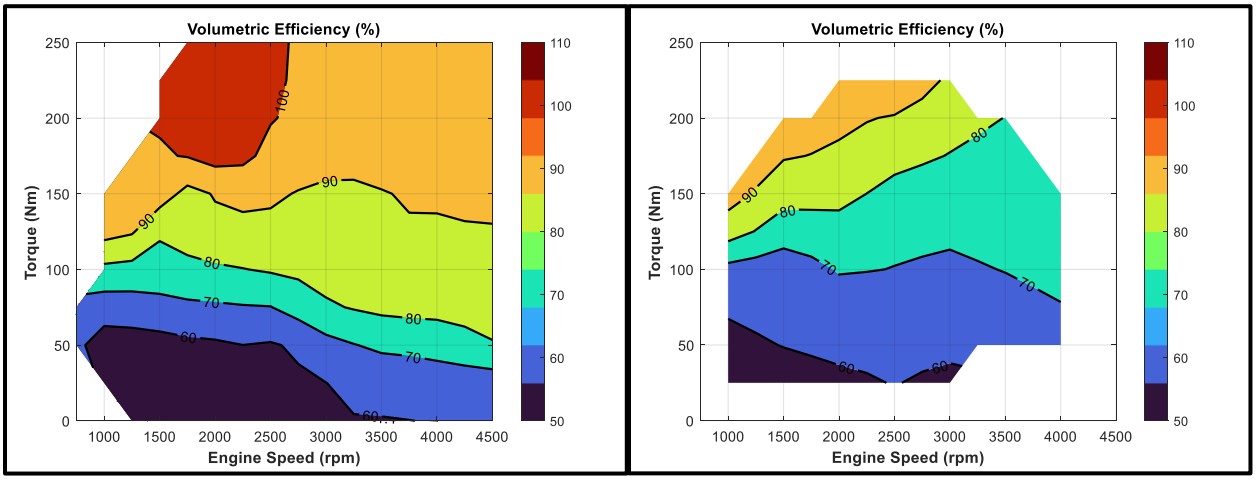

(a) (b)

Figure 4-33: Comparison of volumetric efficiency.

(a) Volumetric efficiency of baseline engine (b) Volumetric efficiency of Miller engine

4.3.3 Exploring with Open Waste-gate Strategy

BMTS's prototype FNT was also equipped with a wastegate similar to conventional fixed geometry turbos. The thought process behind this design was to allow hot exhaust gases to bypass the turbine and reach the closed coupled and underbody catalysts sooner to promote aftertreatment system lightoff. Furthermore, the wastegate allowed for low pumping losses during throttled operation since boost was not required at these conditions. The author explored the possibility of using an open wastegate operation at throttled conditions and recorded further improvement in thermal efficiency.

Recall from Figure 4-22 that above 3000 rpm and low to mid engine loads, the throttle position is more closed with the Miller engine. This is despite the calibration set to the highest Atkinson ratio to get the minimum boost possible (low effective compression ratio combined with more work extracted before exhaust enters turbine). This suggests that despite our efforts to minimize boost, the larger compressor size on the VGT manages to overboost compared to the FGT with a wastegate. There is potential for reducing throttling and pumping losses at these conditions leveraging the wastegate actuator on the BMTS turbocharger.

As can be seen from the comparison of brake specific fuel consumption (Figure 4-35), there is significant improvement (almost 5 g/kWh) at engine speeds greater than 3000 rpm. The reason for this improvement is the reduction of throttling losses and pumping losses as seen in the Figures 4-37 and 4-38 below.

Transient tests were not run by combining the wastegate and nozzle actuation but it is hypothesised that the fuel consumption benefits would come at the expense of slower response and increased turbo lag with the VGT having faster control as opposed to the wastegate.

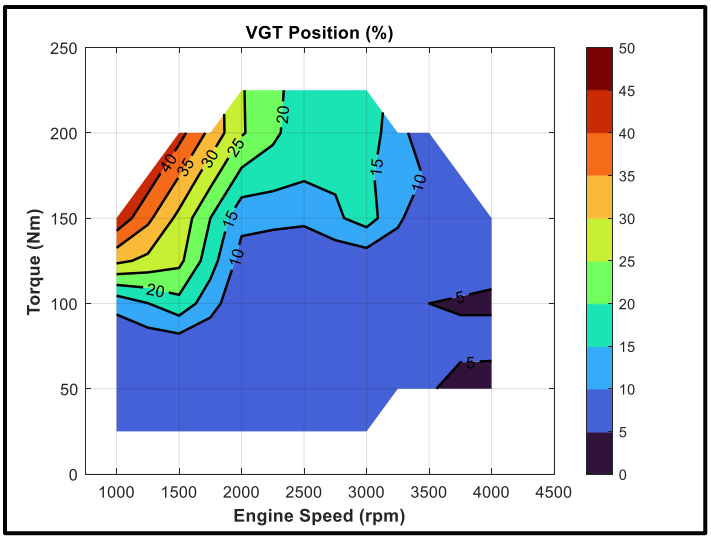

Figure 4-34: Map of Vane Position of BMTS FNT (100% = Fully Closed).

Closed WasteGate **Open WasteGate**

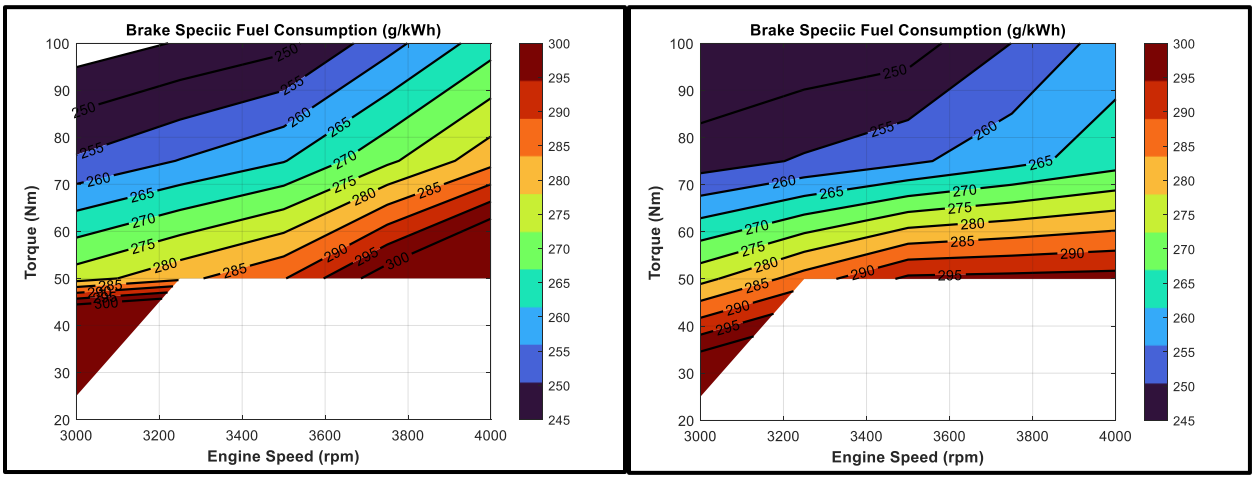

(a) (b)

Figure 4-35: Comparison of brake specific fuel consumption.

(a) BSFC with closed wastegate (b) BSFC with open wastegate; comparison shows BSFC reduction with open wastegate strategy.

Closed WasteGate **Open WasteGate**

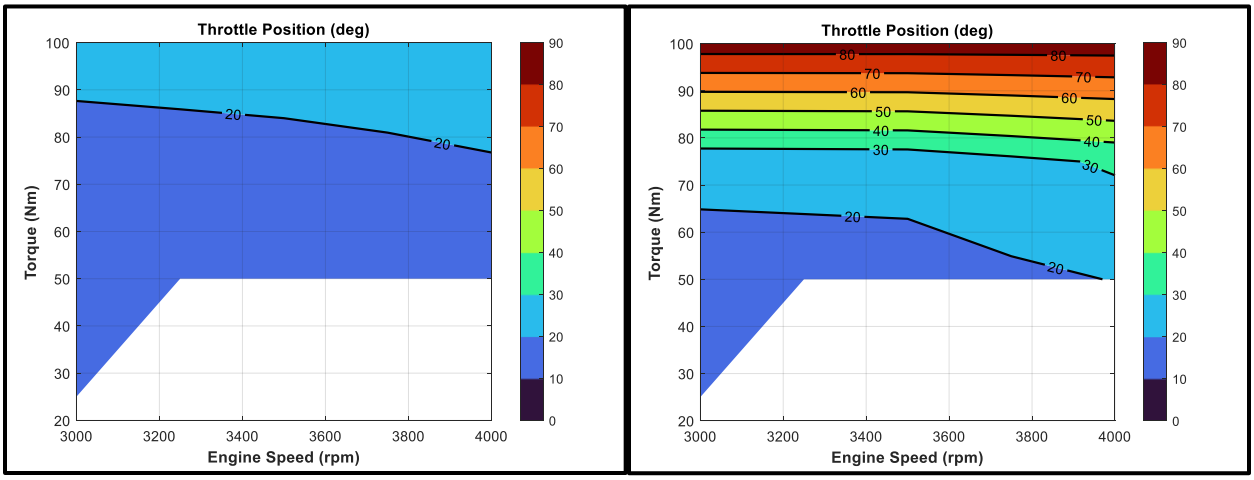

(a) (b)

Figure 4-36: Comparison of throttle position.

(a) Throttle position with closed wastegate (b) Throttle position with open wastegate; comparison shows that the throttle valve is in a more open position for the open wastegate strategy.

Closed WasteGate **Open WasteGate**

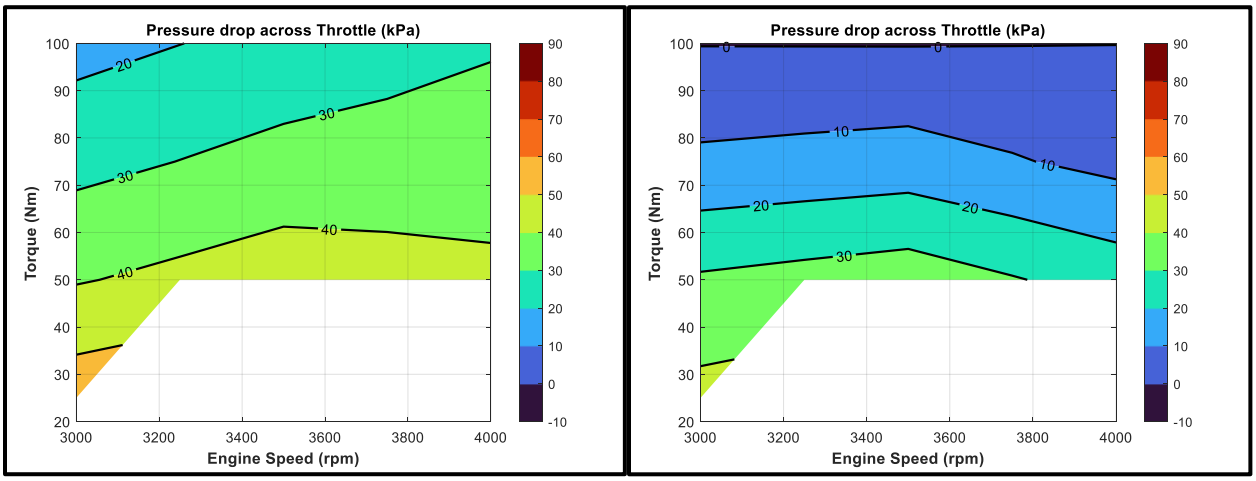

(a) (b)

Figure 4-37: Comparison of throttling losses.

(a) Pressure drop across throttle with closed wastegate (b) Pressure drop across throttle with open wastegate; comparison shows that the open wastegate strategy led to lower throttling losses.

Closed WasteGate **Open WasteGate**

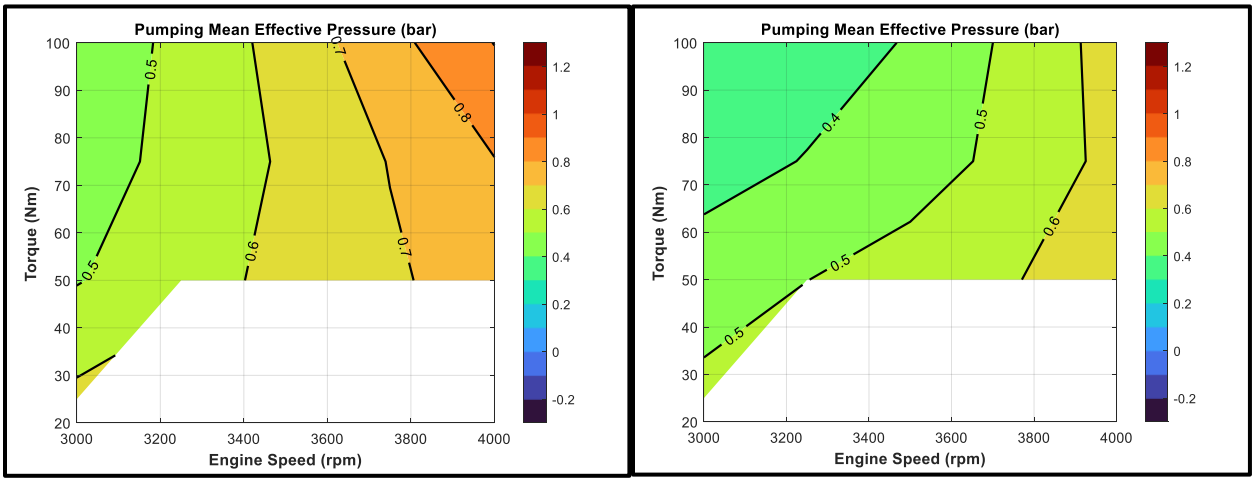

(a) (b)

Figure 4-38: Comparison of pumping mean effective pressure (PMEP).

(a) PMEP with closed wastegate (b) PMEP with open wastegate; comparison shows that the open wastegate strategy led to lower pumping losses due to lower backpressure from turbine vanes.

4.3.4 Transient Test Results

As mentioned earlier in the experimental methods, steady state testing was followed up by transient testing. The tests with the FNT were run with the wastegate closed at all times due to failure of the wastegate actuator. The results from the standardized transient tests that were run are presented in this section.

Federal Test Procedure 75 (FTP-75):

The FTP 75 tests that simulated urban driving conditions in North America showed an improvement in the fuel economy with the Miller engine. As can be seen from Figure 4-42, the engine resided longer in high efficiency islands on the Miller engine compared to the baseline. The benefits of lower engine out NO_X emissions and CO emissions that were seen in the steady

state testing were also seen in the FTP tests. The reason for higher THC and particulate matter was a combination of lower degree of control on lambda and sub-optimal injection strategy as explained earlier. The Figure 4-39 illustrates the difference in control of lambda and as a result fueling. Clearly, the engine resides in lean and rich fueling regimes for a longer duration of time, and this results in a number of engine cycles with low combustion efficiency.

Moreover, there was what appeared to be an issue with the engine idle control for cylinder 1. Figure 4-40 is a snapshot of the AVL Indicom screen during one of the many points on the FTP cycle when the engine is idling. This clearly shows that cylinder 1 (yellow) is not combusting as efficiently as cylinder 3 (red). This happened regularly at transitions to engine idle and heavy decelerations. This issue would not occur at extended idle and hence it was not seen during our steady state testing. At first, it was hypothesized that this could be due to a faulty PFI injector. However, replacing the PFI injector did not change this. So later, it was hypothesized that this could be due to inherent dynamics of the air flow into the cylinder. Since the throttle on this engine is not centrally placed but to the side, it runs the risk of unequal air distribution among the three cylinders. When the throttle shuts quickly during heavy decelerations, it cuts the air supply to the manifold, but since the air comes in from the side, it is possible that the momentum of the air makes it enter cylinder 3 preferentially over cylinder 1. This hypothesis is backed up by the fact that cylinder 3 is also more prone to knock compared to cylinder 1 and it was cylinder 3 that was damaged during our heavy knock event. Also as seen from Figure 4-39, the throttle position oscillates more with the new controller during heavy decelerations which results in higher number of lean and rich cycles.

The combination of these factors results in higher hydrocarbon and particulate matter emissions as seen in the results. A comparison of the particle size distributions over the entire

cycle also show a higher number of particles for the Miller engine especially in the nucleation mode (Figure 4-43).

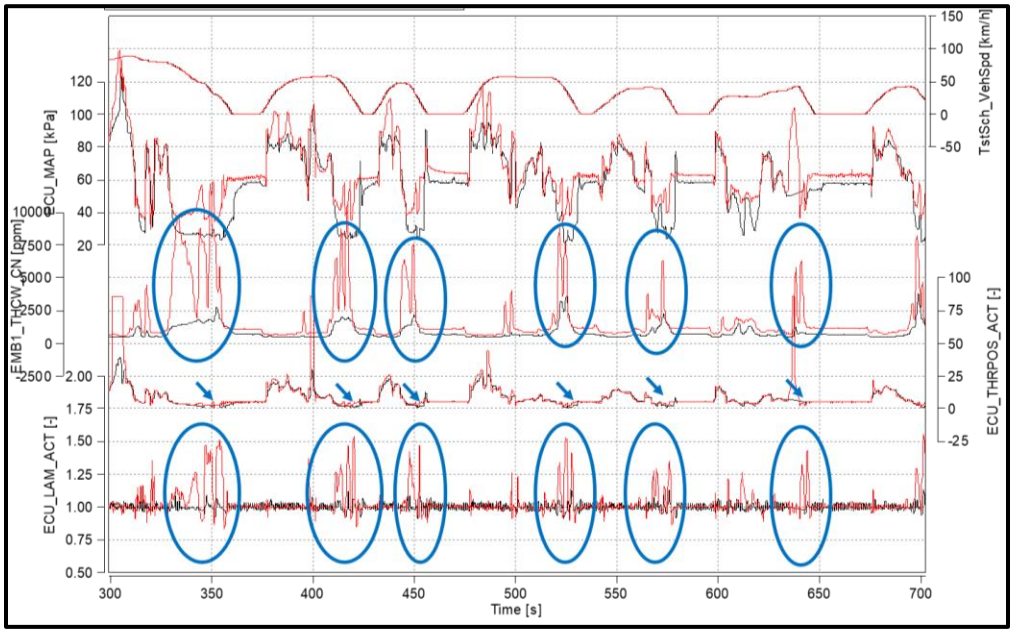

Figure 4-39: Highlighted greater oscillations in air-fuel ratio and THC emissions during heavy decelerations in vehicle speed with overridden throttle controller (Black: Baseline; Red: Miller).

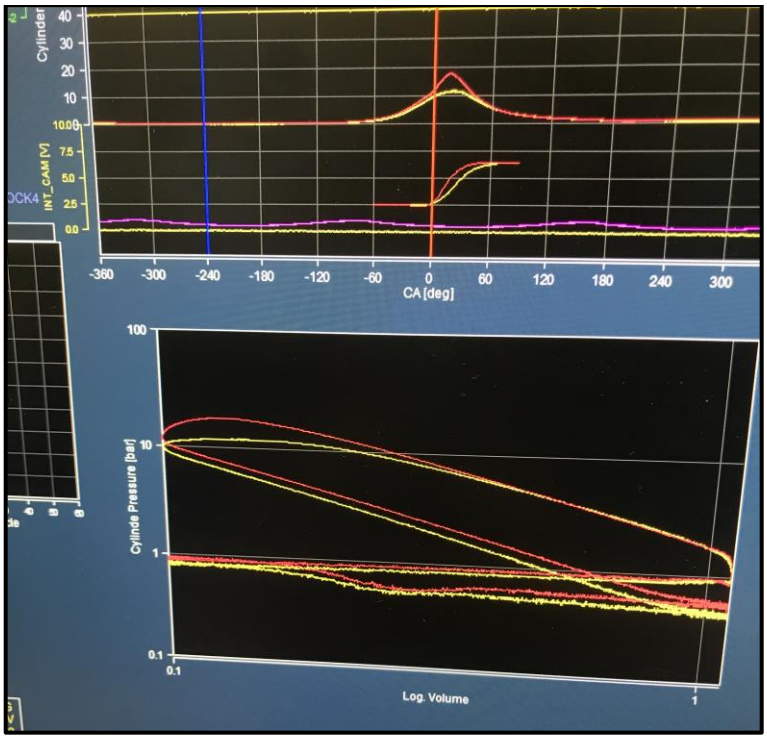

Figure 4-40: Indicom snapshot showing the logP-logV diagram, the cylinder pressure and the burn rate which is worse for cylinder 1 (Yellow: cylinder 1; Red: cylinder 3).

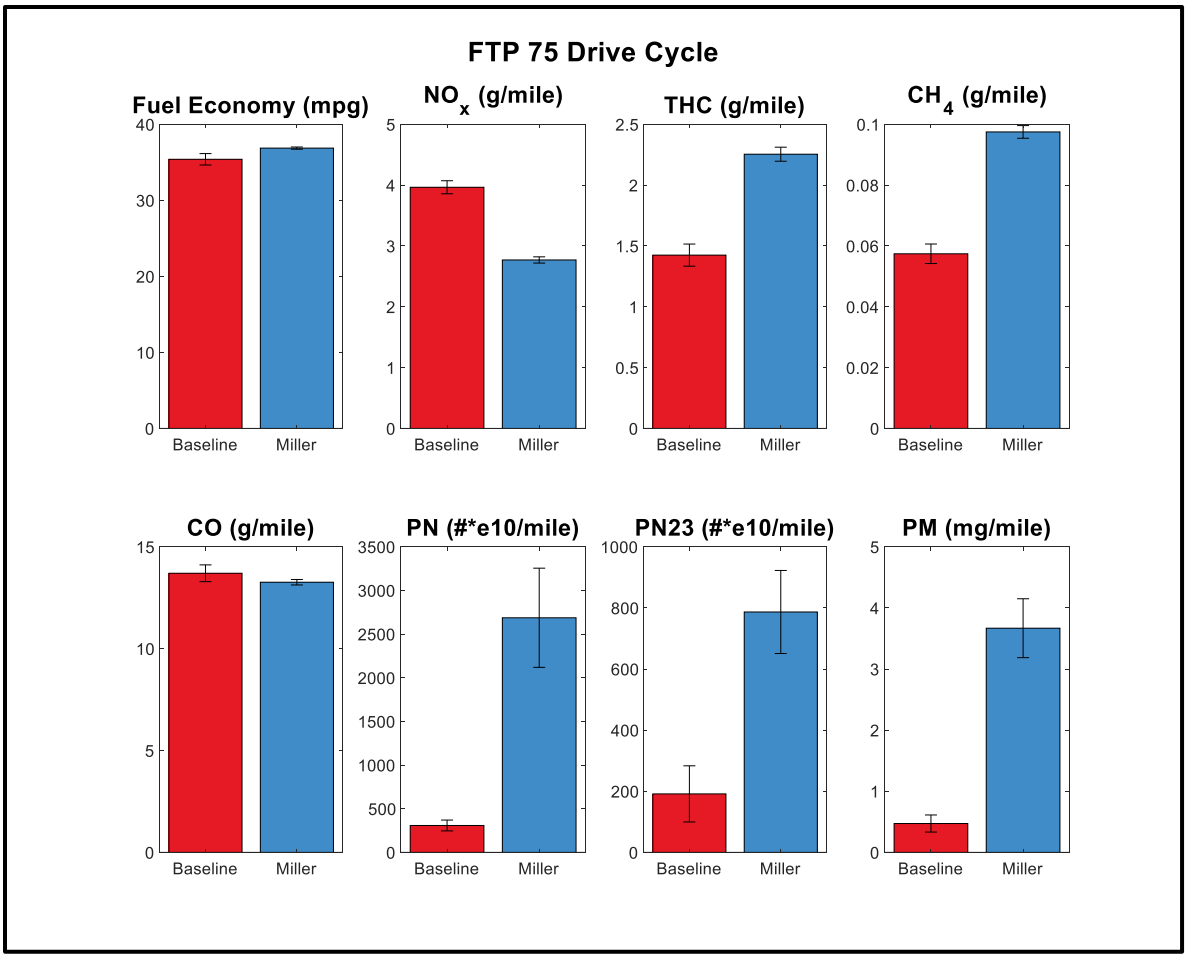

Figure 4-41: Results from FTP-75 testing.

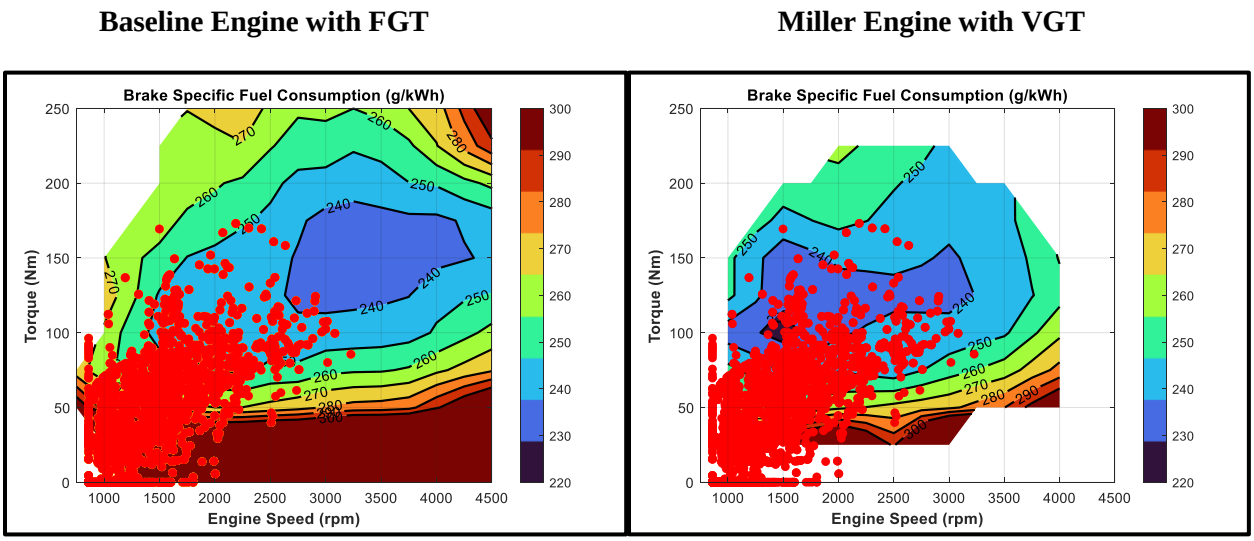

(a) (b)

Figure 4-42: Comparison of residing points of engine during FTP75 cycle on (a) baseline map vs. (b) Miller map.

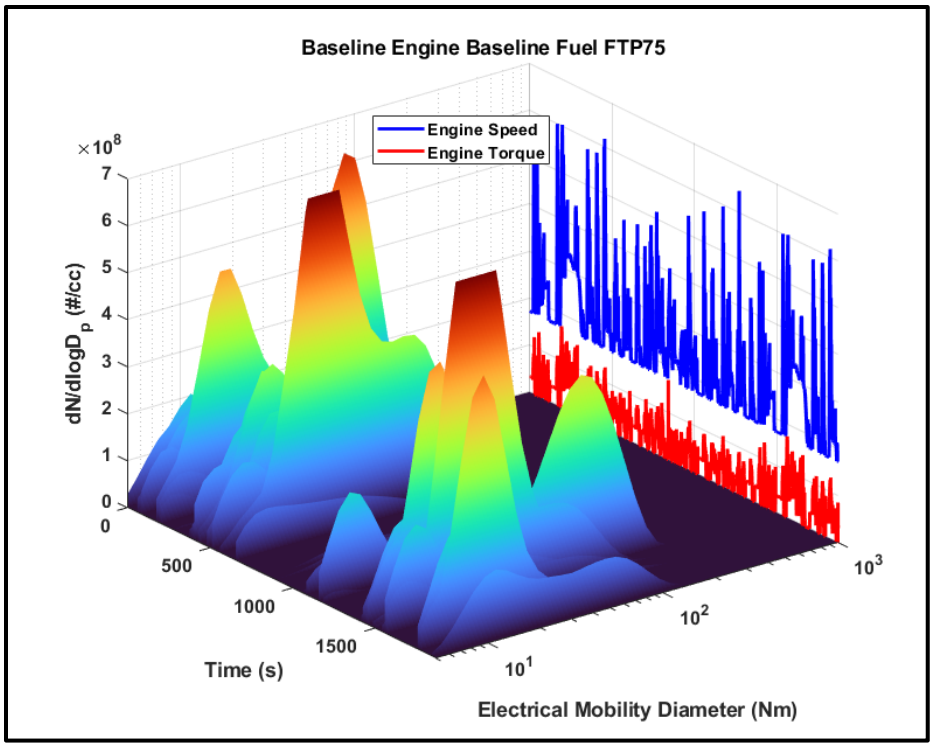

(a)

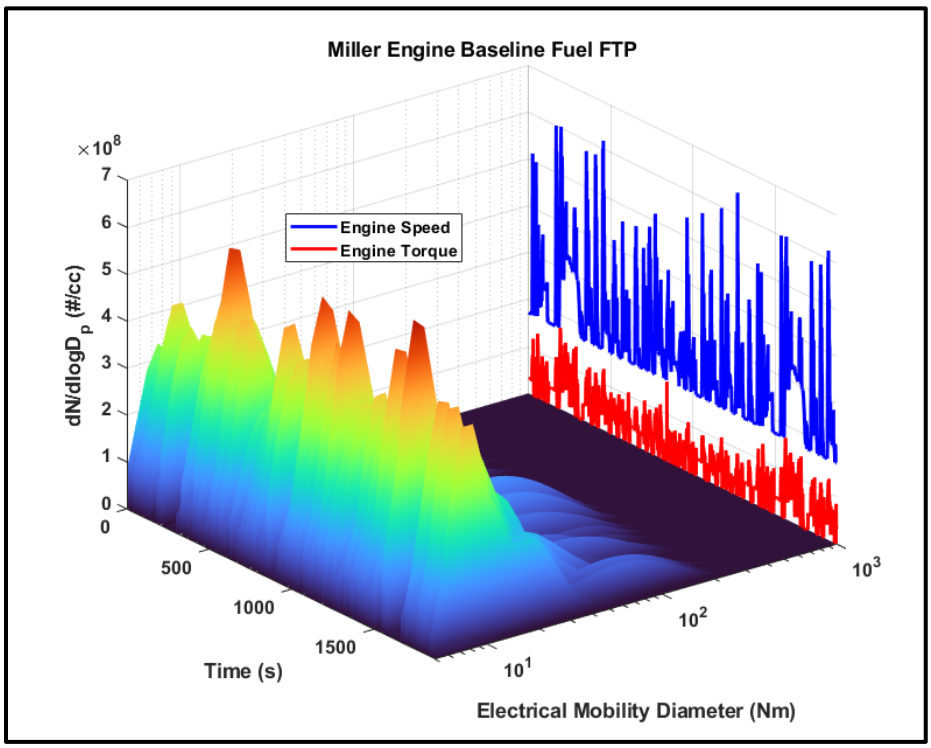

(b)

Figure 4-43: Comparison of particle size distribution for FTP75 cycle (a) baseline engine (b) Miller engine.

Highway Fuel Economy Test (HWFET):

This test simulating cruising driving did not show a significant benefit in terms of fuel economy. As seen from the fuel consumption islands, the engine resides in high thermal efficiency islands for both calibrations. CO and NO_X emissions benefits seen in steady state testing continue to be observed under these driving conditions. THC and particulate matter emissions are observed to increase due to reasons mentioned earlier. A comparison of the PSDs (particle size distribution) shows that particulate matter concentrations are lower for the baseline for all diameters measured. Also, during the phase of the cycle in the middle, where the engine is pretty much at steady state, there appears to be little to no particulates for both engines.

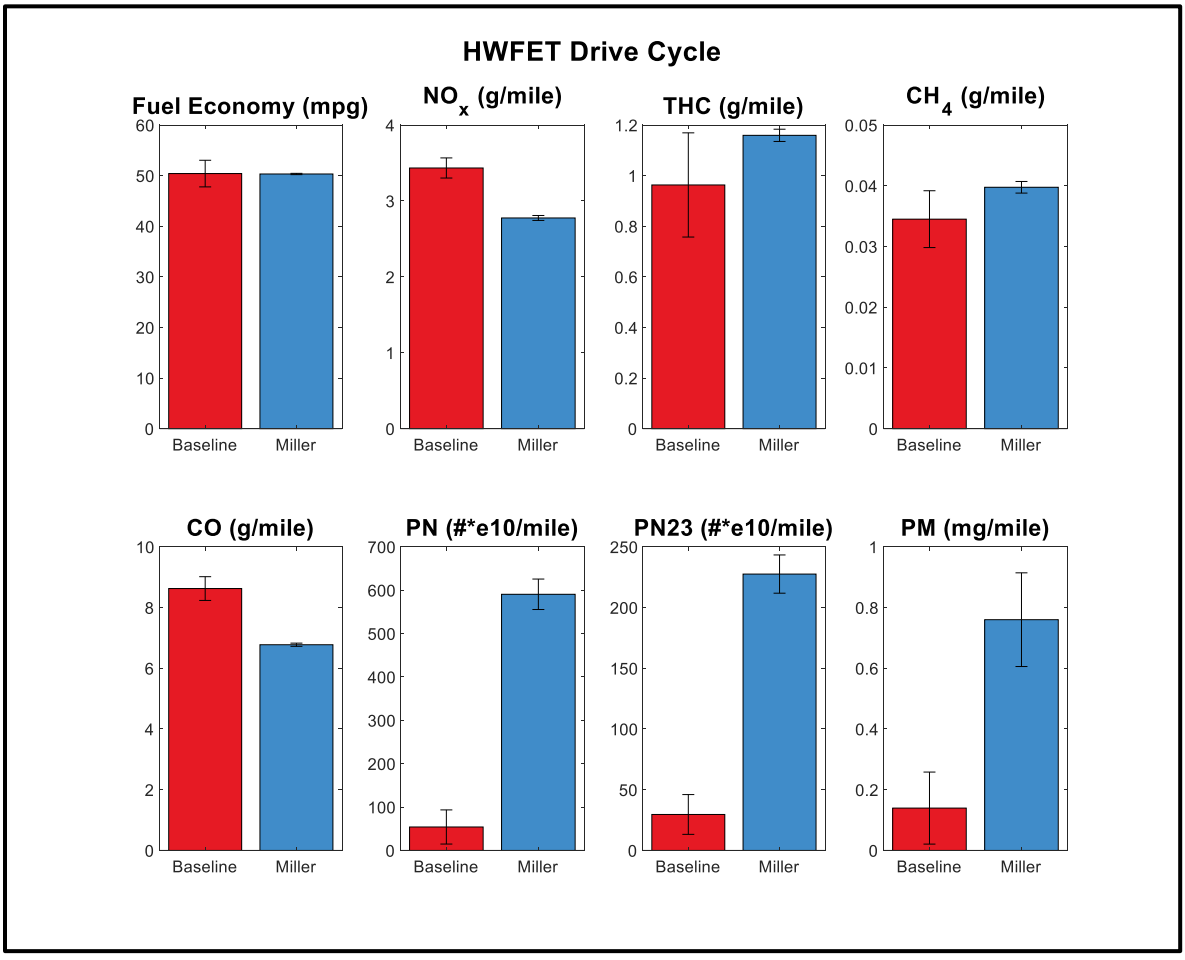

Figure 4-44: Results from HWFET testing.

Baseline Engine with FGT **Miller Engine with VGT**

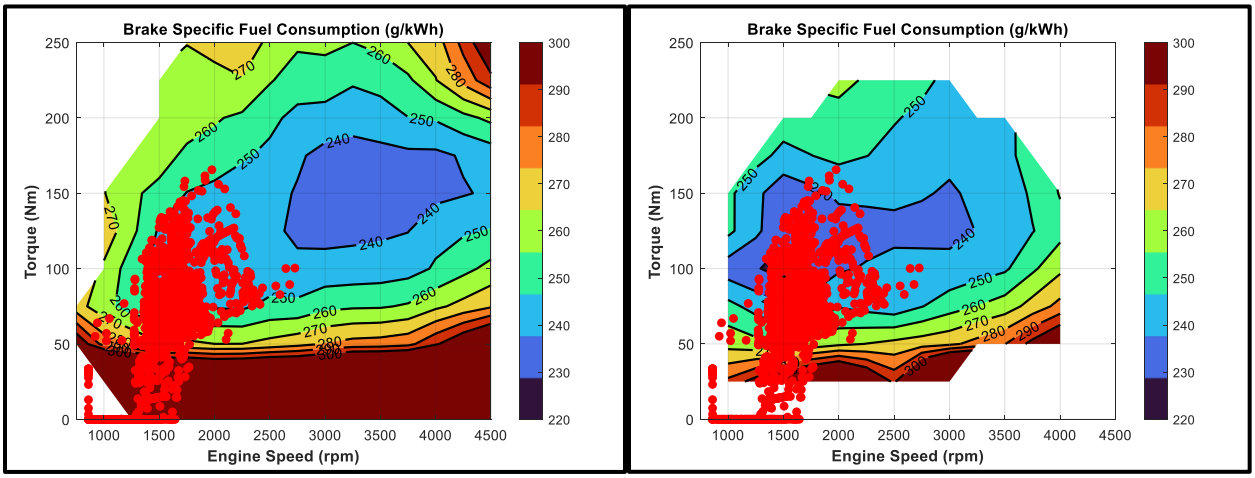

(a) (b)

Figure 4-45: Comparison of residing points of engine during FTP75 cycle on (a) baseline map vs. (b) Miller map.

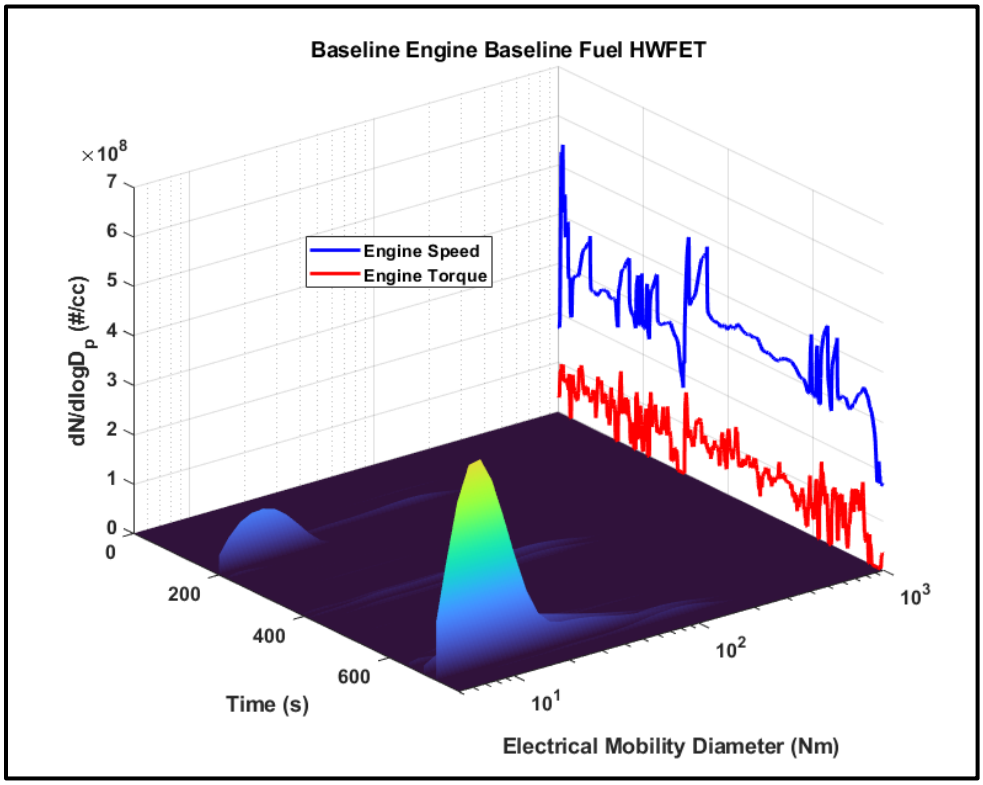

(a)

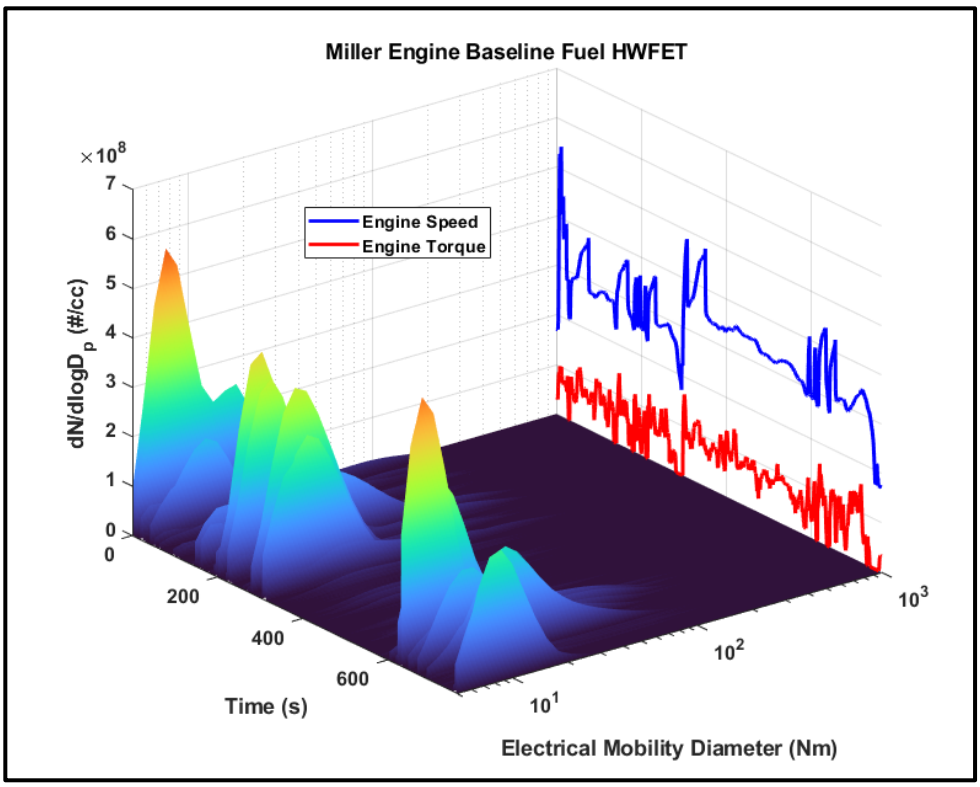

(b)

Figure 4-46: Comparison of particle size distribution for HWFET cycle (a) baseline engine (b) Miller engine.

Due to the nature of the highway cycle which has lesser accelerations and decelerations compared to the FTP, we see lower concentration of particulate matter across the range of all diameters measured. In fact, the baseline engine appears to emit very low concentrations of particulate matter on this scale for the highway cycle.

US06 Supplemental Federal Test Procedure (US06):

This test simulating aggressive driving behavior with the engine residing across a number of different engine speeds and loads does show a small benefit in terms of fuel economy. A comparison of the engine residence on the respective BSFC maps shows that a large fraction of the points lie in the high efficiency islands even at the elevated engine speeds. Above 3000 rpm, the increased boosting capability of the FNT results in greater throttling and pumping losses at low loads but this does not affect the results as much since the engine does not reside at those points during the cycle. The NO_X emissions benefit of Miller operation continues to be seen as it

was in the previous cycles. THC and particulate matter emissions are worsened which is consistent with the rest of the testing. CO emissions are increased as well possibly due to worse gas exchange efficiency with the constant accelerations and decelerations that are a part of this cycle. Lastly, the PSDs of both engines shows that with the exception of a couple of peaks where the baseline concentration is higher, the particulate matter concentration is higher for the Miller cycle for the majority of the test cycle.

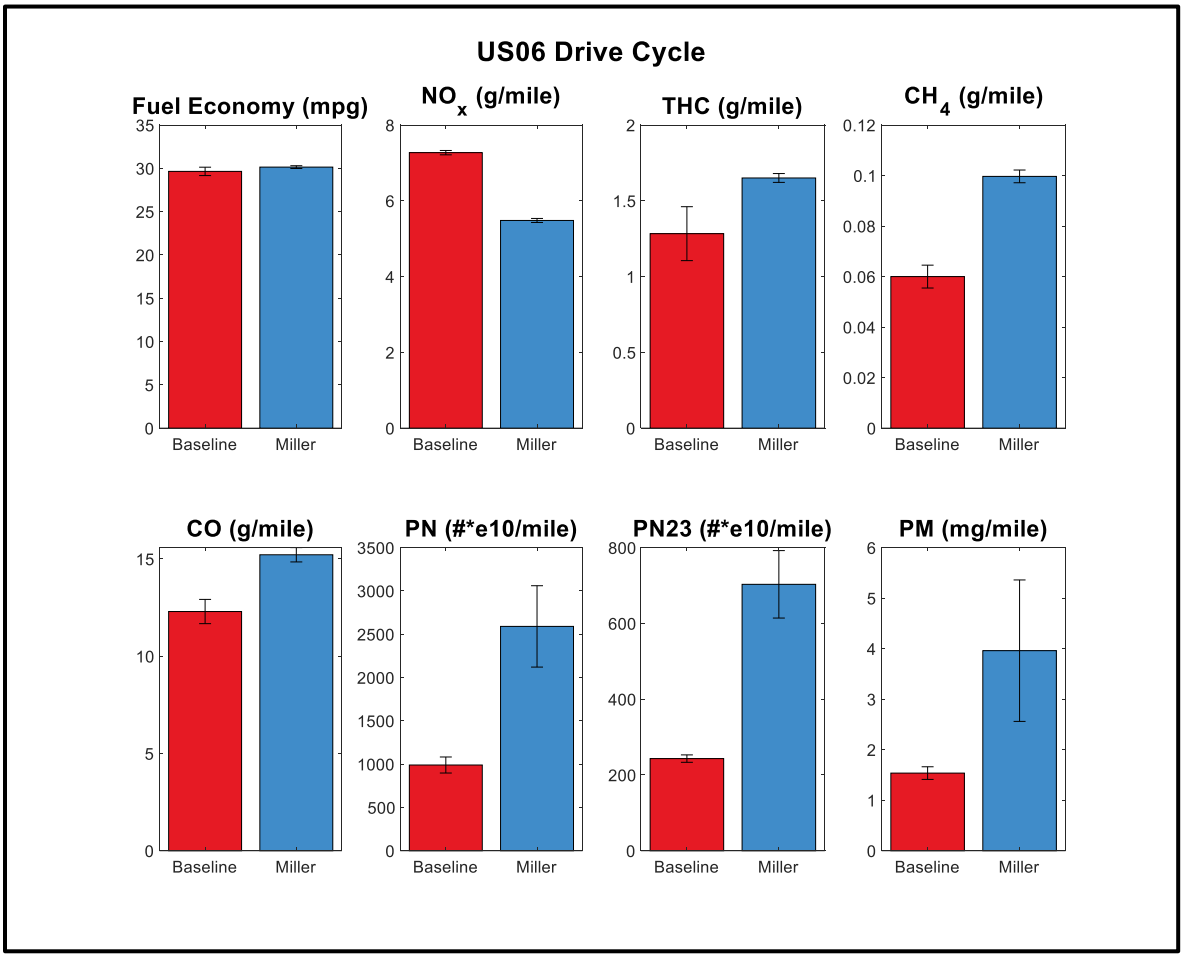

Figure 4-47: Results from US06 testing.

Baseline Engine with FGT **Miller Engine with VGT**

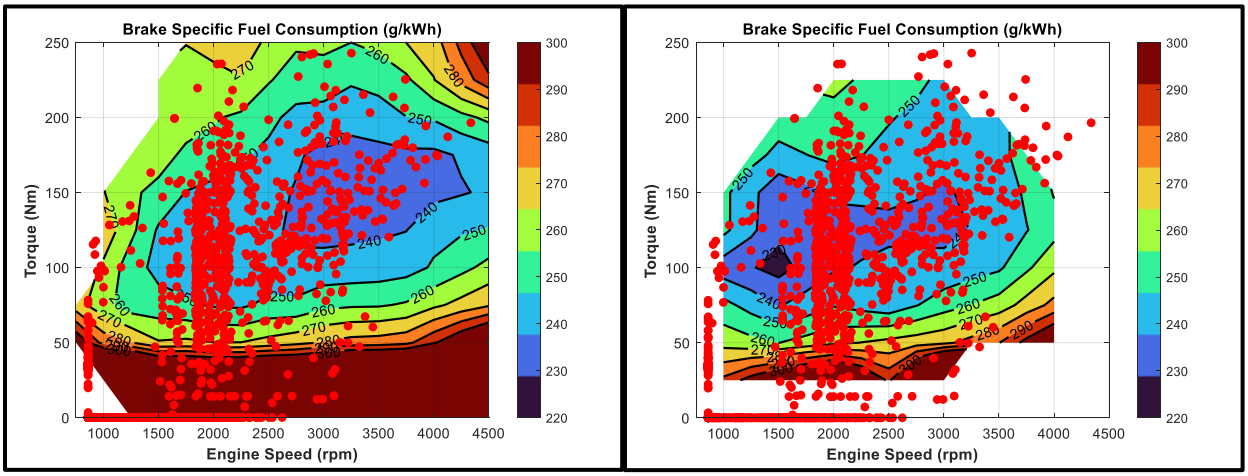

(a) (b)

Figure 4-48: Comparison of residing points of engine during US06 cycle on (a) baseline map vs. (b) Miller map.

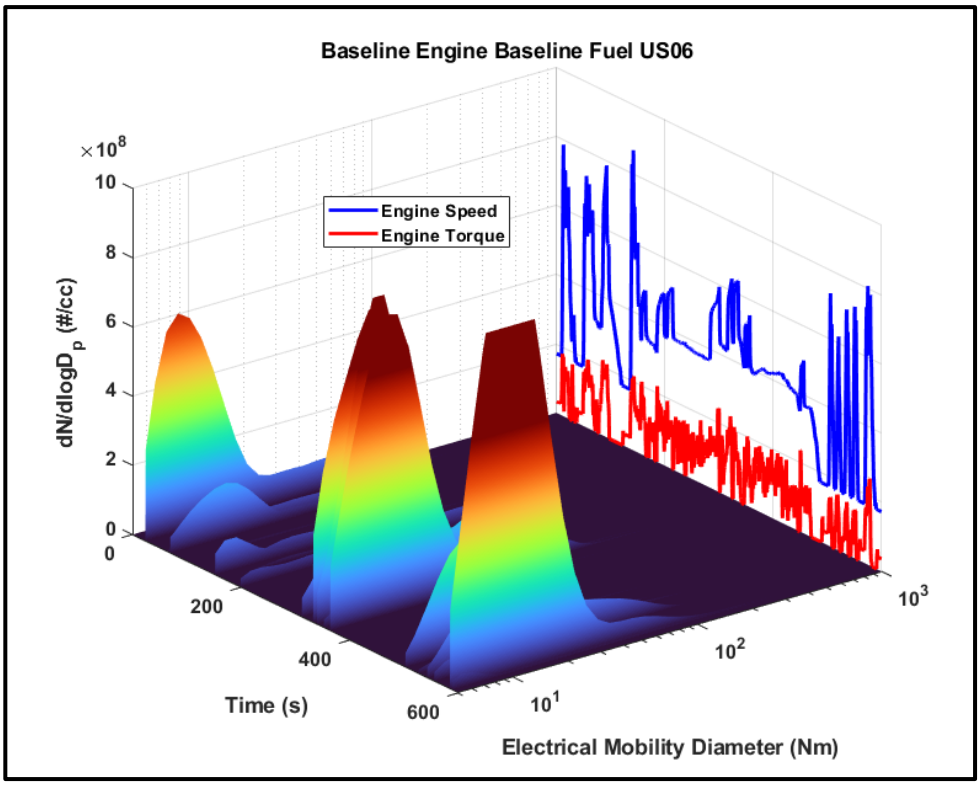

(a)

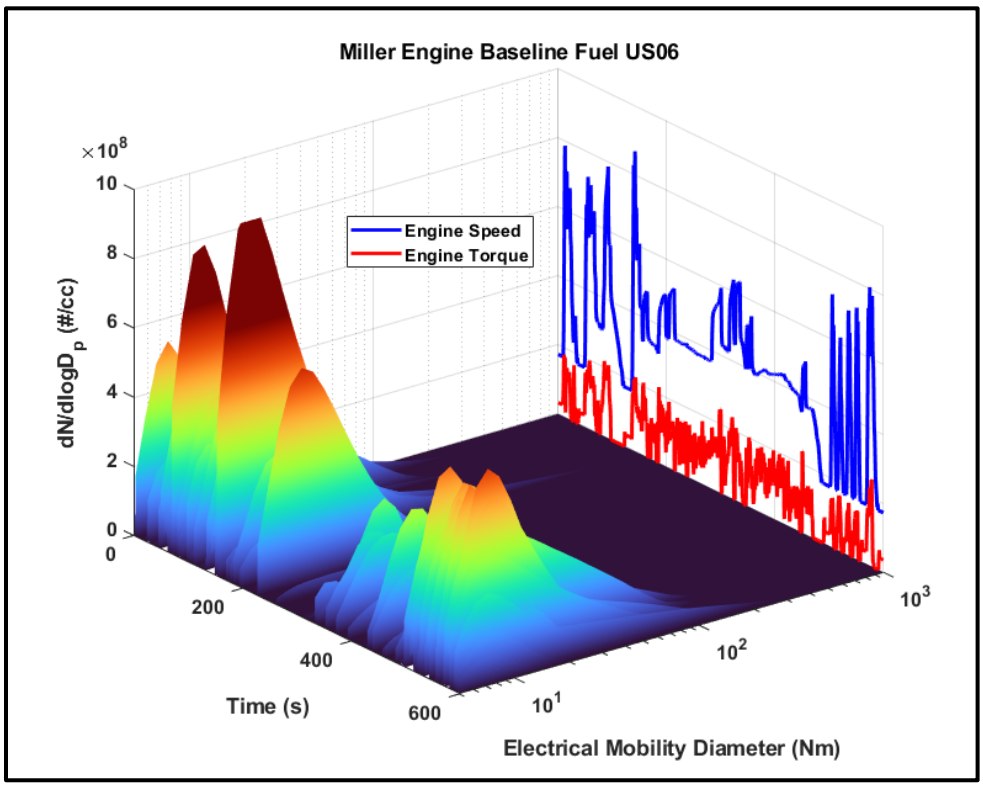

(b)

Figure 4-49: Comparison of particle size distribution for US06 cycle (a) baseline engine (b) Miller engine.

Worldwide Light vehicles harmonized Test Procedure (WLTP):

This drive cycle which is used outside of North America is a combined cycle for urban driving and highway driving with different subparts of the cycle corresponding to different vehicle speeds. Benefits of fuel economy are mostly recognized at lower engine speeds. NO_X and CO emissions are reduced for the same reasons as mentioned above. Likewise, THC and particulate matter emissions increase due to reasons mentioned above.

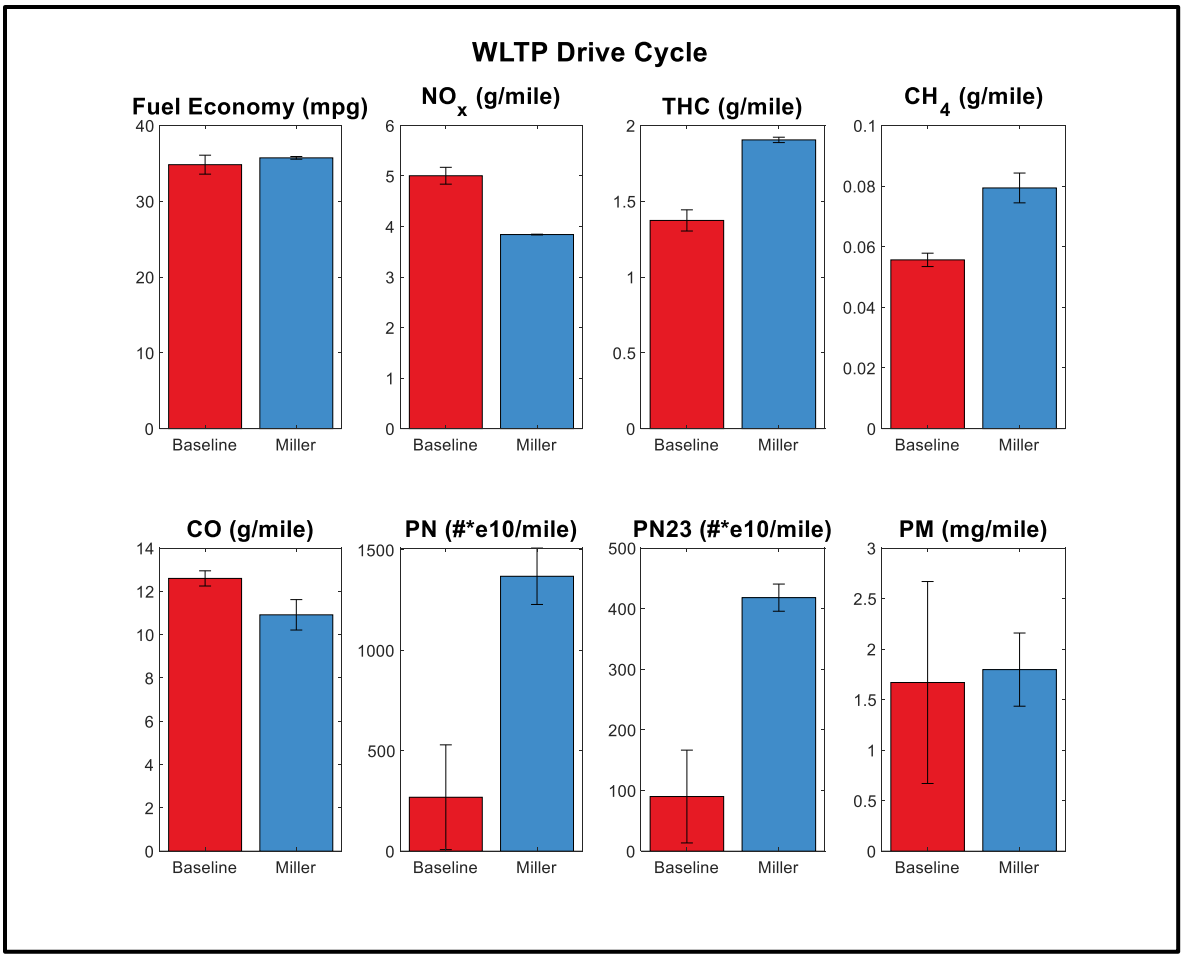

Figure 4-50: Results from WLTP testing.

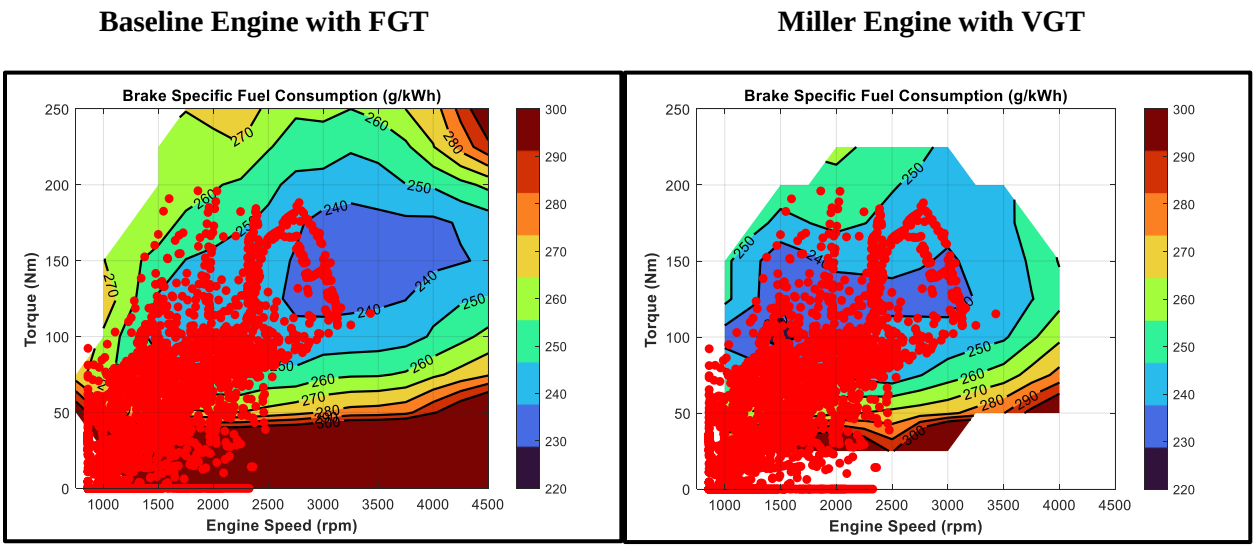

(a) (b)

Figure 4-51: Comparison of residing points of engine during WLTP cycle on (a) baseline map vs. (b) Miller map.

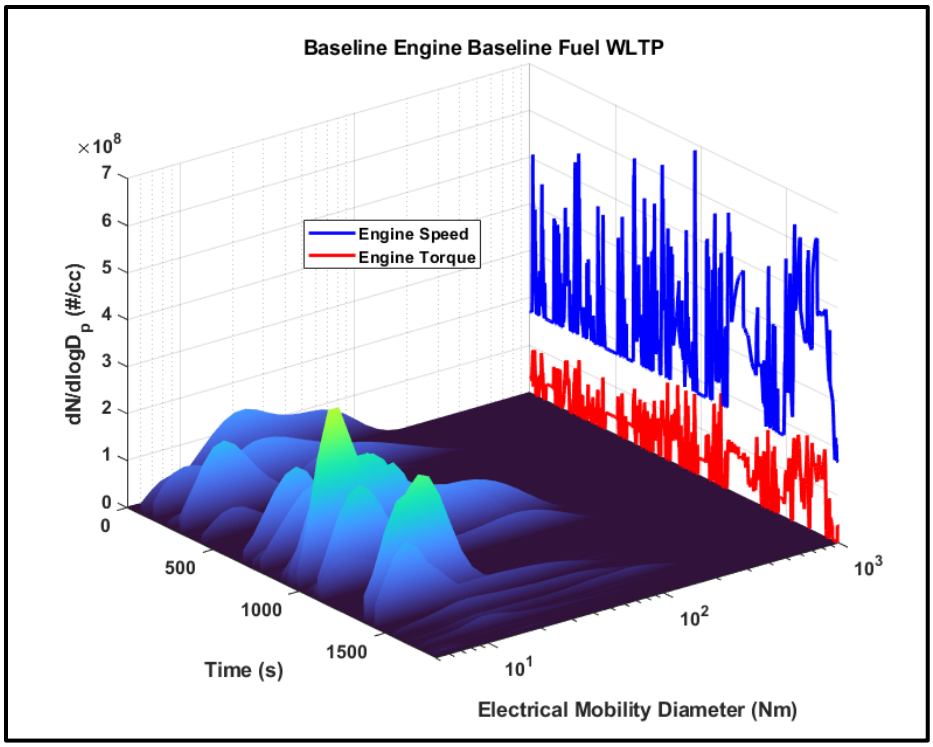

(a)

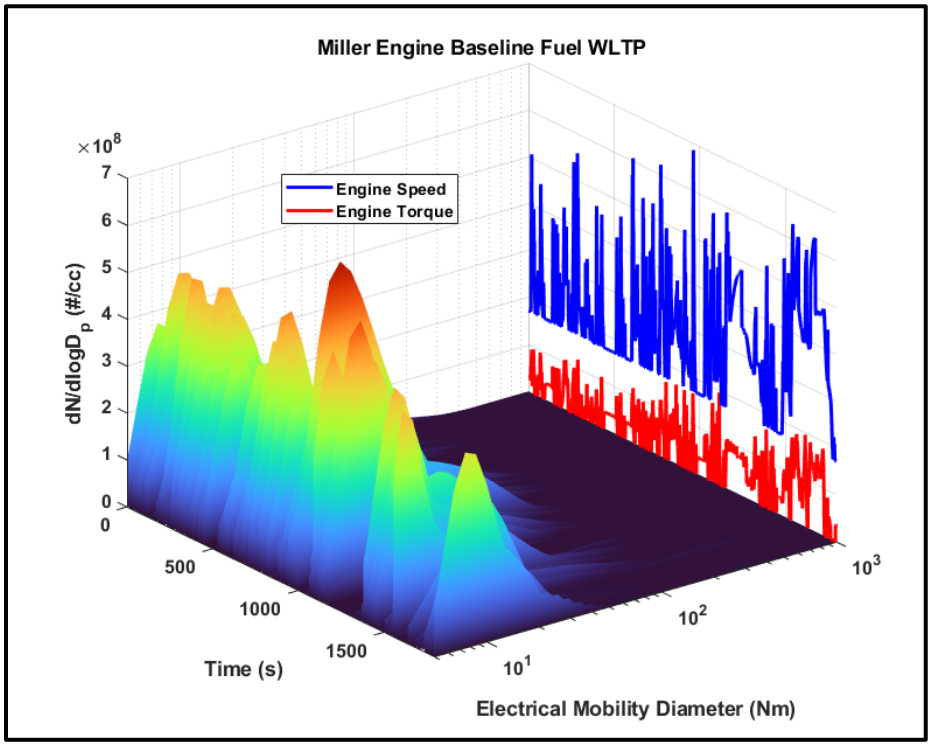

(b)

Figure 4-52: Comparison of particle size distribution for WLTP cycle (a) baseline engine (b) Miller engine.

4.4 Summary and Conclusions

A prototype floating nozzle turbocharger manufactured by BMTS GmbH was successfully integrated with a current generation downsized gasoline engine. The larger compressor size and the flexibility of boost control with the FNT allowed for the implementation of a Miller cycle strategy over the entire engine speed load map as evidenced by the comparisons of Atkinson ratios. The consequences of Miller implementation are summarized below:

1. Lower fuel consumption and higher thermal efficiency over a larger region of the engine speed load map especially at lower engine speeds. This is due to lower throttling and pumping losses. Miller cycle implementation leads to greater amount of work extracted per engine cycle.
2. Lower engine out NO_X emissions due to lower in cylinder temperatures.
3. Lower CO emissions possibly due to higher boost pressures resulting in improved gas exchange efficiency.
4. Not a significant difference in unburnt hydrocarbon emissions during steady state testing except at knock limited conditions where the injection timings were not optimized with the change made to the valve timings.
5. Potential for improving fuel consumption at throttled points at higher engine speeds by leveraging the wastegate to reduce both throttling and pumping losses.
6. Steady state test observations translated to transient tests as well. WLTP and FTP tests showed that urban driving conditions showed a benefit with the Miller cycle leading to lower fuel consumption.

7. HWFET did not show a significant benefit in fuel consumption. Cruising conditions showed a benefit in lower NO_X and CO emissions consistent with the rest of the testing.
8. US06 testing showed that the current iteration of the Miller calibration with the BMTS turbocharger led to small fuel economy benefit despite the engine residing at points of lower thermal efficiency. There was a slight CO emissions penalty but NO_X emissions improvement was observed.
9. All the transient tests with the FNT resulted in higher THC and particulate emissions. This is largely due to suboptimal lambda feedback control combined with suboptimal injection strategy.

The implementation of Miller cycle over the entire speed load map is novel and unlike any work done on downsized GDI engines previously. Previous work on Miller cycle application to gasoline engines has focused only on low engine loads and partial engine loads where the benefit of reduced throttling losses is realized. Moreover, while Miller cycle application has become more commonplace in the past half decade in naturally aspirated engines, the lack of sufficiently capable turbomachinery to meet boost demands has meant that the same strategies could not be applied to downsized boosted engines [47,118,119]. The promising results from this unique study could dictate how future engine manufacturers decide to calibrate their new engines so as to meet future emissions regulations which are bound to be more stringent than ever.

Chapter 5

Exploring the Relation between Knock Intensity and Particulate Emissions of a Light-duty Downsized Turbocharged Gasoline Spark Ignition Engine

5.1 Introduction

Modern GDI engines contribute significantly to ultrafine particulate matter emissions as a result of injecting fuel directly in the combustion chamber. This allows for less time for fuel atomization and results in a higher propensity for cylinder wall wetting. The combined effect results in the formation of pool fires which results in the formation of soot precursors such as polycyclic aromatic hydrocarbons (PAH) [57,58,122,123] which agglomerate and eventually form soot. The widespread issue with high particle number emissions from modern GDI engines has necessitated the installation of gasoline particulate filters similar to their diesel counterpart in light duty vehicles sold in the European and Chinese markets [124].

The trends from vehicle data that has been collected over the years suggests that modern engines have done a good job at meeting the particulate mass standards by reducing larger diameter particles through the implementation of direct injection at very high rail pressures [125]. However, in the absence of standards for particles below 23 nm in diameter, the outcome has resulted in a large fraction of particles emitted in the range of 10 nm - 23 nm. Blending ethanol in gasoline to extend knock limits, as is done in the United States, has also shifted the

range of particles emitted to the lower diameter range. Furthermore, the rise in hybrid vehicle sales which employ engine start-stop technology for their power management control system contribute significantly to high particulate matter emissions as well. Most vehicles sold in the US are not equipped with gasoline particulate filters due to the absence of a particle number standard that would necessitate them [124]. This means that these ultrafine particles are released into the atmosphere if they are not converted to complete combustion products in the vehicles' exhaust after-treatment system.

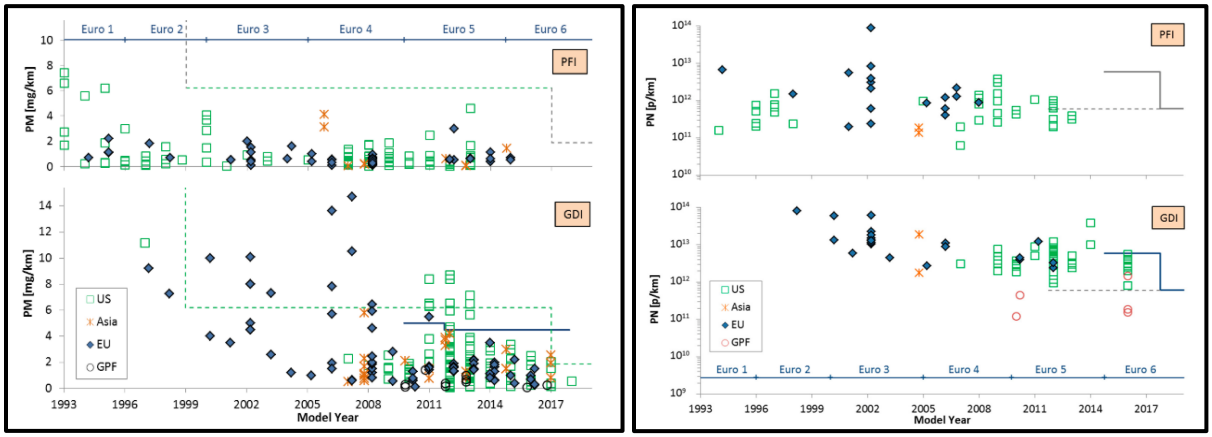

(a) (b)

Figure 5-1: Trends in (a) Particulate mass emissions vs. (b) particulate number emissions show that lowering PM has not necessarily resulted in lower PN [125].

Soot formation from the combustion and pyrolysis of hydrocarbon fuels is a complex mechanism that involves a number of processes. These processes include soot particle inception by formation of gaseous soot precursors, homogenous particle nucleation from gas phase to solid phase, particle surface reactions for simultaneous growth and oxidation and lastly particle coagulation and accumulation [126].

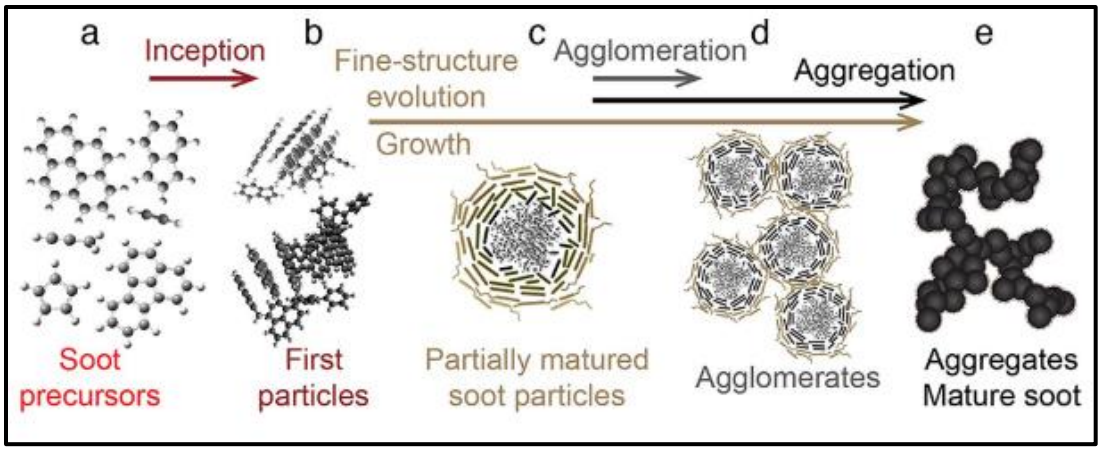

Figure 5-2: Schematic diagram of the major processes in soot formation [127].

Polycyclic aromatic hydrocarbons (PAH) are considered gaseous phase soot precursors [128] and thus their formation from small aliphatics is considered by many as the rate limiting step in soot formation. The following reactions were considered key contributors to the formation of the first aromatic ring which initiates the process [129–133].

$$n\text{-}C_4H_3 + C_2H_2 \rightarrow \text{phenyl}$$

$$n\text{-}C_4H_5 + C_2H_2 \rightarrow \text{benzene} + H$$

The HACA mechanism first proposed by Frenklach and Wang [134] is a popular mechanism that describes the growth of aromatics and eventually particle nucleation. HACA stands for 'H-abstraction-C_2H_2-addition' and involves the repetition of two major steps as the name suggests:

$$\text{Hydrogen Abstraction: } A_i + H \rightarrow A_i\text{-} + H_2$$

$$C_2H_2 \text{ Addition: } A_i\text{-} + C_2H_2 \rightarrow A_{i+1} + H$$

The hydrogen abstraction activates the aromatic molecule leading to further growth by acetylene addition by converting it to a radical. Researchers have shown and concluded from shock tube and flame experiments that the hydrogen abstraction reaction is the one that dominates

[131,135]. HACA also mentions that during this process of aromatic growth, simultaneous oxidation of aromatic radicals takes place due to the presence of O_2 and OH. HACA details that the H atom also destroys O_2 and thus aromatics growth is accompanied by depletion of O_2 [126].

Particle nucleation refers to the step involving the conversion of gas phase PAH species to solid-state soot particles. The growth of PAHs leads to the formation of stable isomers also called stabilomers. Due to their inherent stability, they do not decompose and instead collide to form clusters [126,136]. These clusters then coagulate and agglomerate to form fractal aggregates by sticking together [126].

The health hazards associated with ultrafine soot particles being released into the atmosphere are well documented [56,137,138]. Due to their size, they are more likely to make it into the human bloodstream through the lungs. Thus, it is important to study soot emissions in further detail as it relates to modern GDI engines.

Spark ignition engine knock occurs as a result of the end-gas auto-igniting before the turbulent flame front has consumed it. This auto-ignition occurs because of high in cylinder pressures and temperatures surrounding the end gas air fuel mixture both of which promote the forward reaction for auto-ignition. Typically, with spark ignited engine platforms, this tends to occur at high engine loads at low engine speeds. The high engine loads account for the high in cylinder temperatures and pressures while the low engine speed accounts for sufficient time availability for the auto-ignition to take place [8]. The fact that engine knock can lead to permanent engine hardware damage is well known. Thus, gasoline engine calibrators avoid knock by delaying the combustion phasing and operating at lower thermal efficiencies.

These two phenomena of engine knock and soot appear to be completely distinct at first glance and previous studies in literature have only explored one or the other but not both. Any

correlation between the occurrence of knock and particulate matter emissions has not been published in literature.

Han made the novel observation at the UM Auto Lab that there exists a clear correlation between knock occurrence and increased soot emissions during his experiments on a single cylinder GDI engine as part of his doctoral thesis [30]. Han observed this phenomenon while conducting combustion phasing sweeps for quantifying knock onset. While sweeping combustion phasing from late to early timing, he observed that this phenomenon would begin at knock onset. Moreover, particulate matter emissions increased with increasing knock intensity as combustion was phased earlier. This suggested that the possibility of a correlation with knock intensity as well. During his doctoral thesis, Han observed that this phenomenon occurs across a range of different oxygenated fuels, different injection strategies as well as different dilution strategies.

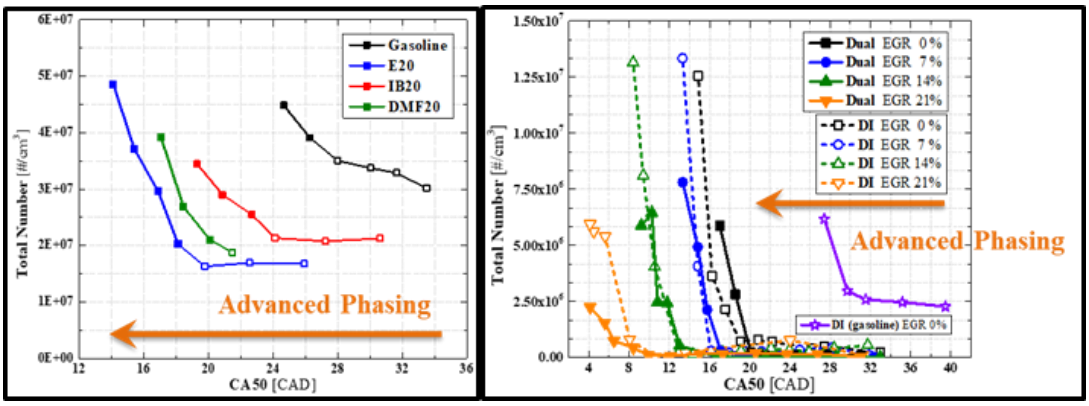

(a) (b)

Figure 5-3: Knock-soot correlation observed by Han [30] using (a) different fuels (b)different injection strategies and EGR dilution.

This phenomenon warranted further exploration and understanding using a state-of-the-art multi cylinder engine platform. This would help confirm this phenomenon across different

engine platforms. Moreover, this chapter follows on from Han's work and explores the effects of advancing the knock limit on the knock-soot correlation. Knock onset and its effect on soot emissions were studied through three sets of experiments.

Miller cycle operation is known to lower knock propensity and advance the knock limit due to reduced in-cylinder pressures and temperatures associated with lower effective compression ratios [115]. This chapter takes a step further to find the effect Miller cycle operation on the knock-soot correlation that was observed by Han. Further experiments explore the effect of injection strategies and fuel chemistry on the knock-soot correlation. More details about the fuel chemistries that were investigated can be found in the section below.

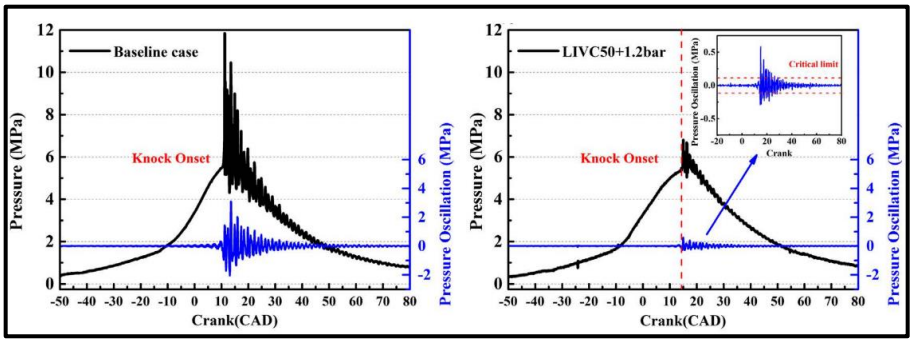

(a) (b)

Figure 5-4: Cylinder pressure and pressure oscillations for the (a) baseline engine vs. (b) Miller engine [115].

5.2 Experimental Methods

Experiments were conducted at four different knock limited points. The four points were selected at two different engine speeds and engine loads to explore the effect of varying engine speed and load. Moreover, these 4 points were selected due to them being popular engine residence points during the transient testing that was conducted as part of Chapter 4.

Baseline Engine with FGT **Miller Engine with VGT**

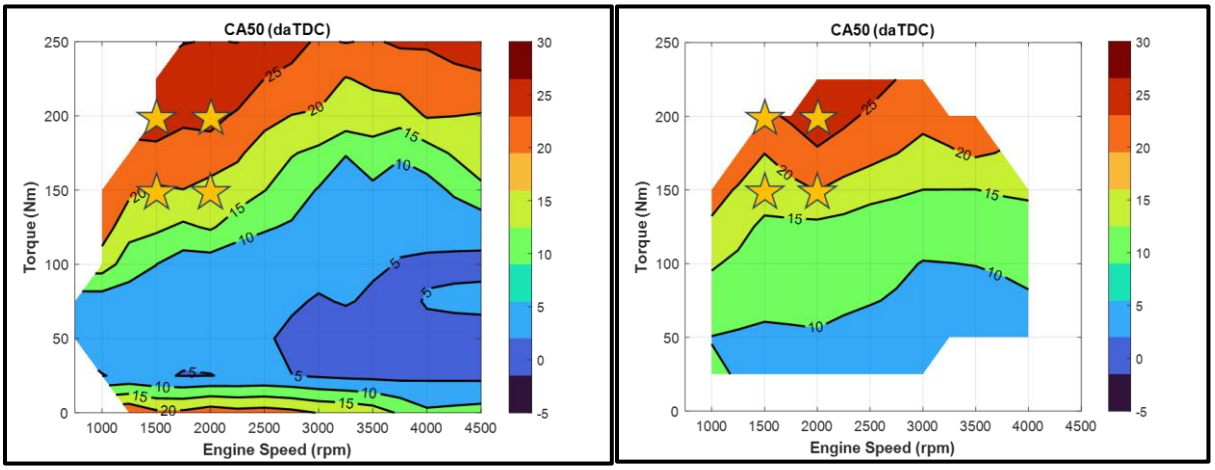

(a) (b)

Figure 5-5: Illustration of knock limited points tested in this chapter (a) Points located on baseline map (b) Points located on Miller map.

Number	Engine speed	Engine Torque	IMEPg
1	1500 rpm	150 N-m	13.5 bar
2	1500 rpm	200 N-m	18 bar
3	2000 rpm	150 N-m	13.5 bar
4	2000 rpm	200 N-m	18 bar

Table 5-1: Knock limited operating points of interest.

Three sets of tests were conducted. For the first set of experiments, the change of hardware was compared to quantify the effect of changing valve timing strategy and boosting hardware on knock and sooting tendency. This was followed by an experiment comparing the DI and PFI injection strategies at knock limited points on the Miller engine. Lastly, a study was conducted comparing two sets of different fuels of similar octane rating and sensitivities on the Miller engine.

The fuels that were investigated as part of this chapter are detailed in the Table 5-2. Two different pathways were chosen for exploring the effects of differing octane rating. Fuels of similar octane rating and sensitivities were formulated by blending gasoline with either ethanol or aromatic compounds. Ethanol and aromatics were considered for blending with gasoline to achieve the desired octane rating. Their effects on influencing the sooting tendency of current generation downsized boosted spark ignited engines was investigated across two sets of fuels (lower octane rated and higher octane rated).

Fuel Property	**Pump Gasoline (Corrigan)**	**Shell Ethanol Blend**	**Shell Aromatic Blend**	**Sunoco Alkylate Blend**	**Sunoco Ethanol Blend**	**Sunoco Aromatic Blend**
RON	98.0	95.0	94.8	95.8	104.0	103.1
MON	88.0	87.1	86.8	93.4	94.2	93.1
AKI (R+M/2)	93.0	91.0	90.8	94.6	99.1	98.1
Sensitivity	10.0	7.9	8.0	2.4	9.8	10.0
Saturates (V%)	-	68.5	56.9	94.8	78.4	57.1
Aromatics (V%)	-	11.7	37.5	0.8	0.7	40.4
Olefins (V%)	-	4.8	4.1	3.7	3.1	2.1
Oxygenates (V%)	-	13.1	0	0	17.3	0
Ethanol (V%)	10.0	13.1	0	0	17.3	0
LHV (MJ/kg)	42.00	41.76	43.11	44.19	41.21	42.81
H:C	-	2.17	1.82	2.3	2.27	1.82
O:C	-	0.047	0	0	0.06	0

Table 5-2: Details of fuels tested in this chapter.

Pump gasoline is 93 rated premium gas that is available for purchase at the gas pump. The Shell formulated ethanol and aromatic blends are formulated from the same BOB by using two different refinery relevant blending streams to achieve similar octane rating as the pump fuel. The Sunoco alkylate blend is also similar octane rating as the Shell fuels and is used as the BOB for the high octane fuels.

The Shell fuels have similar octane rating as the baseline premium 93 AKI rated pump gasoline. Both the Shell fuels were formulated with the same blendstock for oxygenate blending (BOB). The desired octane rating was then met by blending either ethanol or aromatic compounds. The idea was to formulate fuels of similar desired octane rating as available at the pump using refinery-relevant blending streams which could be either rich in aromatics or oxygenates (ethanol). This resulted in fuels of similar octane rating but diverse chemical composition. These Shell fuels were investigated in a previous study by Powell et al. [139] for studying octane index correlations to knocking propensity under a variety of conditions in spark ignited and spark assisted compression ignition combustion.

The Sunoco high octane fuels were formulated by blending their baseline alkylate fuel which is rich in paraffins with high concentrations of ethanol or aromatics to achieve the high octane rating. Octane ratings and sensitivities for both fuels were kept similar. High octane fuels with high sensitivities were preferred for this study based on the findings of Szybist et al. [140] for current generation downsized turbocharged spark ignited engines. Szybist and collaborators found when investigating fuels with similar octane ratings but varying sensitivities that the fuel with larger sensitivity was less prone to knock at high loads. These observations are consistent with the findings of Mittal et al. [141] and Vuillemer et al. [34].

To quantify the effects of the different molecular structures in the gasoline blends on knock intensity and particulate matter as it related to knock limited conditions, spark timing sweeps were conducted for each of the fuels at the four different knock limited points. Sweeps began at late spark timing such that the combustion phasing was considerably late and there was no possibility of knock occurring. As combustion phasing was advanced, knock intensity was monitored using the Kistler cylinder pressure transducers and the AVL Indicom data acquisition

system. Sweeps were ended when knock was audible, and intensities monitored were of high amplitude and frequency.

Lastly, transient testing with the low-octane rated fuels was conducted to verify whether these gasoline candidates formulated from refinery relevant streams are more beneficial than premium pump gasoline. A greater emphasis was placed on studying the particulate emissions aligning with the theme of this Chapter. Differences in particle size distributions due to differences in fuel chemistry were noted.

5.3 Results and Discussion

The findings of all three studies and the transient testing are discussed in the following section.

5.3.1 Turbocharger Comparison

This subsection discusses the comparisons made across the two engine calibrations and the change of associated turbomachinery. The baseline engine test used the Continental fixed geometry turbocharger and baseline valve timings whereas the Miller engine test used the BMTS variable geometry turbocharger and the overridden Miller valve timings (Atkinson ratio >1).

Knock Intensity:

As mentioned earlier, the knock intensities are quantified both on an amplitude and energy basis. The KIp2p and the KI20 can be seen showing a good correlation as seen from the plots for the baseline engine with the Continental fixed geometry turbocharger (Figure 5-6).

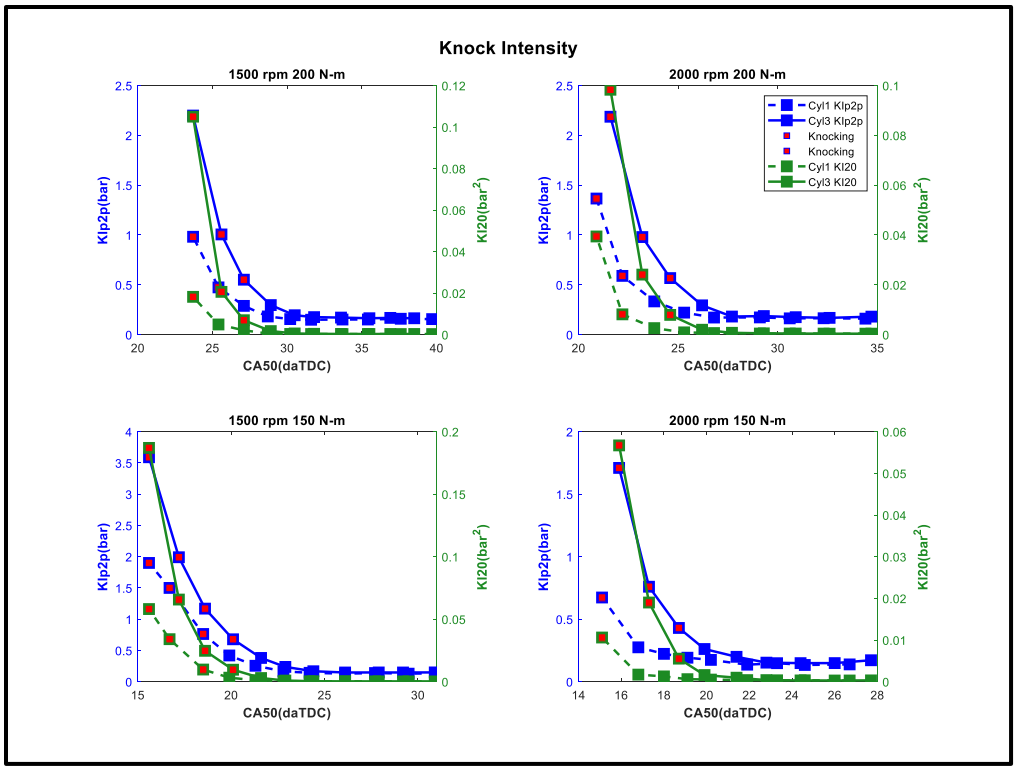

Figure 5-6: Illustration of good correlation between the two metrics of knock intensity used in this study at 4 knock limited points studied in this chapter (Red symbols indicate knocking).

Blue lines indicate knock intensity based on amplitude and green lines indicate knock intensity based on energy; Dashed lines are for cylinder 1 while solid lines are for cylinder 3; This confirms that either of the metrics can be used to determine whether the cylinder is knocking.

A comparison of the knock intensities of the baseline engine versus that of the Miller engine shows the effect of Miller timing on reducing knock propensity. The Miller engine is able to advance combustion phasing by 3^o at the engine speed of 1500 rpm. The effect of the Miller timing is not as pronounced at the higher engine speed and reduces as the engine speed is increased further due to higher boost pressures in the cylinder leading to high peak cylinder pressures. Moreover, higher engine speeds do not involve a large spark delay to begin with due to the lower residence times of in-cylinder charge and less time available for end gas auto-ignition. Thus, the benefits of Miller timings with respect to lowering knock propensity are reduced as engine speed increases.

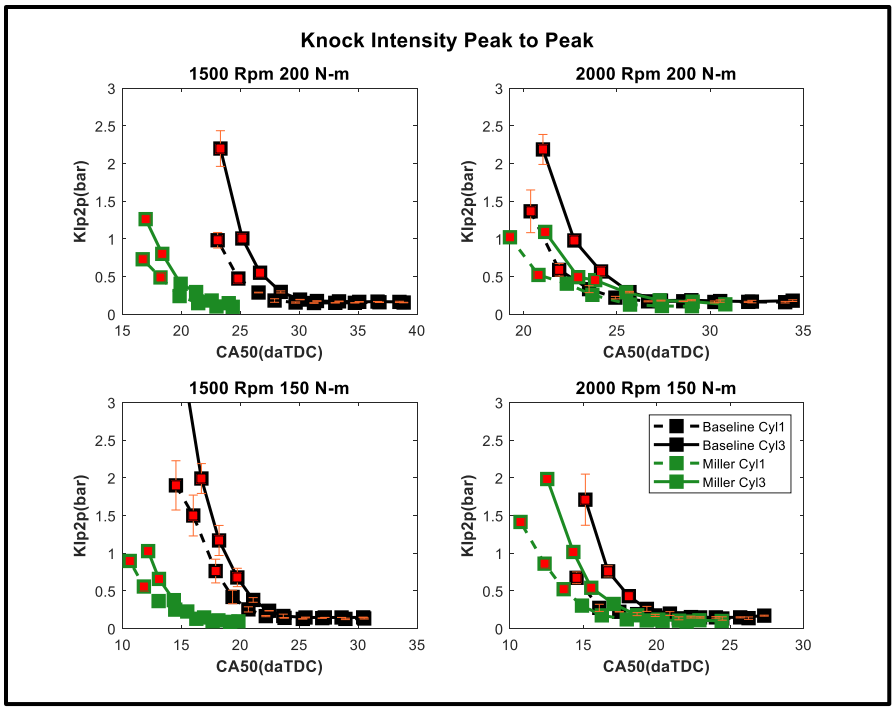

(a)

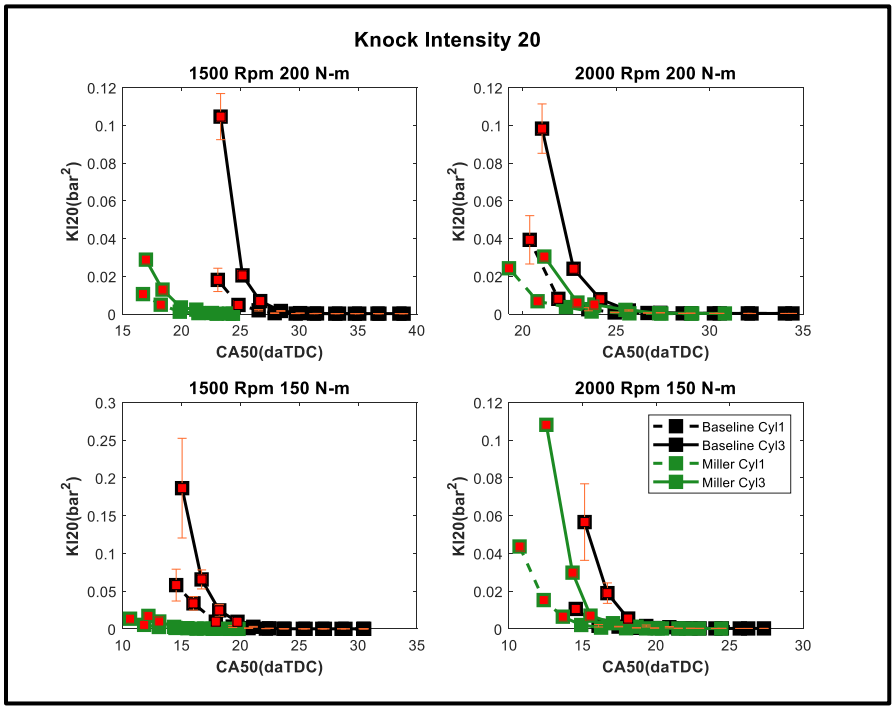

(b)

Figure 5-7: Comparison of Knock intensities of baseline and Miller engine (Red symbols indicate knocking).

(a) Comparison of baseline vs. Miller based on Kip2p (b) Comparison of baseline vs. Miller based on KI20

Particulate Emissions:

The particulate number data confirms the knock-soot correlation observed by Han [30] with the Miller engine at 2000 rpm and 200 N-m torque being the exception. A potential theory is that the knock intensity (Figure 5-7) associated with those points was not high enough in magnitude to cause the rapid increase in concentration of accumulation mode particles. This is confirmed from the PN23 data (Figure 5-8) as well as the particle size distribution (Figure 5-9 and 5-10). In fact, for the case of 2000 rpm and 200 N-m on the Miller engine, the PSD suggests a reduction in nucleation mode particle concentration but no significant change in accumulation mode particles leading to an overall reduction in particle number concentration.

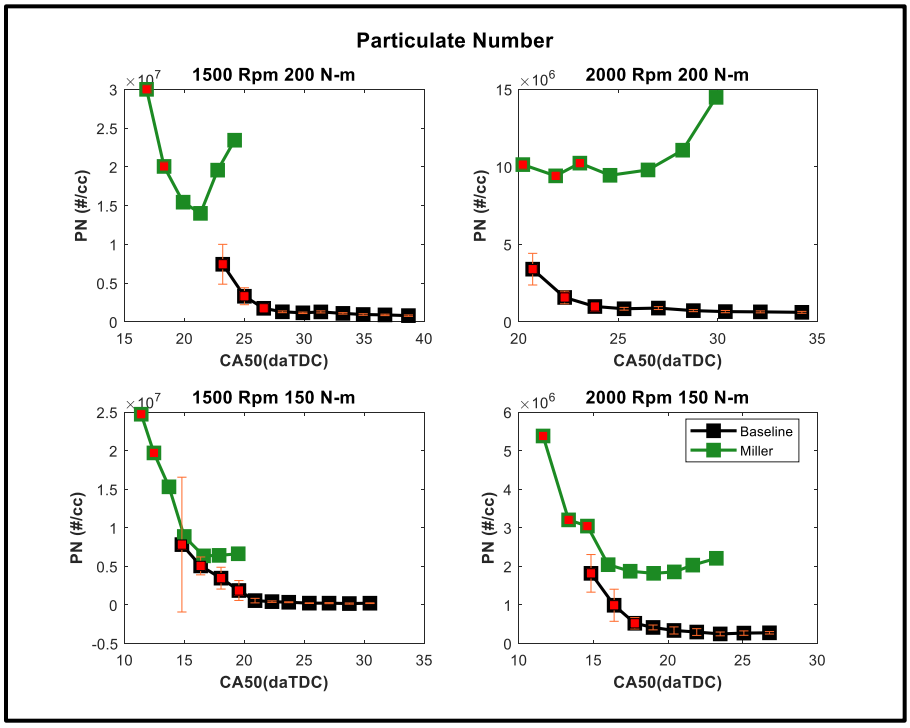

(a)

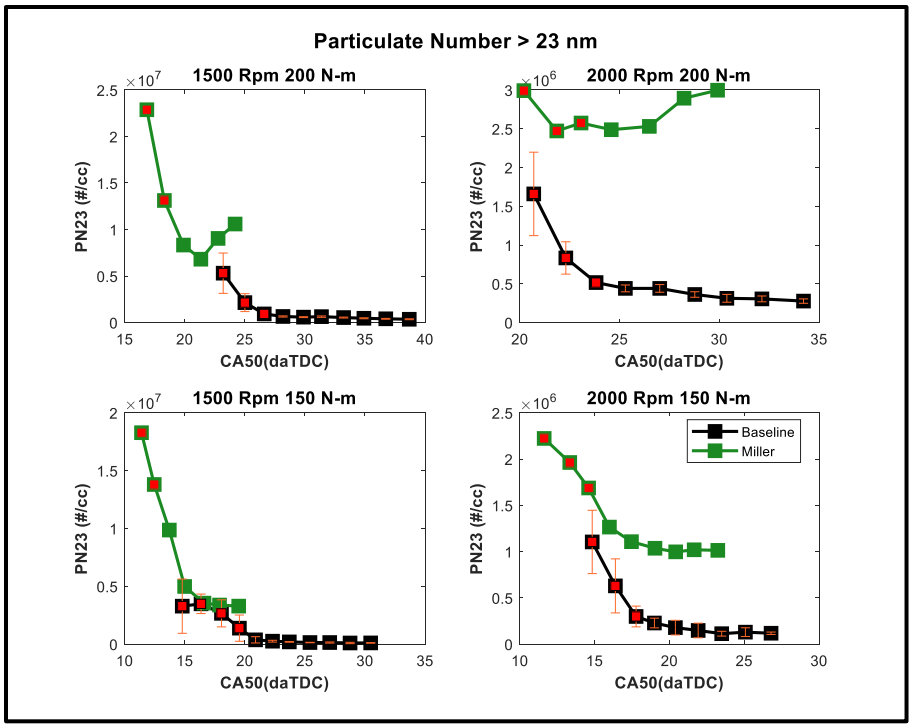

(b)

Figure 5-8: Particle Number and Particle Number >23 nm concentrations for the 2 engine calibrations (Red Symbols indicate knocking).

Particle Size Distribution:

The particle size distributions for both the baseline and Miller engines suggests that the knock-soot correlation that we see from our particle number data is a consequence of increased accumulation mode particle concentration. This is consistent with the observations made by Han on his single cylinder engine [30].

Comparing the PSDs from both engines, it can be seen that the findings are consistent with those of Szybist et al. [40] who also noticed a higher concentration of particulate matter emissions with an LIVC (Late Intake Valve Closing) Miller breathing strategy compared to Otto cycle operation (Figure 5-11). As explained in the previous chapter, this is likely due to suboptimal fuel injection timings. The fuel injection strategy for the Miller operation was not

calibrated or optimized for the new valve timings and thus there is a possibility of fuel spray impinging on the piston during the intake stroke with air entering the cylinder later compared to the baseline engine. Fuel impinging on the walls and piston can remain in liquid form which could result in fuel rich pool fires. Comparing the PSDs at the knock limited combustion phasing shows that the emissions from the Miller engine are almost an order of magnitude higher than that observed from the baseline engine at 1500 rpm. The difference in the concentrations of particulate matter emitted from both engines is not as high at the 2000 rpm conditions which suggests a greater need for optimizing the injection strategy at the 1500 rpm points.

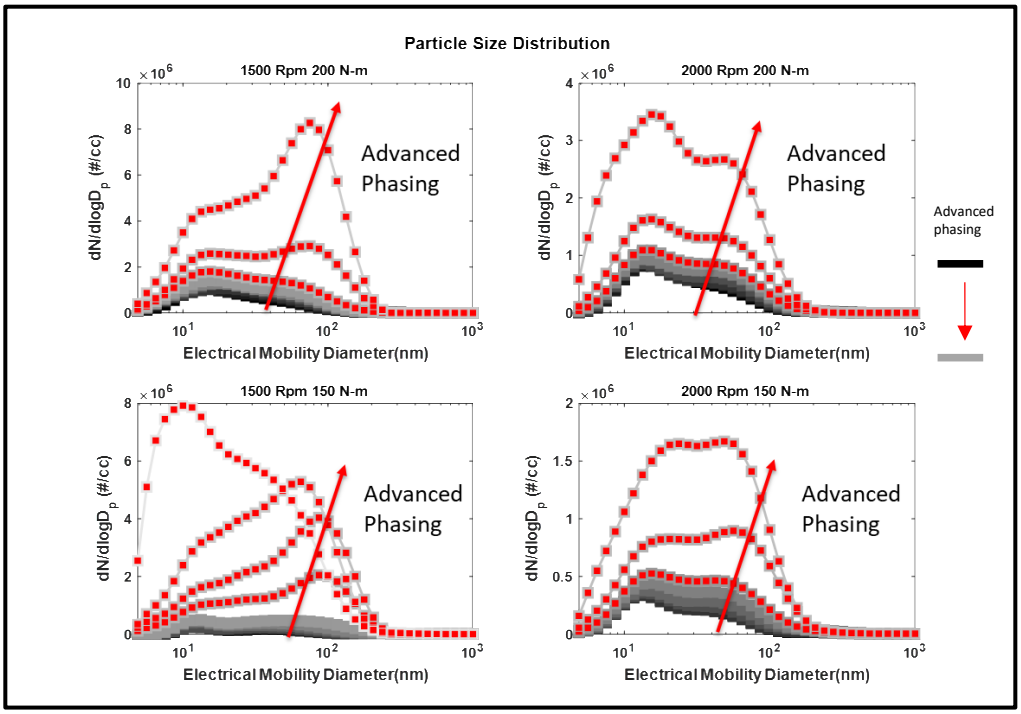

Figure 5-9: Particle Size Distribution of the Baseline engine (Red symbols indicate knocking).

All 4 points tested showed a sudden increase in accumulation mode particle concentration after knock onset.

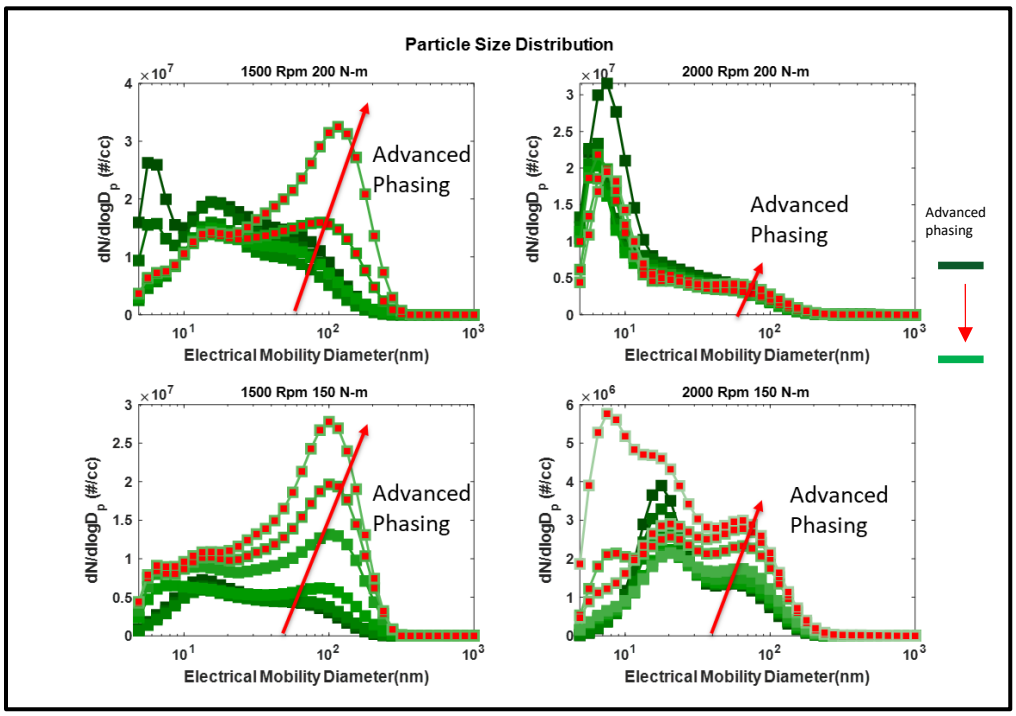

Figure 5-10: Particle Size Distribution of the Miller engine (Red symbols indicate knocking).

Similar observation of increased accumulation mode concentration with the exception of the point at 2000 rpm 200 N-m

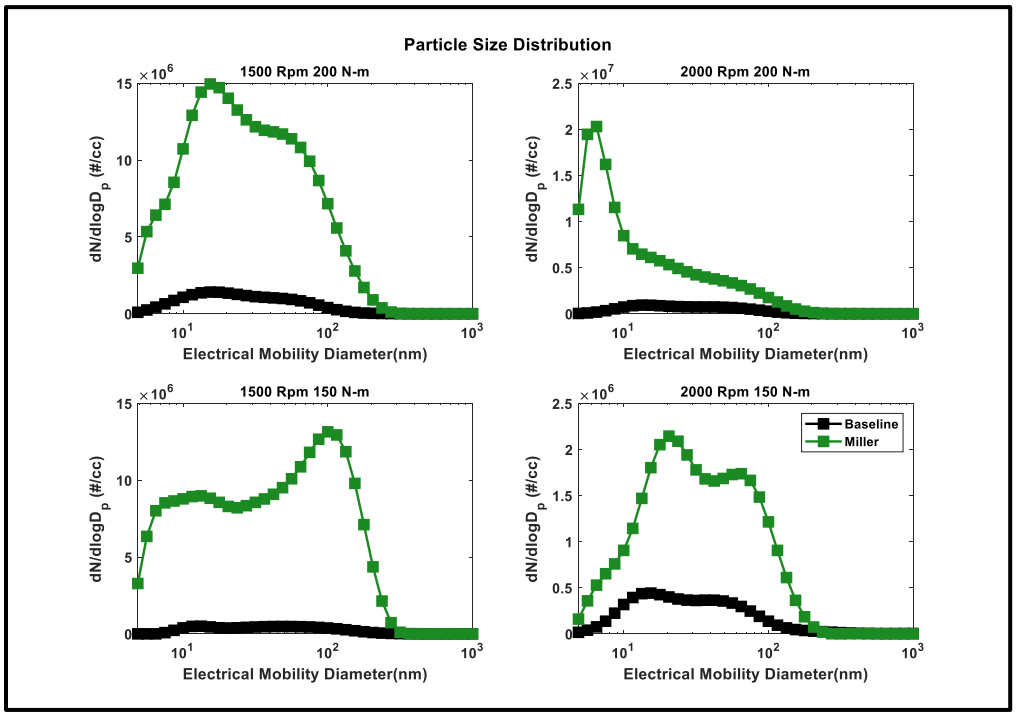

Figure 5-11: Particle size distribution at knock limited combustion phasing for baseline vs. Miller.

Gaseous Emissions:

CO Emissions

A comparison of the carbon monoxide emissions from the baseline and Miller engines at knock limited points (Figure 5-12) is consistent with the observations that were made during steady state testing in Chapter 4. The Miller engine emits less carbon monoxide at all 4 knock limited points. Once again, it is hypothesized that this is due to the higher boost pressures of the Miller engine combined with the Miller valve timings which could have resulted in enhanced scavenging. The enhanced scavenging could have resulted in higher combustion efficiency and thus lower carbon monoxide [121]. Moreover, the higher boost pressures of the Miller engine could have resulted in a greater fraction of locally lean regions in the combustion chamber during air fuel mixing which could have resulted in lower CO emissions.

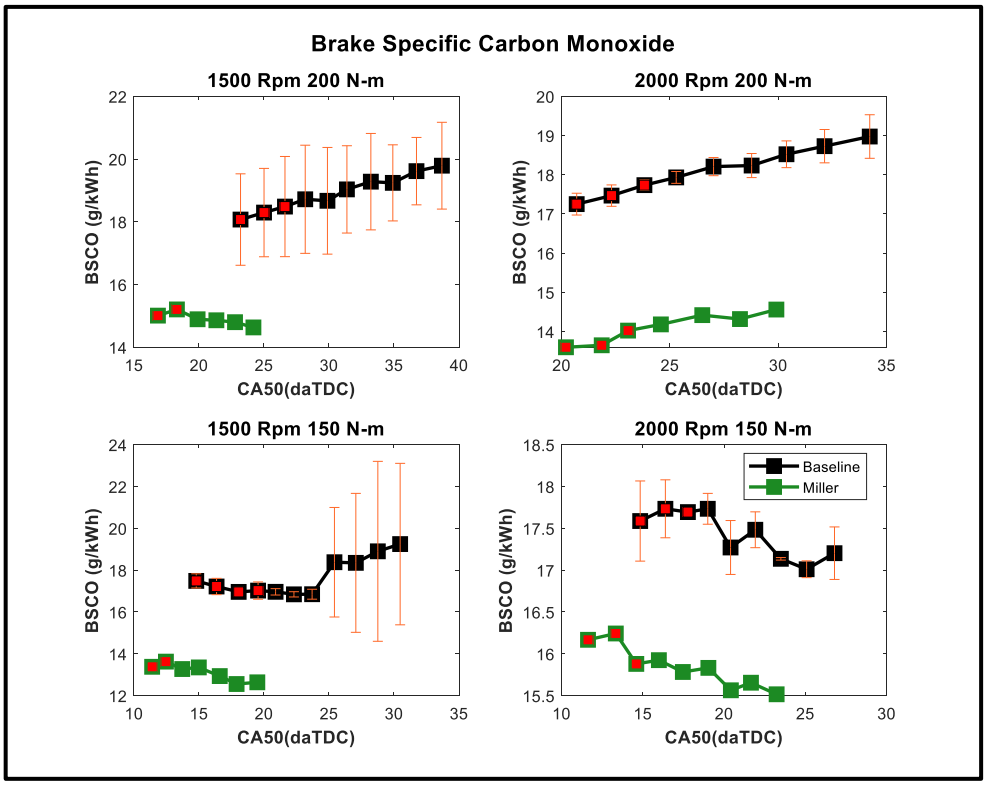

Figure 5-12: Brake specific CO emissions of baseline vs. Miller engine (Red symbols indicate knocking).

NO_X Emissions

Like the CO emissions, the NO_X emissions from the combustion phasing sweeps run at the 4 knock limited points show trends that are consistent with the steady state mapping efforts in Chapter 4. The NO_X emissions from the Miller engine are consistently lower than the baseline engine at all 4 knock limited points (Figure 5-13). This is due to lower in-cylinder temperatures in the Miller engine which are a consequence of the reduced effective compression ratio. High in-cylinder temperatures are known to promote the forward reaction for NO_X formation. Thus, the result of lower in-cylinder temperatures is lower NO_X formation in the Miller engine and thus lower engine out NO_X emissions.

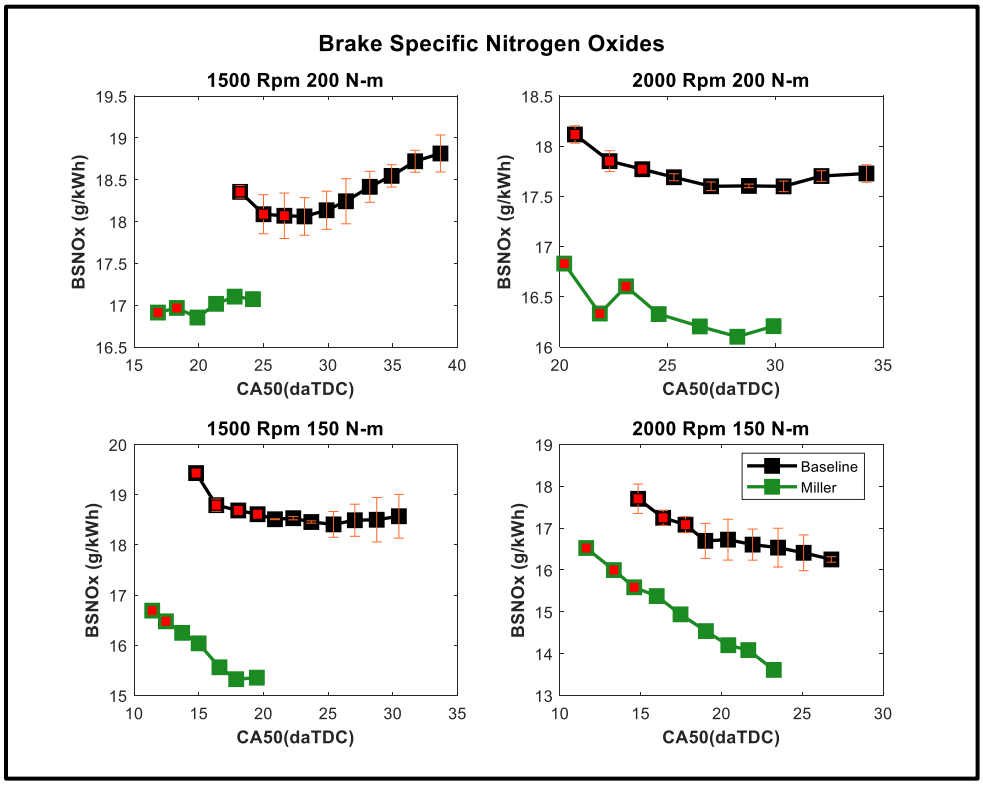

Figure 5-13: Brake specific NO_X emissions from the baseline engine vs. Miller engine (Red symbols indicate knocking).

THC Emissions

The observations made from the comparison of the THC emissions continue the theme of being consistent with the steady state mapping efforts in Chapter 4. Just like the mapping results, the combustion phasing sweeps also show increased unburnt hydrocarbon emissions from the Miller engine compared to the baseline. As hypothesized in the previous chapter, it is thought that this is because the injection strategies were kept the same for both engines which could have resulted in sub-optimal injection timings which could result in higher hydrocarbon emissions.

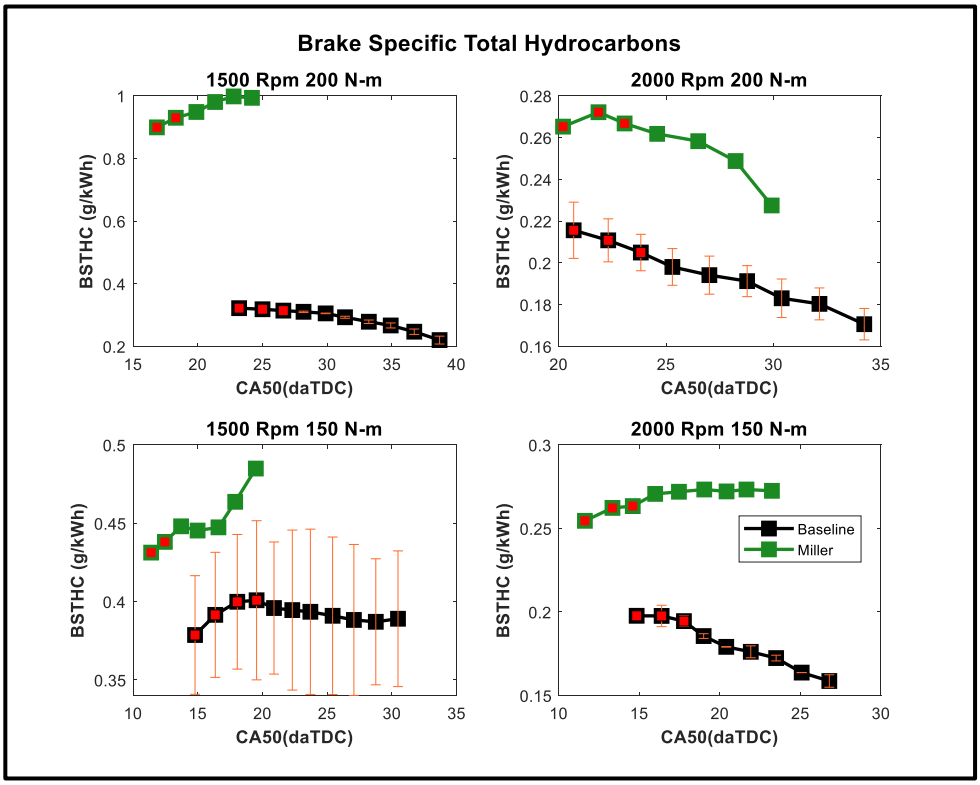

Figure 5-14: Brake specific THC emissions of baseline engine vs. Miller engine (Red symbols indicate knocking).

CO_2 Emissions

Since gasoline spark ignited engines are run at the stoichiometric air fuel ratio (equivalence ratio =1), the CO_2 emissions reduce as combustion phasing is swept from late to early timing. This is due to the increase in thermal efficiency and thus lower fuel consumption to

meet the same load as combustion phasing is advanced to timings closer to MBT timing. Lower fuel consumption means that lower amounts of fuel is converted to complete combustion product of CO_2. Therefore, at knock limited timings, the Miller engine emits less CO_2 (Figure 5-15) which is consistent with the observations made in the next section about fuel consumption (Figure 5-16).

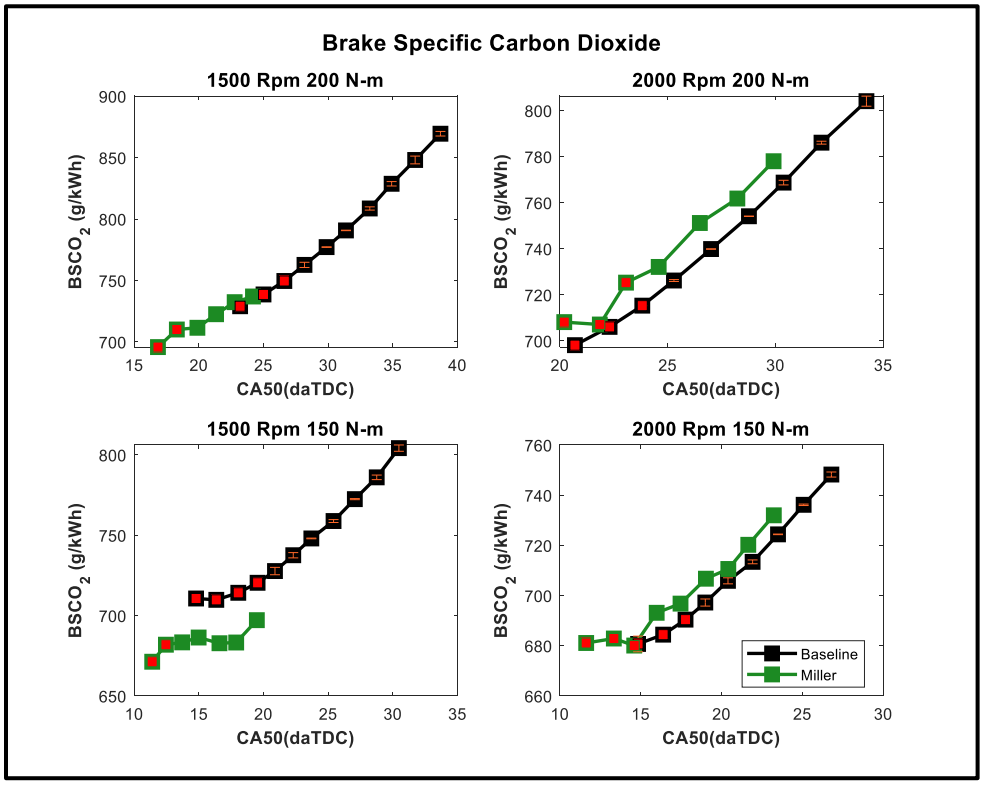

Figure 5-15: Brake specific carbon dioxide emissions from baseline engine vs. Miller engine (Red symbols indicate knocking).

Fuel consumption and thermal efficiency:

The fuel consumption reduces as combustion phasing is swept towards MBT timing (Figure 5-16). Likewise, the thermal efficiency which is inversely proportional to the fuel consumption increases as timing is swept towards MBT (Figure 5-17). Consistent with the observations made in Chapter 4, the Miller engine has higher thermal efficiency compared to the

baseline at all but one of the knock limited points where sweeps were run. At 2000 rpm, 200 N-m the Miller timings did not display a significant improvement on the baseline in terms of reducing knock propensity and as a result there is no significant improvement of thermal efficiency compared to the baseline.

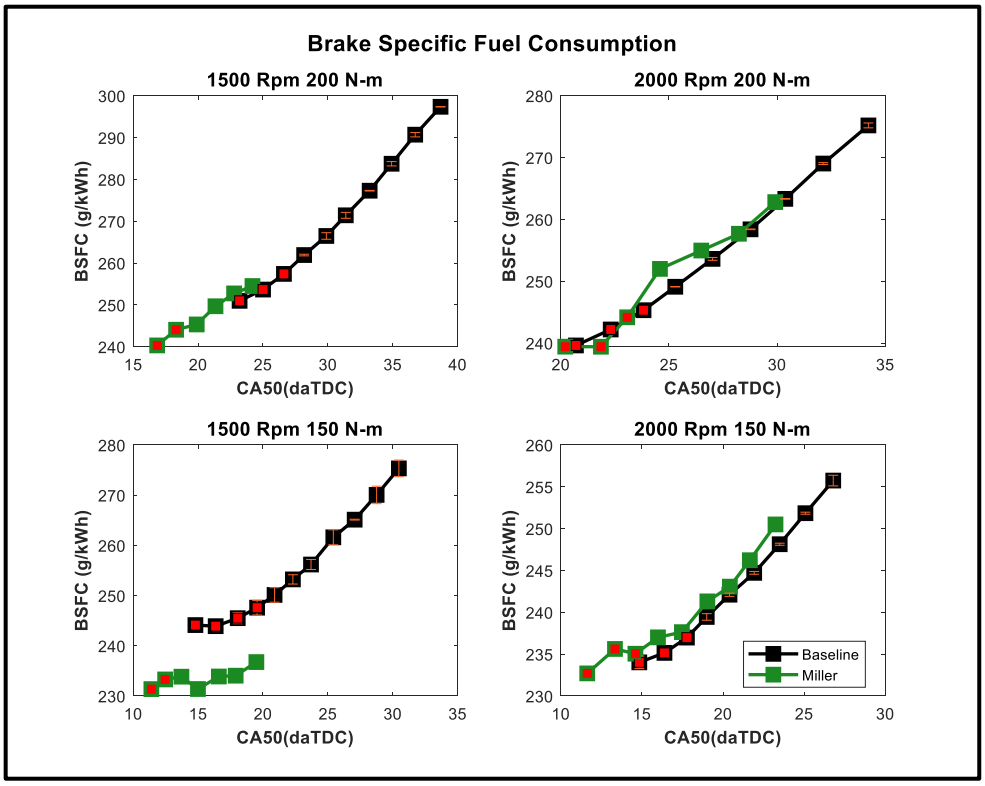

Figure 5-16: Brake specific fuel consumption of baseline engine vs. Miller engine (Red Symbols indicate knocking).

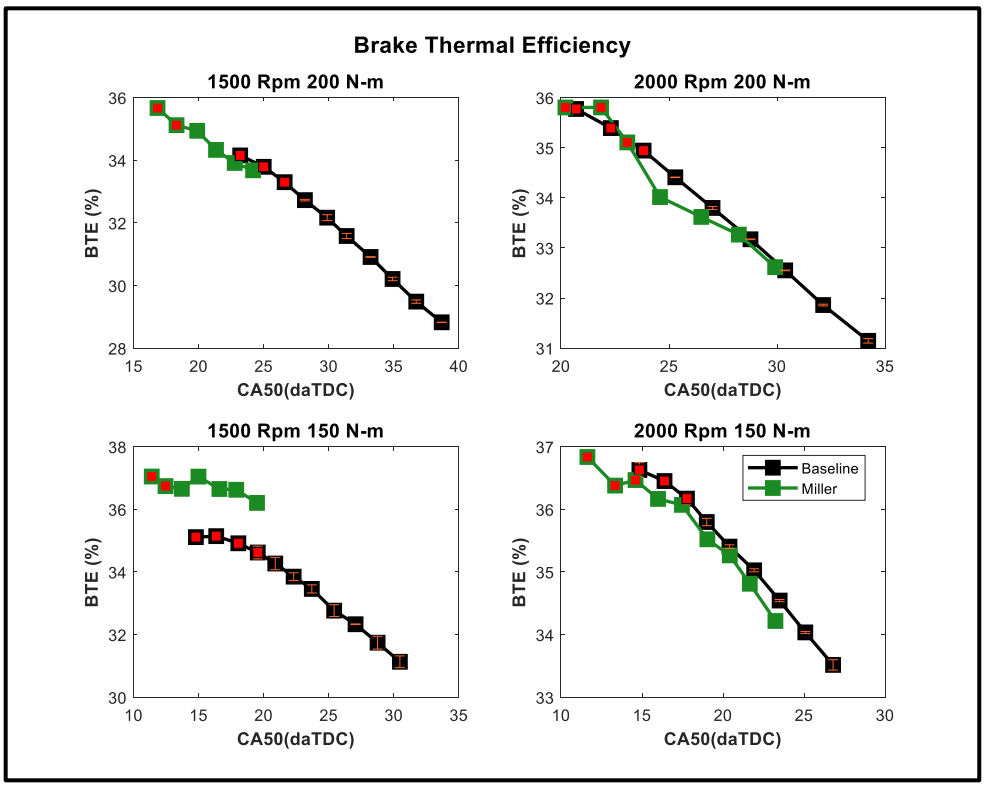

Figure 5-17: Brake thermal efficiency of baseline engine vs. Miller engine (Red symbols indicate knocking).

Knock limited cylinder pressure and heat release rate:

A comparison of the knock limited cylinder pressures (Figure 5-18) and the apparent heat release rates (Figure 5-19) helps us visualize how different the combustion is for the baseline engine and the Miller engine at knock limited combustion phasing. The cylinder pressure data shows that there is barely any difference between the two at the higher engine speed of 2000 rpm except for a slight advance in combustion phasing for the Miller engine.

The effect of Miller in allowing more advanced combustion phasing without knocking is more pronounced at the lower engine speeds where the baseline engine had a much larger spark delay. As a result, the cylinder pressure is decreasing due to expansion before combustion occurs for the baseline engine. The AHRR plots for 1500 rpm also show that most of the heat release

from the baseline engine is much later in the expansion stroke and thus less useful work is extracted from the baseline engine compared to the Miller engine.

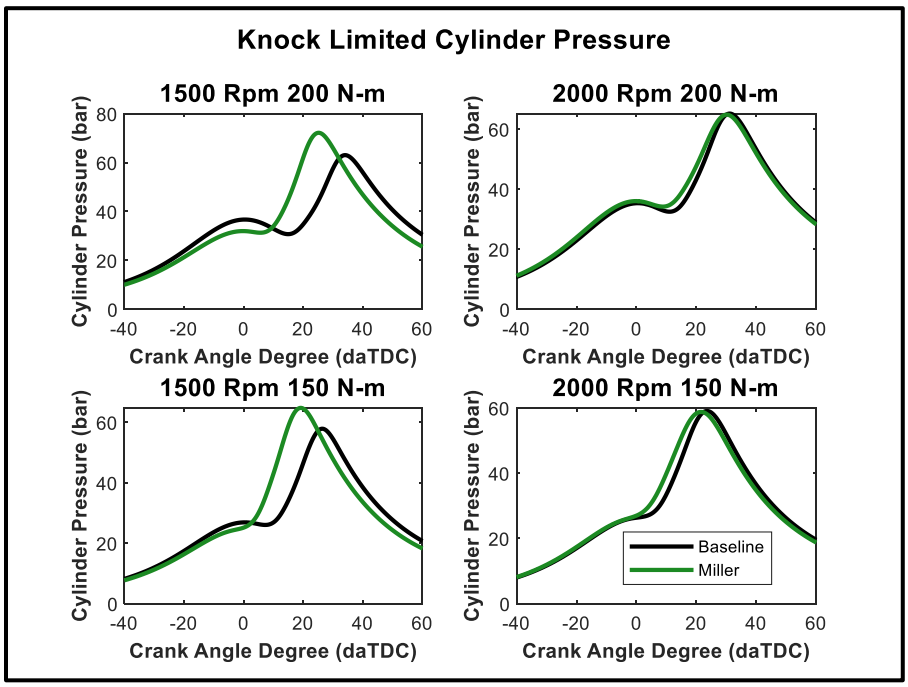

Figure 5-18: Comparison of cylinder pressure traces at knock limited combustion phasing for baseline engine vs. Miller engine.

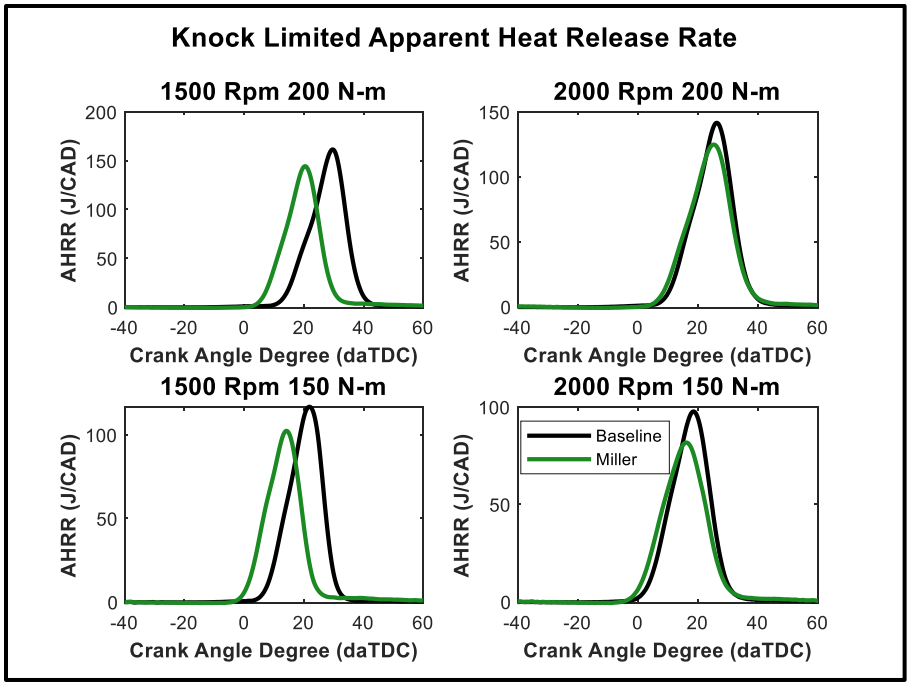

Figure 5-19: Comparison of apparent heat release rate at knock limited combustion phasing for baseline engine vs. Miller engine.

Combustion duration:

A comparison of the combustion duration (CA1090) for both engines shows that the Miller engine has a longer combustion duration than the baseline engine at all 4 points. This is consistent with observations about combustion duration made by Perceau et al. [142]. The shorter compression ratio leads to lower turbulence levels in the cylinder by the time the piston approaches top dead center at the end of the compression stroke. This loss of turbulence leads to longer combustion duration. Advancing the combustion phasing has a greater effect on the thermal efficiency than the loss of turbulence at the low engine speeds. At higher engine speeds, where the Miller timings do not have a large effect on lowering knock propensity, the lower turbulence levels can dominate and lead to lower thermal efficiency.

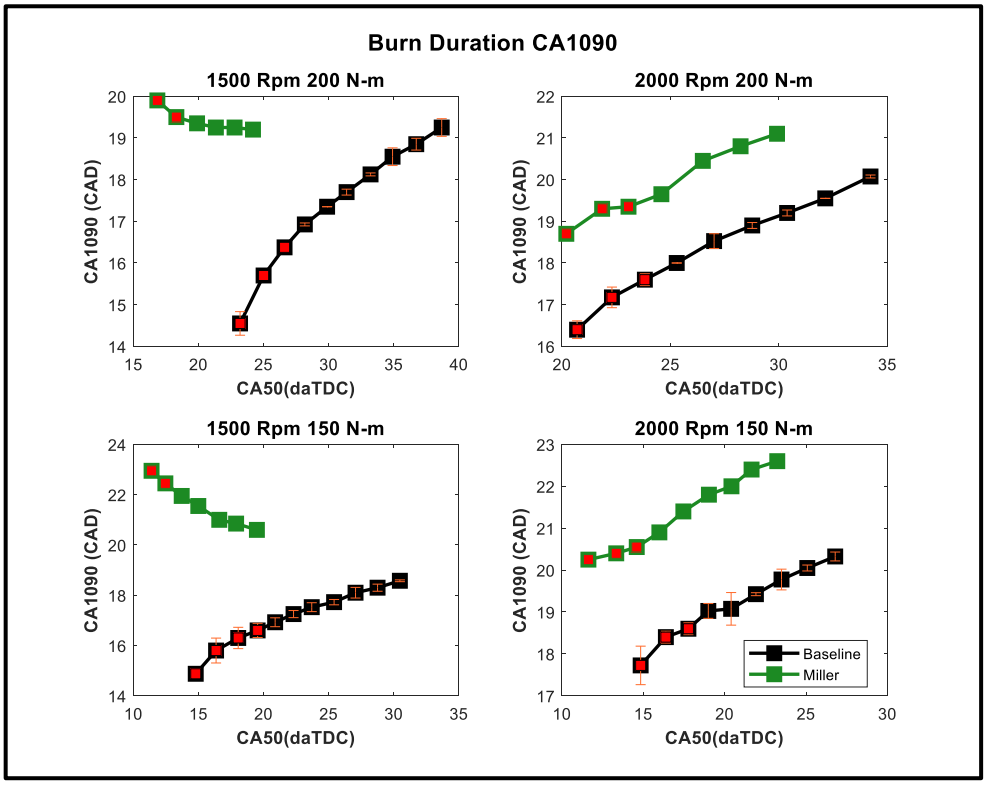

Figure 5-20: Burn duration approximated by CA1090 for baseline engine vs. Miller engine (Red symbols indicate knocking).

5.3.2 Injection Strategy Comparison

This subsection discusses the effect of changing injection strategy on the knock limit of the Ford Dragon Miller engine at the four knock limited points. Experiments were carried out with 100% port fuel injection and 100% direct injection. This is the second of 3 sets of experiments conducted for further understanding the knock-soot correlation.

Knock Intensity:

The comparison of knock intensities shows the advantage of operating with a direct injection strategy at these knock limited points as opposed to operating with a port injection strategy. Comparisons on a peak to peak (Figure 5-21 a) and energy basis (Figure 5-21 b) both show that the direct injection strategy allows a 4^{o} spark advance towards MBT timing which allows the engine to run more efficiently. This is largely due to the charge cooling effect of the fuel that is directly injected into the cylinder. The latent heat of vaporization absorbed by the fuel droplets lowers the in-cylinder temperature. This has the effect of reducing the probability of end-gas auto-ignition [14,17,143].

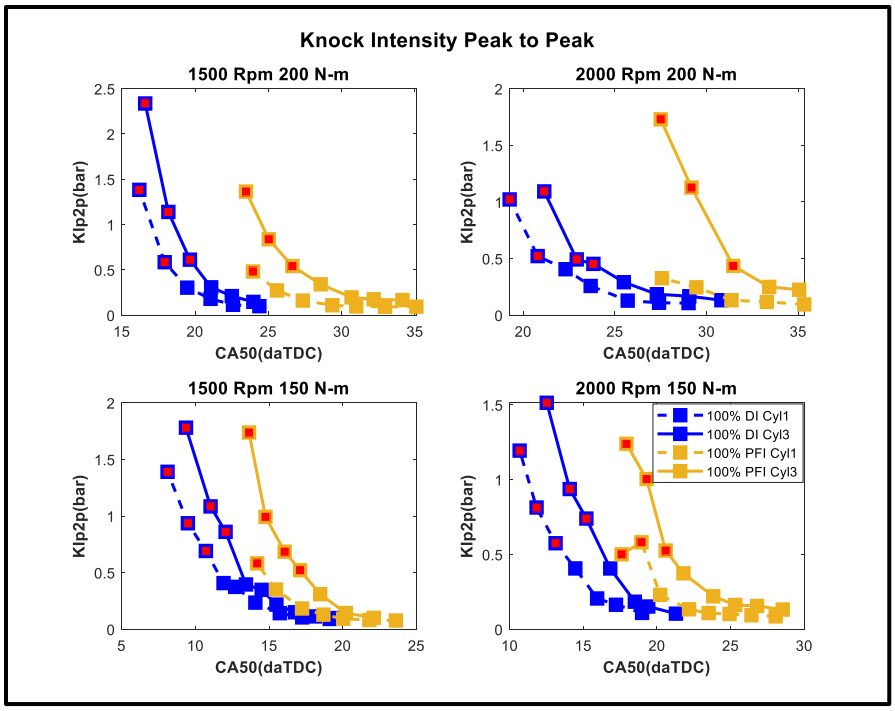

(a)

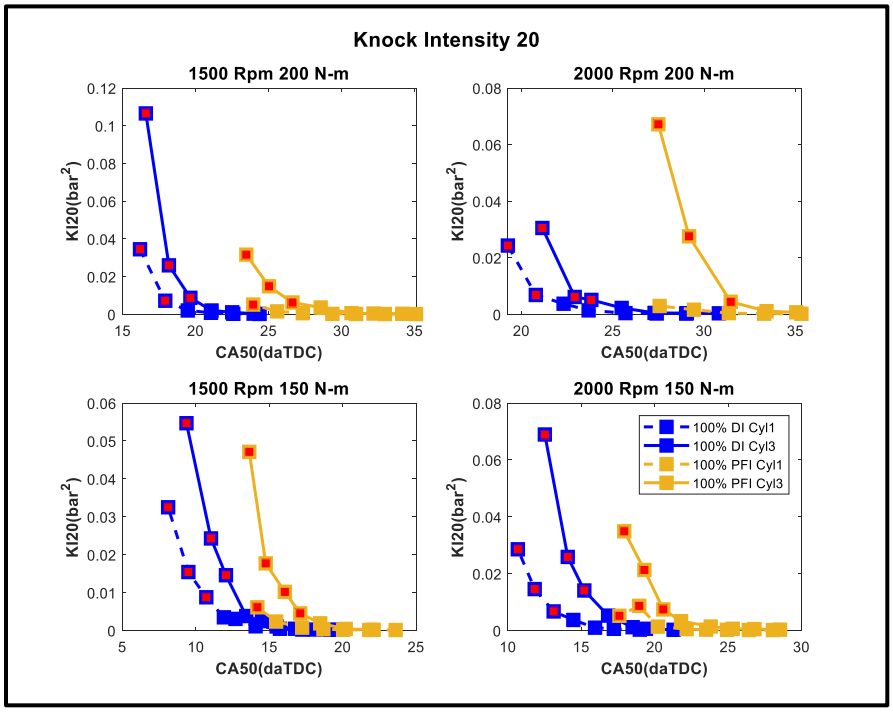

(b)

Figure 5-21: Comparison of knock intensity of different injection strategies (Red symbols indicate knocking).

(a) Comparison of KIp2p of PFI vs. DI (b) Comparison of KI20 of PFI vs. DI

Particulate Emissions:

Just like the previous set of experiments, a comparison of the particle number concentrations once again confirms the knock-soot correlation that was observed by Han [30]. A comparison of the PN23 data versus the overall PN data tells a very similar story as the previous data set. While the overall particle number data appears to contradict the correlation, the PN23 is consistent with it. This confirms that while Han's knock-soot correlation exists for accumulation mode concentrations, no such correlation exists for the nucleation mode particles.

Comparison of the two injection strategies shows that the port fuel strategy leads to higher particulate emissions compared to the direct injection. Previous studies in the literature [57,144–147] have shown that direct injection leads to higher particulate emissions compared to port injection. The reasons cited in these studies have been that the injection of fuel directly into the cylinder can lead to wall wetting and fuel impingement on the piston surface, both of which can lead to high particulate emissions. On the other hand, the same studies have mentioned that the fact that fuel is injected much earlier in the ports well before the intake stroke allows more time for the fuel to atomize and results in a homogenous charge entering the cylinder.

However, the observations made in this study contradict those previous observations. This could be due to following factors. The knock limited points that were considered as part of this study are all relatively high engine load points. This means that they require high fueling rates to be able to meet the load demand. The port injectors are not high-pressure fuel injectors which means that they must be run for longer duration than a high-pressure direct injector would have to for the same fueling rate. This could have resulted in impingement of fuel onto the intake valves as well as less time available for fuel atomization. As a result, there is the possibility that the charge entering the cylinder for the port injection strategy is not completely homogenous and

this could have been the reason for the higher particulate emissions seen with the port injection strategy.

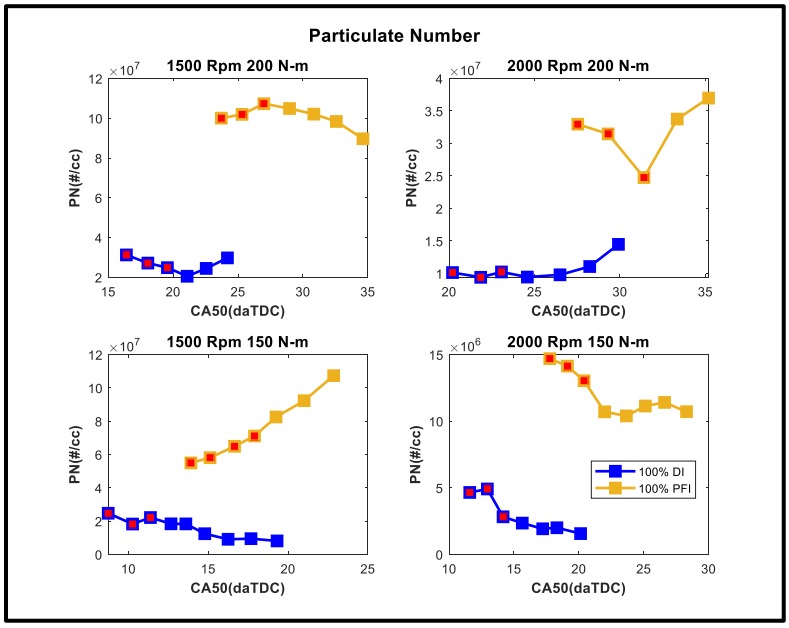

(a)

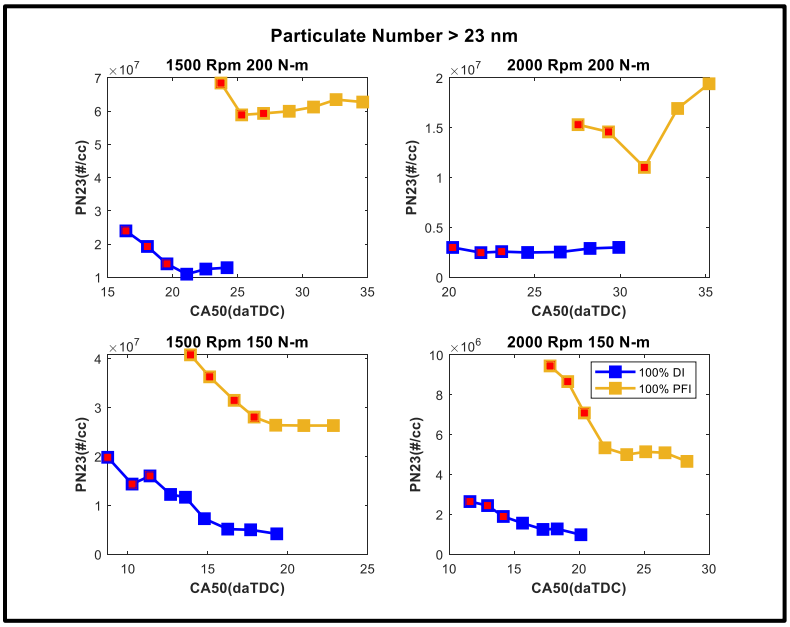

(b)

Figure 5-22: Comparison of particulate matter emissions of both injection strategies (Red symbols indicate knocking).

(a) Total PN concentrations comparison of PFI vs. DI (b) PN>23 nm concentrations comparison of PFI vs. DI

Particle Size Distribution:

A look at the particle size distributions also confirms that the knock-soot correlation does indeed exist for accumulation mode particles. Both the PFI and DI injection strategies led to an increase in accumulation mode particles when knocking occurred. Another observation made from the particle size distributions is that it appears that the knock-soot correlation is one that is based on the knock intensity. As the combustion is phased earlier and knock intensity increases, so does the concentration of accumulation mode particles. The low knock intensities associated with the higher engine speed of 2000 rpm could be the reason why the correlation appears more prominently with the 1500 rpm data. Lastly, a comparison at knock limited timings (Figure 5-25) shows that the port injection leads to higher concentration of emissions for the entire range.

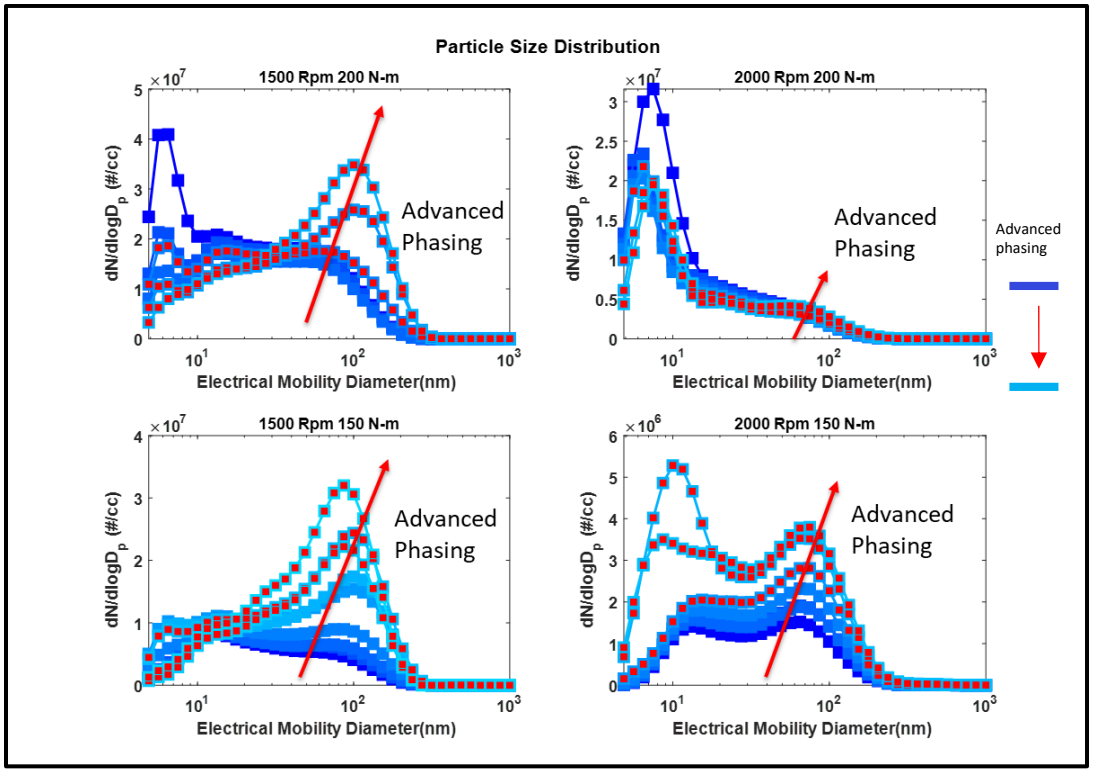

Figure 5-23: Particle Size Distribution of 100% DI Injected fuel (Red Symbols indicate knocking).

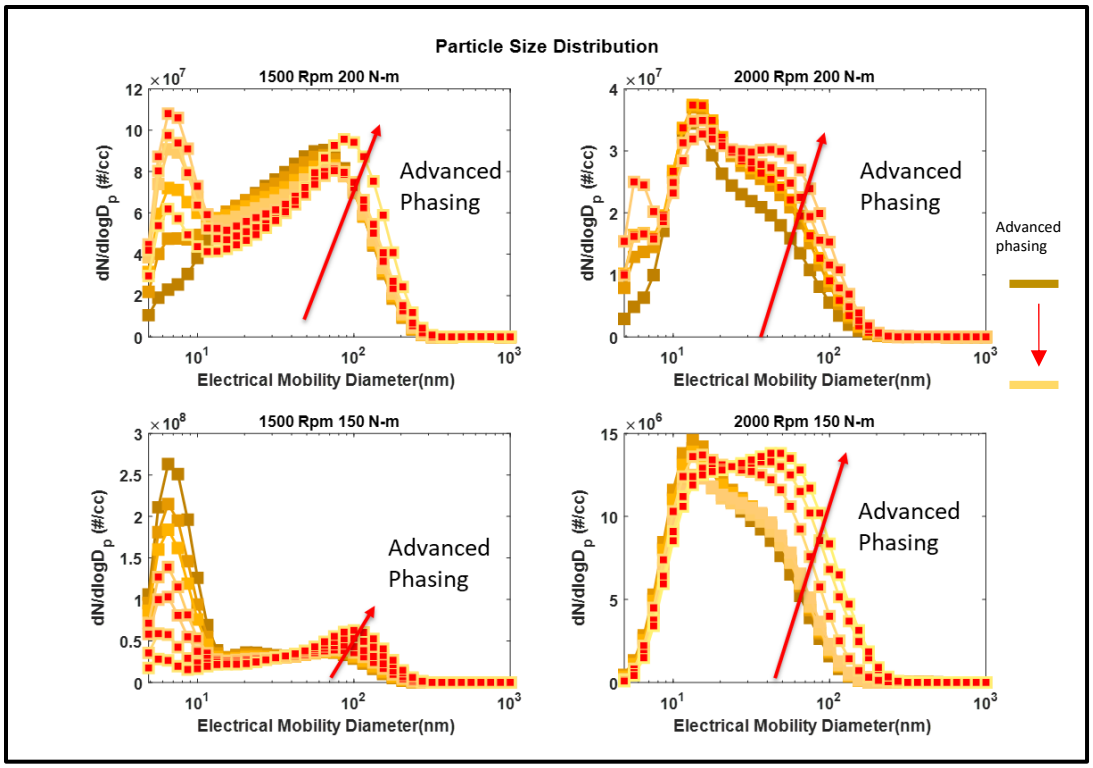

Figure 5-24: Particle Size Distribution for 100% PFI Injected fuel (Red symbols indicate knocking).

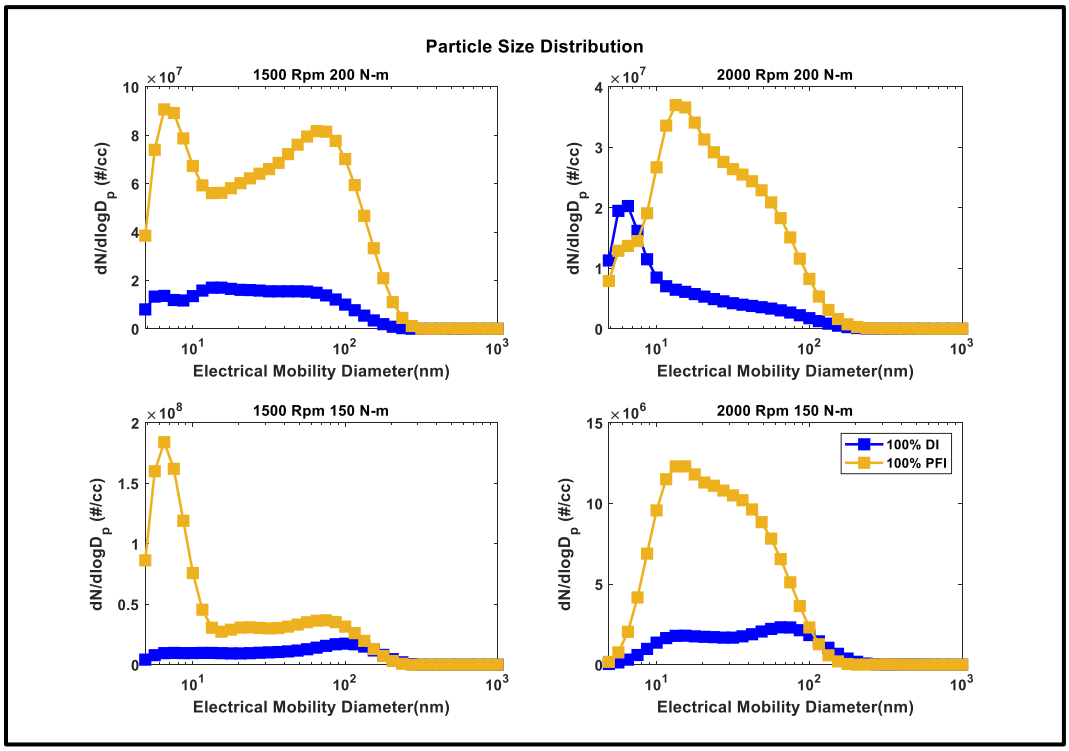

Figure 5-25: Particle Size Distribution for each of the injection strategies at knock limited combustion phasing.

Gaseous Emissions:

CO Emissions

Since all the tests were conducted at stoichiometric air-fuel ratios, the differences in carbon monoxide emissions are most likely due to differences in air fuel distribution within the cylinder. As expected, the fuel injected directly into the cylinder leads to less homogeneity with respect to mixing and this is a possible reason for the higher carbon monoxide emissions.

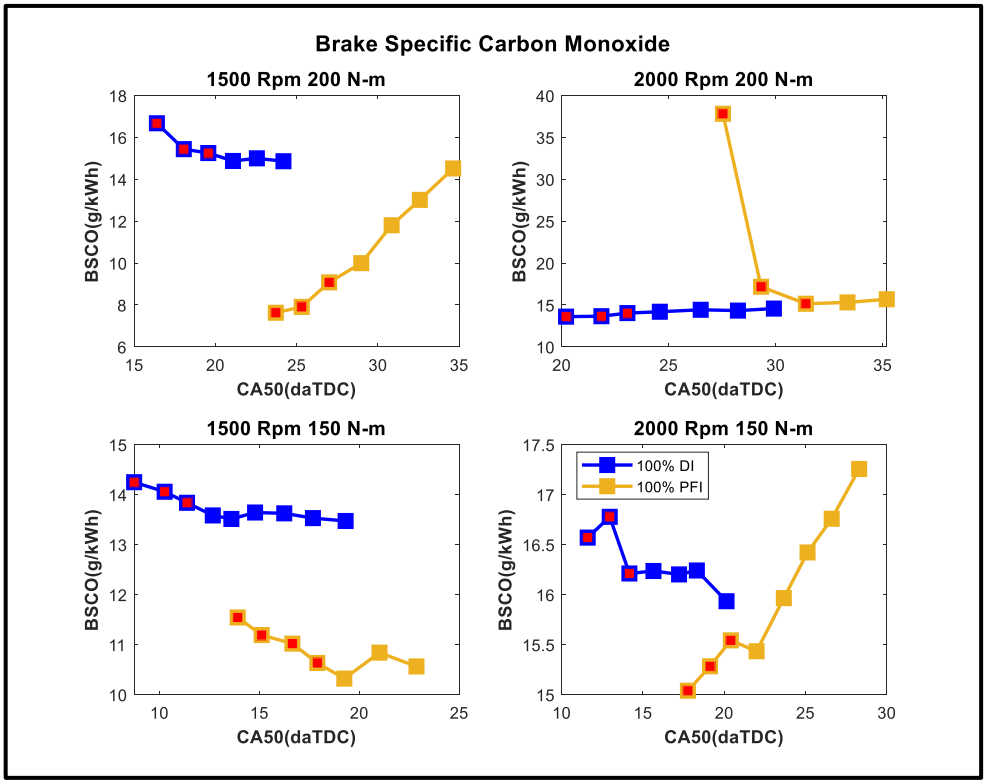

Figure 5-26: Carbon monoxide emissions of both injection strategies (PFI vs. DI) (Red Symbols indicate knocking).

NO_X Emissions

NO_X formation in the cylinder is driven forward by the in-cylinder temperature. The charge cooling effect because of latent heat of vaporization of the fuel injected directly into the cylinder with the DI strategy is the reason for lower NO_X emissions compared to the port injection (Figure 5-27).

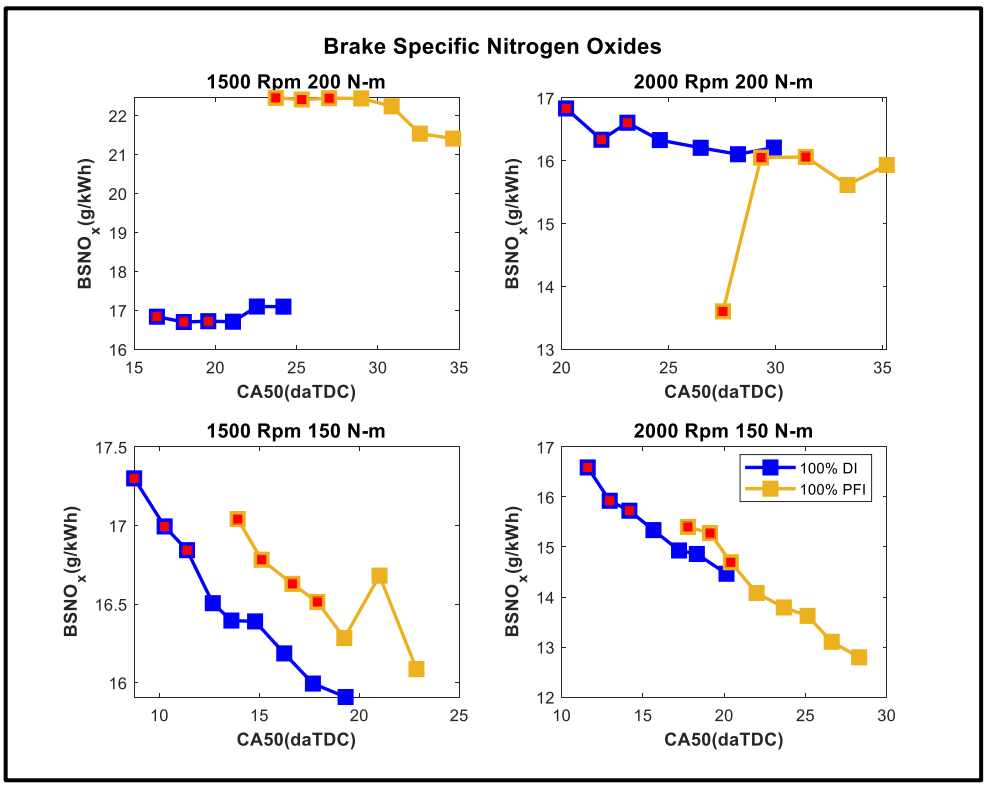

Figure 5-27: NO_X emissions of both injection strategies (PFI vs. DI) (Red symbols indicate knocking).

THC Emissions

A comparison of the hydrocarbon emissions from both injection strategies shows the same trends as the particulate data. The low fuel pressure associated with the port injectors result in relatively long injection duration. This could result in less time available for atomization and it is possible that liquid fuel droplets remain in the charge entering the cylinder. Some amount of the air fuel charge with relatively higher concentration of liquid fuel could potentially be stuck in the crevice between the piston and the liner. Being stuck in the crevice, this could result in this fuel not being consumed by the flame front after the spark event. This fuel could then undergo pyrolysis to form particulate matter or exits the combustion chamber as unburnt hydrocarbons. Thus, similar trends are seen for both the hydrocarbon and particulate matter emissions.

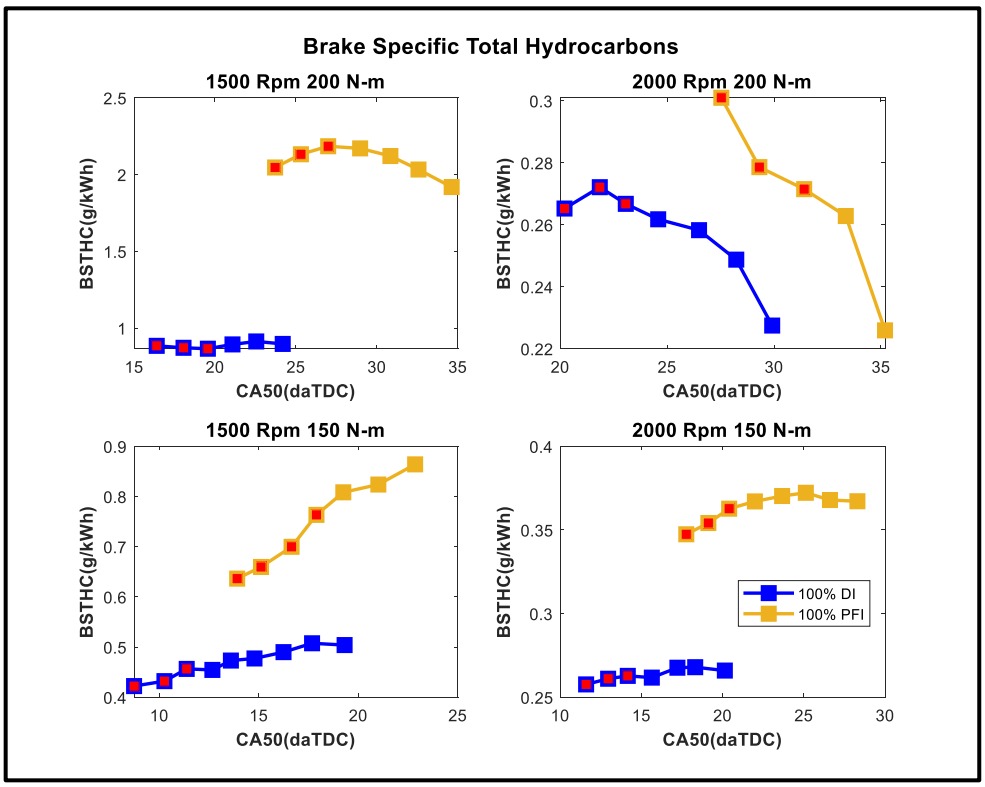

Figure 5-28: Total unburnt hydrocarbon emissions of both injection strategies (PFI vs. DI) (Red symbols indicate knocking).

CO_2 Emissions

Since this particular data set involved using the same fuel chemistry and same air fuel ratio throughout, the carbon dioxide emissions (Figure 5-29) trend the same as fuel consumption (Figure 5-30). Carbon dioxide emissions are reduced as spark timing is swept towards MBT. This is a result of the engine running more efficiently and consuming less fuel. At knock limited combustion phasing, direct injection leads to lower carbon dioxide emissions compared to port injection due to higher thermal efficiency (Figure 5-31).

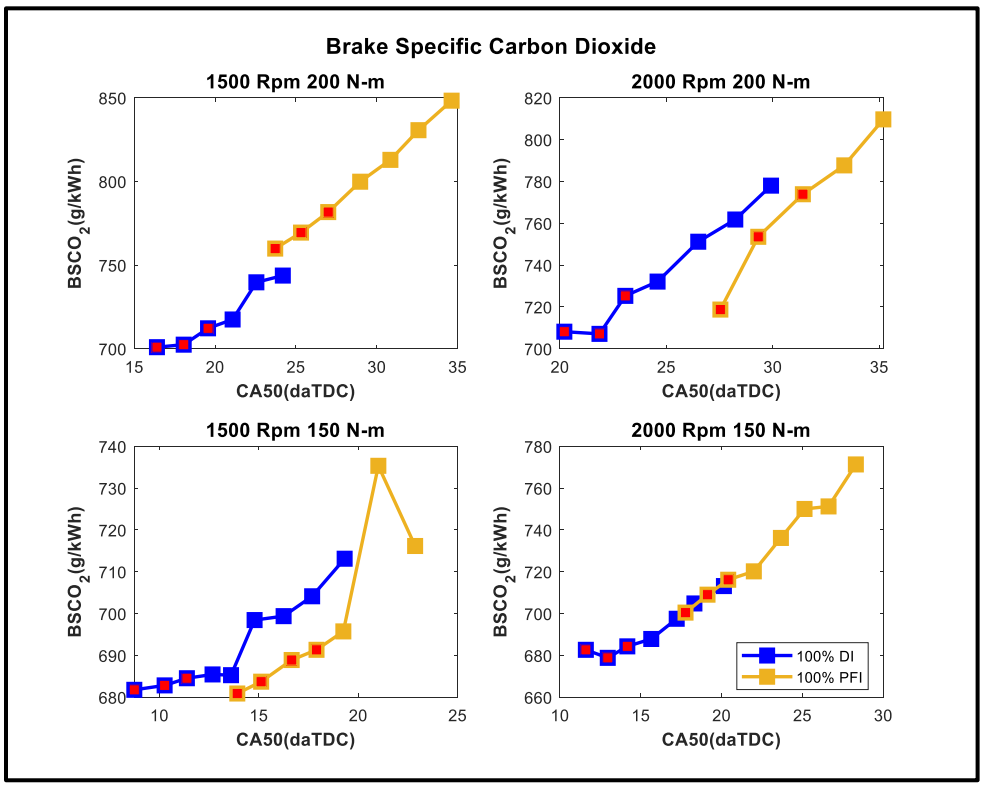

Figure 5-29: CO_2 emissions of both injection strategies (PFI vs. DI) (Red symbols indicate knocking).

Fuel consumption and thermal efficiency:

The fuel consumption is lowered as the combustion is phased towards MBT timing (Figure 5-30). The thermal efficiency (Figure 5-31) which is inversely proportional to the fuel consumption increases as combustion is phased towards MBT timing. At knock-limited combustion phasing, the direct injection strategy was more thermally efficient than the port injection strategy at all four points tested. The charge cooling effect of the fuel injected directly into the cylinder reduces knock propensity and allows the combustion to be phased to earlier timings. As a result, the engine operates with a higher thermal efficiency.

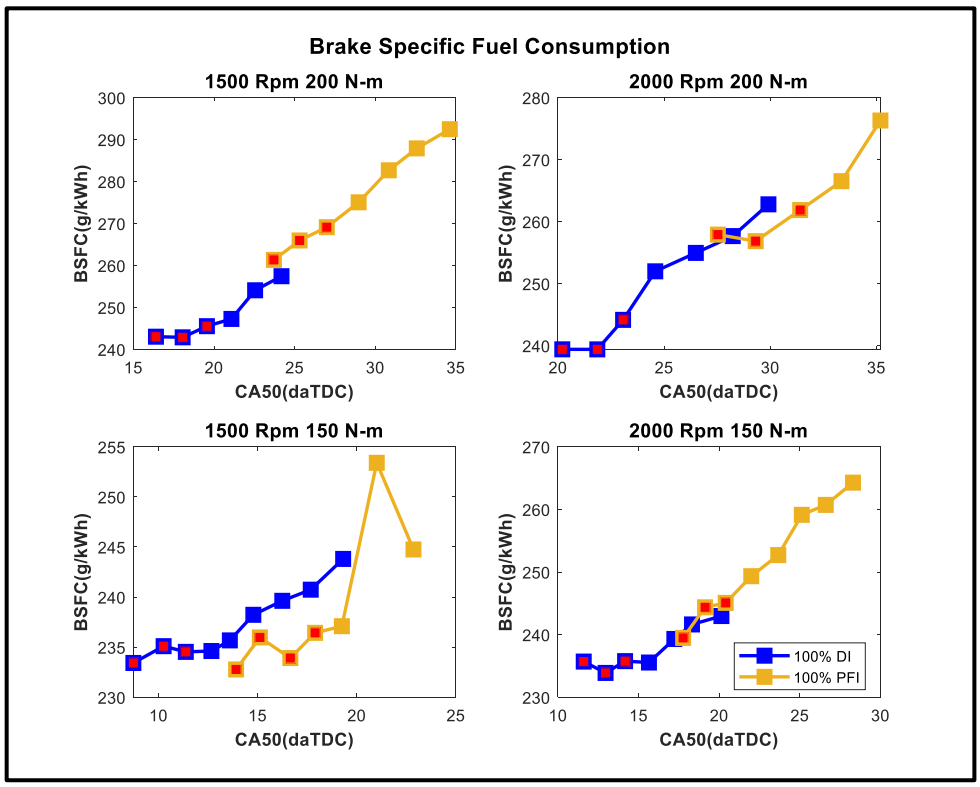

Figure 5-30: Fuel consumption for both injection strategies (PFI vs. DI) (Red symbols indicate knocking).

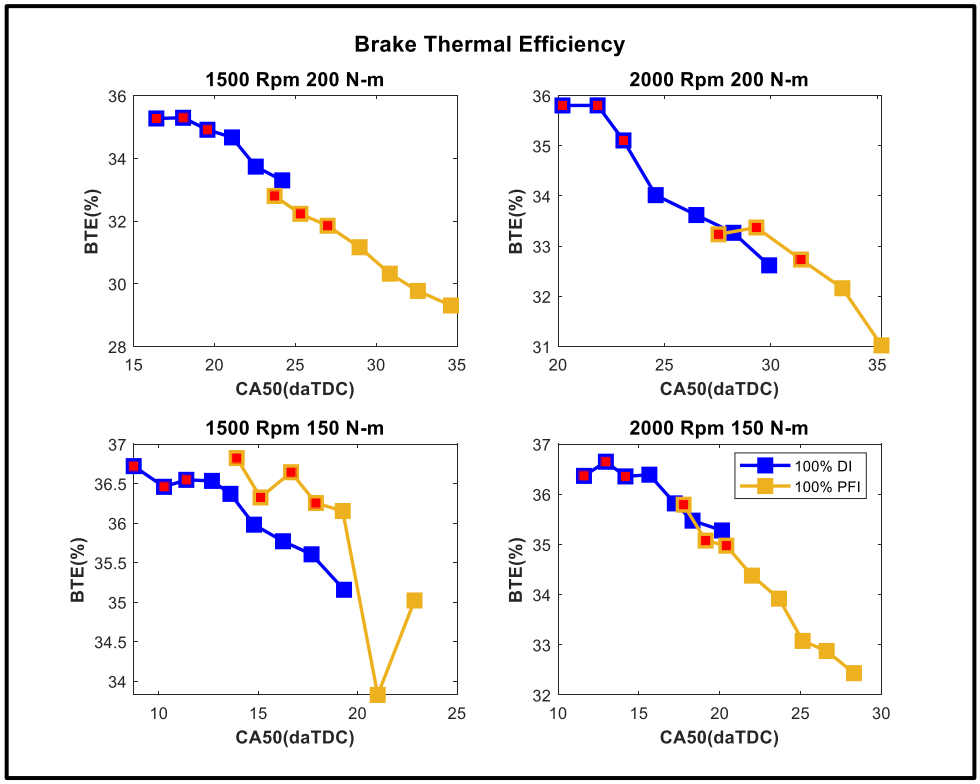

Figure 5-31: Brake thermal efficiency for each of the injection strategies (Red Symbols indicate knocking).

Knock limited cylinder pressure and heat release rate:

The cylinder pressure traces at knock limited combustion phasing for each of the injection strategies (Figure 5-32) shows how different the combustion is in the engine depending on the injection strategy that is employed. The direct injection which has a lower propensity for knock compared to the port injection can be seen to allow earlier spark timings which is confirmed from the earlier timings of the pressure rise from the start of combustion. The earlier start of combustion allows for more useful work to be extracted from the process during the expansion stroke. The comparison of the apparent heat release rates (Figure 5-33) also tells a similar story. The heat release profiles indicate that a direct injection strategy allows earlier combustion phasing compared to the port injection. Moreover, the heat release profiles are narrower for the direct injection indicating shorter combustion duration which is more efficient.

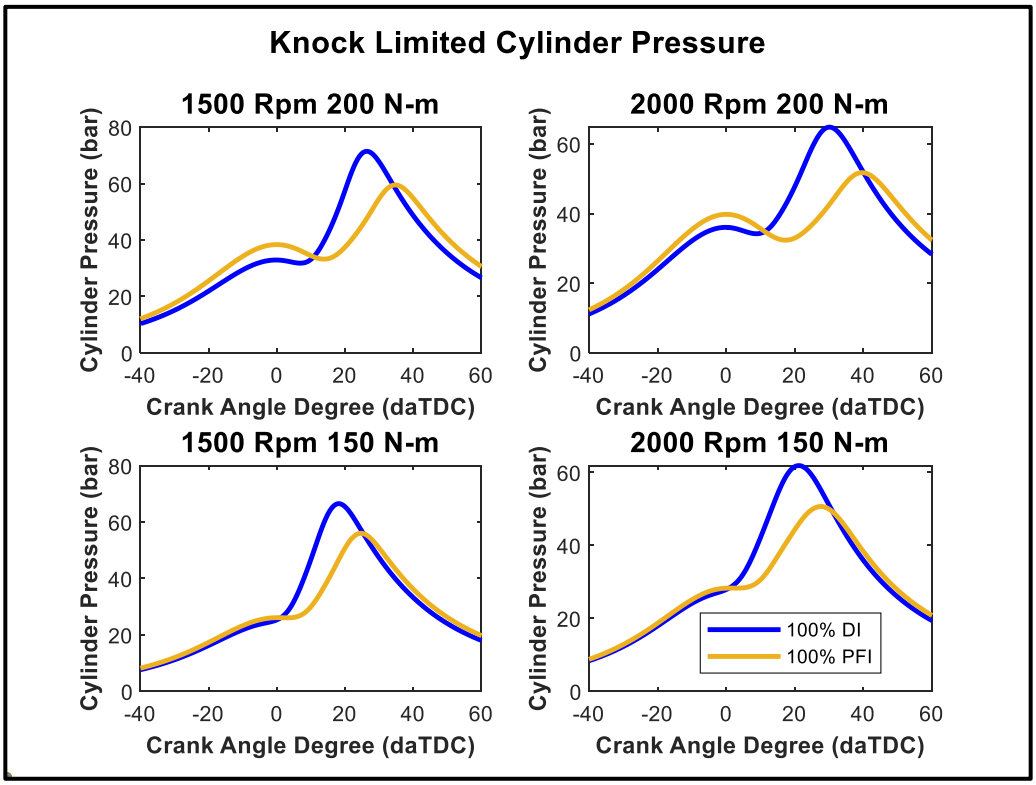

Figure 5-32: Cylinder pressures for both injection strategies at knock limited combustion phasing.

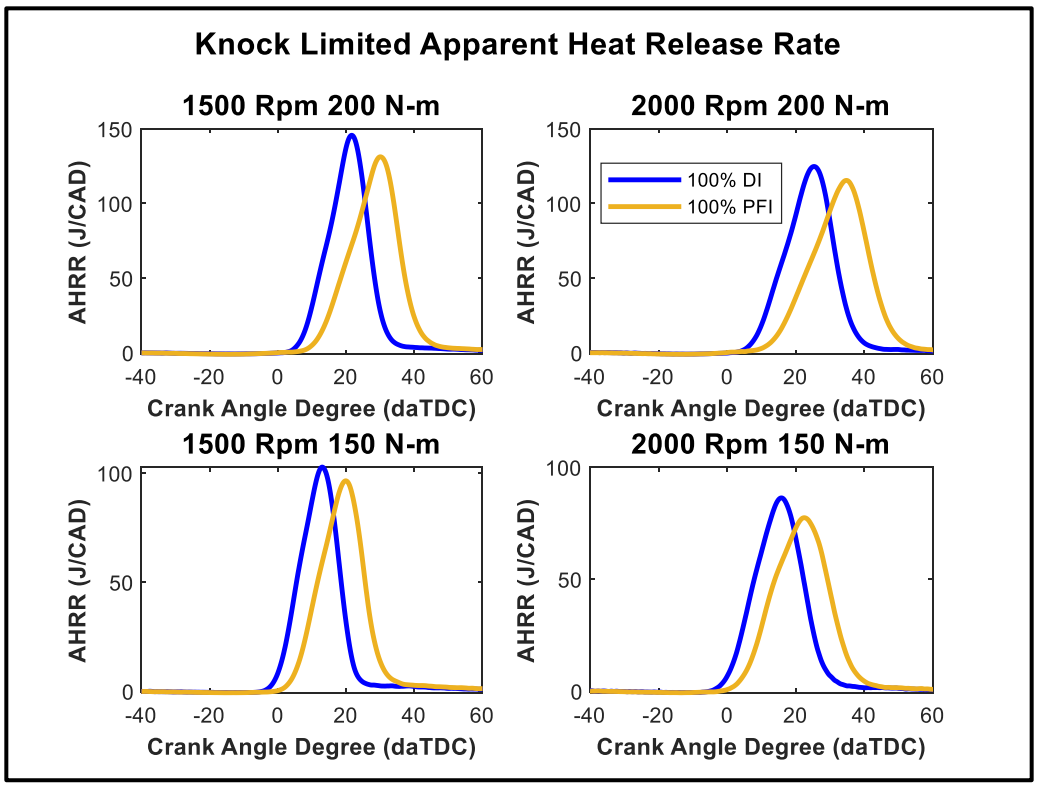

Figure 5-33: Apparent heat release rate for both injection strategies at knock limited combustion phasing.

Combustion duration:

The combustion duration is approximated as the CA1090 (the number of crank angle degrees swept to go from consuming 10 percent of the fuel to 90 percent of the fuel injected per cycle). This data backs up the observations from the heat release rate profiles and confirms that a direct injection strategy leads to faster combustion compared to port injection (Figure 5-34).

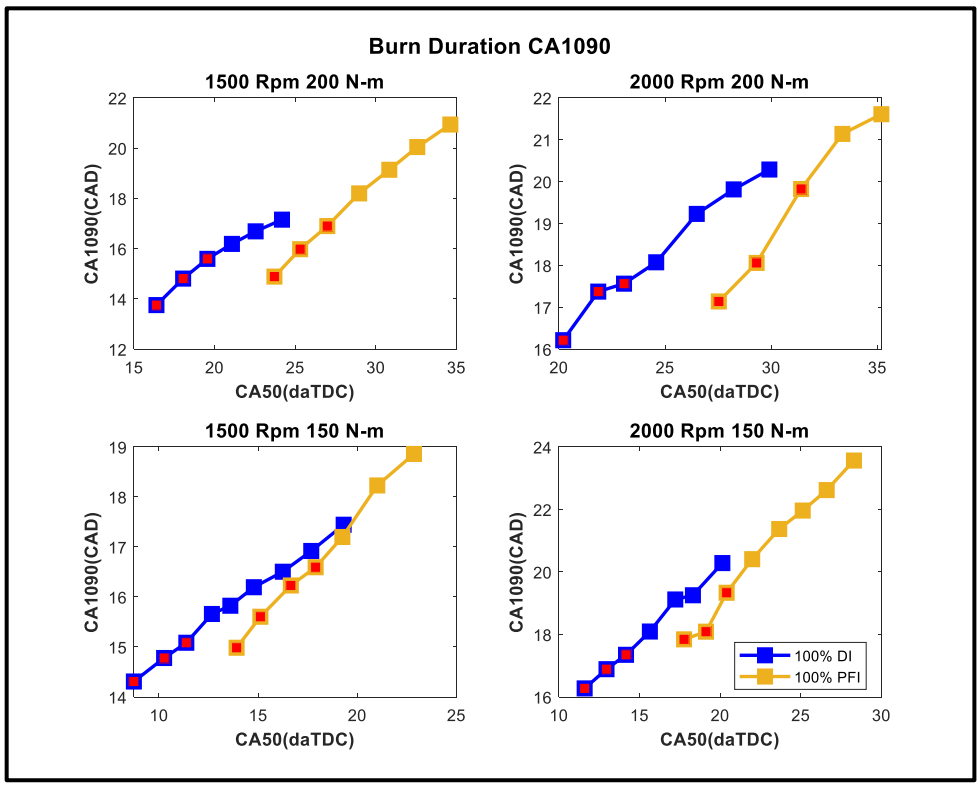

Figure 5-34: Burn duration for each of the injection strategies (Red symbols indicate knocking).

5.3.3 Fuels Comparison

This subsection discusses the effect of fuel chemistry on advancing knock limit and particulate emissions. This is the last of the 3 sets of experiments that were conducted to explore Han's knock-soot correlation. The fuels tested are described in the previous section.

Knock Intensity:

A comparison of the knock intensities at all four knock limited conditions of the 6 fuels shows a clear correlation between the octane ratings and the knock limits. The two high octane Sunoco fuels are less prone to knock as evidenced by their advanced combustion phasing and advanced knock limits. With these two fuels, the engine permits combustion phasing to achieve maximum

brake torque timing. This is not possible with the rest of the fuels that are of significantly lower octane rating. The baseline pump gasoline and the Shell fuels which have similar octane ratings to the baseline pump gas have the next most advanced knock limit. It is interesting to see that the Sunoco alkylate fuel which mostly contains branched alkanes and the highest heating value has the most delayed knock limited combustion phasing. This is despite the alkylate fuel having a superior octane rating to that of the baseline pump gas and either of the Shell fuels. It should be noted that it does have a lower sensitivity compared to the baseline and the Shell fuels which is not desirable at knock limited speed-load points according to Szybist et al. [140]. This suggests that the ethanol and aromatics have a greater effect on knock resistance compared to that of branched alkanes.

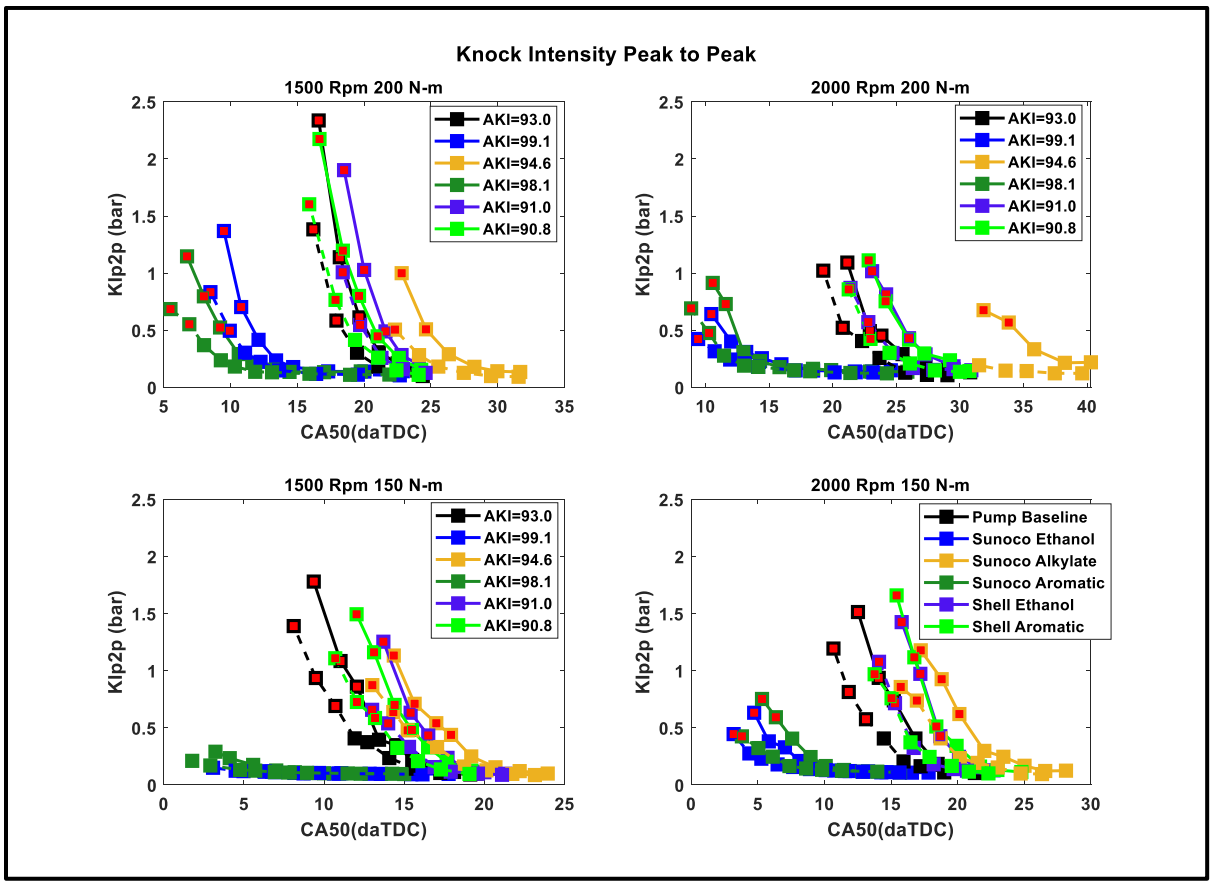

(a)

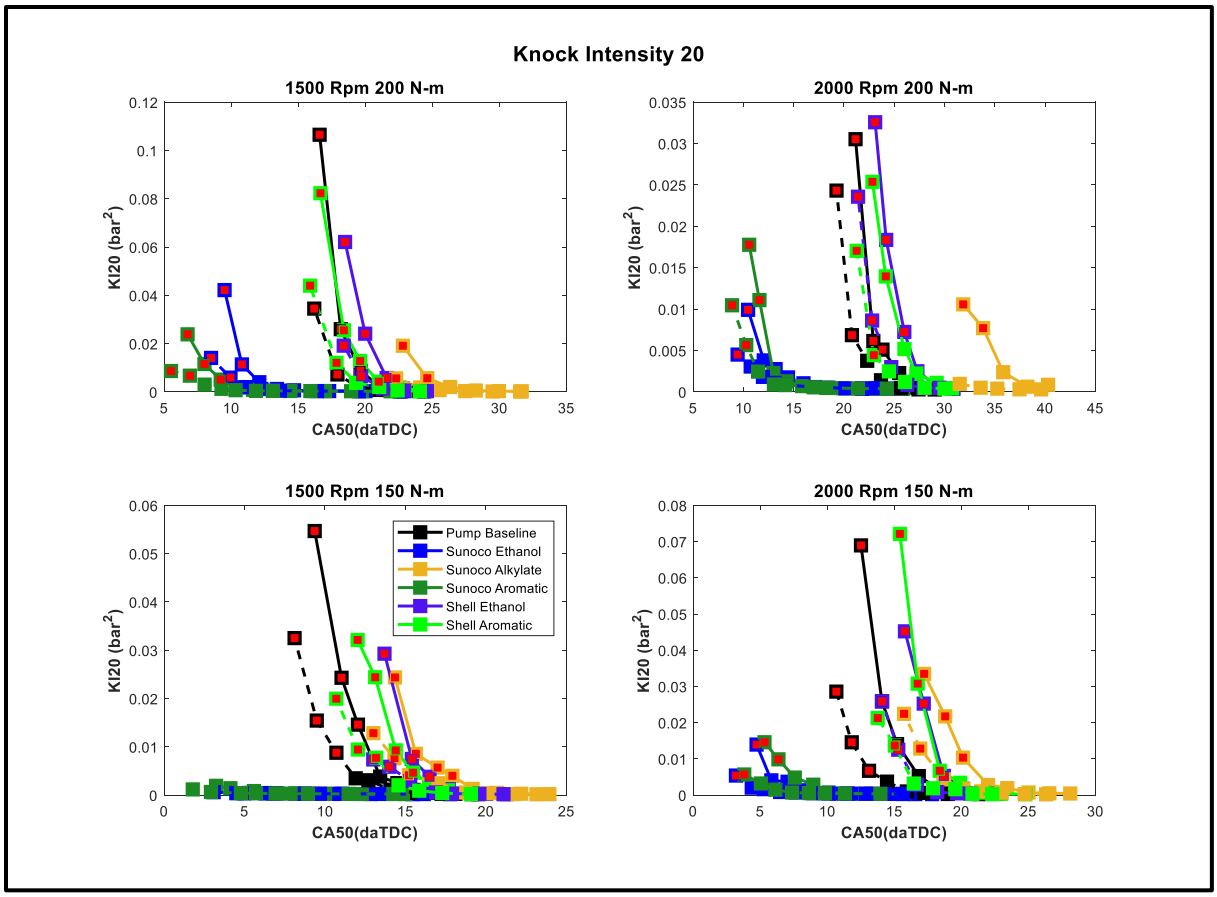

(b)

Figure 5-35: Comparison of knock intensities of all six fuels (Red symbols indicate knocking).

(a) Comparison of KIp2p of all six fuels (amplitude basis) (b) Comparison of KI20 of all six fuels (energy basis)

Particulate Emissions:

Han's knock-soot correlation is confirmed at knock limited points. A comparison of the particulate emissions using the different fuels against combustion phasing shows a steep increase in the number of particles beyond knock onset. There are some exceptions which include the baseline and Shell aromatic data sets at the high load points. However, when the total particle number above 23 nm is plotted, the correlation is confirmed. This suggests that the correlation likely comes around due to increase in accumulation mode particle number rather than

nucleation mode which is confirmed from the comparison of the nucleation and accumulation mode concentrations as seen from the particle size distributions in Figures 5-39 to 5-44.

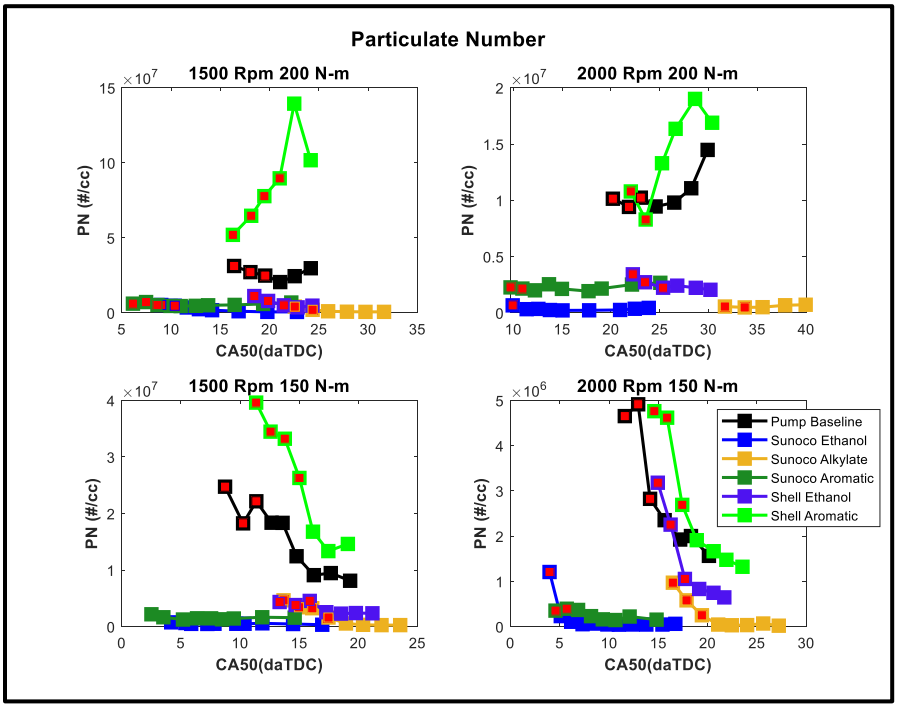

Figure 5-36: Comparison of the total particle number of the six fuels (Red symbols indicate knocking).

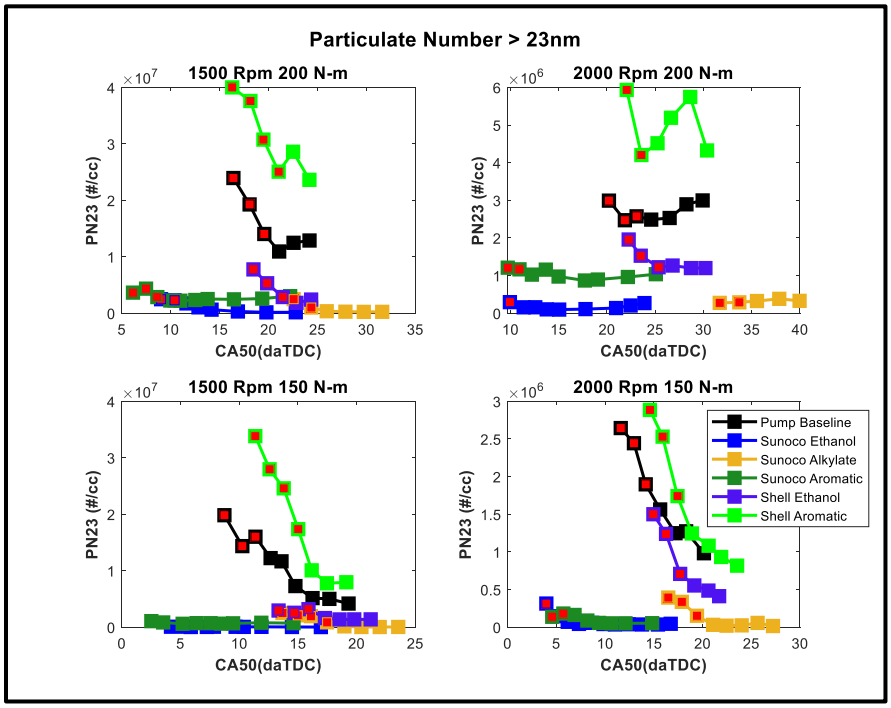

Figure 5-37: Particle number concentrations for particle diameters > 23 nm (Red symbols indicate knocking).

The baseline gasoline and the Shell aromatic blend led to significantly high particulate matter emissions. The Shell ethanol blend yielded the next highest particulate matter emissions. Since both blends from Shell were formulated from the same BOB (bio-blendstock for oxygenate blending), it was confirmed that the aromatics yielded higher number of particles possibly due to their higher sooting tendencies which is confirmed from the smoke point data (Figure 5-38). The results of the smoke point data are consistent with the observations from the engine except for the Sunoco high octane rated aromatic blend. It is possible that a different index for sooting tendency such as the particulate matter index (PMI) developed by Aikawa et al. [148,149] or the oxygen extended sooting index (OESI) developed by Barrientos et al. [150,151] that incorporate the effects of fuel molecular structure and volatility would show a better correlation.

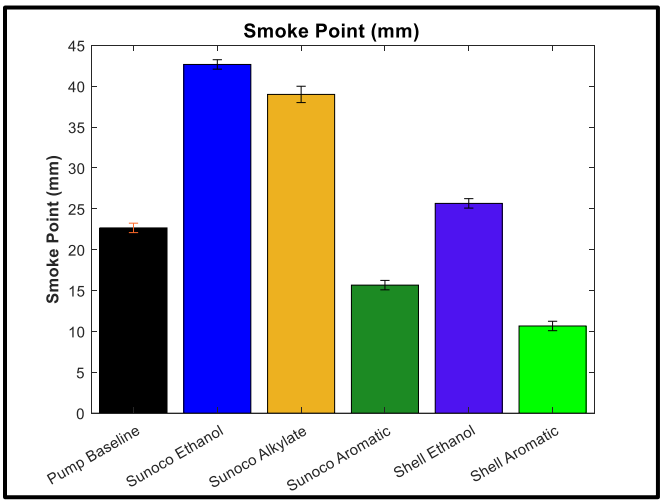

Figure 5-38: Comparison of smoke point of all six fuels.

It is interesting to note that both high-octane fuels as well as the alkylate blend formulated by Sunoco emitted the least soot. The observation that the aromatic blend led to higher concentration of soot compared to the ethanol blend holds true for the high-octane fuels only at high loads. At the relatively lower load of 150 N-m both the aromatic and the ethanol blends have comparable soot emissions and significantly lower than that of the baseline pump

gasoline. Despite only a few knock-limited points available for each of the high-octane fuels due to their anti-knock capability, a sharp increase in particle number was seen when knock occurred. This suggests that the correlation still holds true for high-octane fuels.

Particle Size Distribution:

The particle size distribution data for each of the six fuels further confirms the knock-soot correlation seen in the previous tests conducted in this chapter. It is clear from the particle size distribution for each of the fuels that the onset of knocking coincides with a sudden increase in the number of accumulation mode particles particularly those of electrical mobility diameters greater than 100 nm. This phenomenon is consistent across all the fuels irrespective of octane rating or compound used for blending whether that be ethanol or aromatics. The particle size distributions also confirms that there is no clear trend among the nucleation mode particles. In fact, there are some cases when the concentration of nucleation mode particles reduces as phasing is advanced. It is also notable that the sharp increase in concentration of accumulation mode particles is more pronounced at a lower engine speed for both engine loads (except for low load with high octane fuels where knock was not possible, and combustion was advanced beyond MBT timing). One reason for this could be the possibility of larger residence time of the precursors for soot formation whether that be engine oil or pool fires in the combustion chamber due to lower engine speed. Also, the lower engine speed ensures that the high oscillatory pressure waves that are a consequence of knock reside in the combustion chamber for a longer duration before the start of the next cycle.

In the particle size distributions plotted in Figures 5-39 to 5-44, the fainter colors show advancing phasing. Legends were avoided to reduce clutter.

Baseline Pump Gasoline from Corrigan Oil:

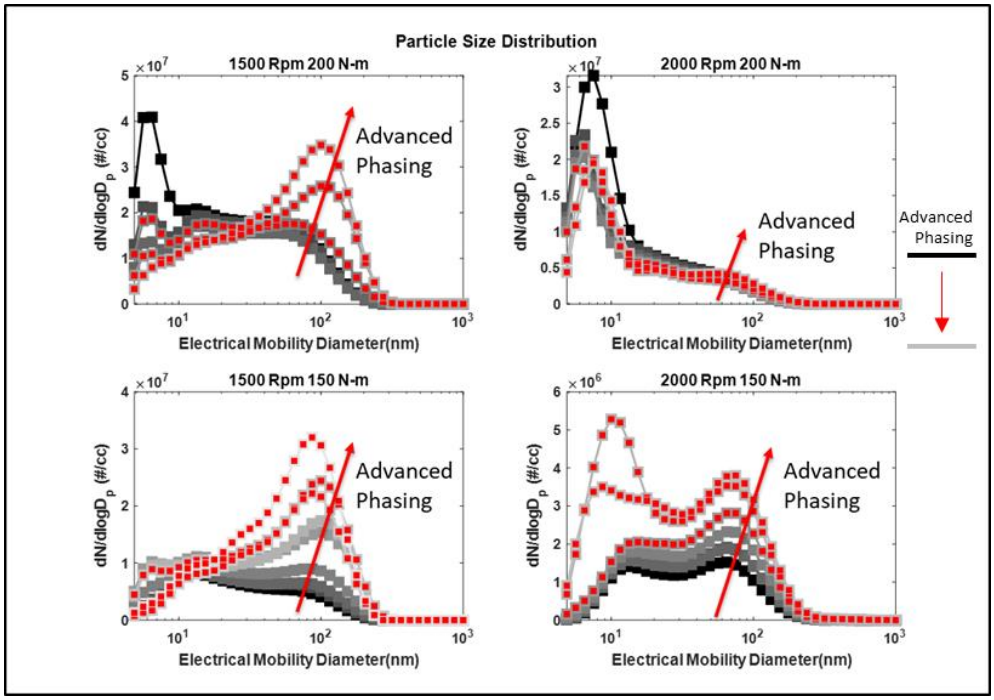

Figure 5-39: Particle size distribution of baseline pump premium gasoline (Red symbols indicate knocking).

Shell Ethanol Blend:

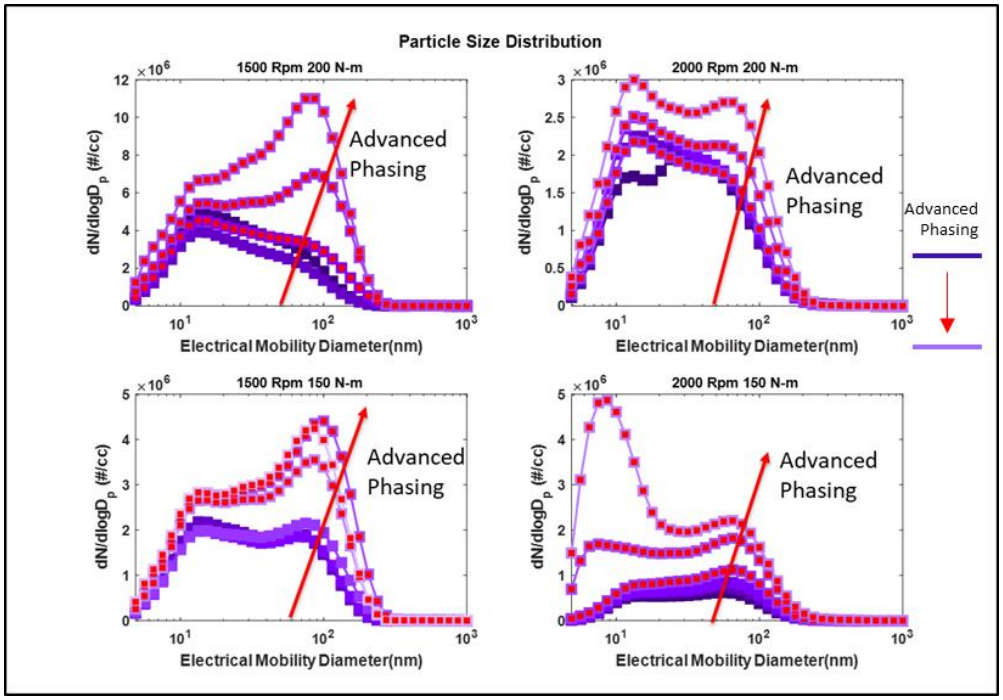

Figure 5-40: Particle size distribution of Shell ethanol blend (Red symbols indicate knocking).

Shell Aromatic Blend:

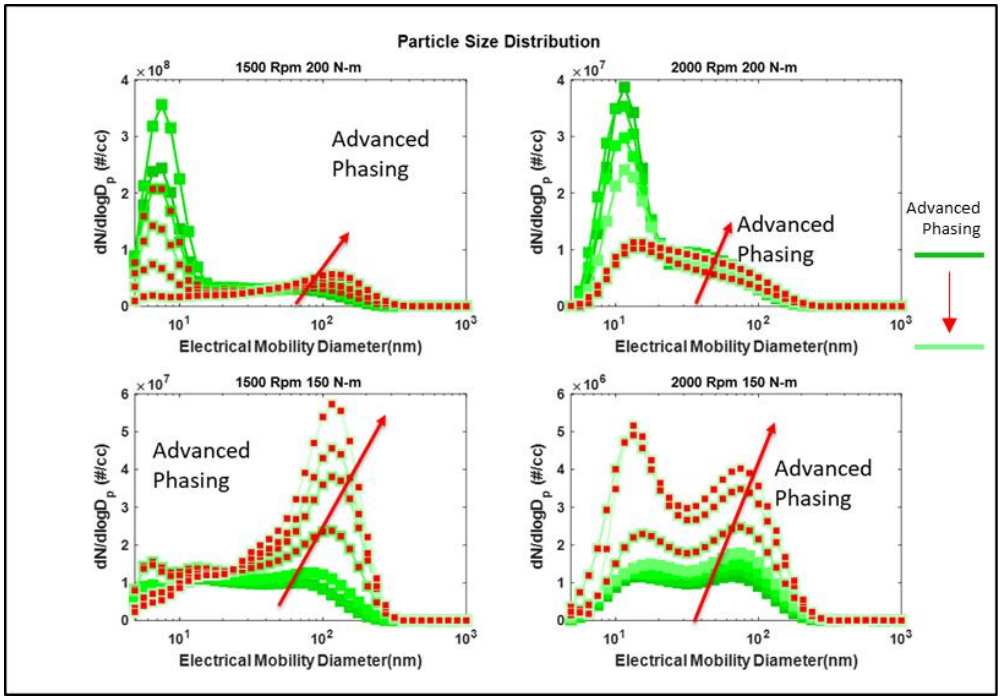

Figure 5-41: Particle size distribution of Shell aromatic blend (Red symbols indicate knocking).

Sunoco Alkylate Blend:

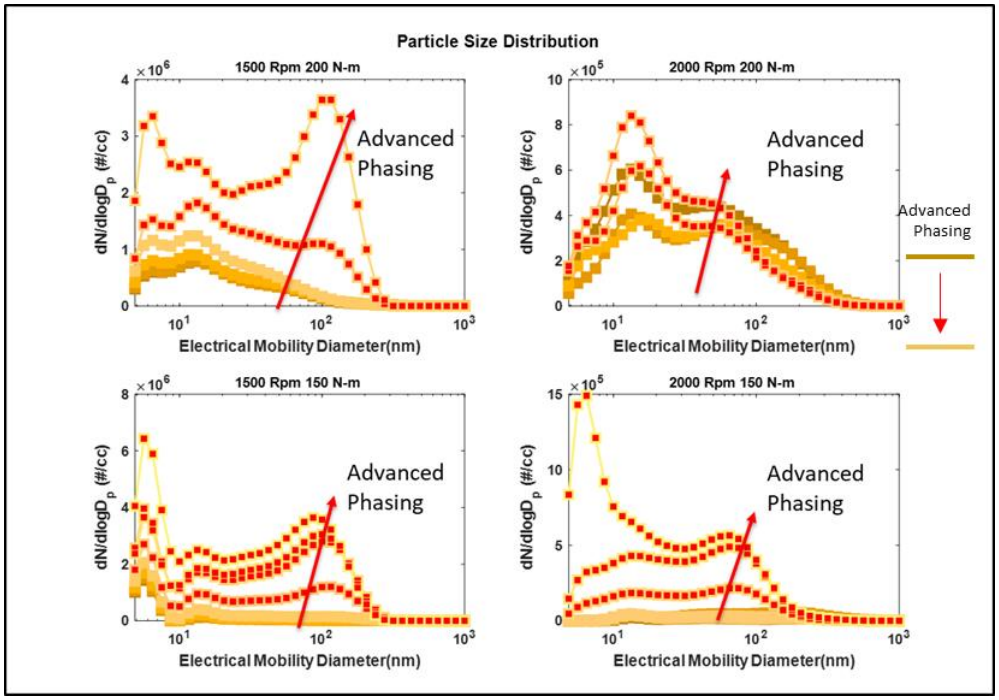

Figure 5-42: Particle size distribution of Sunoco alkylate blend (Red symbols indicate knocking).

Sunoco Ethanol High Octane Blend:

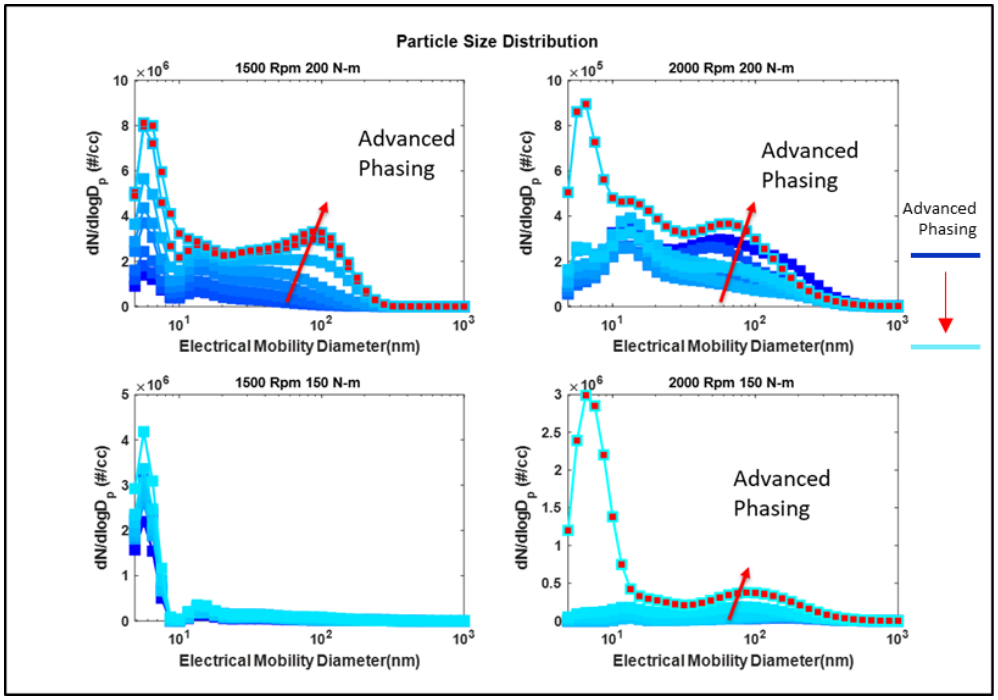

Figure 5-43: Particle size distribution of Sunoco ethanol blend (Red symbols indicate knocking).

Sunoco Aromatic High-Octane Blend:

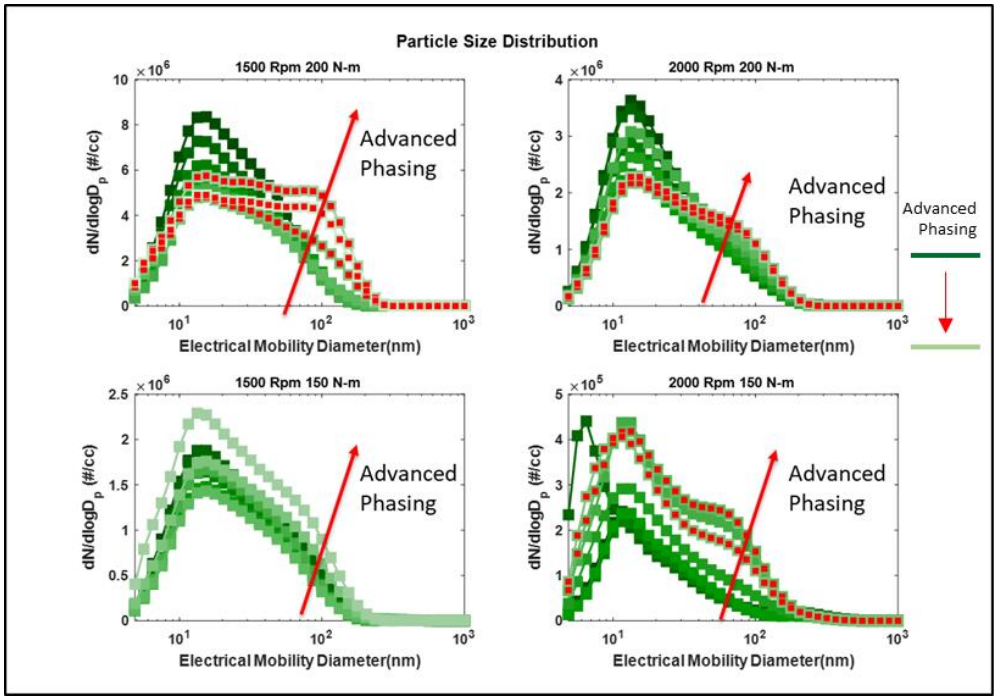

Figure 5-44: Particle size distribution of Sunoco aromatic blend (Red symbols indicate knocking).

The particle size distributions at the points of highest thermal efficiency whether that be at knock limit or at combustion phasing that leads to MBT are shown in Figure 5-45. The size distributions confirm the observations of total concentration that the Shell aromatic blend and the baseline pump gasoline are significantly higher emitters of particulate matter. At the lower knock limited load condition, all candidate fuels emitted lower particulate matter compared to the baseline pump gasoline. The high bond dissociation energy associated with aromatic compounds is a possible reason for the high concentration of particulate matter for the aromatic blended fuels. The Sunoco high-octane fuels lead to the least particulate matter emissions irrespective of the concentrations of different compounds used for blending up the alkylate to a higher-octane rating. The Sunoco alkylate also leads to low particulate emissions in the absence of either ethanol or aromatics. A possible reason for the Shell formulated ethanol blend leading to higher particulate matter emissions compared to the Sunoco formulated alkylate is the higher heat of vaporization and the lower chemical energy of ethanol compared to gasoline. Low heating value of ethanol blended gasoline results in longer injection durations and more fuel flow leading to fuel impingement on pistons and cylinder walls. Requirement for greater amounts of heat to evaporate from the surface of pistons and liners could result in locally fuel rich pool-fires which could then lead to high concentrations of particulate matter formation [147]. Thus, any choice for large fractions of ethanol to be blended for future gasoline fuels and flex fuels should consider this.

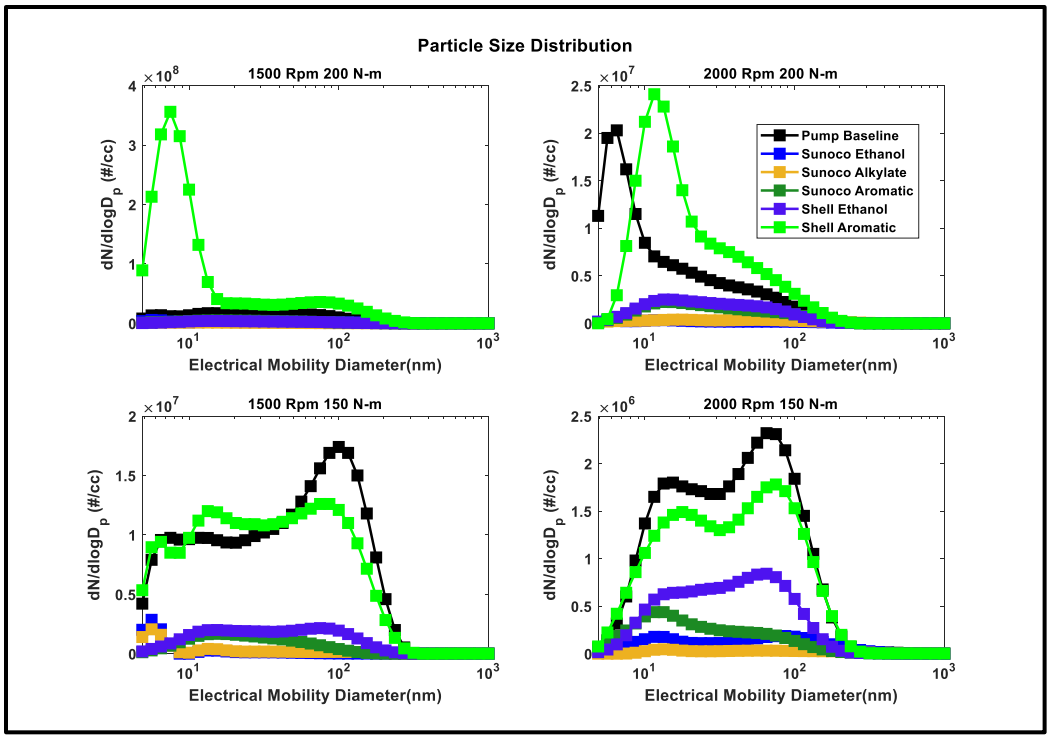

Figure 5-45: Comparison of the particle size distributions at knock limited or MBT combustion phasing.

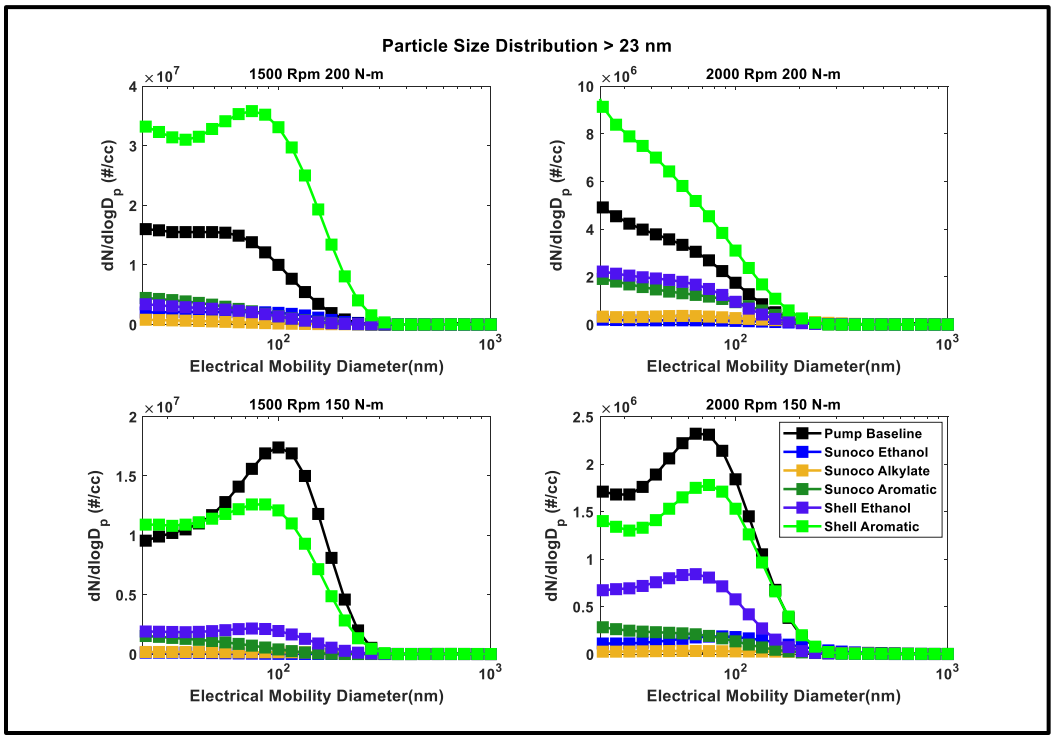

Figure 5-46: Particle size distributions for diameters > 23 nm at knock limited or MBT combustion phasing.

Gaseous Emissions:

CO Emissions:

Carbon monoxide emissions are typically dependent on air-fuel equivalence ratios. The equivalence ratio was maintained at 1 for all the experiments and so the minute differences in the carbon monoxide emissions could be due to the differences in locally rich zones. Differences in the physical ignition delay of the different fuels due to their physical properties could be the reason for the difference in atomization and hence combustion efficiency. The high soot emitting fuels appear to be low emitters of carbon monoxide. Also, the high-octane fuels lead to high emissions of carbon monoxide at the lower engine speed of 1500 rpm.

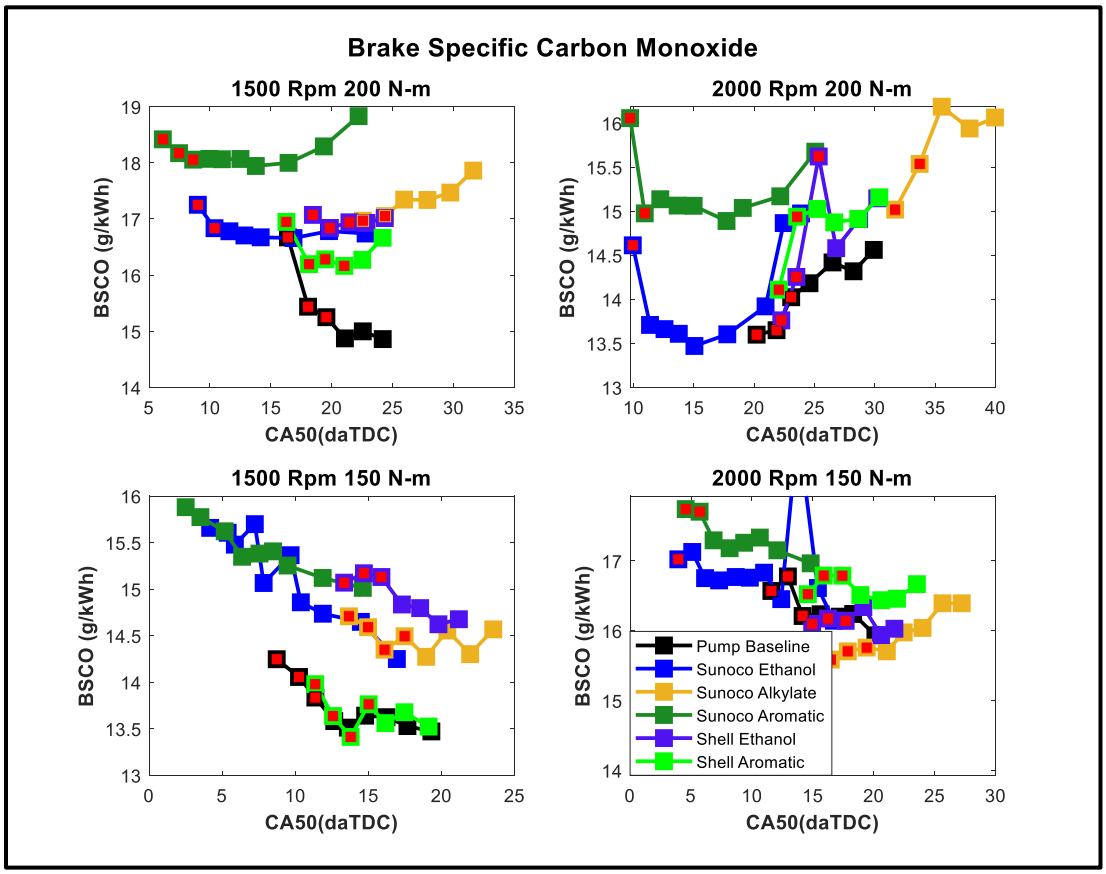

Figure 5-47: Carbon monoxide emissions of all six fuels (Red symbols indicate knocking).

NO_X Emissions:

NO_X emissions increase monotonically as combustion phasing is advanced with spark timing. This is understandable due to the increase in in-cylinder temperature as spark timing is advanced. The lower octane fuels such as the baseline and the Shell formulated blends emit higher concentrations of NO_X compared to the Sunoco high octane fuels. This is possibly due to the knocking phenomenon increasing the cylinder temperature at comparable combustion phasing. It is interesting to see that the Sunoco alkylate which is also a low octane fuel debunks this theory. The alkylate is rich in alkanes and has a higher heating value and a comparable heat of vaporization. It is interesting that both ethanol blends do not emit lower concentrations of NO_X despite the higher heat of vaporization of ethanol. This is possibly due to the greater mass of fuel injected per cycle to compensate for the lower heating value of ethanol to maintain constant load.

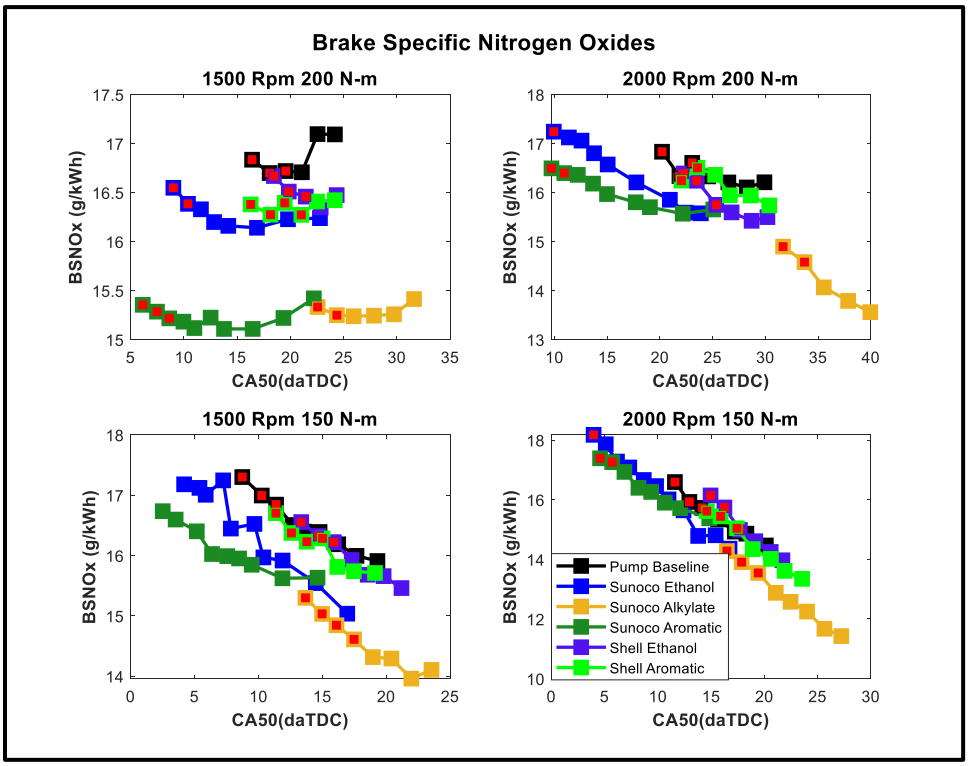

Figure 5-48: NO_X emissions of all six fuels (Red symbols indicate knocking).

THC Emissions:

All the fuels led to lower concentrations of the unburnt hydrocarbons compared to the baseline fuel, except for the Shell aromatic blend at the lower engine speed. This suggests greater combustion efficiency associated with the candidate fuels compared to the baseline.

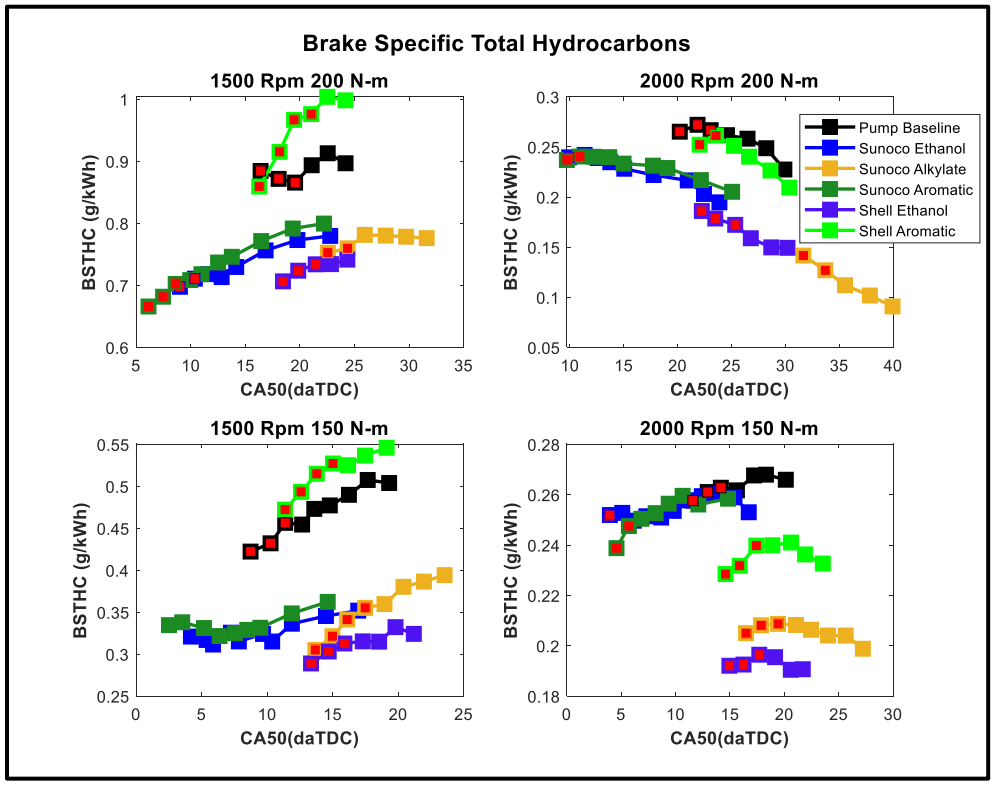

Figure 5-49: Total unburnt hydrocarbon emissions of all six fuels (Red symbols indicate knocking).

CO_2 Emissions:

The carbon dioxide emissions monotonically decrease with advanced phasing due to reduced fueling at the same engine load. This trend matches that of fuel consumption. Both Shell fuels as well as the Sunoco fuels show the trend of lower CO2 emissions with the aromatic blend compared to the ethanol blend. The ethanol blended fuels emit higher concentrations of carbon dioxide when the combustion is phased according to the knock limits of the baseline fuel. This depicts the issue that could potentially arise when the engine control unit of an engine is

calibrated without a knock learning or searching algorithm. Eventually, leveraging the high octane rating and advancing the combustion phasing, the Sunoco ethanol blend does emit lower concentrations of carbon dioxide.

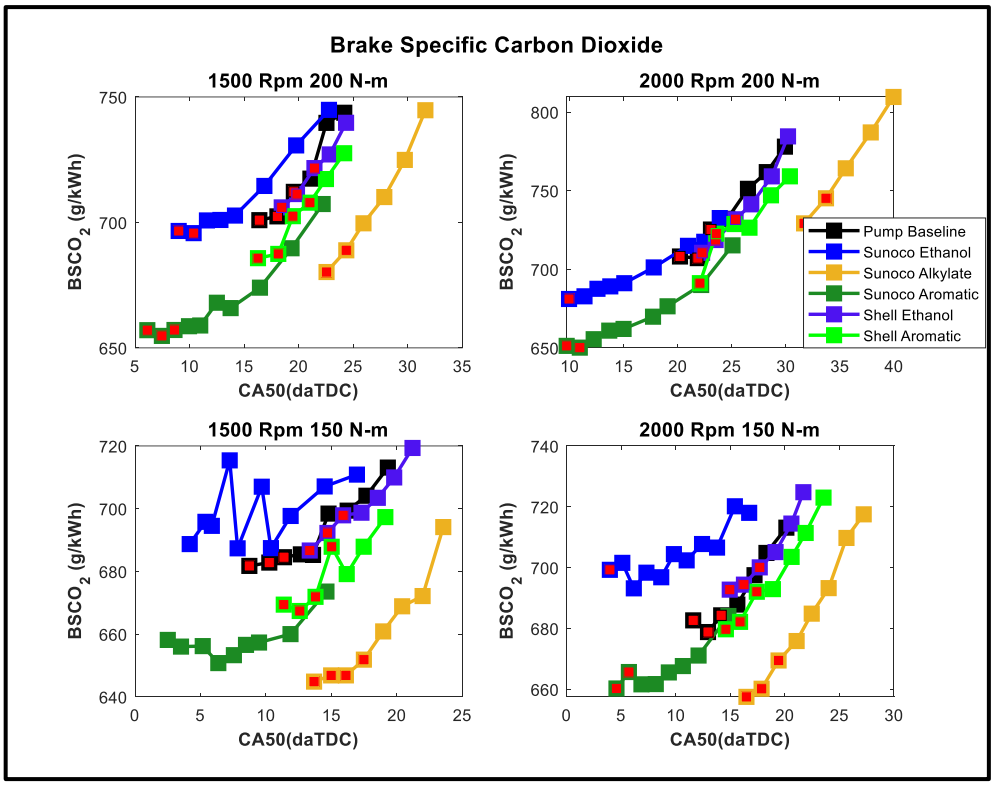

Figure 5-50: Carbon dioxide emissions of all six fuels (Red symbols indicate knocking).

Fuel consumption and thermal efficiency:

A comparison of the fuel consumption and thermal efficiencies confirms the trends from the CO_2 emissions. Sunoco aromatic blend displays the lowest fuel consumption and thus the highest thermal efficiency. The Sunoco ethanol blend displays high fuel consumption but still maintains high thermal efficiency due to its relatively lower heating value. In fact, the Shell blends show that although the aromatic blend has a lower fuel consumption compared to the ethanol blend. However, it is the ethanol blend that has the higher thermal efficiency. Although the Sunoco alkylate blend had a late knock limit due to its low octane rating, it recorded a lower

fuel consumption due to its high heating value. Due to the very same reason, it has the lowest thermal efficiency of all the blends that were a part of this study.

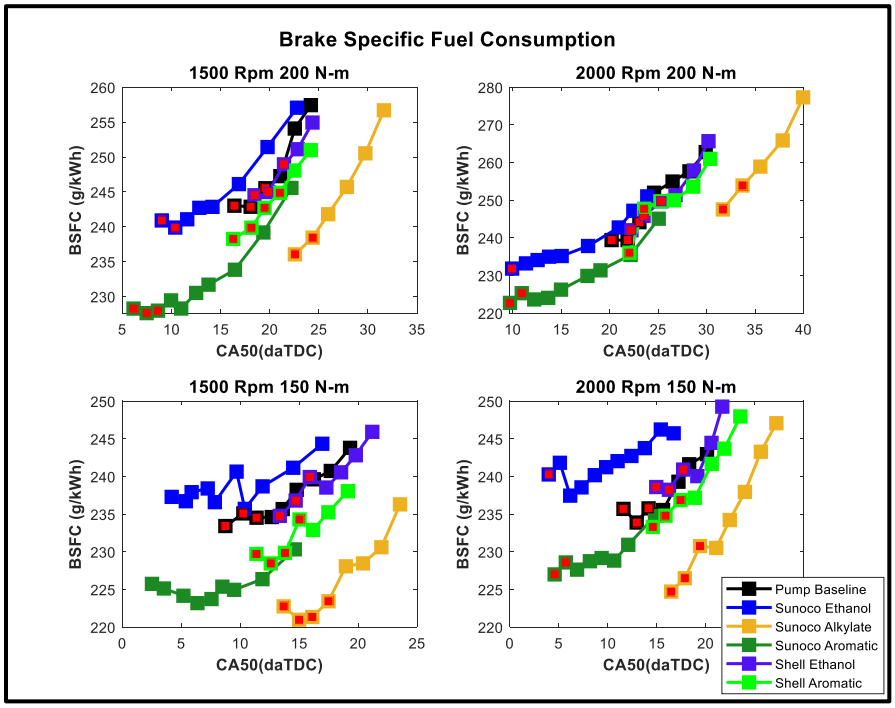

Figure 5-51: Brake specific fuel consumption of all six fuels (Red symbols indicate knocking).

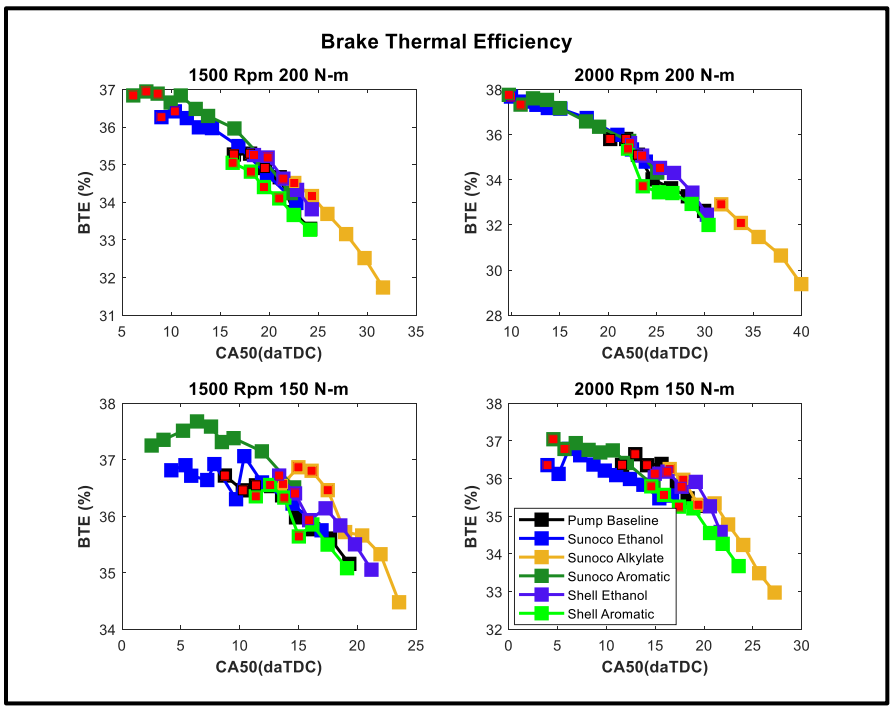

Figure 5-52: Brake thermal efficiency of all six fuels (Red symbols indicate knocking).

Knock limited cylinder pressure and heat release rate:

A comparison of the cylinder pressure traces at knock limited combustion phasing is shown in Figure 5-53. The Sunoco fuels do not knock at all the points tested and so if knock did not occur, the cylinder pressure trace for the combustion phasing that led to maximum brake torque was used for comparison. Thus, comparisons were made across all the fuels at the points of maximum thermal efficiency.

As seen from Figure 5-53, the combustion phasing trends for the fuels trends according to the thermal efficiencies (Figure 5-51). The earlier, the combustion is phased, the more thermally efficient is the performance. The Sunoco alkylate fuel was phased the latest while the Sunoco high-octane fuels were phased the earliest at MBT timing. The baseline and the Shell fuels were phased in between these. Delaying the spark timing led to reduced in-cylinder pressure since the late combustion phasing meant that the piston is on its way down during the expansion stroke.

A comparison of the apparent heat release rates tells the same story. The difference in combustion phasing in terms of crank angle degrees can be seen in Figure 5-54. In addition, in the case of the high-octane fuels, the area under the curve is the highest which represents that it led to the highest amount of useful work extracted from the fuel. The area under the heat release rate trace reduces to the minimum value in the case of the Sunoco alkylate fuel which is consistent with our observations of thermal efficiency (Figure 5-51).

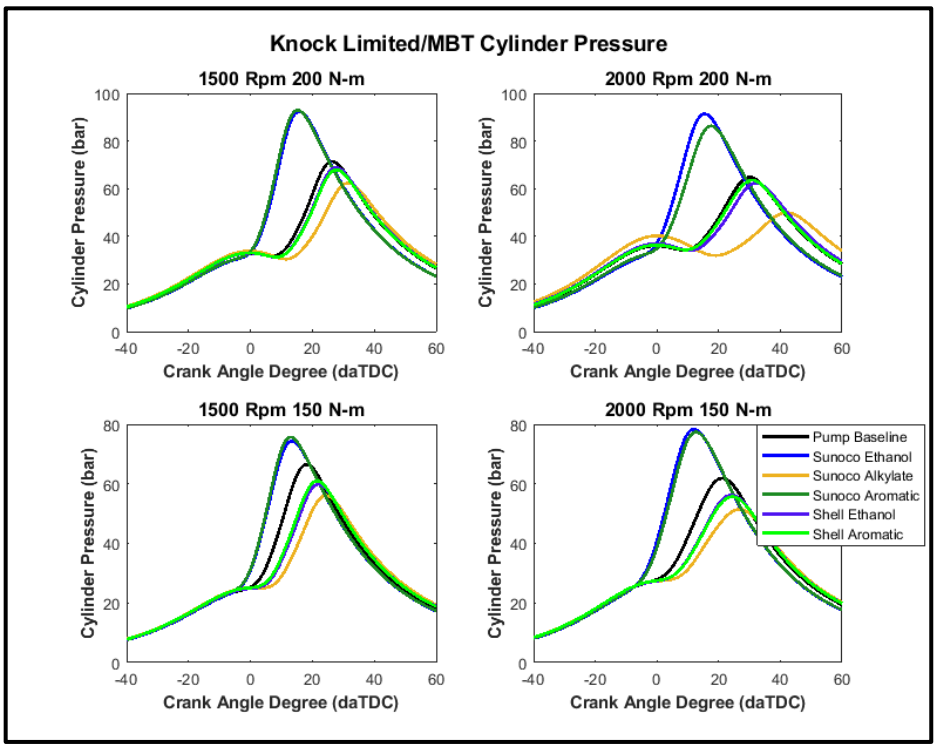

Figure 5-53: Cylinder pressure of all six fuels at knock limited combustion phasing or MBT combustion phasing (for high-octane Sunoco fuels).

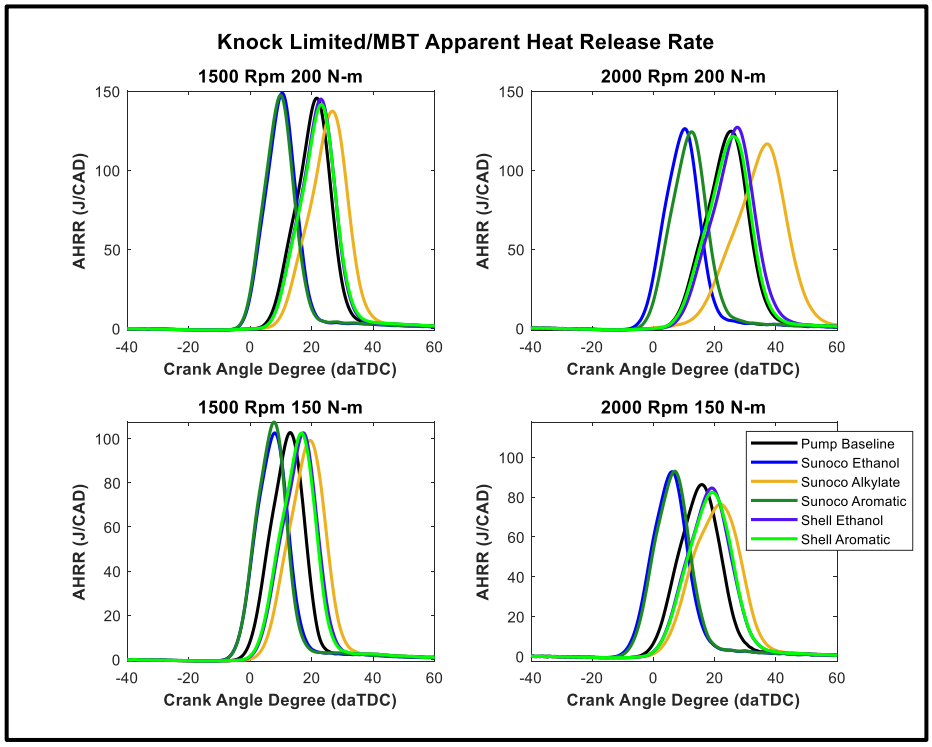

Figure 5-54: AHRR of all six fuels at knock limited combustion phasing or MBT combustion phasing (for high-octane Sunoco fuels).

Combustion duration:

A comparison of the combustion durations estimated from CA1090 is consistent with the traces of apparent heat release rate (Figure 5-54). The Sunoco alkylate fuel has the longest duration since it has the largest spark delay of all the fuels. At knock limited combustion phasing, the high octane fuels have the least combustion duration. Since the spark timing for these fuels is at MBT timing or close to MBT timing, it led to high magnitudes of cylinder pressure and fast consumption of the fuel. A combination of these factors contributed to high thermal efficiency for the two Sunoco high-octane fuels.

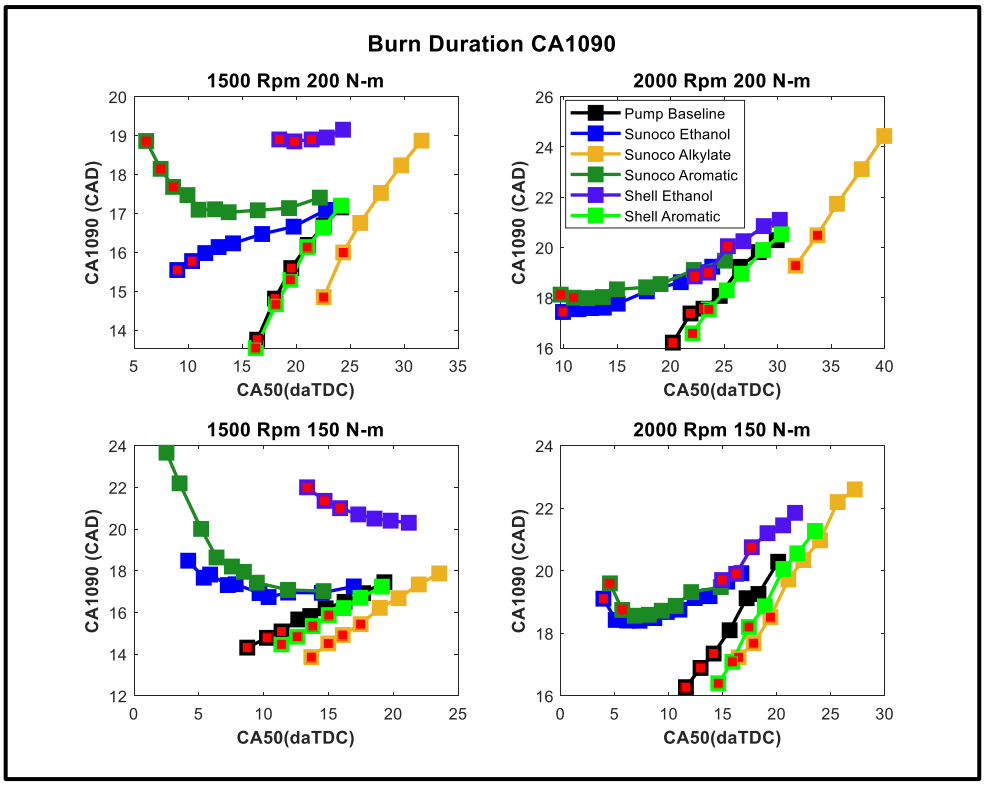

Figure 5-55: Burn duration of all six fuels (Red symbols indicate knocking).

5.4 Empirical theories for the knock-soot correlation

A common theme from the three set of experiments that were conducted as a part of this chapter is the confirmation of the existence of the knock-soot correlation in each of them. One can then conclude that the knock-soot correlation that was first observed by Han exists in gasoline engines irrespective of the whether it is operating on a traditional Otto cycle or the overexpanded Miller cycle. Furthermore, the phenomenon was found to exist irrespective of the injection strategy and the fuel chemistry used. Also, all three experiments confirmed that the rise in particulate matter emissions is due to the rise in accumulation mode particles. Lastly, it was also seen from the particle size distributions that the accumulation mode particles for each of the tests increased as phasing was advanced and knock intensity increased which suggests a proportional relationship with knock intensity. Some of the theories that could explain this phenomenon are highlighted below.

1. Ring Crevice Theory:

This empirical theory suggested by Han [30] mentions that the in-cylinder pressure oscillations that arise from the knock event are responsible for the sudden rise in formation of accumulation mode particles in the engine. According to this theory, the high intensity oscillations cause liquid fuel and oil droplets stuck in the crevice above the piston ring to get knocked out of the crevice and into the combustion chamber. Once in the combustion chamber, these unburnt hydrocarbons which are a combination of fuel and oil undergo pyrolysis. This environment after the auto-ignition event promotes the chain of multiple reactions that eventually lead to high particulate matter formation.

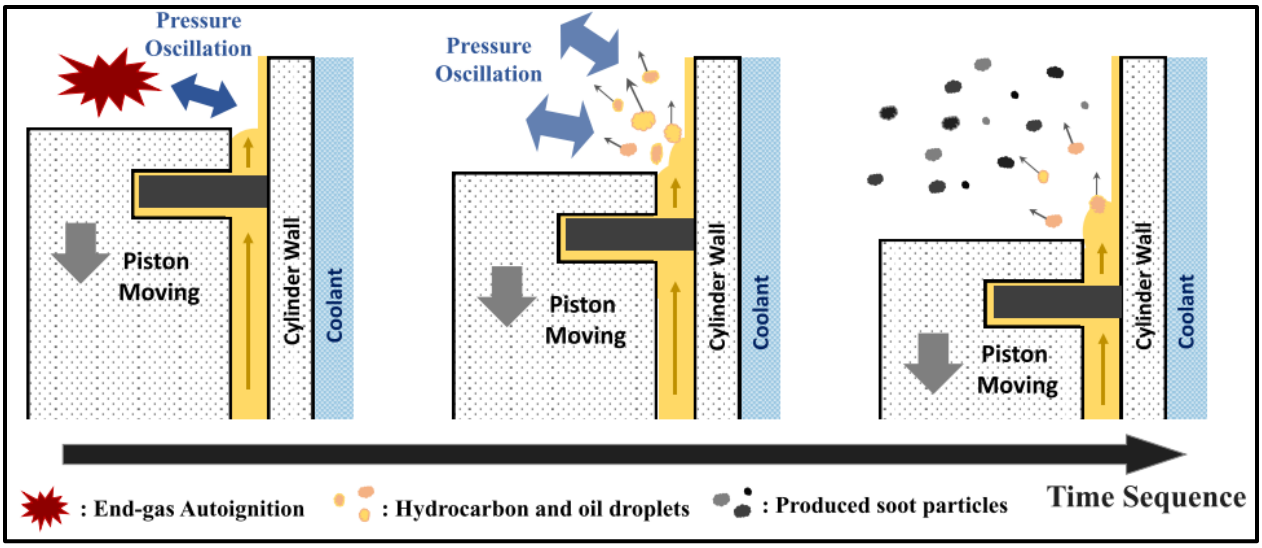

Figure 5-56: Conceptual diagram highlighting the ring crevice theory proposed by Han [30].

2. Insufficient mixing theory:

A second theory suggested by Han [30] mentions that the occurrence of a knocking cycle leads to less time available for the fuel and air to mix before auto-ignition occurs. A regular non-knocking cycle on the other hand has sufficient time available for air-fuel mixture homogeneity. The insufficient mixing is theorized to lead to local rich hotspots in the combustion chamber. These fuel rich hotspots under detonation conditions of knock in the cylinder can lead to high concentrations of particulate matter formation. Previous studies have shown that fuel rich combustion can lead to high particulate matter formation [57,144,145,147].

Shock tube pyrolysis studies of engine relevant fuels in the literature [152–158] have shown temperature dependence of soot yield exhibiting a bell-shaped curve. Soot yield is shown to increase with temperature up to the 1800^{o}C -2000^{o}C temperature range before further rise in temperature leads to reduction in soot yield. The initial rise in soot yield with temperature is due to the increase in rate of formation of soot precursors but further increase in temperature leads to the rate of oxidation dominating the rate of formation [154]. Moreover, Alexiou et al. [155] has

shown that the addition of aromatics namely toluene to iso-octane can lead to shifting of maximum soot yield to lower temperatures which suggests that under detonating conditions such as engine spark knock, aromatic blended gasoline will tend to form larger concentrations of particulate matter for a given in-cylinder temperature. Agafonov et al. [156] has shown that the induction period of soot formation is substantially longer for aliphatic hydrocarbons compared to aromatic species.

5.5 Transient Test Results

Fuel formulation impacts on transient operation of the engine were explored by running standardized drive cycles. Tests were not run with the high-octane Sunoco fuels since they were limited in quantity the absence of a knock learning algorithm on the engine control unit would most likely not result in any fuel economy benefits. Moreover, as seen earlier from the fuel consumption and CO_2 emissions (Figure 5-50 and 5-51), the results are likely to be skewed when high-octane ethanol blended fuel is run at late combustion phasing in the absence of overridden spark timings.

The transient tests helped verify the effect of the fuel chemistry on the performance of the engine and the emissions generated from it when operating under simulated real-world conditions. A greater emphasis was placed on studying the effect of the fuel chemistry on the particle size distributions when the engine was operated under these standardized drive cycles.

FTP 75:

The federal test procedure drive cycle results (Figure 5-57) show a slight improvement in fuel economy when the engine is running on the Shell ethanol blend. It should be noted that the baseline gasoline found at pumps across North America also contains ethanol at a volume

fraction of 10%. The ethanol blend formulated by Shell however contains a 13% volume fraction of ethanol and the extra 3% of ethanol is hypothesized as being responsible for the slight improvement in fuel economy. Although the engine control unit was not equipped with a knock learning algorithm, the minute difference in ethanol fraction meant that existing spark timing tables were used without significant spark delay added on to them. All candidate fuels tested against the baseline led to lower particulate emissions both on a number and mass basis. As seen from the respective particle size distributions (Figure 5-58), the ethanol and alkylate blend showed a high fraction of nucleation mode particles. The aromatic blend showed relatively lower fractions of nucleation mode particles but higher concentrations of accumulation mode particles, which contribute more significantly to the mass.

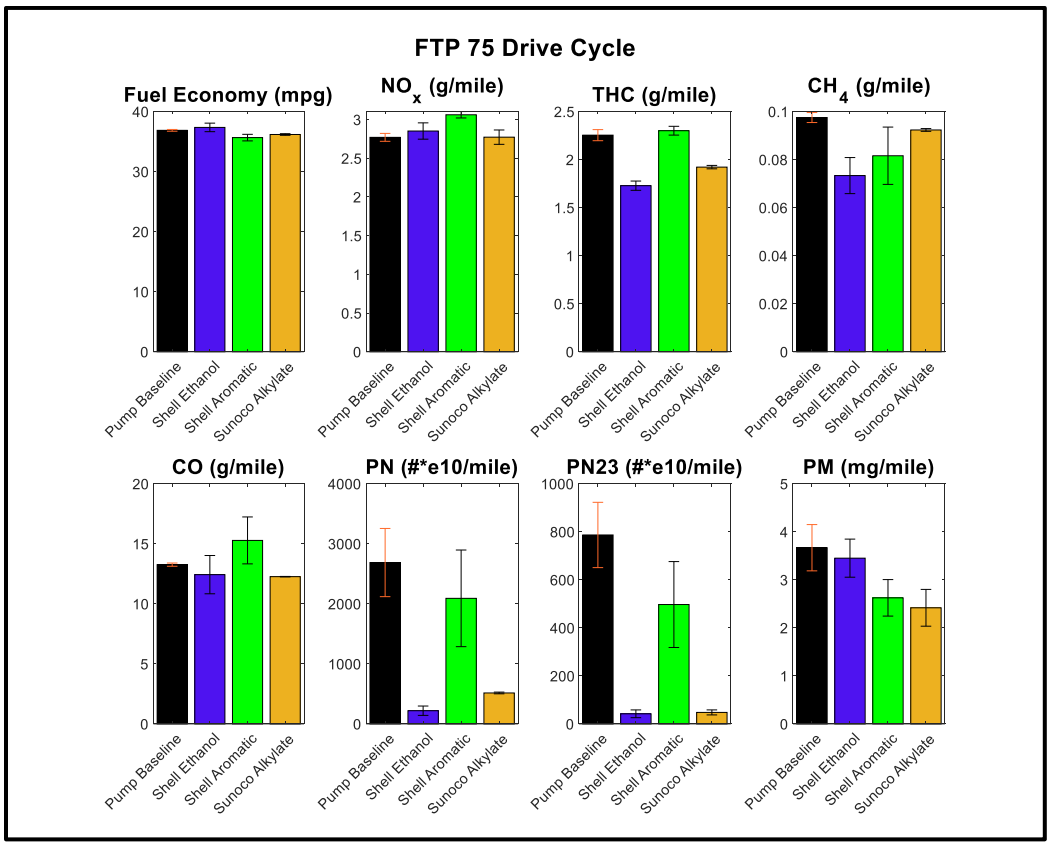

Figure 5-57: Cumulative results comparing fuel performance over FTP 75 drive cycle.

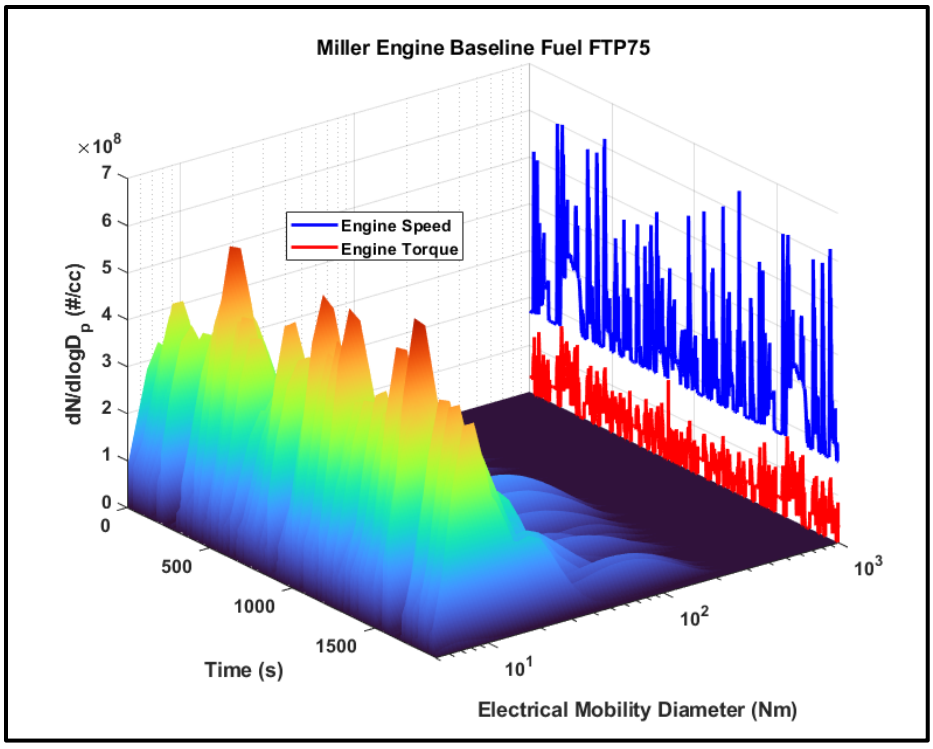
Miller Engine Baseline Fuel FTP75
Engine Speed
Engine Torque
dN/dlogD_p (#/cc)
×10^8
Time (s)
Electrical Mobility Diameter (Nm)

(a)

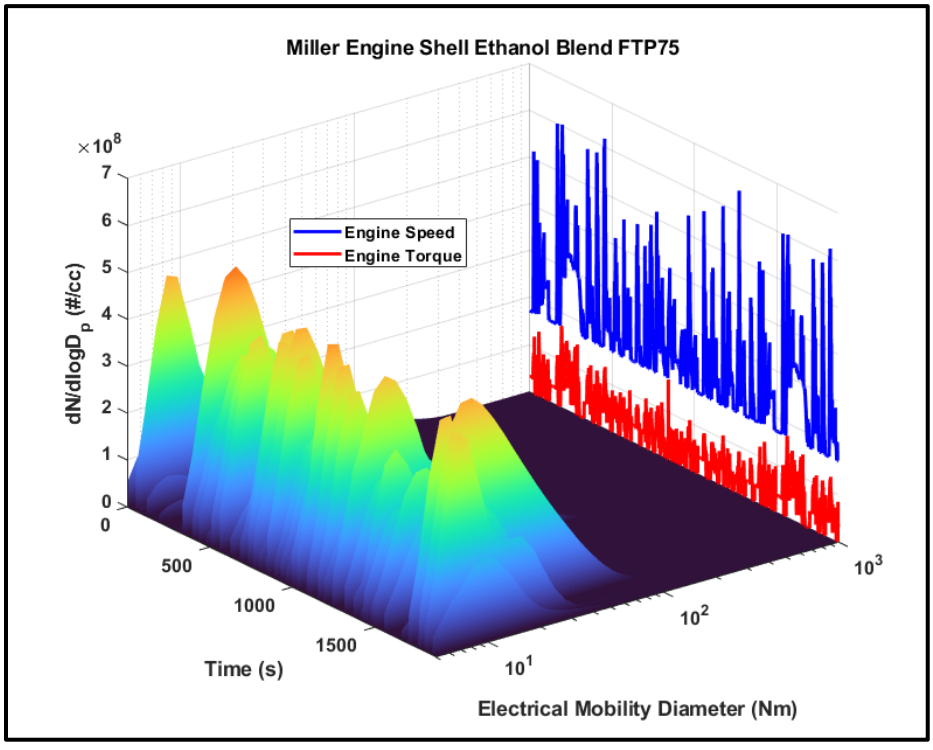
Miller Engine Shell Ethanol Blend FTP75
Engine Speed
Engine Torque
dN/dlogD_p (#/cc)
×10^8
Time (s)
Electrical Mobility Diameter (Nm)

(b)

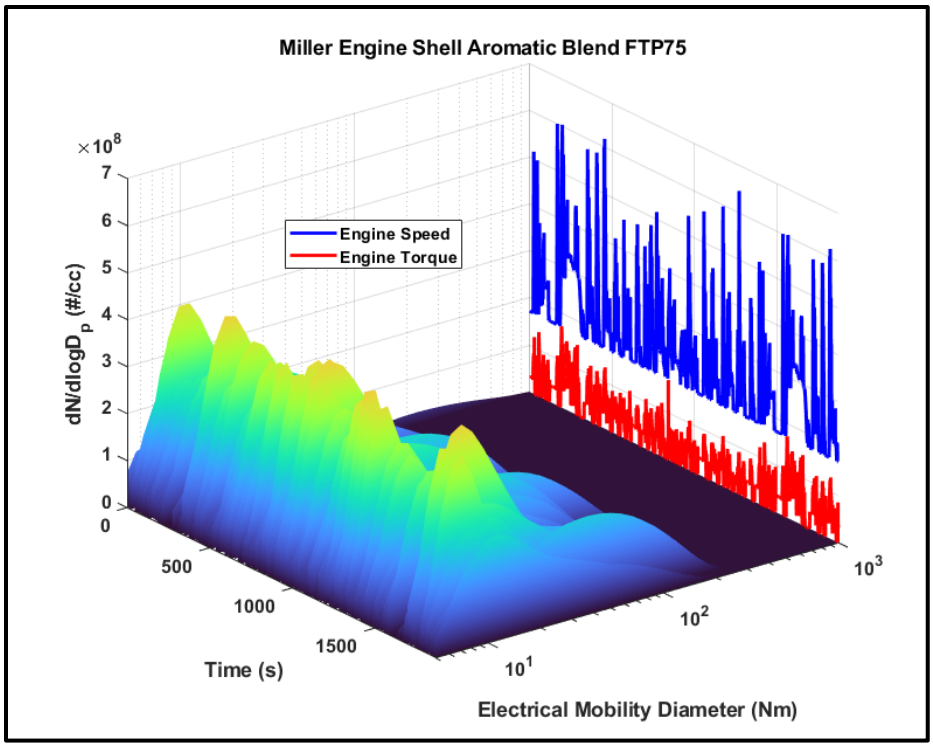

(c)

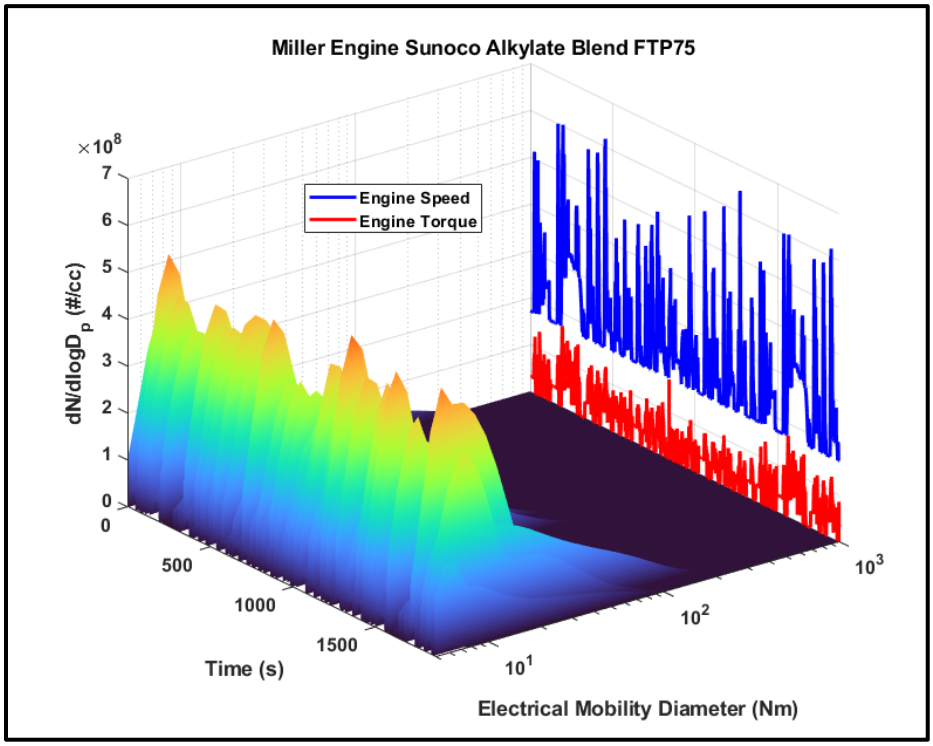

(d)

Figure 5-58: Particle size distribution over the entire FTP 75 test cycle for (a)Baseline pump gas (b)Shell ethanol blend (c)Shell aromatic blend (d)Sunoco alkylate blend.

HWFET:

Since the highway fuel economy test simulates real world cruising conditions, the engine resides at the point of highest thermal efficiency for a large portion of the cycle. As a result, the engine is almost at steady state as can be seen from the traces of engine speed and load next to the particle size distributions (Figure 5-60). The high fuel economy numbers and the low particulate emissions are due to the fact that there is less transient behavior in this test compared to the FTP. In fact, as can be seen from the particle size distributions, particulate emissions are more than an order of magnitude lower in the middle phase of the test. Similar to the results of the FTP test, the Shell aromatic blend led to slightly higher NO_X, THC and CO emissions compared to the other fuels.

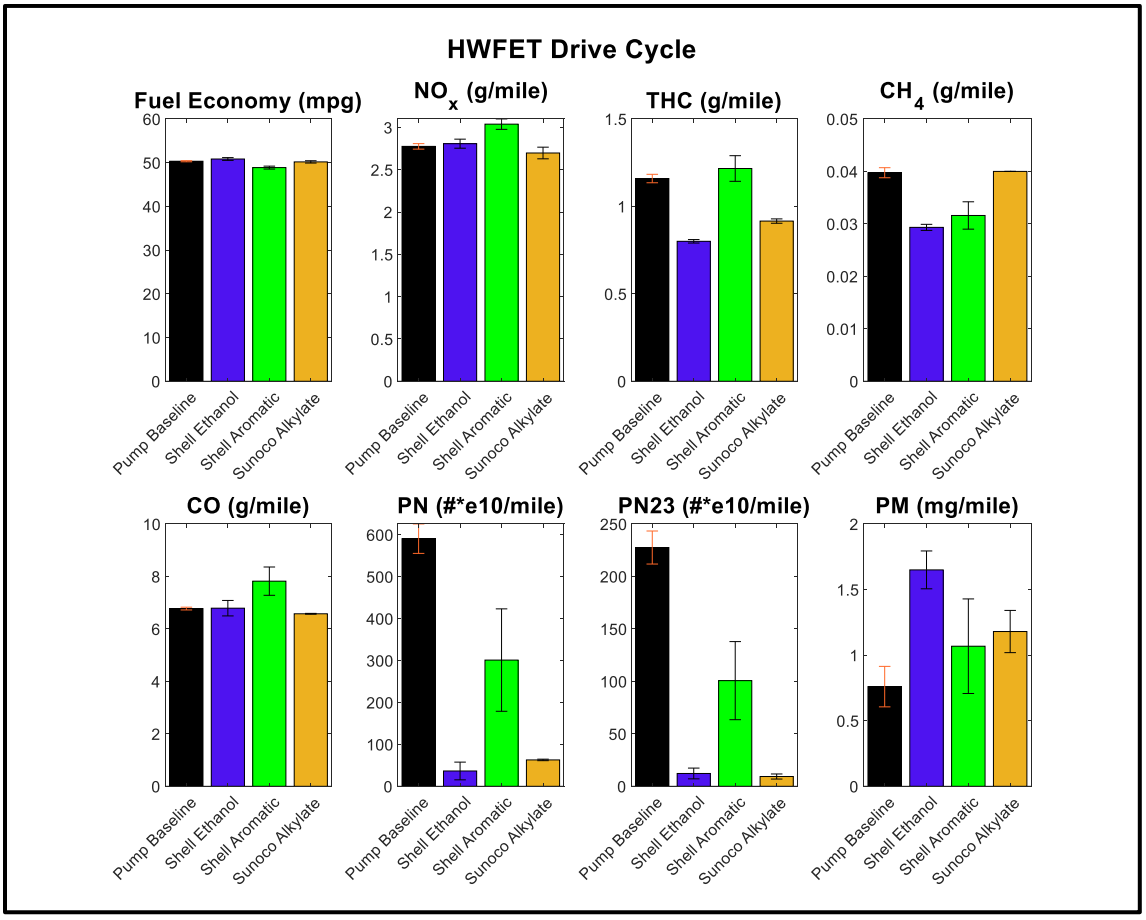

Figure 5-59: Cumulative results comparing fuel performance over HWFET drive cycle.

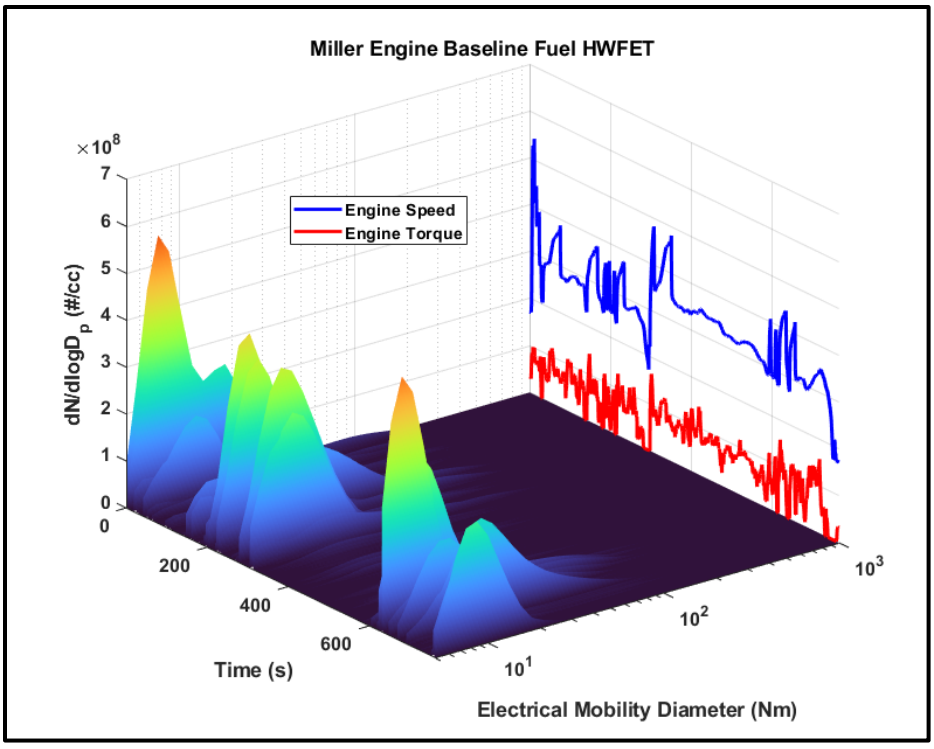
Miller Engine Baseline Fuel HWFET
Engine Speed
Engine Torque
dN/dlogD_p (#/cc)
×10^8
Time (s)
Electrical Mobility Diameter (Nm)

(a)

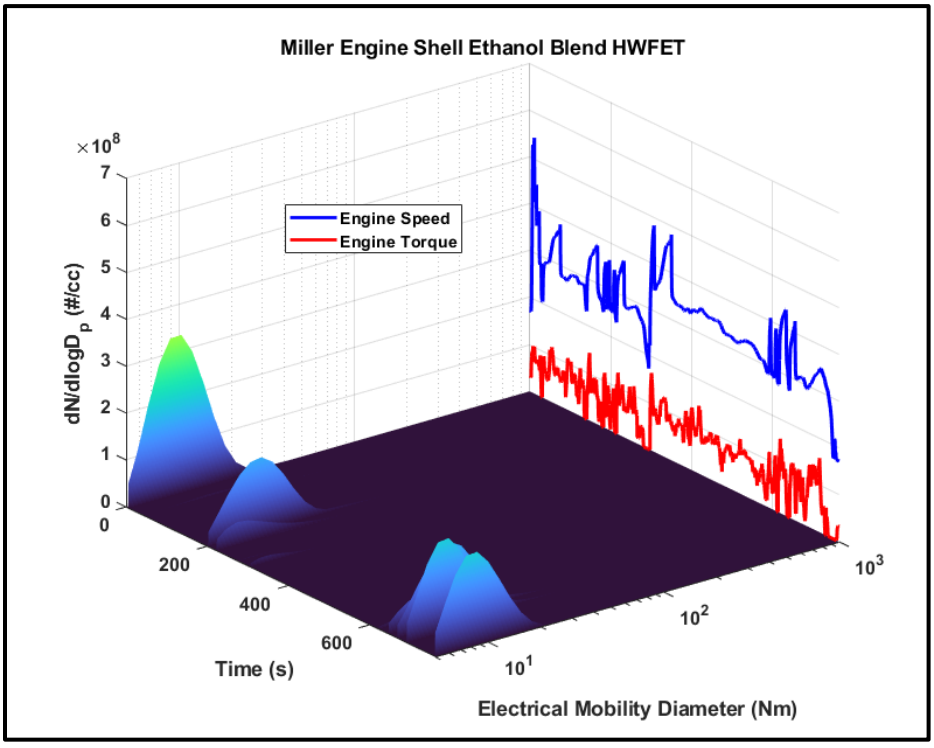
Miller Engine Shell Ethanol Blend HWFET
Engine Speed
Engine Torque
dN/dlogD_p (#/cc)
×10^8
Time (s)
Electrical Mobility Diameter (Nm)

(b)

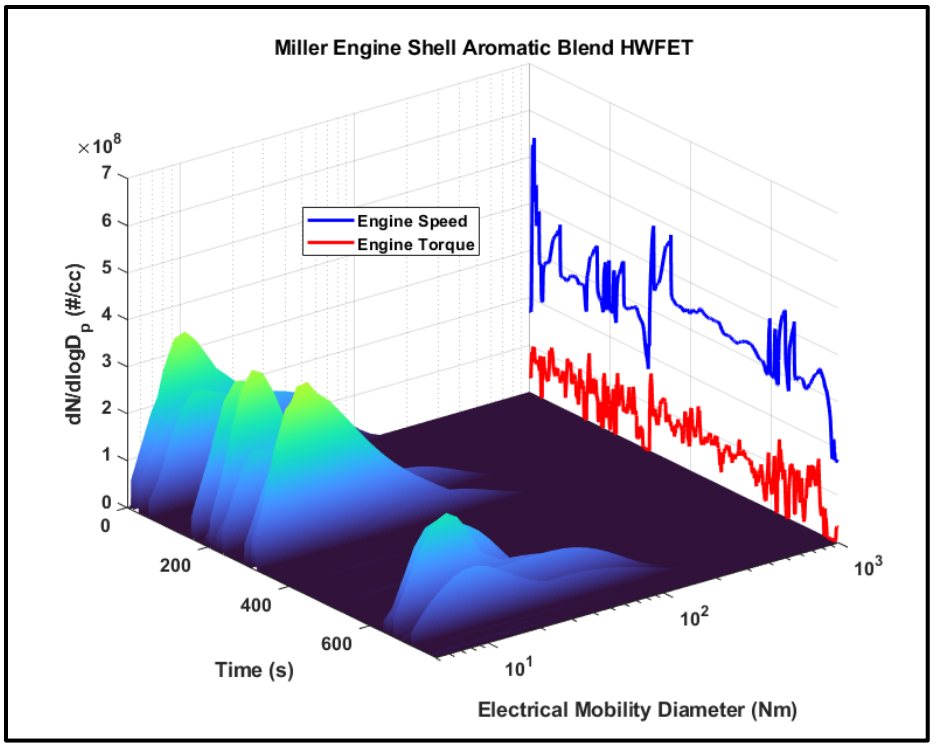

(c)

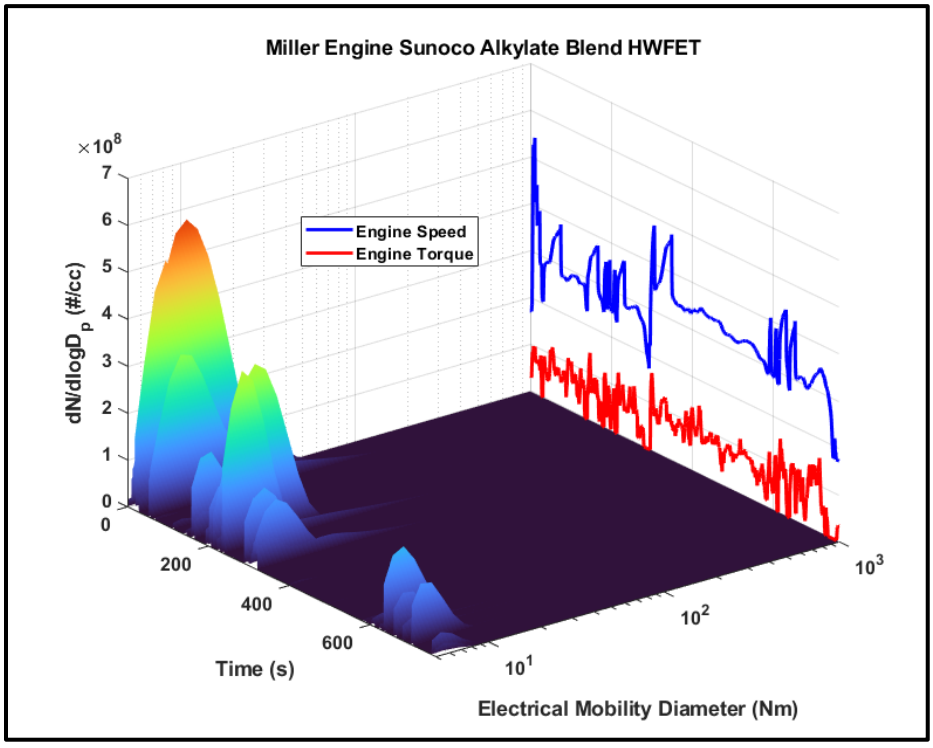

(d)

Figure 5-60: Particle size distribution over the entire HWFET test cycle for (a)Baseline pump gas (b)Shell ethanol blend (c)Shell aromatic blend (d)Sunoco alkylate blend.

US06:

The US06 cycle is the most aggressive of all the cycles that were tested in this Chapter in terms of heavy accelerations and decelerations (Figure 5-62). During this simulated aggressive driving behavior, the engine does venture into knock-limited regions on the engine speed-load map. Having confirmed the existence of the knock-soot correlation in the previous section of this Chapter, we can now attribute the high particulate emissions from this drive cycle to engine spark knock. Both the alkylate blend and the ethanol blend led to high nucleation mode particle concentrations. The aromatic blend led to the highest accumulation mode particle concentration among the fuels tested.

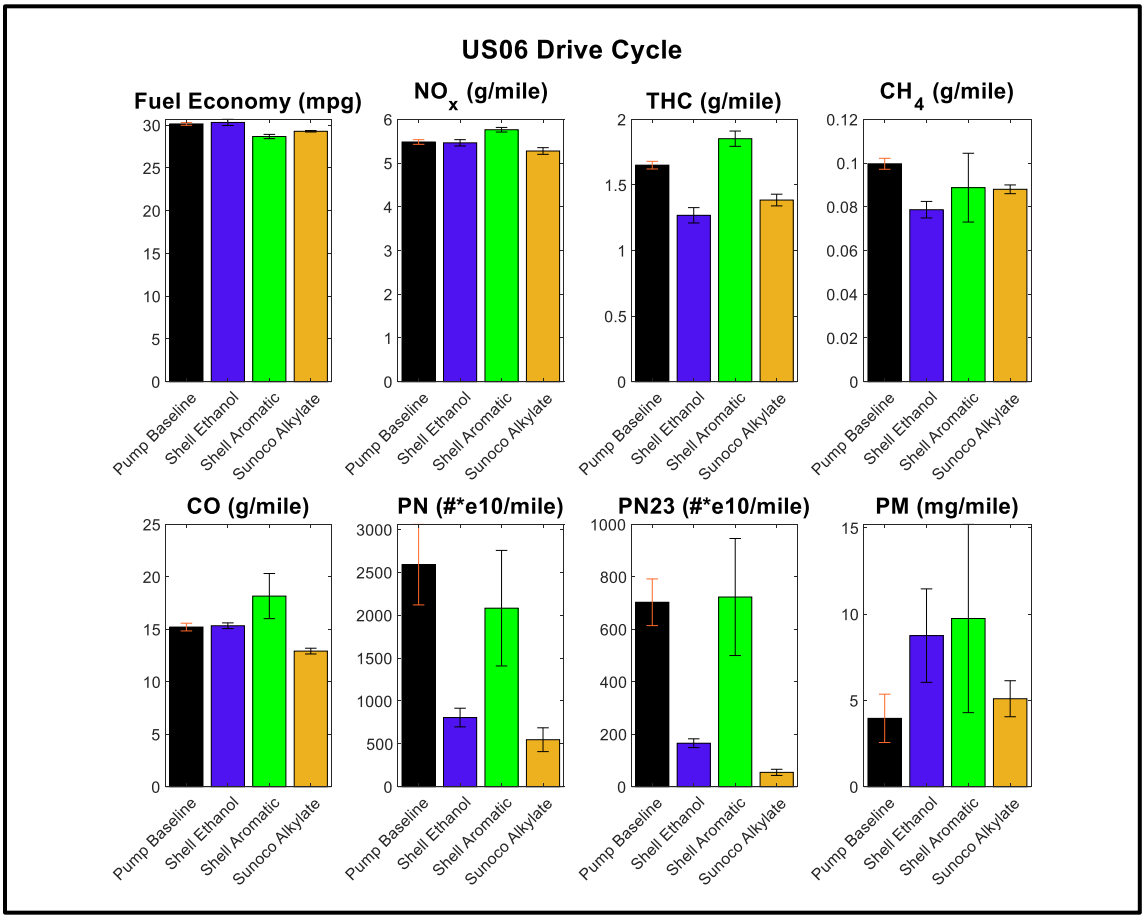

Figure 5-61: Cumulative results comparing fuel performance over US06 drive cycle.

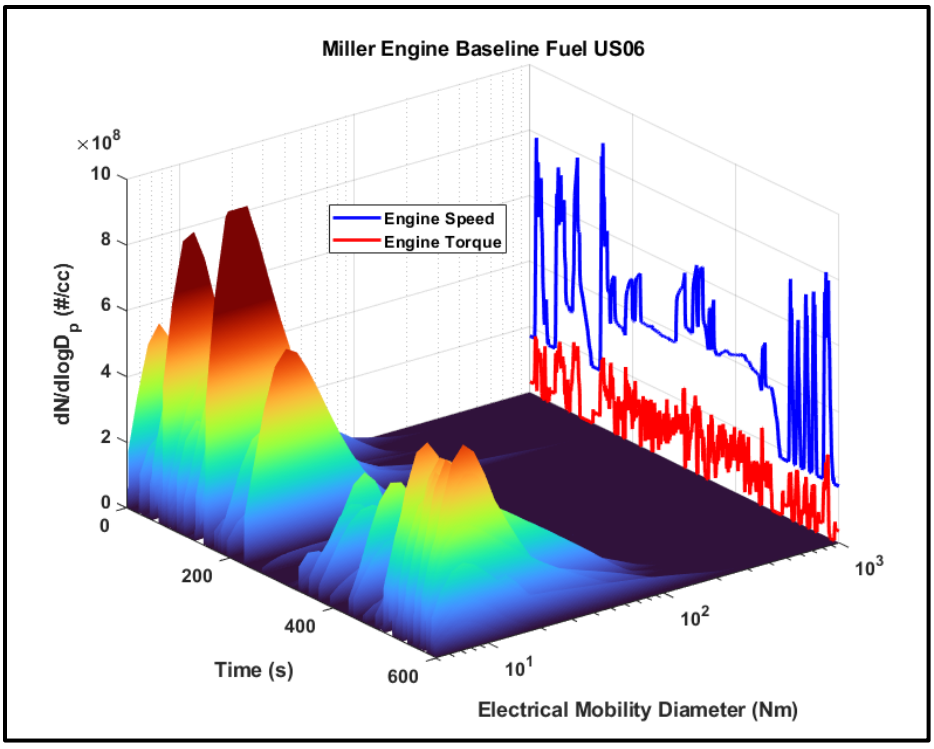
Miller Engine Baseline Fuel US06
×10^8
10
8
6
4
2
0
dN/dlogD_p (#/cc)
Engine Speed
Engine Torque
0
200
400
600
Time (s)
10^1
10^2
10^3
Electrical Mobility Diameter (Nm)

(a)

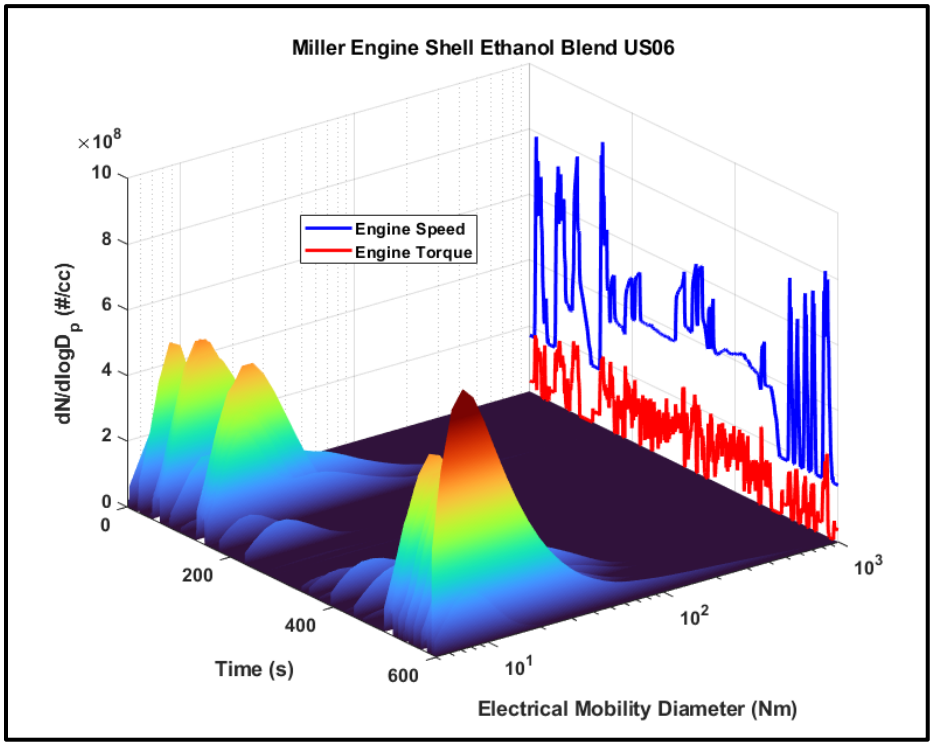
Miller Engine Shell Ethanol Blend US06
×10^8
10
8
6
4
2
0
dN/dlogD_p (#/cc)
Engine Speed
Engine Torque
0
200
400
600
Time (s)
10^1
10^2
10^3
Electrical Mobility Diameter (Nm)

(b)

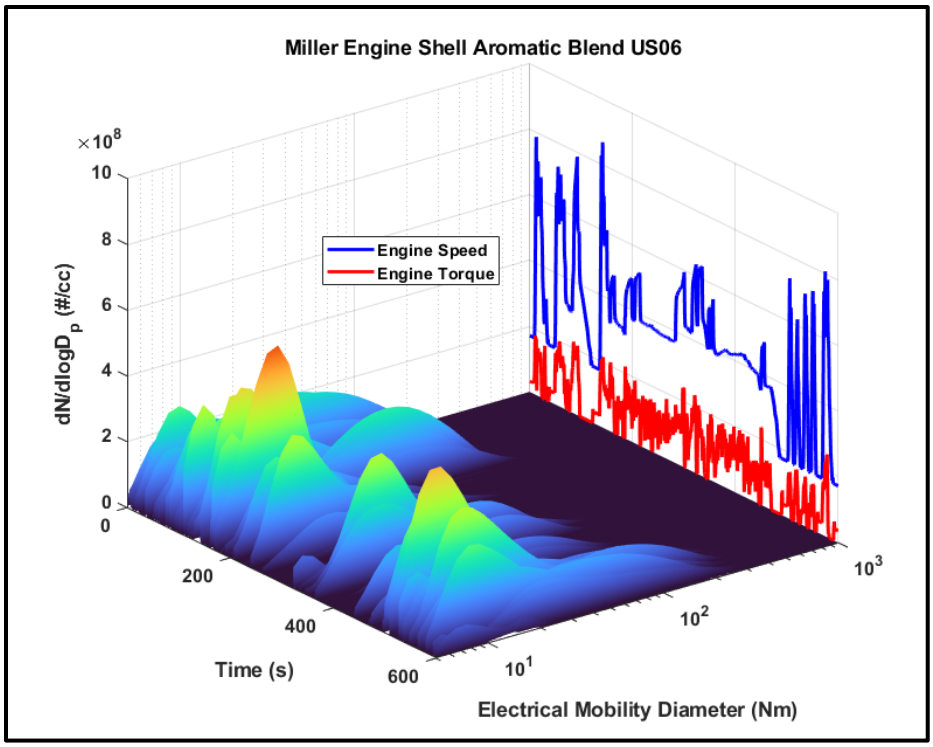

(c)

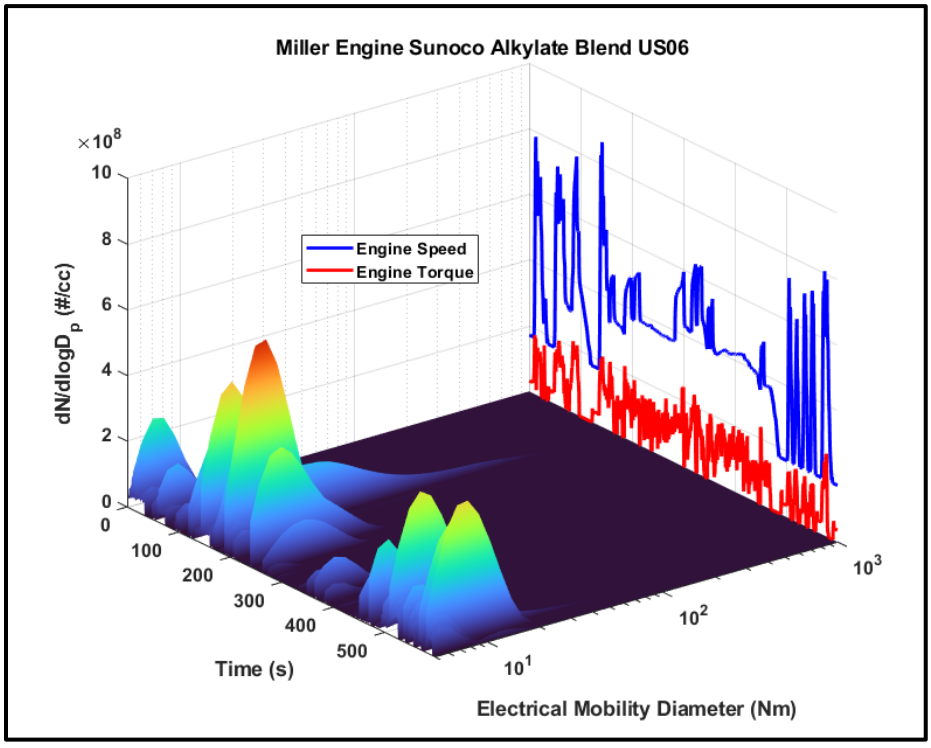

(d)

Figure 5-62: Particle size distribution over the entire US06 test cycle for (a)Baseline pump gas (b)Shell ethanol blend (c)Shell aromatic blend (d)Sunoco alkylate blend.

WLTP:

The WLTP test is a standardized test similar to the FTP but applied to non-North American market vehicles. Thus, the results from this test (Figure 5-63) are similar to those obtained from the FTP testing (Figure 5-57). No significant changes were seen in terms of fuel economy. The aromatic blend led to slightly higher NO_X, THC and CO emissions consistent with the rest of the testing. The particle size distributions (Figure 5-64) confirm that the aromatic blend led to significantly higher concentrations of accumulation mode particles.

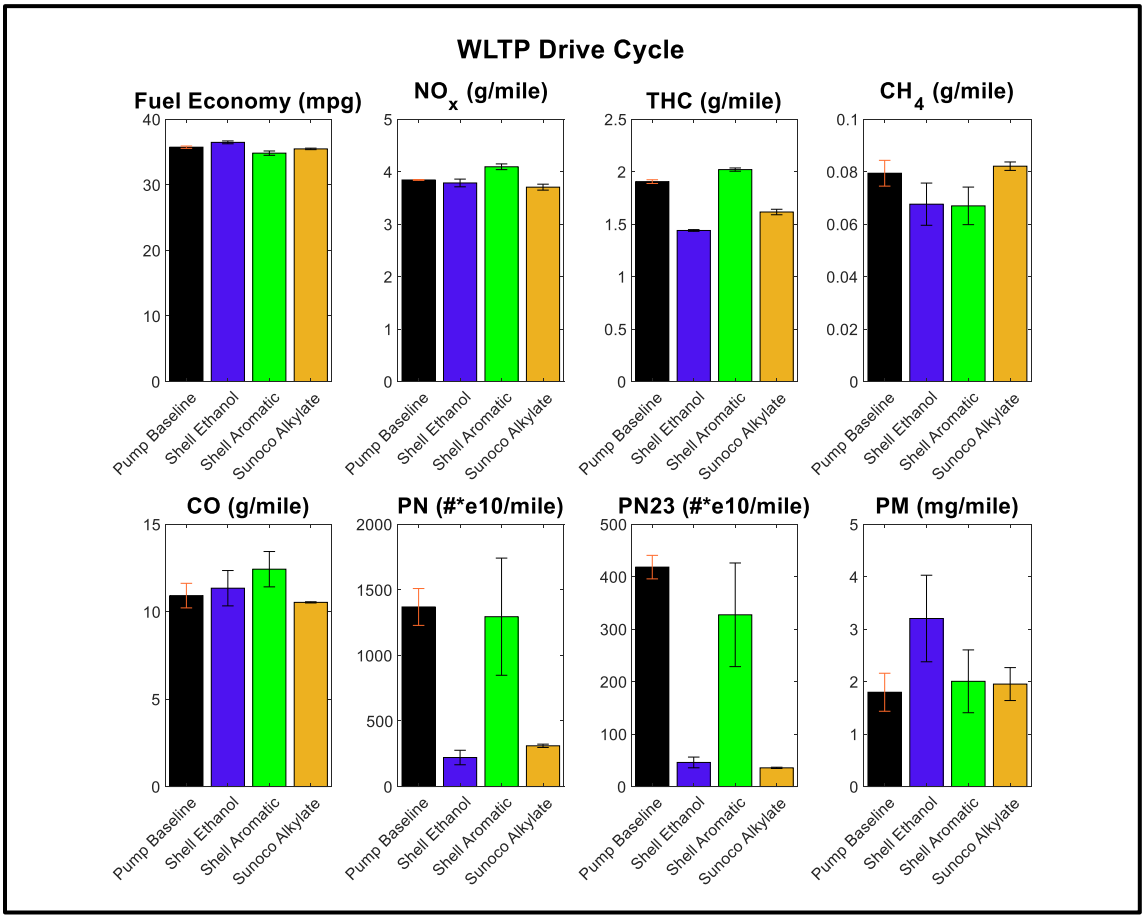

Figure 5-63: Cumulative results comparing fuel performance over WLTP drive cycle.

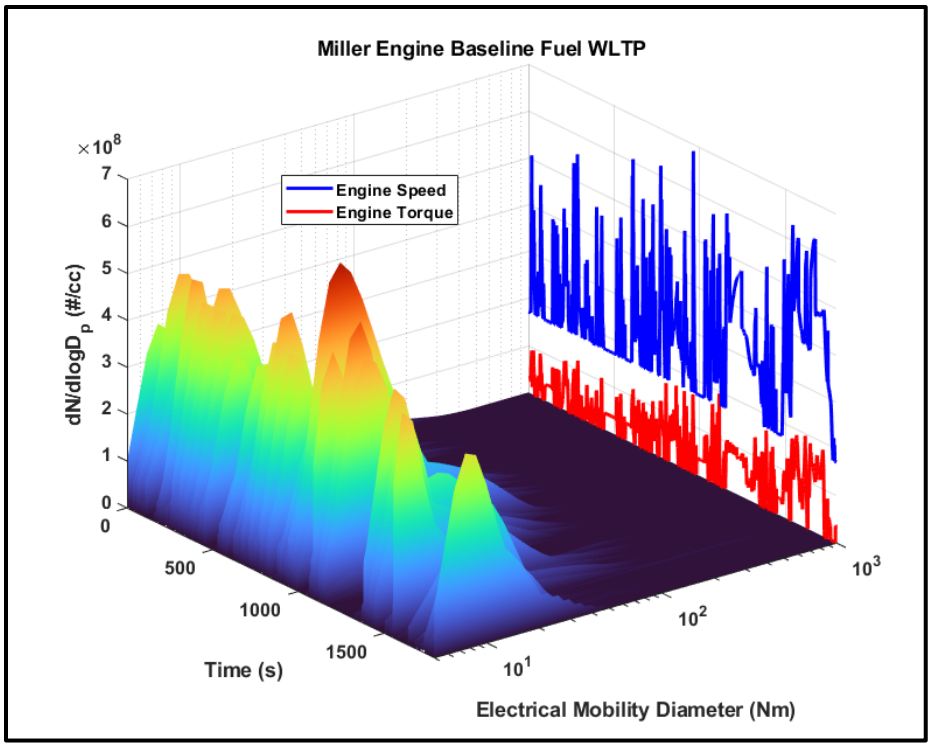
Miller Engine Baseline Fuel WLTP
×10^8
dN/dlogD_p (#/cc)
Engine Speed
Engine Torque
Time (s)
Electrical Mobility Diameter (Nm)

(a)

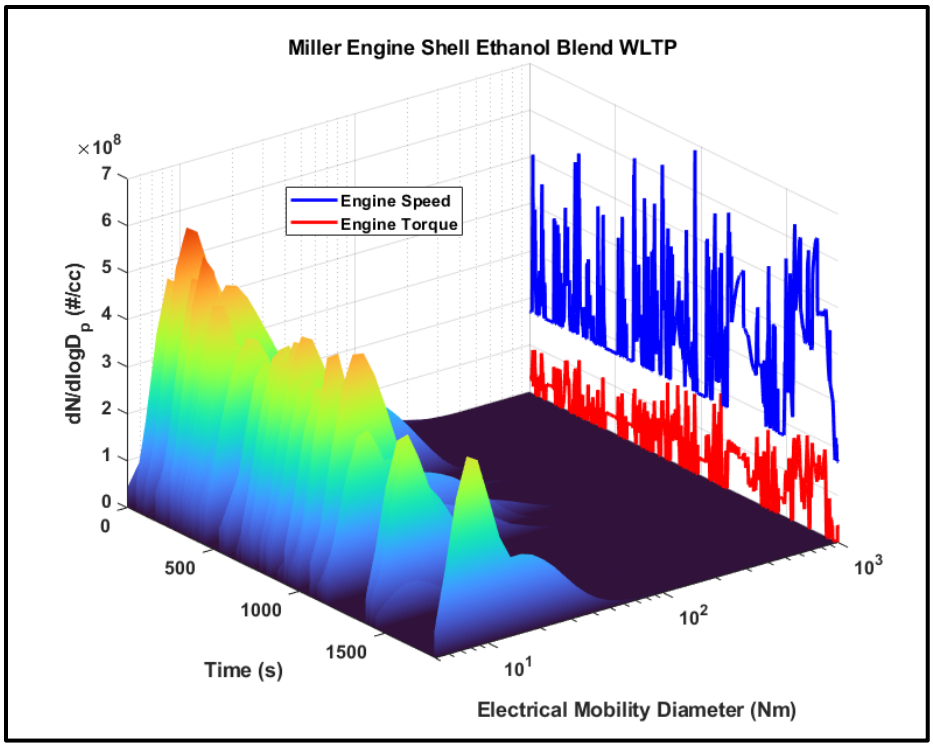
Miller Engine Shell Ethanol Blend WLTP
×10^8
dN/dlogD_p (#/cc)
Engine Speed
Engine Torque
Time (s)
Electrical Mobility Diameter (Nm)

(b)

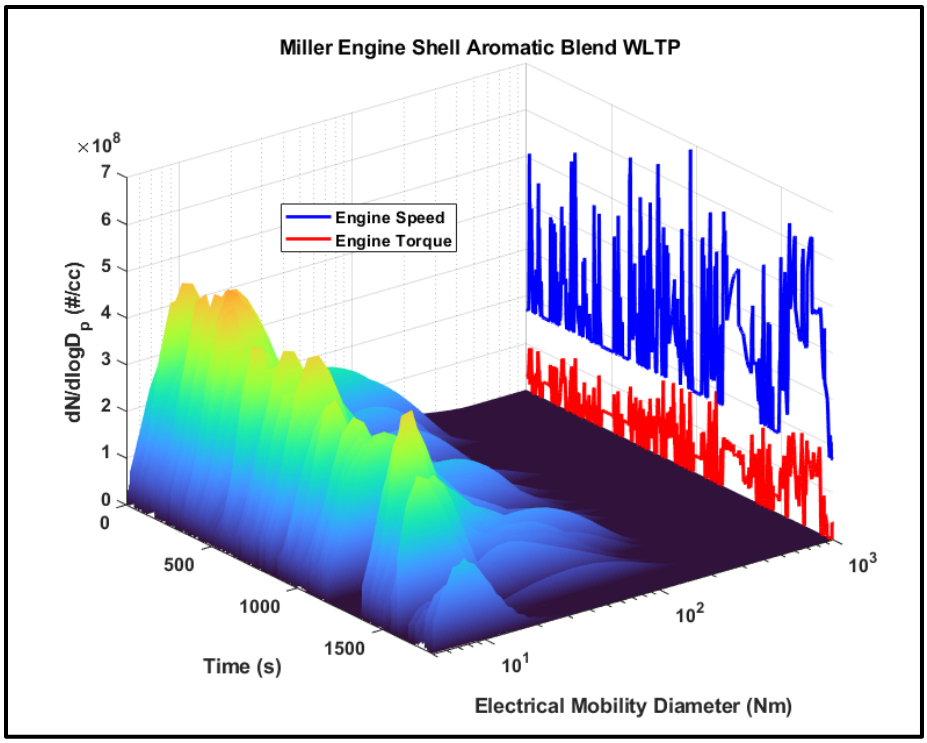

(c)

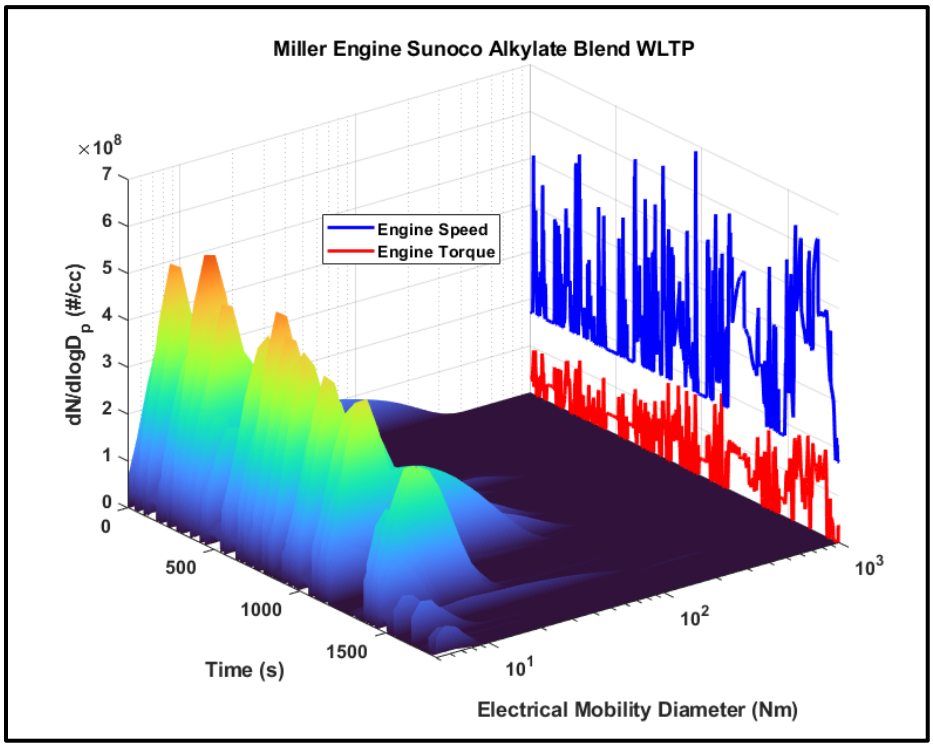

(d)

Figure 5-64: Particle size distribution over the entire WLTP test cycle for (a)Baseline pump gas (b)Shell ethanol blend (c)Shell aromatic blend (d)Sunoco alkylate blend.

5.6 Summary and Conclusions

The knock-soot correlation as first observed on a single cylinder platform by Han [30] is confirmed to exist on a production, current generation, multi-cylinder spark ignited engine. To confirm this phenomenon, knock limited points were studied across three different studies. These studies illustrate the effect of changing hardware, valve timings, injection strategies and fuel compositions on knock limit extensions and thus indirectly the particulate matter emissions. After studying the effect of fuel chemistries on the particulate emissions at knock limited conditions, the alternate gasoline fuels formulated by Shell and Sunoco are tested over standardized drive cycle tests to study the effect on particulate emissions under real-world driving conditions.

The findings of these three studies and the follow up transient testing of the low-octane rated fuels is summarized below:

1. The particulate matter size distribution data across the three different studies confirms a sudden increment in accumulation mode concentration after the onset of knock. This phenomenon exists irrespective of the injection strategy or valve timing used. This phenomenon also exists across all the fuels that were tested. The fuels were selected across a range of octane rating and sensitivities.
2. The knock-soot correlation was seen more prominently at the lower engine speed where the magnitudes of knock intensity were higher. The particle size distributions across all three studies confirmed that as the knock intensity increased with advancing spark timing, so did the concentration of accumulation mode particles. No clear relation was found with respect to nucleation mode particles. It did seem at some points however, that

the nucleation mode concentrations reduced with advancing spark timing especially at the higher engine speed where knock intensities were low.

3. The valve timing study showed that Miller timings led to knock limit advance as well as lower NO_X and CO emissions. However, the unchanged injection strategy from the earlier calibration led to high THC and soot emissions. These observations are consistent with those made by Szybist et al. [40]. The knock-soot correlation was shown to exist for both engine calibrations.
4. The comparison of the injection strategy showed that the high pressure direct injection was desirable at the knock limited conditions due to its benefits of advanced knock limited combustion phasing and lower particulate emissions. While port injectors are usually associated with lower particle emissions than direct injectors, it is shown in this study that the reverse is true at the knock limited points. Due to the high engine loads of these knock-limited points and the low fuel rail pressure of the port injectors, not sufficient time is available for the fuel to mix homogenously with the air resulting in locally fuel rich hotspots and high particulate emissions.
5. The fuel study showed that while the octane rating and sensitivities were directly responsible for the propensity to knock, they were also indirectly responsible for the particulate emissions. When run on the either of the high octane fuels, the engine emitted less particulate emissions despite the fact that the fuel was either heavily doped with ethanol or aromatics.
6. At similar octane ratings, the aromatic blends led to higher particulate emissions than the ethanol blends. On the other hand, the ethanol blends led to higher fuel consumption and

carbon-di-oxide emissions due to the lower chemical energy of the fuel resulting in greater mass of fuel being injected per cycle.

7. The follow up study involving operating the engine on the low-octane rated fuels over standardized test cycles showed that the aromatic blend led to relatively higher concentration of accumulation mode particles and relatively lower nucleation mode particles. The ethanol blend and the alkylate on the other hand led to relatively higher nucleation mode particles.

This is the first report of the knock-soot correlation in a multi-cylinder production GDI engine. It follows up the novel observation made by Han on the single cylinder platform [30] and acknowledges its existence on the multi-cylinder platform across multiple valve timing and injection strategies. This is also the first report of the existence of the knock-soot correlation across fuels of varying octane ratings. The study is novel as it isolates the impact of fuel chemistry on the knock-soot correlation since fuels of similar octane rating and sensitivities were formulated by two different refinery-relevant streams, namely ethanol and aromatics.

Part 2: Gasoline Compression Ignition Combustion

Chapter 6 discusses the research that was conducted on a gasoline compression ignition engine platform at Aramco Americas, Detroit Research Center.

Chapter 6
Impact of On-demand Reactivity Enhancement on the Combustion Stability of a Light-duty Gasoline Compression Ignition Engine

6.1 Introduction

6.1.1 Cold Start in GCI Engines

One of the major challenges with GCI using market gasoline identified in previous work is achieving stable combustion at idle, low-load, and cold-start operating conditions [159]. Idle conditions are usually associated with low intake air pressures and temperatures both of which hinder auto-ignition of gasoline. This affects the stability of the combustion process and can lead to low combustion efficiency and misfires, and can result in high carbon monoxide (CO) and hydrocarbon (HC) emissions. HC and CO emissions occurring at cold start before the hydrocarbon oxidation catalyst has lit-off are especially problematic [159,160].

Higher intake temperature and pressure may be used to achieve stable GCI combustion low-load and cold start conditions. One approach is to use a turbocharger to boost the intake temperature and pressure to stabilize combustion [161]. However, this approach may require an impractically large compressor on the turbocharger due to the low exhaust enthalpy. Another approach is to use a supercharger or electrical intake air heater to promote combustion. However, these concepts lead to parasitic losses while increasing cost and complexity and may

also lead to higher NO_X emissions due to higher combustion temperature and pressure. Some researchers have explored different injection strategies such as heavy fuel stratification but with limited success [61,75,83]. Zhao et al. explored the use of a spark plug to promote auto ignition at low loads and cold temperatures in a heavy duty compression ignition engine [160]. An alternate approach is to recycle hot exhaust residuals, for example by employing exhaust rebreathing using modified cams to control valve timings [76]. Although exhaust gas rebreathe can increase the start of compression temperature and help stabilize combustion, it may not be useful for starting the engine and avoiding initial misfire events. Additionally, none of these approaches can address the effects of cold coolant, lubricant oil, and metal temperature present at cold start conditions.

6.1.2 Fuel Strategies for GCI Engines

In addition to advanced hardware, optimal fuels and combinations of fuels have been proposed to improve GCI combustion under challenging conditions.

One approach is to select a fuel which has lower reactivity than diesel, but higher reactivity than gasoline, as the optimal fuel for GCI engines. A medium-reactivity fuel can preserve the emissions benefits of longer ignition delay, while enhancing cold start and low-load combustibility relative to diesel fuel [80,162–169]. One challenge with this approach is the feasibility of sourcing fuels which are not already widely available in the marketplace—which might only be feasible for large fuel consumers with dedicated refueling equipment.

Another approach is to blend market gasoline and diesel fuel to produce the optimal reactivity [163,170,171]. Roberts et al. [172] explored the effects of pre-blending gasoline with different portions of diesel fuel specifically for low load GCI, and found that adding diesel to

gasoline significantly reduced the minimum intake pressure requirement but increased the engine out NO_X. This combustion concept of using two separate fuels on demand to control the overall reactivity of the fuel air mixture is termed as reactivity controlled compression ignition (RCCI) within the research community [173,174]. Using dual fuel combustion with gasoline and diesel has demonstrated benefits of using the low reactivity gasoline for medium to high loads while switching to higher reactivity fuels at low loads for better stability and controlled combustion phasing [91,175]. RCCI as a combustion strategy has also been explored with fuels other than conventional gasoline and diesel [176–178]. Roberts et al. [91] utilized a prototype fuel injector which seeds high reactivity fuel into the main fuel stream for on demand reactivity enhancement during simulated drive cycle experiments. Diesel fuel was used as the high reactivity fuel and blends of 10-20% allowed stable low load operation enabling high efficiency and low emissions over the entire engine speed load map. However, any practical application of this concept would require two separate fuel systems with fuel from two different fuel stocks. Depending on the blend, this approach may also result in a fuel with vapor pressure characteristics that could make it more ignitable that gasoline or diesel alone [163].

Lastly, previous work has explored the feasibility of adding compounds to gasoline to increase its cetane number. 2-ethyl-hexyl nitrate (2-EHN) and di-tert-butyl-peroxide (DTBP) are two additive compounds that are well known cetane enhancers of diesel fuel [179]. Previous research has shown that adding small quantities of these additives have a significant effect on reducing ignition delay of diesel fuel [180]. This property led researchers to explore their applicability in GCI by blending them with gasoline fuel.

Tanaka et al. [69] found that an addition of 2% DTBP by volume had a greater effect in decreasing the ignition delay of gasoline-like fuels for HCCI applications compared to adding

2% EHN. DTBP achieves this by decomposing into alkoxy radicals $(CH_3)_3CO$ at low temperatures which have high reactivities and go on to create fuel radicals which accelerates the ignition process [181]. The possibility of increasing engine-out NO_X emissions due to the introduction of nitrogen from the fuel additive has led to DTBP being preferred to 2-EHN. Eng et al. [182] showed that adding small quantities of DTBP (< 3% by volume) to gasoline resulted in a significant reduction in ignition delay, improved efficiency and better stability under low-load HCCI operation. Splitter et al. [183] conducted RCCI engine experiments using port fuel injected gasoline and direct injected DTBP blended gasoline which yielded similar emissions levels to gasoline-diesel dual fuel RCCI operation. The DTBP blended gasoline showed a small efficiency benefit due to reduced NTC (Negative Temperature Coefficient) behavior compared with the diesel-gasoline blend, demonstrating the potential of this fuel as a single, medium reactivity fuel for GCI engines.

6.1.3 On-board Fuel Reactivity Enhancement

Production of organic hydroperoxides in-situ has been explored as a possible solution for increasing the cetane content of gasoline. This concept avoids the effort of producing, distributing, and mixing a pure additive product with gasoline, while retaining the core function – enhancement of the fuel reactivity, providing an optimal medium reactivity fuel for GCI engines, while still refueling with market gasoline.

Al-Taher et al. [184] has conducted experiments oxidizing different hydrocarbons that are present in gasoline fuels to hydroperoxides using *n*-hydroxyphthalimide (NHPI) catalysts. They observed that Toluene and aromatic compounds had the most significant potential of generating high concentration of hydroperoxides compared to the other compounds. Following the tests on

toluene, similar tests were conducted using gasoline and similar trends were observed. As a result, this technology was proposed as a method to enhance the reactivity of gasoline fuels using the hydroperoxide compounds generated.

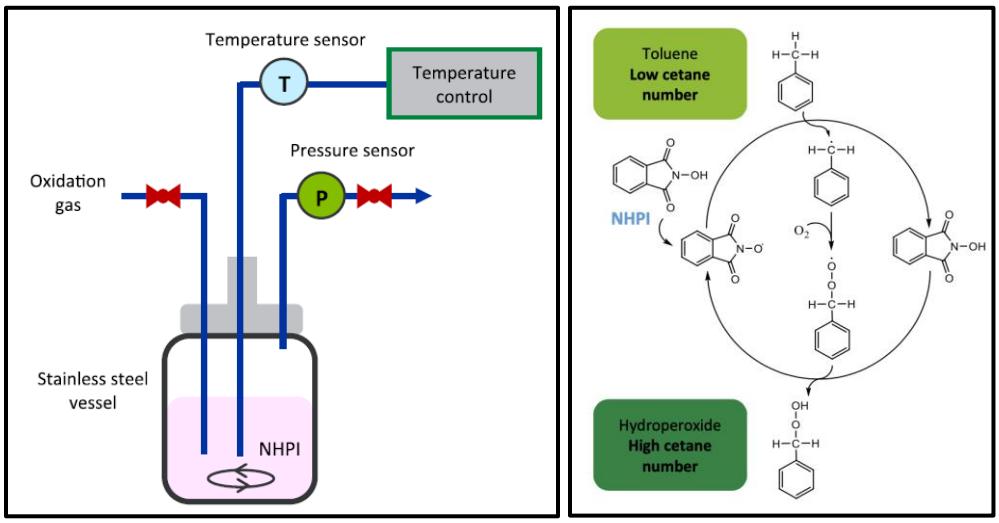

Figure 6-1: Figure of the organic batch reactor and proposed reaction mechanism from [184].

This is similar to the observations made by Hashimoto et al. [185] who found that the auto-oxidation of diesel fuels led to the production of hydroperoxide compounds and effectively enhanced the cetane rating of the fuel.

Al-Taher et al. [184] observed that a concentration of 50-250 mmol/L of hydroperoxides needed to be generated for achieving a target derived cetane number of 25-40. Moreover, a reaction time of the order of 3 hours was needed for maximum hydroperoxide formation. The time coupled with the limited volume available for a hypothetical reactor placed in a vehicle suggests that there is a need for minimizing the consumption of hydroperoxide blended high cetane gasoline. For the rest of this chapter, this fuel will be referred to as cetane enhanced gasoline (CEG). CEG consumption can be minimized if its consumption is limited to engine speed load points where its use is most beneficial compared to regular pump gasoline. One such

engine speed-load point is engine idle especially during cold starts. As mentioned earlier, gasoline compression ignition struggles with combustion stability at low loads and cold starts. To get stable combustion at low engine loads and cold temperatures, one would have to use very high levels of manifold boost pressure to promote the forward reaction for auto-ignition. This point of interest is one engine speed-load point where using CEG is beneficial.

The current study investigated the potential of peroxide compounds on enhancing the reactivity and increase stability of GCI operation at low load at different ambient conditions with a focus on cold conditions. In particular, di-tert butyl peroxide was chosen as an initial candidate before further testing involving hydroperoxide compounds which resembled the compounds generated from the batch reactor more closely than DTBP. The hydroperoxides tested were cumene hydroperoxide and tert-butyl hydroperoxide.

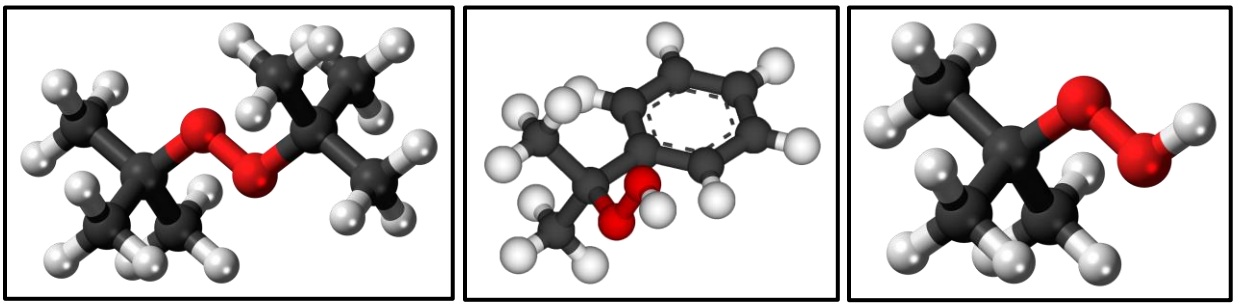

(a) (b) (c)

Figure 6-2: Chemical structures of the three peroxide compounds that were tested: (a) Di-tert-butyl peroxide (DTBP) (b) Cumene hydroperoxide (CHP) (c) Tert-butyl hydroperoxide (TBHP).

6.2 Experimental Methods

6.2.1 Fuels Investigated

Baseline data was generated using 87 rated AKI pump gasoline that was injected using the stock DI injectors. The gasoline was supplied by Haltermann Solutions. Infinium R655

lubricity additive was added in the ratio of 200mg/kg of gasoline to protect the stock high pressure fuel common rail and direct injectors.

Initial comparisons for single fuel testing were done using gasoline blended with DTBP as the higher reactivity fuel. For the single fuel testing, a 2% by weight blend of DTBP with gasoline was used as CEG which was selected due to sufficient increment in cetane rating of the fuel and the fact that further addition of DTBP lead to plateauing of cetane rating enhancement.

Later experiments that were conducted after the installation of the prototype dual fuel injector used gasoline blended with hydroperoxide compounds as the higher reactivity fuel. As mentioned earlier, the hydroperoxide compounds that were studied in particular were cumene hydroperoxide and di-tert-butyl peroxide. In order to make a like to like comparison of the blended fuels, all three CEG blends were maintained at the same mmol of additive/ kilogram of fuel. A comparison of the derived cetane number measurements of the three higher reactivity fuels with the baseline gasoline can be seen in the Figure 6-3 below.

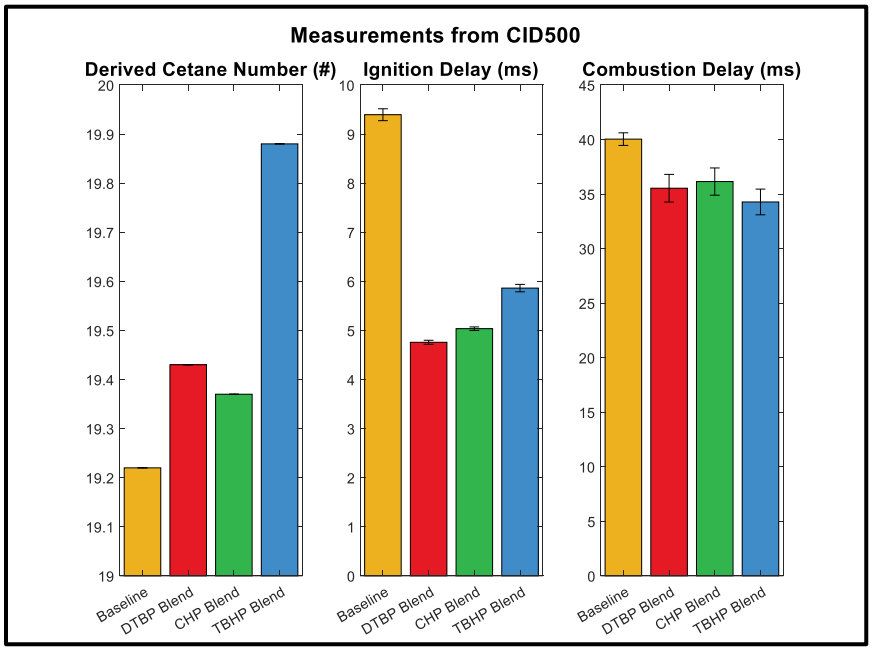

Figure 6-3: Comparison of derived cetane number, ignition delay and combustion delay of CEG vs Gasoline.

The CID 500 manufactured by Petroleum Analyzer Co (PAC) LP measures the derived cetane number (DCN), ignition delay (ID) and combustion delay (CD) of the fuels according to ASTM D7668. According to ASTM D7668, ignition delay is defined as the time in milliseconds between the start of fuel injection and start of combustion (usually the start of low temperature heat release). The same standard defines the combustion delay as the time in milliseconds between the start of fuel injection and the mid-point of the combustion pressure curve. As can be seen from Figure 6-3, all three peroxide compounds have an effect of reducing the ignition delay and combustion delay to certain degrees. A slight increase in derived cetane number is also observed.

All the tests were run at a constant engine speed of 1500 rpm and a constant load of 2 bar gIMEP which represents a popular low load idling point for engines of this size. All experiments were conducted without any external EGR since the low engine load meant that pressure rise rates were not too high. Exhaust rebreathe strategy which involved reopening the exhaust valve during the intake stroke to suck in hot exhaust gases in the combustion chamber was used to help reduce intake pressure requirement for auto ignition.

6.2.2 Preliminary study to determine injection strategy

Initially, single fuel testing was conducted comparing baseline gasoline and 2% DTBP blended CEG. However, before comparisons could be made, it was important to understand which injection strategy to use for each of the fuels. This study illustrated the difference in performance and emission characteristics of GCI combustion based on the injection strategy that is employed with each of the fuels. The injection splits studied were limited to 2 injections with a 50:50 mass split ratio due to the pulse width limitations of the baseline stock injector.

Dempsey et al. [75] has classified different LTC injection strategies based on the level of stratification. Using the same nomenclature of classifying the different strategies, injection timing sweeps were conducted for heavy fuel stratification (HFS), moderate fuel stratification (MFS) and partial fuel stratification (PFS).

These studies were conducted at a baseline operating point where the controlled parameters were as listed in Table 6-1. The intake air temperature was fixed at 80ºC which was representative of a compressor outlet temperature that would help maintain stable GCI operation for single fuel gasoline testing at low loads. The intake pressure was fixed at 1.25 bar absolute. This was reduced to 1 bar which was representative of ambient naturally aspirated pressure for the single fuel testing with the 2% DTBP blend. Low fuel rail pressure was chosen for baseline gasoline fuel since an initial rail pressure sweep at the same conditions demonstrated higher thermal efficiency at the lower rail pressures and the creation of gasoline rich hotspots for auto ignition was helpful for auto-igniting gasoline in cold conditions. On the other hand, a high rail pressure and later timing was chosen for the cetane enhanced gasoline due to its shorter ignition delay and hence enhance mixing before auto ignition.

Fuel	87 AKI Gas	2% DTBP CEG
Engine Speed	1500 rpm	1500 rpm
gIMEP	2 bar	2 bar
Rail Pressure	80 bar	400 bar
Intake Air Temperature	80ºC	80ºC
Coolant Temperature	90ºC	90ºC
Oil Temperature	90ºC	90ºC
Intake Air Pressure	1.25 bar	1 bar
SOI1: SOI2 Mass fraction	50:50	50:50

Exhaust Gas Rebreathe	ON	ON
Backpressure dP	Intake Pressure + 10 kPa	Intake Pressure +10 kPa

Table 6-1: Control parameters for injection strategy experiments.

SOI1 (daTDC)	-270 to -150	-90 to -40	-35 to -20
Injection Strategy	Partial Fuel Stratification (PFS)	Moderate Fuel Stratification (MFS)	Heavy Fuel Stratification (HFS)

Table 6-2: Injection strategies explored with both fuels.

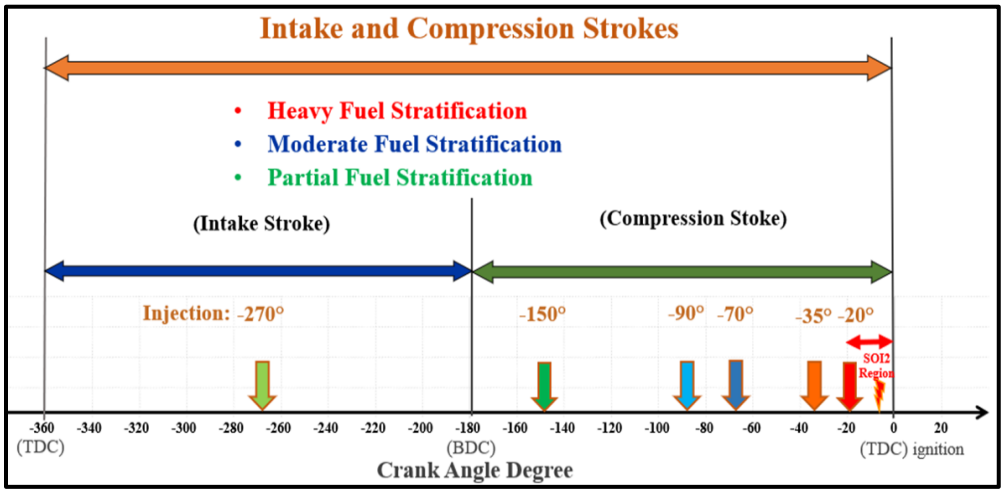

(a)

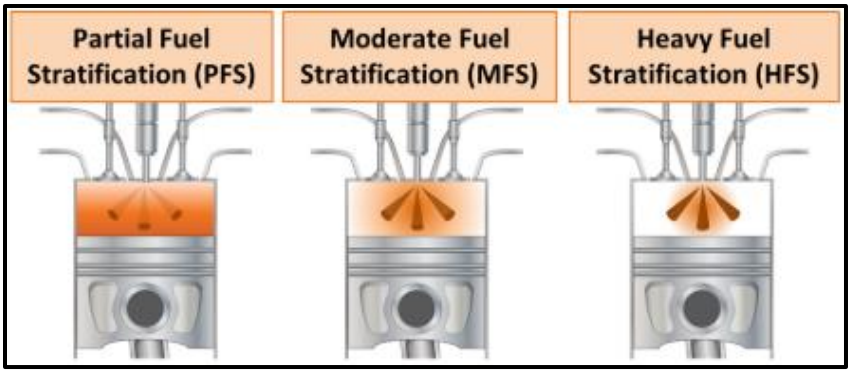

(b)

Figure 6-4: Illustration of the three different injection strategies explored.

(a) The fuel injection timings explored and the respective strategies indicated by the color; (b) sketches depicting the injection strategies [61].

6.2.3 Single fuel testing

Intake pressure sweeps were conducted over a 3x3 design of experiment (DOE) matrix of intake air and coolant temperatures representative of a variety of different engine conditions (Table 6-3). The cold intake temperatures and coolant temperatures are representative of cold start conditions and thus are of most interest in this study. Moderate and high intake temperatures are representative of conditions that could be achieved with the assistance of external heating devices such as intake air heaters. One thing to note would be that any such devices would add to parasitic losses of the vehicle.

Intake Air Temperature / **Coolant Temperature**	30ºC	80ºC	130ºC
90ºC	I30/C90	I80/C90	I130/C90
60ºC	I30/C60	I80/C60	I130/C60
30ºC	I30/C30	I80/C30	I130/C30

Table 6-3: Intake air temperatures and coolant temperatures.

Intake air pressure is a promoter of gasoline auto ignition and hence stable operation. The minimum intake pressure to achieve 7.5% COV (gIMEP) [S.Dev(gIMEP)=15kPa] was considered the minimum intake pressure requirement for stable GCI operation at low load. This minimum intake pressure requirement was used as the metric for low load combustion stability in this chapter. The lower the pressure requirement, the higher the combustion stability. The results from these experiments illustrated the effect of reactivity enhancement on the feasibility of low load GCI operation at different intake air and coolant temperatures. Injection timing and

duration were adjusted to maintain constant load of 2 bar gIMEP and combustion phasing CA50 = 8 (baseline CA50 for efficient GCI operation).

6.2.4 Dual Fuel testing with QuantLogic Adaptive Dual Fuel Injector

To begin the dual fuel testing with the prototype QuantLogic injector, significant time and effort was put in getting the test cell ready to accommodate the new injection system. This involved the installation of a new fuel balance and conditioner as well as a new high-pressure fuel pump to supply the second fuel. Moreover, since the geometry of the injector was different to that of the stock injector, the engine head had to be machined to accommodate the new injector. Lastly, a completely new set of controls software had to be setup so that the experiments could be conducted in a controlled manner.

Dual fuel testing with the QuantLogic injector focused on the minimum fraction of high reactivity fuel required to run stable GCI operation at atmospheric pressure. If atmospheric pressure operation could not be achieved at certain conditions, then intake pressure sweeps were conducted similar to the single fuel testing to find the minimum pressure requirement. The prototype injector was equipped with two fuel supplies but with one set of injector holes. The reactivity of the fuel entering the combustion chamber was controlled using injection events. The timing and duration of the injection event and the fuel rail pressure was used to control the amount of either fuel entering the mixing chamber before it was injected in the combustion chamber. An illustration of the mechanism of the prototype injector is shown in Figure 6-6. As seen in this diagram, the injector did not allow independent injection of CEG and gasoline into the cylinder. If CEG needed to be injected into the cylinder, it had to be diluted with gasoline

fuel since the gasoline side injector needle was the one that controlled the fuel entering the cylinder.

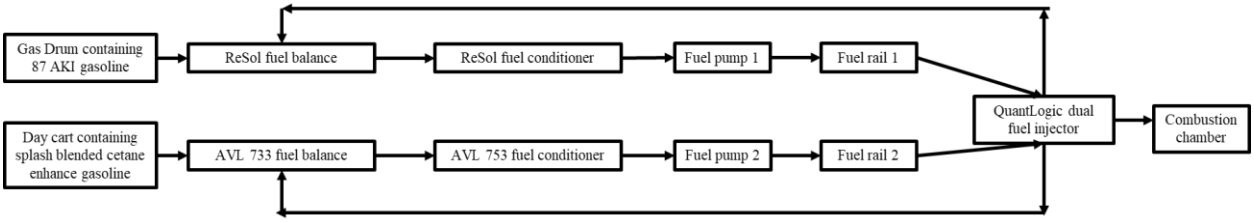

Figure 6-5: Test cell layout for fuel flow to the dual fuel injector.

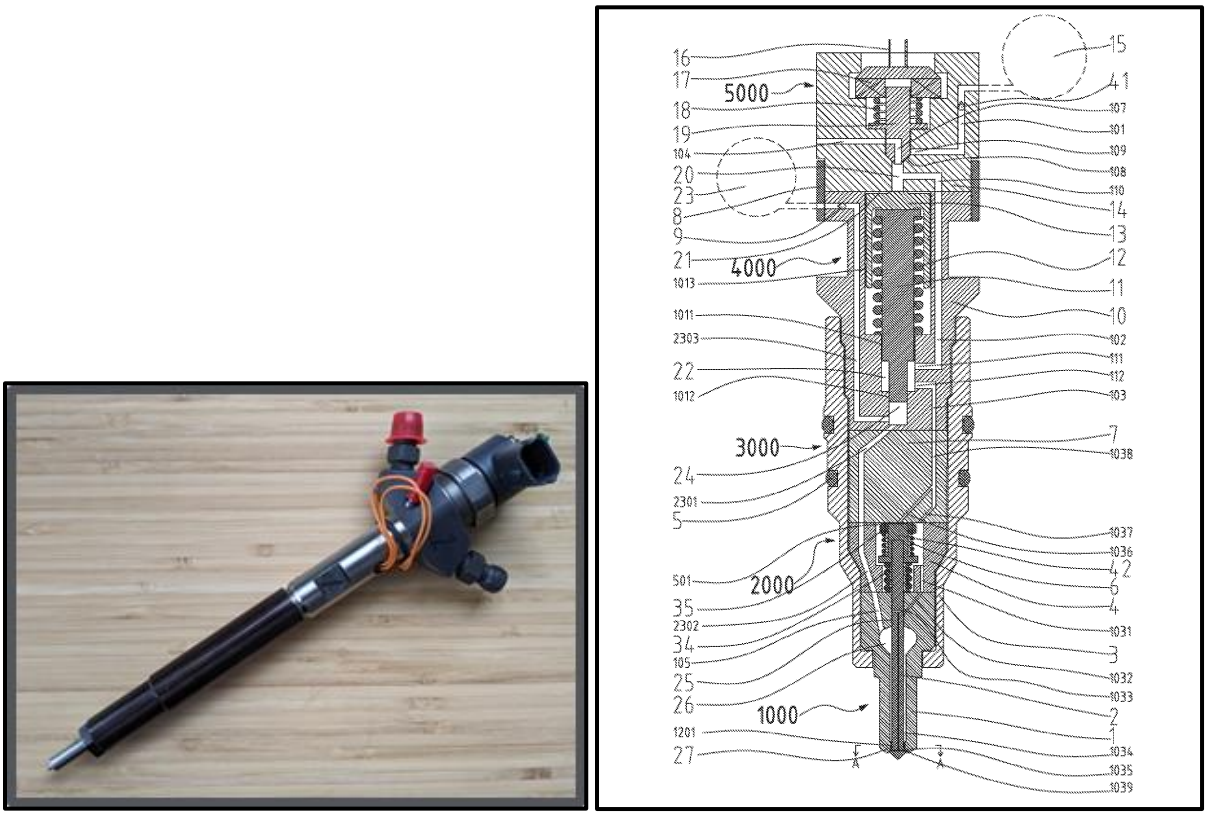

(a) (b)

Figure 6-6: (a)Protoype QuantLogic dual fuel injector and (b) its internal mechanism [186].

The engine control parameters were the same for single fuel and dual fuel testing with the exception of fuel rail pressure. This was due to certain limitations in fuel pump hardware with the dual fuel setup. These parameters are summarized in the table 6-4 below.

Control Parameters	87 AKI Gas	2% DTBP CEG	Dual Fuel Gas+CEG
Engine Speed	1500 rpm	1500 rpm	1500 rpm
gIMEP	2 bar	2 bar	2 bar
Fuel Rail Pressure	80 bar	400 bar	200 bar
Intake Air Temperature	30°C/80°C/130°C	30°C/80°C/130°C	30°C/80°C/130°C
Coolant Temperature	30°C/60°C/90°C	30°C/60°C/90°C	30°C/60°C/90°C
Oil Temperature	70°C/90°C	70°C/90°C	70°C/90°C
Intake Air Pressure	Varied	Varied	Varied
Exhaust Gas Rebreathe	ON	ON	ON
Backpressure dP	Intake + 10 kPa	Intake + 10 kPa	Intake + 10 kPa
SOI1:SOI2 Split	50:50	50:50	Varied
CA50	8 daTDC	8 daTDC	8 daTDC

Table 6-4: Control parameters for minimum intake manifold pressure experiments.

For the dual fuel experiments, CEG was used only with the second injection. The split in 1st and 2nd injection events was used to control the reactivity of the fuel entering the combustion chamber.

6.3 Results and Discussion

The results of the experiments are discussed over multiple subsections. The first subsection discusses the effect of varying levels of stratification on the performance and emission characteristics of GCI combustion at low load. This helps us narrow down our preferred injection strategy for the bulk of our experiments. After choosing our preferred injection strategy, the

following subsections discuss the effect of on demand reactivity enhancement on the robustness of low load GCI combustion.

6.3.1 Preliminary study to determine injection strategy

The results of this study are summarized in the bar chart below. Note that the acronyms stand as follows: HFS (Heavy Fuel Stratification), MFS (Moderate Fuel Stratification), PFS (Partial Fuel Stratification), Gas (87 AKI Gasoline), CEG (2% by wt. DTBP blended Cetane Enhanced Gasoline). Further data analysis and plots for this study can be found in Appendix D.

The COV (gIMEP) indicates that the higher cetane number of the CEG leads to stable GCI operation irrespective of the level of fuel stratification (Figure 6-8). The Gasoline only data indicates higher levels of stability with heavy fuel stratification.

HFS strategies led to lower fuel consumption (Figure 6-7) and thus higher thermal efficiency for both fuels. This was a result of a combination of favorable combustion phasing close to MBT timing for this engine at light loads extracting maximum work during the expansion stroke. The higher volatility and the longer ignition delay for the gasoline fuel compared to the CEG meant that an earlier injection timing and lower fuel rail pressure was more efficient.

Pressure rise rates for most of the data points were under the recommended 5 bar/CAD limit to ensure engine hardware protection. High pressure rise rates were an issue with the CEG at points where SOI2 was in the range of 20-10 dbTDC for PFS and MFS strategies. This suggests that PFS and MFS strategies should be avoided at these injection timings especially at higher loads.

CA50 data (Figure 6-8) shows that combustion phasing could be controlled with injection timing for baseline gasoline only with the HFS strategy. For CEG, CA50 trended with the second

injection timing irrespective of the level of stratification. CA1090 data shows that the burn duration of the CEG was shorter than that of the gasoline at all levels of stratification.

PFS strategies led to low soot and NO_X emissions for both fuels as combustion approaches LTC island. However, it leads to high CO and UHC emissions due to the lower combustion efficiency. The CEG has a higher combustion efficiency for all levels of stratification compared to the gasoline as evidenced by the lower CO and UHC emissions. Retarding SOI2 timings with HFS strategies irrespective of the fuels led to a nonlinear increase in particulate emissions suggesting piston and liner fuel impingement at these points. For HFS strategy with the CEG, higher particulate emissions were observed compared to gasoline at the same injection timings due to the longer diffusion burn with the CEG. The shorter ignition delay of the CEG leads to lower levels of premixing and higher fraction of fuel per cycle burnt through diffusion. NO_X emissions were slightly higher for HFS strategies with CEG compared to gasoline and correlates well with the bulk cylinder temperature which is calculated from the average cylinder pressure traces (Refer to Appendix D).

Due to the combination of higher degree of control over combustion phasing, higher degree of combustion robustness and higher combustion efficiency, HFS injection strategies were used for all remaining experiments that are a part of this chapter.

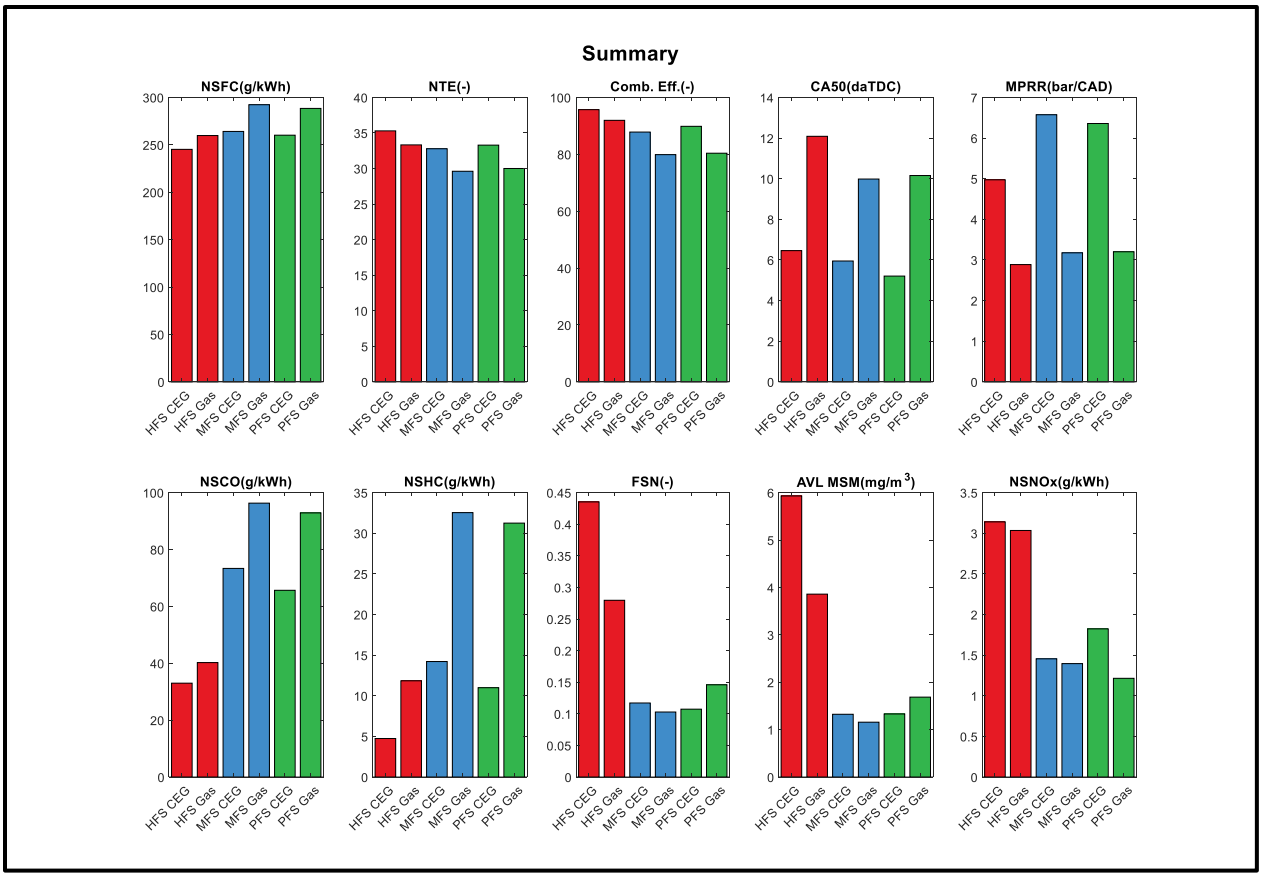

Figure 6-7: Summary of stratification study.

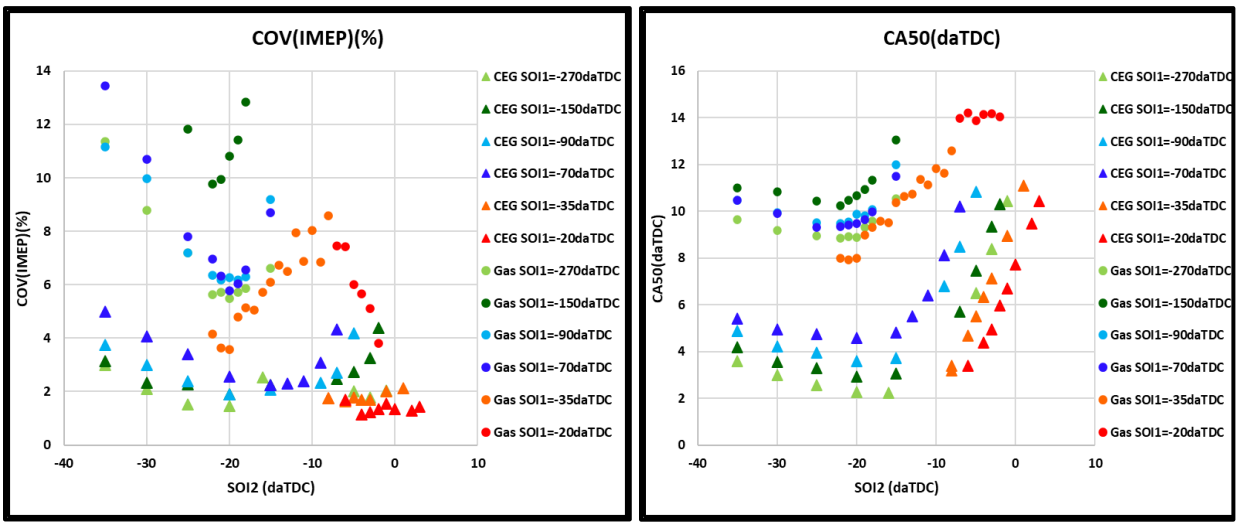

Figure 6-8: CoV (IMEP) and CA50 control based on stratification at low load GCI combustion.

6.3.2 Single fuel testing

As mentioned earlier, intake pressure sweeps were run to quantify the minimum intake pressure required for stable combustion. The effect of intake pressure on the activation energy for the forward reaction of gasoline auto-ignition can be seen in Figure 6-9. Increasing the intake manifold pressure clearly reduces the combustion instability but it comes at the cost of parasitic losses.

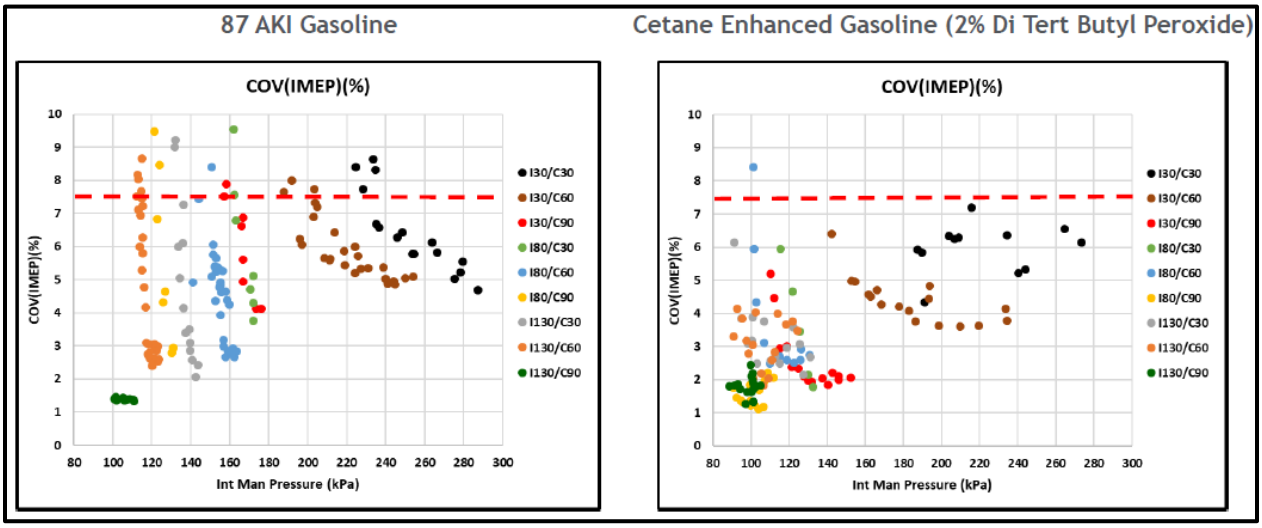

Figure 6-9: Intake Manifold Pressure Sweeps effect on COV (IMEP).

The rest of the data that is presented in this section is at the COV limited points (at the point of minimum intake pressure where COV (gIMEP)=7.5%). Note that CEG could not be used as a single fuel at the I130/C90 condition since the short ignition delay led to high particulate matter emissions and risked damaging the soot measuring devices. Moreover, advancing start of injection timings risked increasing pressure rise rate beyond the recommended limit for the engine hardware.

Minimum Manifold Pressure Requirement:

Clearly just adding 2% by mass of DTBP to our 87 AKI base gasoline reduced manifold pressure requirements (Figure 6-10) up to 58 kPa and the effect was more profound at the lower temperatures where high manifold pressures were required to light off the base gasoline. Atmospheric operation with baseline gasoline was only possible at the I130/C90 condition. Every other point required boost. However, with 2% DTBP blended, stable atmospheric GCI operation was possible for additional points on our mini map. These observations are consistent with previous work in the literature involving DTBP as a cetane enhancer [182,187,188].

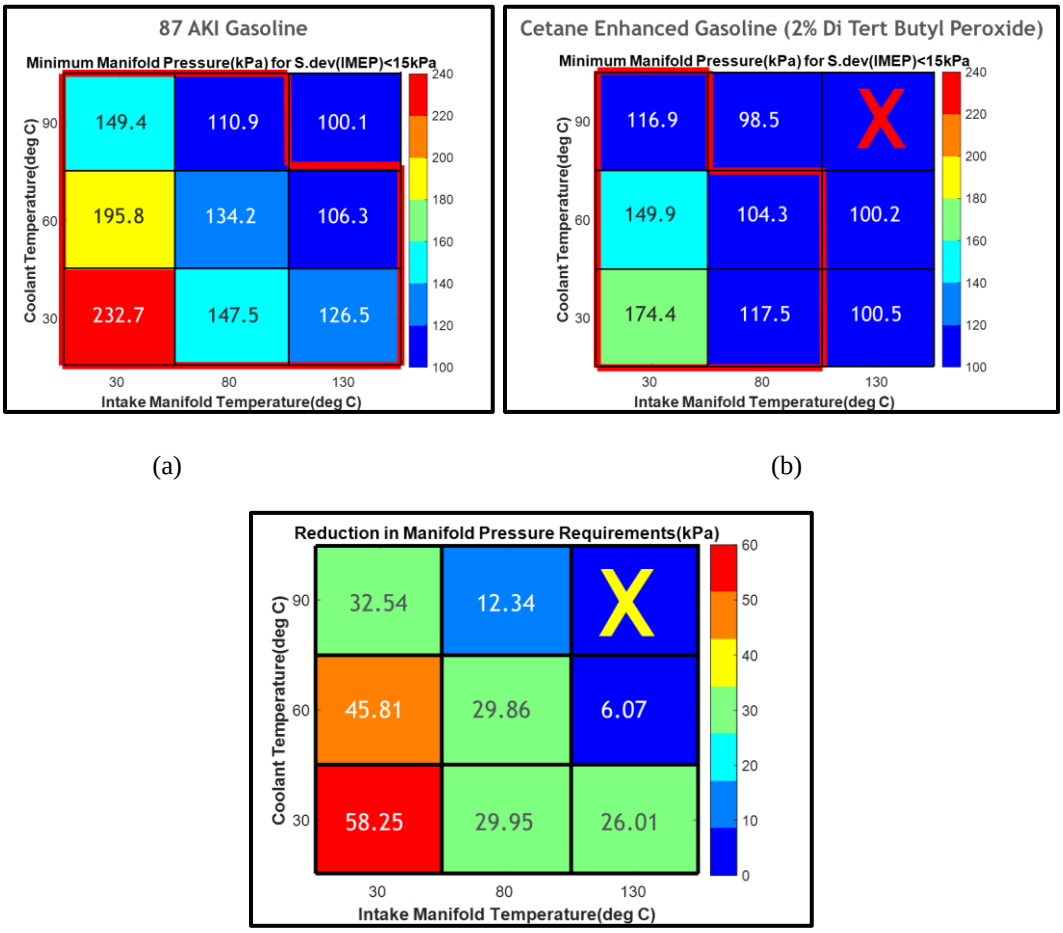

(a) (b)

(c)

Figure 6-10: Effect of CEG in reducing manifold pressure requirement.

(a) Minimum manifold pressure for stable combustion of gasoline; (b) Minimum manifold pressure for stable combustion of CEG; (c) Difference in manifold pressure requirements (Gas-CEG)

Fuel Consumption and Thermal Efficiency:

CEG also exhibited a significant reduction in fuel consumption (Figure 6-11) compared to the base gasoline especially at cold conditions. High boost requirements needed to be partnered with high fuel flow to get constant load stable GCI operation at cold conditions. The lower boost requirements with the use of CEG meant that air fuel ratios at cold conditions were not too high like they were in the case of the baseline gasoline. This led to higher thermal efficiency with the CEG.

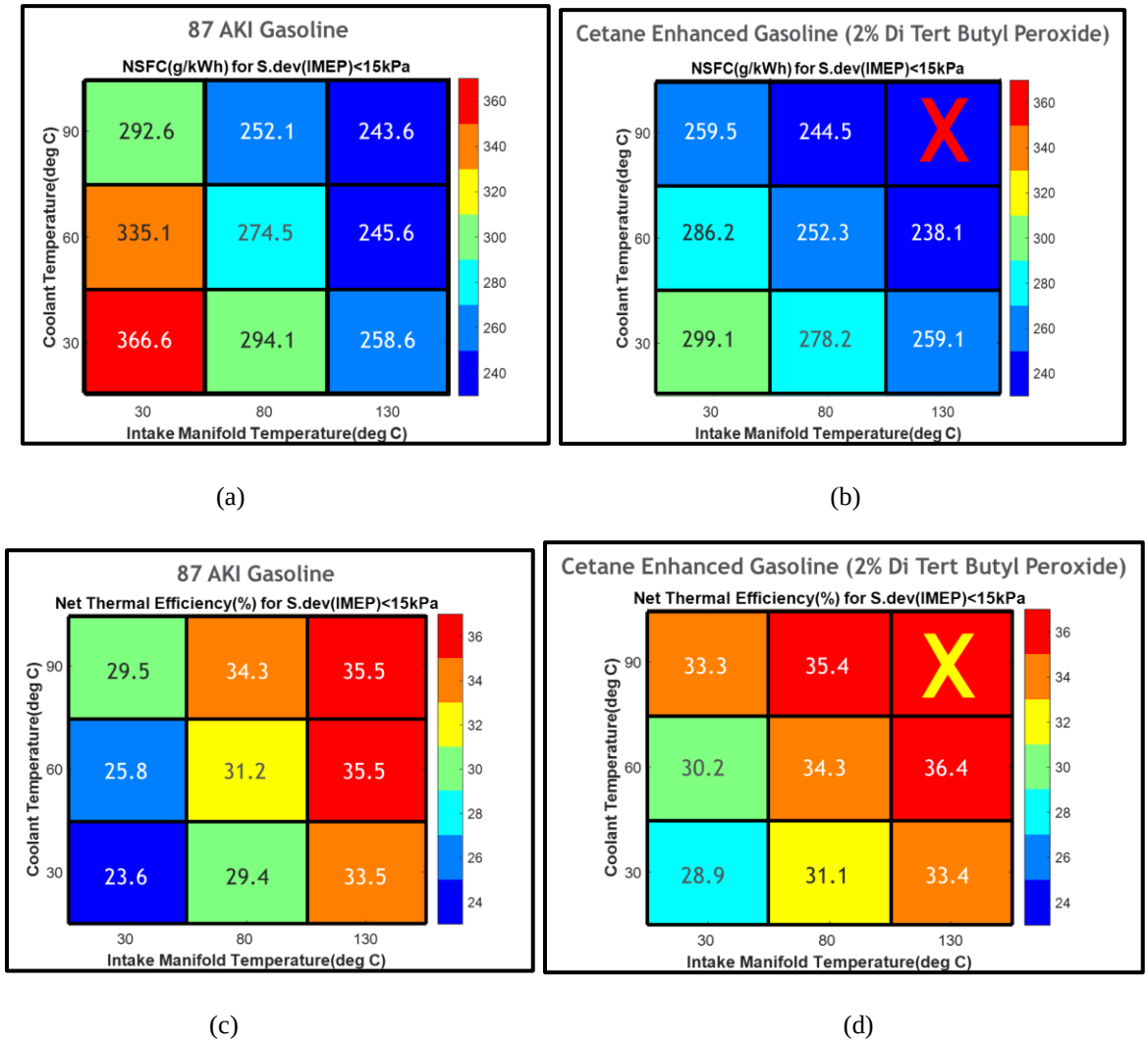

Figure 6-11: Effect of CEG in reducing fuel consumption and increasing thermal efficiency at cold conditions.

At stability limited manifold pressure: (a) Fuel consumption of gasoline; (b) Fuel consumption of CEG; (c) Thermal efficiency of gasoline; (d) Thermal efficiency of CEG.

Combustion Efficiency and Ignition Delay:

CEG combustion at CoV limited manifold pressure also exhibited high combustion efficiency. This is due to the combination of shorter ignition delay and more stratified fuel air mixture in the case of the CEG. Ignition delay measurements have been approximated from CA05-start of main injection. Negative values seen in the case of CEG at hot conditions indicates that the air fuel mixture had already auto ignited even before the second injection began. As a result, the combustion is a more mixing controlled diffusion burn similar to diesel as opposed to largely premixed for baseline gasoline.

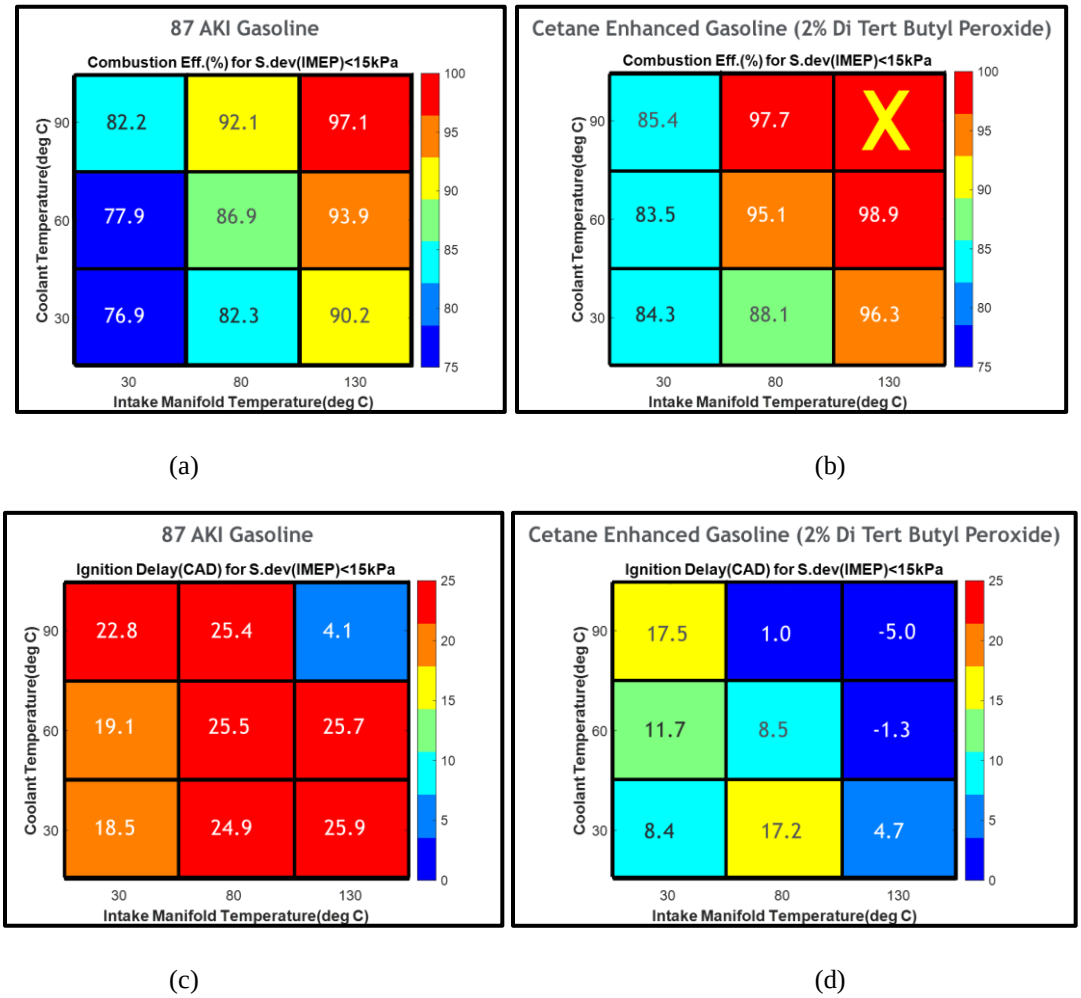

Figure 6-12: Effect of CEG in increasing combustion efficiency and reducing ignition delay.

At stability limited manifold pressure: (a) Combustion efficiency of gasoline; (b) Combustion efficiency of CEG; (c) Ignition delay of gasoline; (d) Ignition delay of CEG.

Carbon Monoxide and Unburnt Hydrocarbon emissions:

CEG effectively reduced parasitic losses associated with high boost pressure while increasing combustion efficiency. The enhanced combustion efficiency coupled with the shorter ignition delay led to complete combustion and thus reduced carbon monoxide and unburnt hydrocarbon emissions.

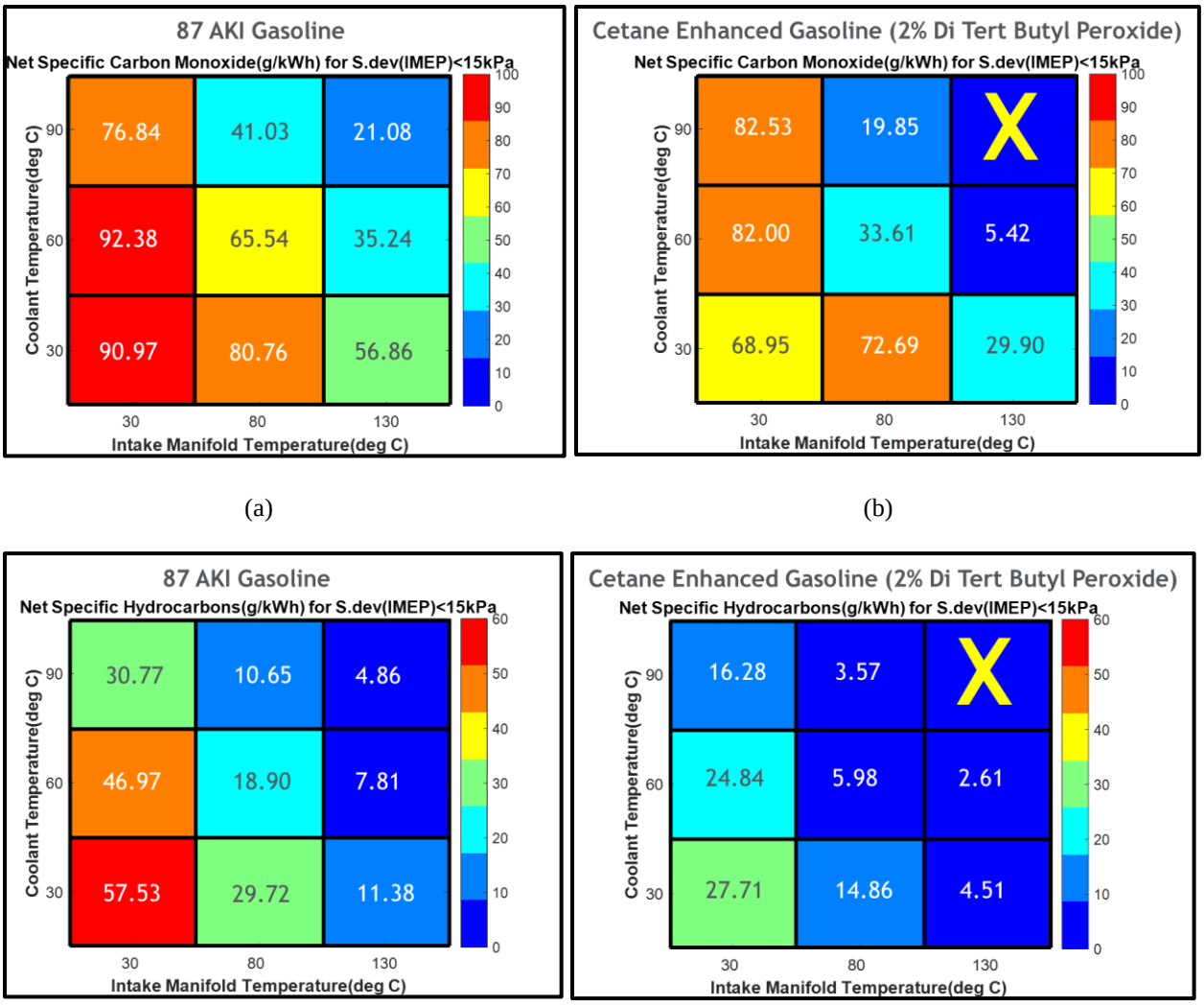

Figure 6-13*:* CEG combustion reduced CO and UHC emissions.

At stability limited pressure: (a) CO emissions of gasoline; (b) CO emissions of CEG; (c) UHC emissions of gasoline; (d) UHC emissions of CEG.

Particulate Matter emissions:

An AVL smokemeter and AVL microsoot meter were used to collect instantaneous particulate matter data. The smokemeter records a nondimensional Filter Smoke Number which correlates well with the opacity of the soot emissions. The microsoot meter on the other hand is a more sophisticated instrument which records instantaneous particulate mass.

CEG did have higher particulate emissions (Figure 6-14) compared to baseline gasoline as evidenced by both the filter smoke number measurements from the smoke meter and the mass measurements from the micro soot meter. This was due to the more diffusion nature of the combustion which was a consequence of the shorter ignition delay which meant fuel continued to be sprayed after auto-ignition. This effect was more prominent at the hotter conditions where the ignition delay for CEG was small. This further reinforces the point that CEG use should be limited to cold conditions only. It is at the cold conditions where it provides the most benefit compared to baseline gasoline. This also shows the need for a setup that allows to switch between the fuels when necessary, allowing for optimized performance and emissions. QuantLogic's prototype dual fuel injector is one such setup.

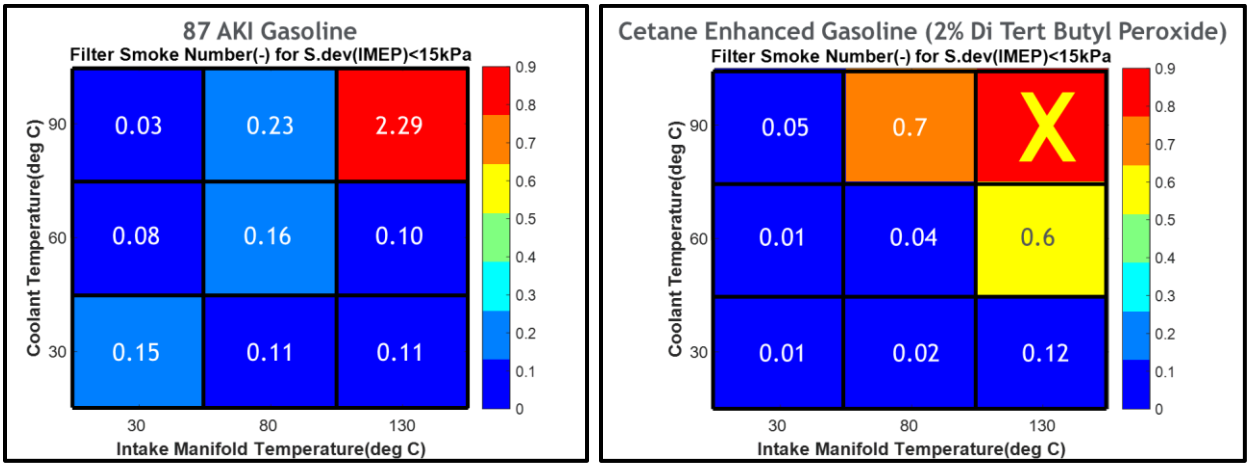

(a) (b)

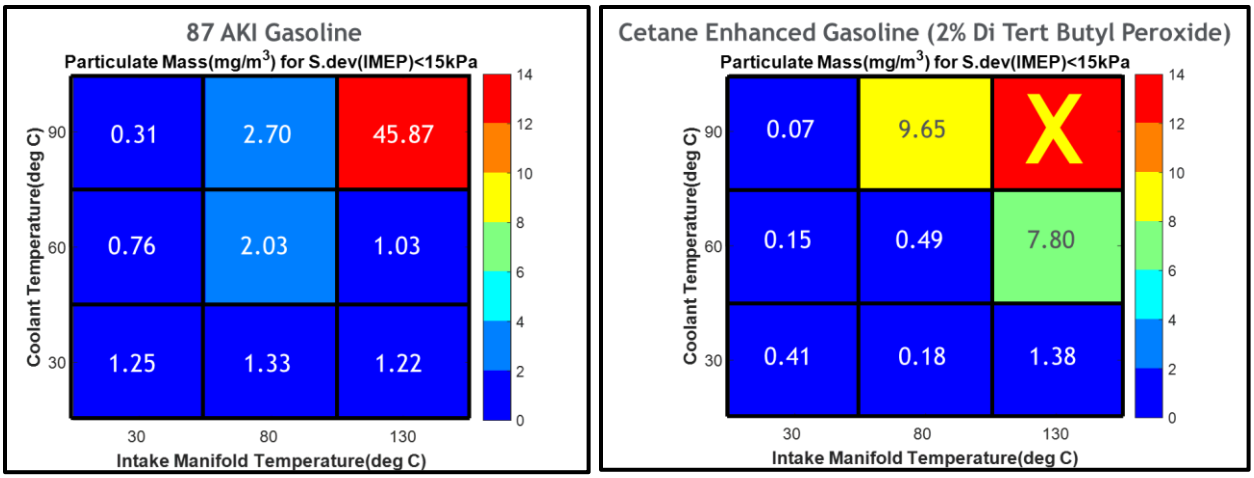

(c) (d)

Figure 6-14: Increased particulate emissions at hot conditions with CEG.

(a) Filter smoke number of gasoline at stability limited pressure; (b) Filter smoke number of CEG at stability limited pressure; (c) Particulate mass of gasoline at stability limited pressure; (d) Particulate mass of CEG at stability limited pressure.

NO_X emissions:

It is interesting to note here that despite its higher combustion efficiency and higher bulk cylinder temperature, CEG did not emit higher NO_X (Figure 6-15) probably due to the heavily stratified injection strategy which resulted in higher soot emissions. Also, the fact that CoV limited points with CEG were run relatively rich compared to the baseline gasoline due to lower manifold pressure requirements could have resulted in lowering NO_X emissions at the expense of higher particulate matter.

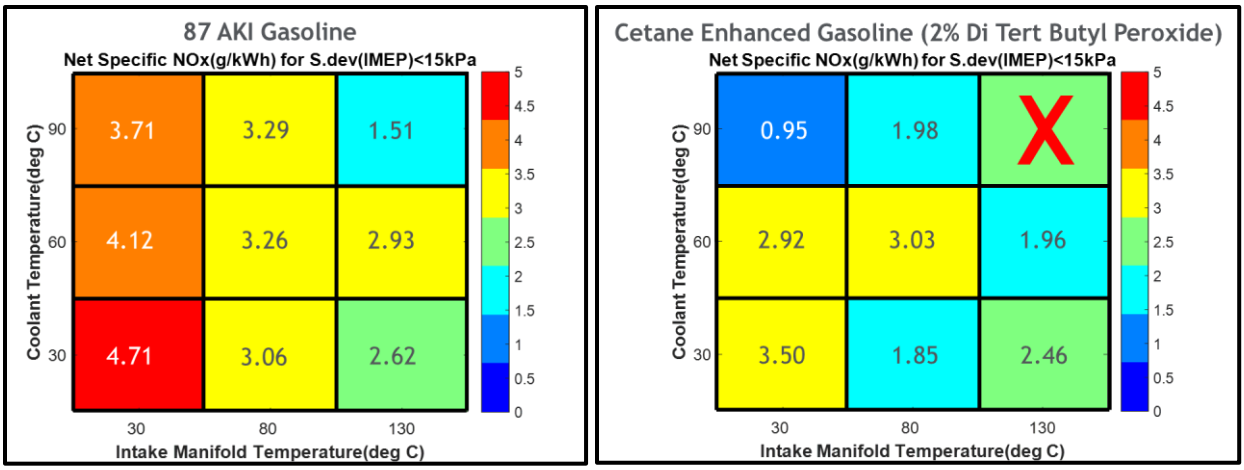

(a) (b)

Figure 6-15: No significant increase in NO_X emissions with CEG.

(a) NO_X emissions of gasoline at stability limited pressure; (b) NO_X emissions of CEG at stability limited pressure.

Cylinder Pressure and Apparent Heat Release Rate:

As mentioned earlier cylinder pressure data was recorded at the resolution of 0.1 CAD between IVC and EVO. This data was used to calculate the AHRR using the first law of thermodynamics.

The cylinder pressures are higher for gasoline operation compared to the Cetane enhanced gasoline since a higher minimum intake pressure was required for stable GCI operation especially at colder temperatures. At high temperatures, gasoline autoignition occurs at atmospheric pressure and boost is not required for stable operation. Hence, the cylinder pressure measurements at these conditions are similar in magnitude for both fuels.

Gasoline exhibits a higher peak heat release rate due to a combination of higher in-cylinder pressure and longer ignition delay which allows for higher rate of premix burn. Due to the positive ignition dwell and delay time, there is no diffusion burn phase when combusting gasoline.

At higher ambient temperatures particularly at I130/C60 and I130/C90, we notice a clear double hump in the heat release profile of the CEG since the peroxide blended gasoline auto ignites very quickly. There exists a mixing-controlled diffusion burn for these cases for the CEG since the injector continues to inject fuel while the mixture has already auto ignited. This phenomenon is very similar to what is seen during conventional diesel combustion.

At the other end of the spectrum at the colder temperatures, particularly I30/C30 and I30/C60, we see what appears to be low temperature heat release for the DTBP blended gasoline followed by a negative temperature coefficient (NTC) regime. This is due to the decomposition of DTBP into alkoxy radicals (namely tert-butoxy radicals) at low temperatures which have high reactivities and go on to create fuel radicals (namely methyl radicals) which have a significant effect on accelerating the ignition process [182].

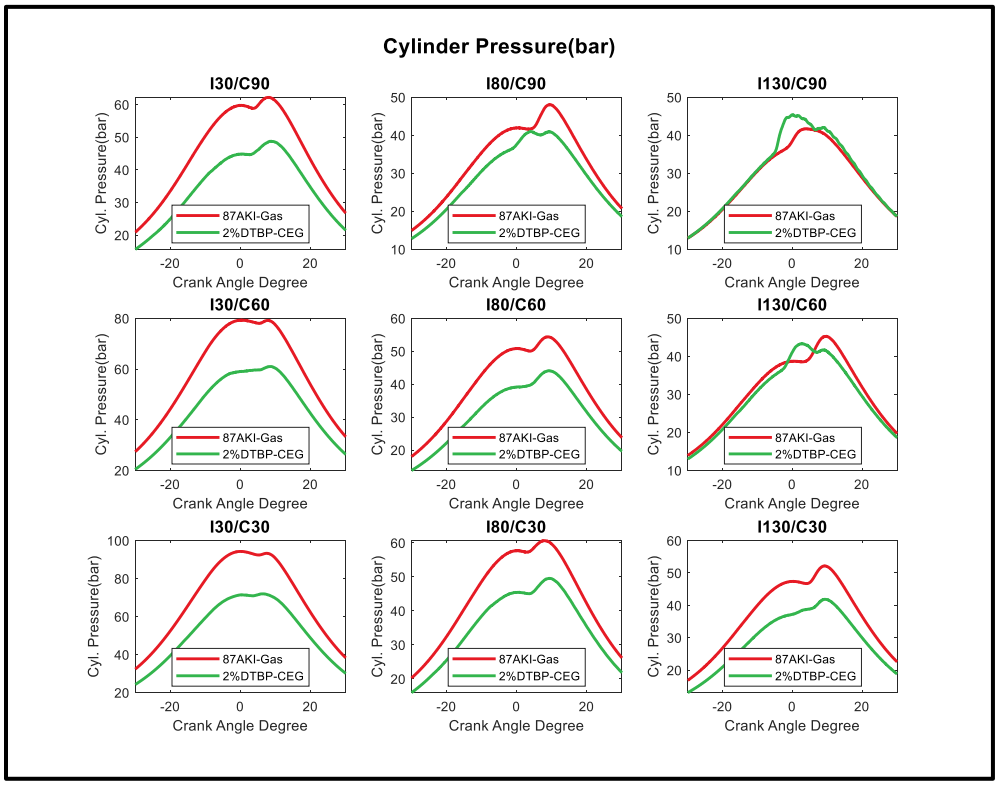

Figure 6-16: Cylinder Pressure measurements for CoV limited manifold pressures.

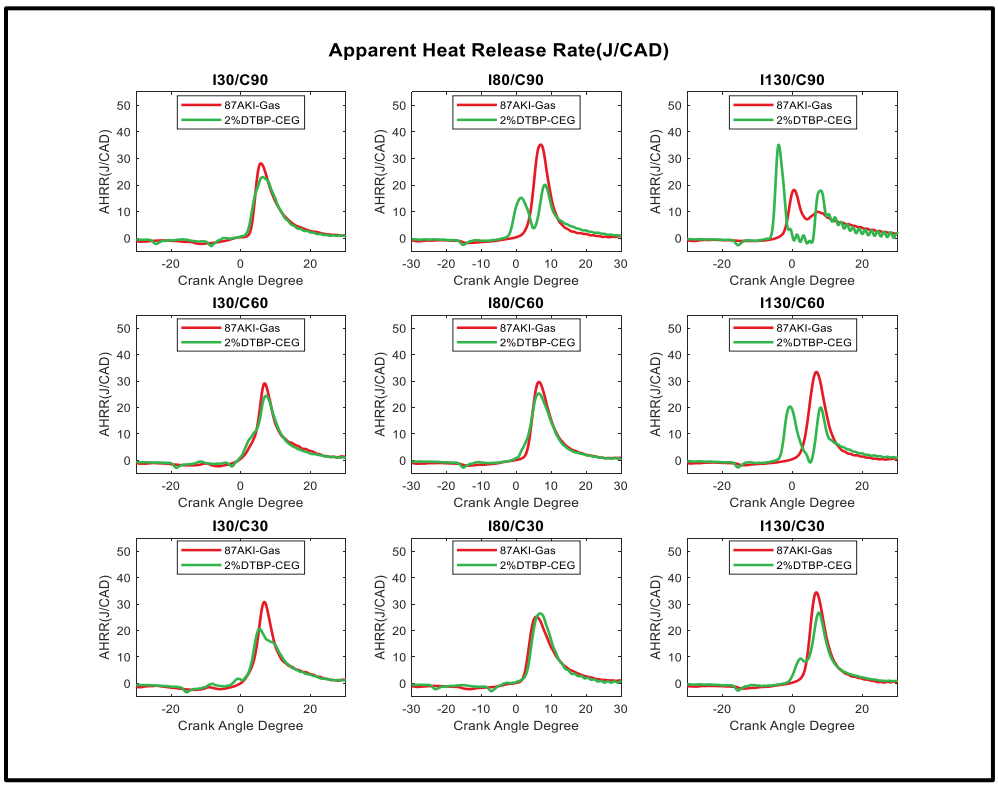

Figure 6-17: AHRR for CoV limited manifold pressures.

The chemical mechanism for the pyrolytic decomposition of DTBP is as described below. The initiation reaction occurs from the homolytic cleavage of the O-O bond to form tert-butoxy radicals:

$(CH_3)_3COOC(CH_3)_3 \rightarrow (CH_3)_3CO\bullet + (CH_3)_3CO\bullet$ **(6-1)**

Propagation reactions continue leading to the formation of more free radicals like the methyl radical and acetone which is a major byproduct of the DTBP decomposition at low temperatures:

$(CH_3)_3CO\bullet \rightarrow CH_3\bullet + (CH_3)_2CO$ **(6-2)**

The methyl radicals react with oxygen to form hydroxyl radicals through the following set of reactions. These hydroxyl radicals are a major contributor to accelerating the auto-ignition process:

$CH_3\bullet + O_2 + M \leftrightarrow CH_3O_2\bullet + M$ **(6-3)**

$CH_3O_2\bullet + CH_3O_2\bullet \rightarrow O_2 + CH_3O\bullet + CH_3O\bullet$ **(6-4)**

$CH_3O\bullet + O_2 \rightarrow CH_2O + HO_2\bullet$ **(6-5)**

$CH_3O_2\bullet + HO_2\bullet \rightarrow CH_3O\bullet + OH\bullet + O_2$ **(6-6)**

The hydroxyl radicals then rapidly react with the alkane molecules of the paraffinic parent fuel leading to the formation of more alkyl radicals. The alkyl radicals undergo oxidation addition similar to the methyl radicals to form alkylperoxy radicals:

$RH + OH\bullet \rightarrow R\bullet + H_2O$ **(6-7)**

$R\bullet + O_2 + M \leftrightarrow RO_2\bullet + M$ **(6-8)**

These radicals then undergo internal isomerization leading to low temperature chain branching oxidation mechanism for paraffinic fuels as illustrated below:

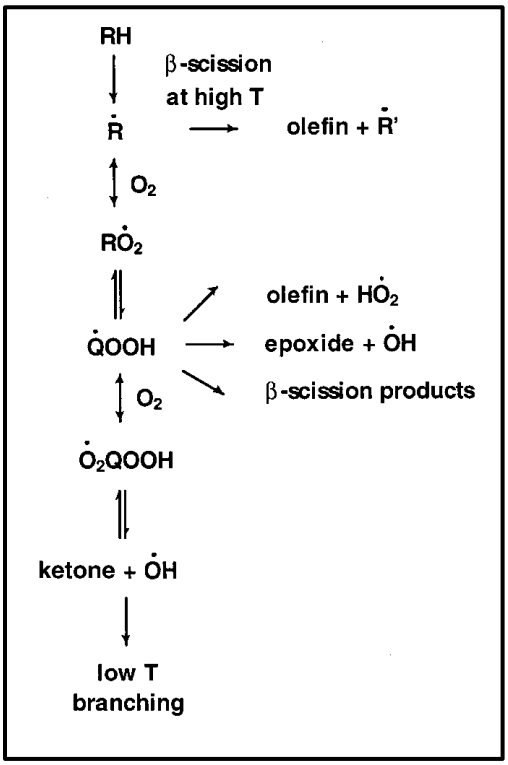

Figure 6-18: Schematic of oxidation mechanism of paraffinic fuels [189].

Moreover, low temperature heat release as was seen in the case of CEG is known to promote auto ignition. However, too high of a magnitude of low temperature heat release can

lead to the adverse effect of contributing highly towards compression work and thus negate the benefits of lower fueling.

In summary, the data from the single fuel testing with DTBP blended CEG showed that it has significant potential as a fuel that can improve GCI cold start characteristics. However, as indicated earlier, existing batch reactors and flow reactors hardware can only create a small volume of CEG in a couple hours. Moreover, the data suggests that it is beneficial to run gasoline as the primary fuel once the engine warms up. This necessitates limiting CEG consumption to when the engine is cold and switching to a more abundant low reactive fuel when the engine and its surroundings are warmer.

6.3.3 Dual fuel testing with QuantLogic Adaptive Dual Fuel Injector

The following section discusses the results from the controlled experiments that were run with the QuantLogic Adaptive Dual Fuel injector installed on the engine. The control parameters for these experiments have been explained in detail in a previous section. Due to the injector having one set of injector holes from which to inject fuel into the combustion chamber, the ratio of CEG to the total fuel flow was controlled according to the diagram below. In subsequent plots, total CEG injected is represented as fraction of the total fuel injected. This is what is termed as the CEG fraction in Figures 6-20 to 6-29. According to this terminology, a 0% CEG fraction represents gasoline only data where no CEG was injected into the cylinder. On the other hand, a 100% CEG fraction means all the fuel entering the cylinder is CEG. Values in between the these two represent fractional amounts of CEG entering the cylinder. Since CEG was injected in the second injection only, the injector waveform for each of the fuels looked like they do in Figure 6-19.

Recall from Figure 6-6 that the injector manufactured by QuantLogic does not allow CEG to be injected independently into the cylinder. It can only be injected into the cylinder by diluting it with gasoline in the mixing chamber inside the injector. Since the single fuel testing showed the potential benefits of injecting 2% DTBP blended CEG in the cylinder, it was decided that the CEG concentration would be kept the same for the dual fuel testing. However, the fact that the concentration of the CEG entering the cylinder is diluted meant that the CEG entering the injector was formulated with a higher concentration (4% DTBP such that diluting it with gasoline led to a 2% blend entering the combustion chamber). Comparisons with the hydroperoxides were made on a constant molar basis as shown in the table below.

Similar to the results of the single fuel testing, all the results presented in this section are at the CoV(IMEP) limit of 7.5% which was considered the minimum acceptable variability in combustion stability.

Fuel	Weight %	Volume %	mmol/kg
DTBP Blend	4.00	3.73	273.54
CHP Blend	4.16	2.94	273.54
TBHP Blend	2.47	2.05	273.54

Table 6-5: Specifications of CEG blends formulated for testing with QuantLogic dual fuel injector (blends formulated on constant molar basis).

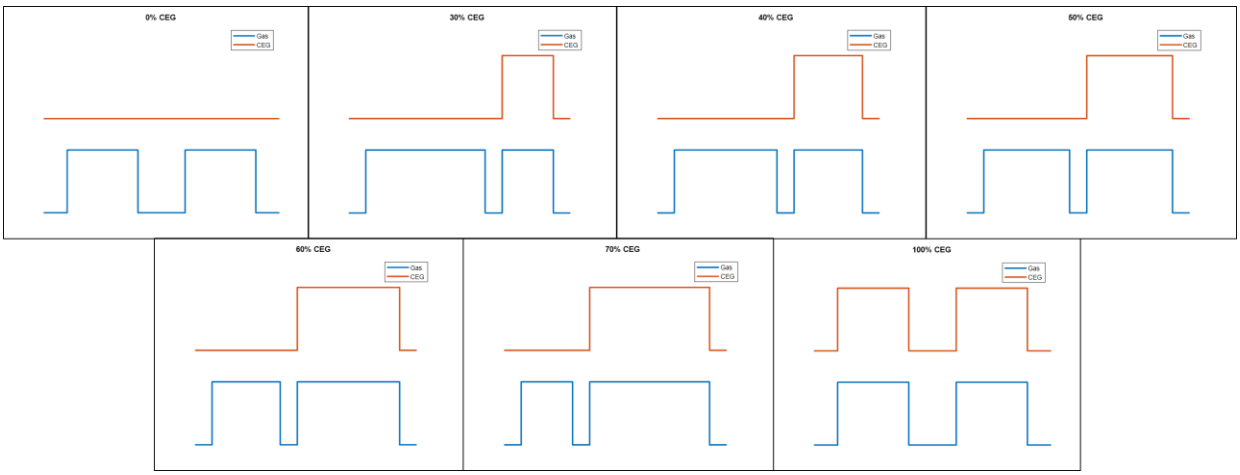

Figure 6-19: Injector controls for the QuantLogic dual fuel injector.

Minimum Manifold Pressure Requirement:

The minimum manifold pressure required for stable GCI combustion at low load is reduced monotonically as the fraction of CEG injected per cycle is increased (Figure 6-20). The effect of reduced manifold pressure is most pronounced at the coldest temperatures of air and coolant tested. This is because the low temperatures hinder gasoline auto-ignition, and the manifold pressure has to be increased to be able to promote the forward reaction. Also, from looking at the results at hot conditions, it can be concluded that there is not much benefit to injecting CEG as the manifold pressure requirements for gasoline autoignition are low. Thus, this data set illustrates the importance of hardware that allows switching of fuel reactivities based on in-cylinder temperatures. Injectors such as the QuantLogic dual fuel injector will allow the engine calibrator to switch between CEG and baseline gasoline operation based on in-cylinder conditions.

A comparison of the performance of the three high cetane fuels formulated from their respective peroxide compounds shows that the organic peroxide DTBP has greater potential of reducing manifold pressure requirements compared to the hydroperoxide compounds. This is

consistent with measurements from the CID (Figure 6-3) which show that the DTBP blend shows greater reduction in ignition delay compared to the hydroperoxide blends. This difference in performance is reduced at higher temperatures where all three compounds performed similarly. Both cumene hydroperoxide and tert-butyl hydroperoxide performed similarly with respect to their ability to reduce manifold pressure requirements at all the temperatures tested. It is hypothesized that DTBP reduces manifold pressure to a greater extent and therefore contributes more towards combustion stability compared to the hydroperoxides because it has a lower bond dissociation energy compared to the other two. The lower the bond dissociation energy, the easier is the formation of the alkyl radicals which promotes NTC (negative temperature coefficient) behavior and thereby auto-iginition [182].

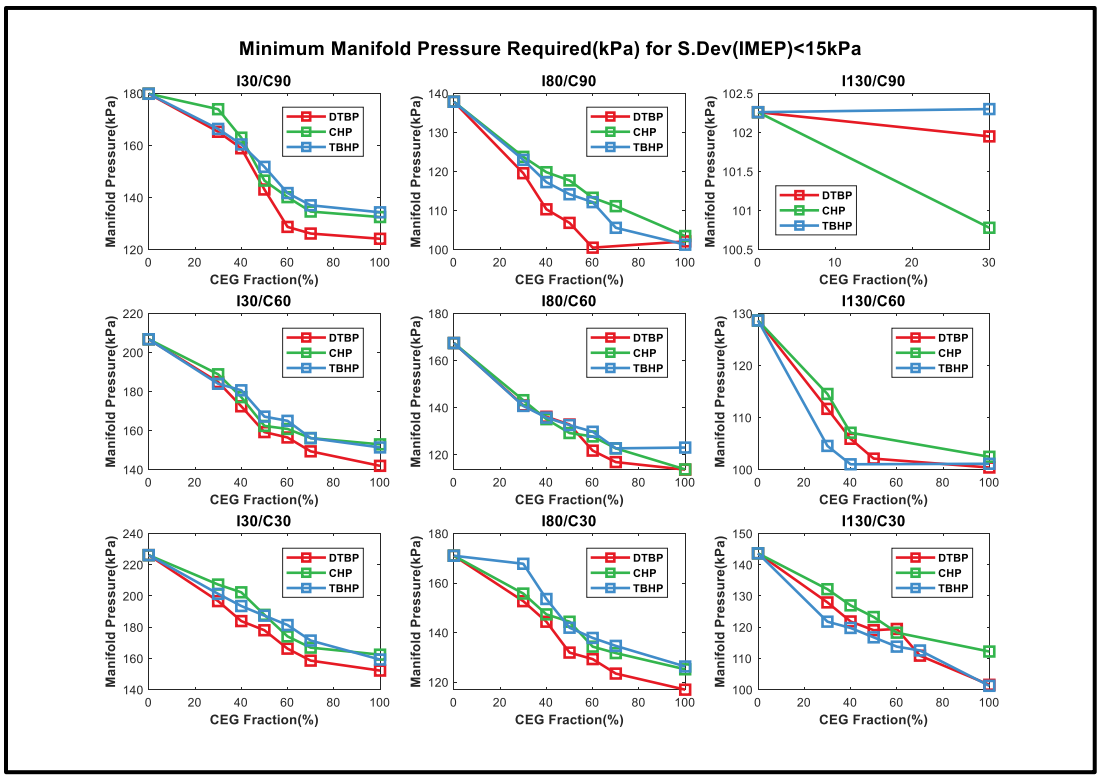

Figure 6-20: Minimum manifold pressure requirement of all three CEGs tested at different conditions.

Fuel Consumption and Thermal Efficiency:

Data across all the temperatures tested shows a common trend. CEG blends with 30%, 40% and 100% CEG fraction displayed either similar or higher thermal efficiency compared to the baseline gasoline. This is desirable since it shows that using certain injection strategies, manifold pressure requirements can be reduced without compromising on thermal efficiency.

The reason for lower thermal efficiency displayed with the 50%, 60% and 70% CEG fraction is the injection strategy that is employed (Figure 6-19). At these values of CEG fraction, the larger pulsewidth of the second injection containing CEG becomes the dominant injection of the two affecting auto-ignition. This is due to lesser baseline gasoline being available in the cylinder to burn before CEG is injected. Thus, too late of a start of injection timing for the second pulse means the air fuel mixture does not auto-ignite. As a result, the injection is timed earlier in the compression stroke.

While the trend of reduced manifold pressure requirement is maintained as CEG fraction is increased, the earlier injection timings lead to a less stratified mixture which as seen from our initial stratification study leads to lower thermal and combustion efficiency (Figure 6-7). It can be concluded from these results, that it is not desirable to operate using those injection strategies.

The difference in performance amongst the three compounds tested is once again seen at the lower temperatures tested. At low temperatures, it can be seen that the DTBP blend operates at a higher thermal efficiency compared to the two hydroperoxide compounds. At warm and hot conditions, there is no significant difference in fuel consumption or thermal efficiency.

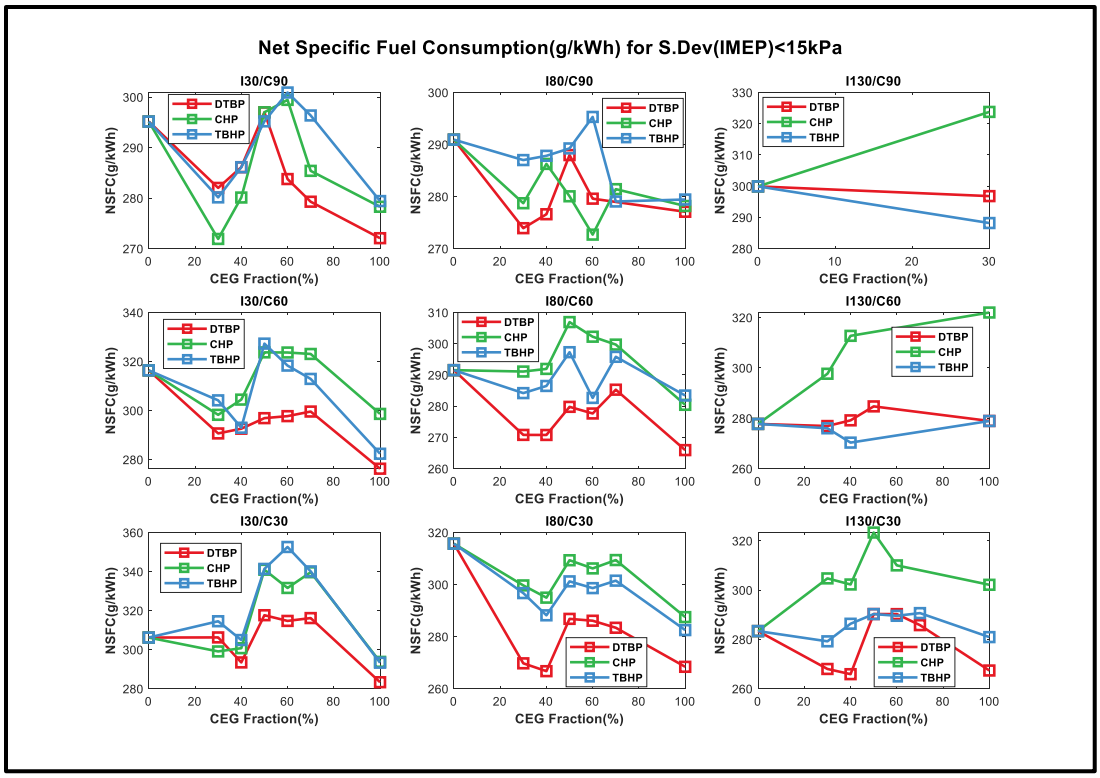

Figure 6-21: Fuel consumption of all three CEGs tested at stability limited manifold pressures.

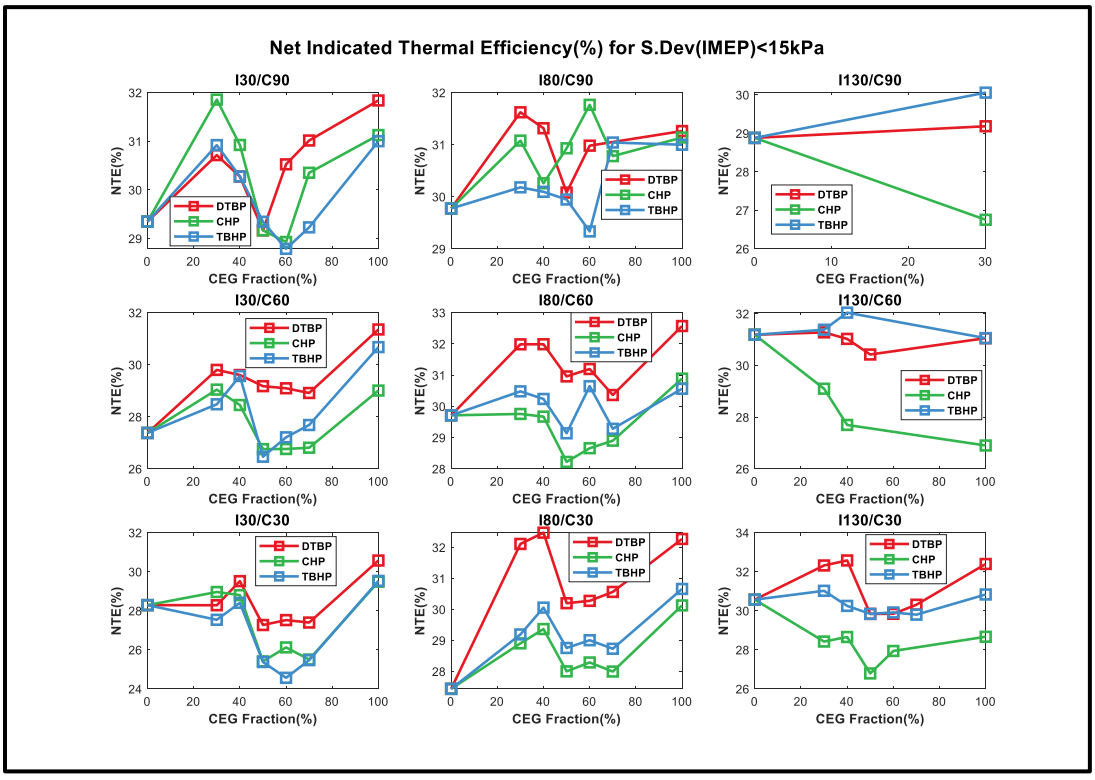

Figure 6-22: Net indicated thermal efficiency of all three CEGs tested at stability limited manifold pressures.

Combustion Efficiency and Ignition Delay:

Another encouraging observation is that increased CEG fraction increased combustion efficiency in addition to the increased thermal efficiency. The exception to this trend is once again seen at the CEG fractions of 50%, 60% and 70%. This is due to the injection strategy employed at those CEG fractions and is the same reason that contributed to poor thermal efficiency.

A high combustion efficiency is the result of the increased affinity of the air fuel mixture to auto-ignite with increased fractions of CEG. This is consistent with the trends of ignition delay that is estimated as the difference in start of injection and the crank angle at which 5% of the fuel mass has burned (CA05 – SOI2). Ignition delay trends show that ignition delay is reduced as CEG fraction is increased. Once again, the exception to this trend is seen at fractions of 50%, 60% and 70%. A comparison of all three compounds shows that DTBP displays slightly higher combustion efficiency compared to the hydroperoxides at low temperatures.

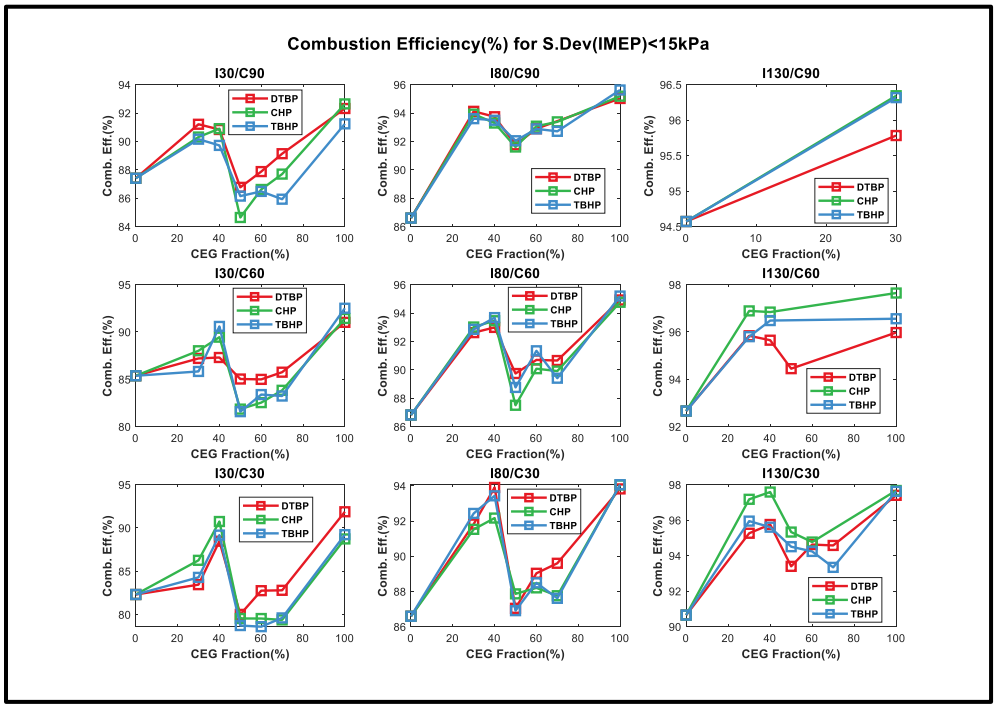

Figure 6-23: Combustion efficiency of all three CEGs tested at stability limited manifold pressures.

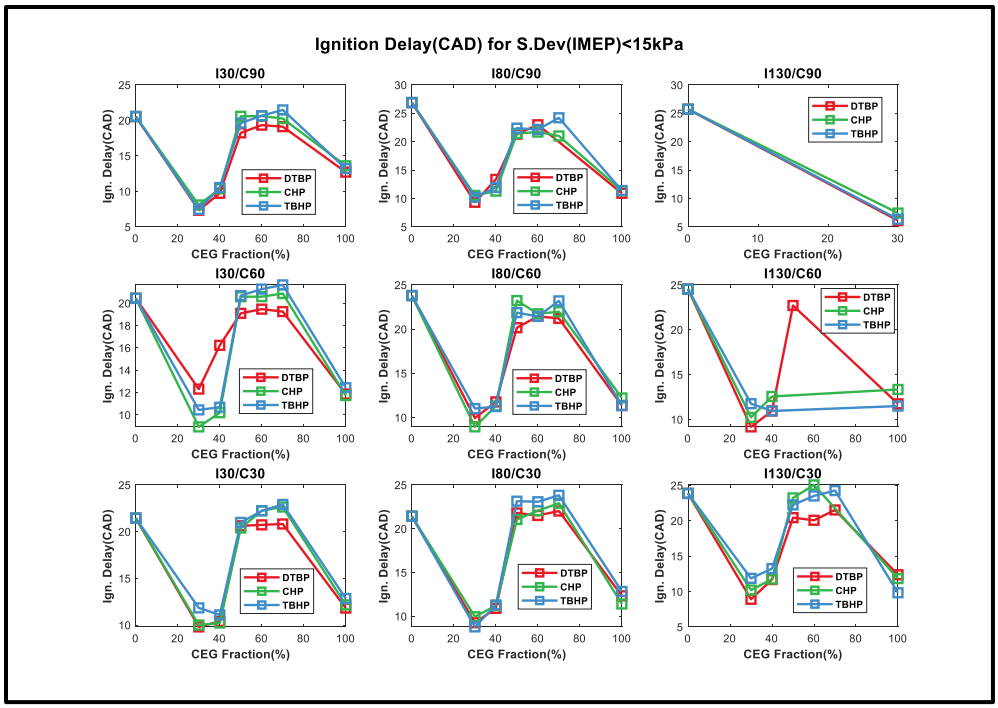

Figure 6-24: Ignition delay of all three CEGs tested at stability limited manifold pressures.

Carbon Monoxide and Unburnt Hydrocarbon emissions:

Increased combustion efficiency with increasing fractions of CEG results in more complete combustion and lower concentrations of incomplete combustion products being emitted. As a result, higher CEG fractions leads to lower concentrations of carbon monoxide and unburnt hydrocarbon emissions. Lilik et al. [68] observed similar trends during their experiments with diesel and low temperature Fischer-Tropsch (LTFT) fuel. LTFT reduced ignition delay compared to conventional diesel when run in PCCI (Partially premixed charge compression ignition) mode. This was attributed to reductions in ignition delay which reduced the levels of premixing and increased combustion efficiency by increasing the fraction of diffusion burn.

GCI operation with the DTBP blend leads to lower CO and UHC emissions compared to the hydroperoxide blends at low temperatures due to the higher combustion efficiency using the DTBP blend.

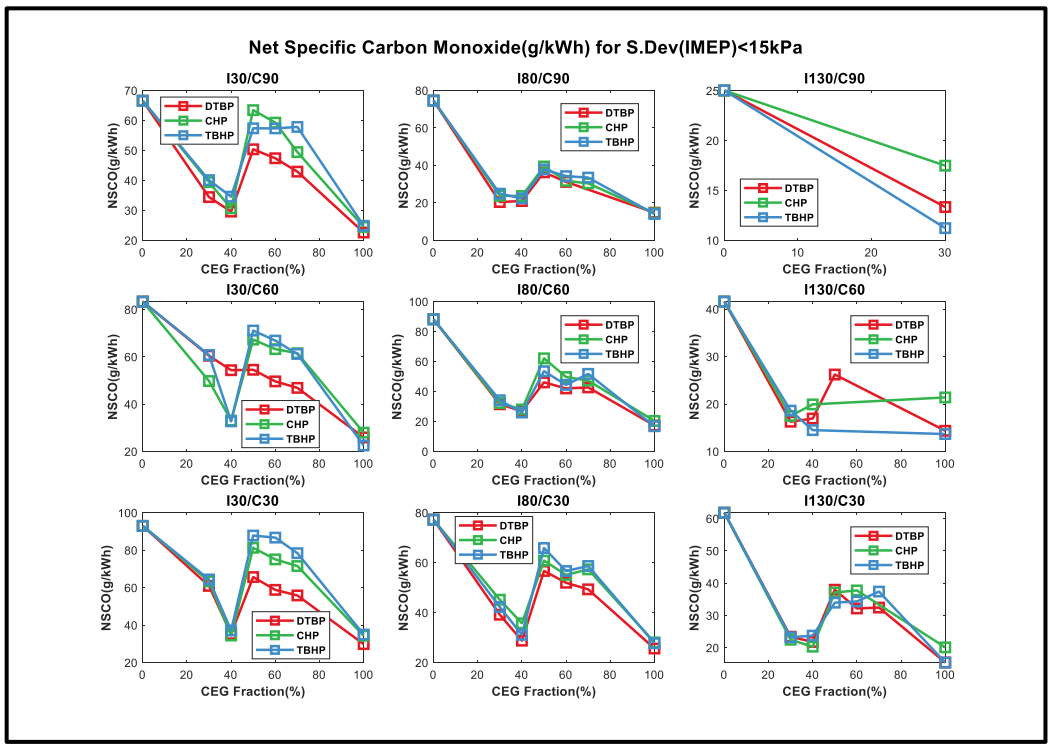

Figure 6-25: CO emissions of all three CEGs tested at stability limited manifold pressures.

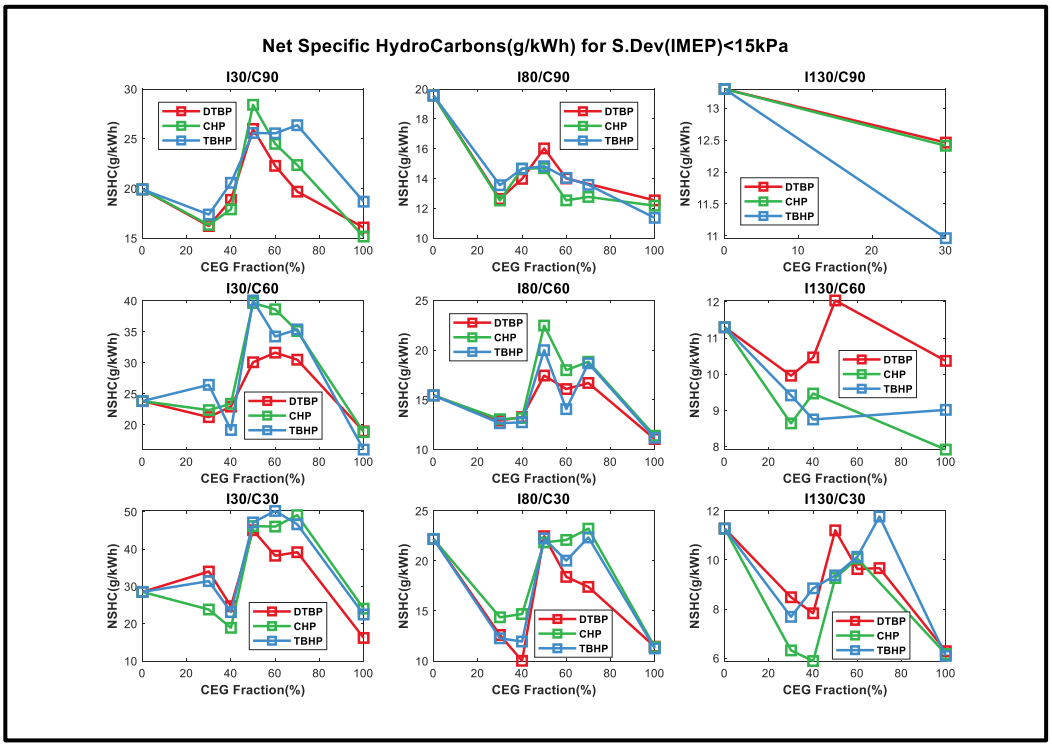

Figure 6-26: THC emissions of all three CEGs tested at stability limited manifold pressures.

Particulate Matter emissions:

While lowering manifold pressure leads to lower air fuel ratios which would usually result in higher particulate emissions, the increased combustion efficiency of CEG compared to gasoline means that there is no significant increase in particulate matter emissions as evidenced by the trends in filter smoke number and particulate mass recorded by the AVL microsoot meter. The filter smoke number is an indicator of opacity of particulate matter and trends similarly to the particulate mass measured by the microsoot meter.

A common trend observed from all the tests was the high particulate matter recorded at 100% CEG fraction. This is due to the combination of low air-fuel ratios at minimum manifold pressure and the increased propensity of CEG to auto-ignite. A lower ignition delay means there is less time available for air and fuel to mix before autoignition. This also means that the combustion is similar to stratified diesel combustion with a lower fraction of premixed burn followed by a longer mixing controlled diffusion burn which contributes to soot formation.

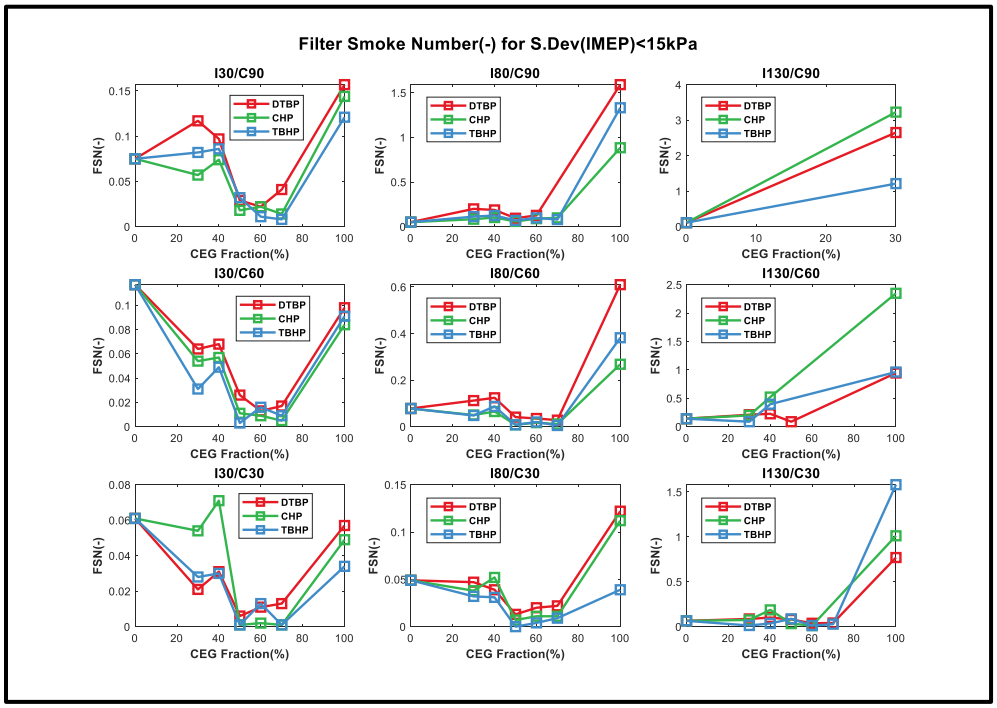

Figure 6-27: Filter smoke number of all three CEGs tested at stability limited manifold pressures.

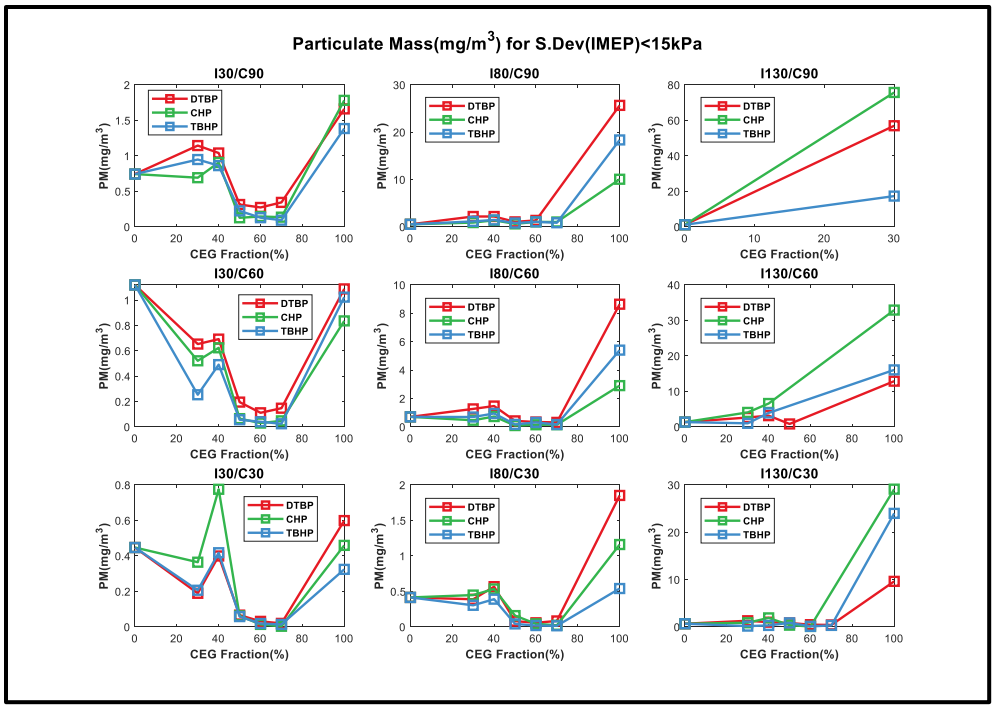

Figure 6-28: Particulate mass of all three CEGs tested at stability limited manifold pressures.

NO_X emissions:

While the benefits of CEG over baseline gasoline at low load GCI operation have been highlighted in the previous sections, one drawback is the increased NO_X emissions. The high in-cylinder temperatures associated with high combustion efficiency of the CEG contributes to greater NO_X formation as seen from the trends in Figure 6-29. No significant differences can be seen in NO_X emissions among the three compounds tested.

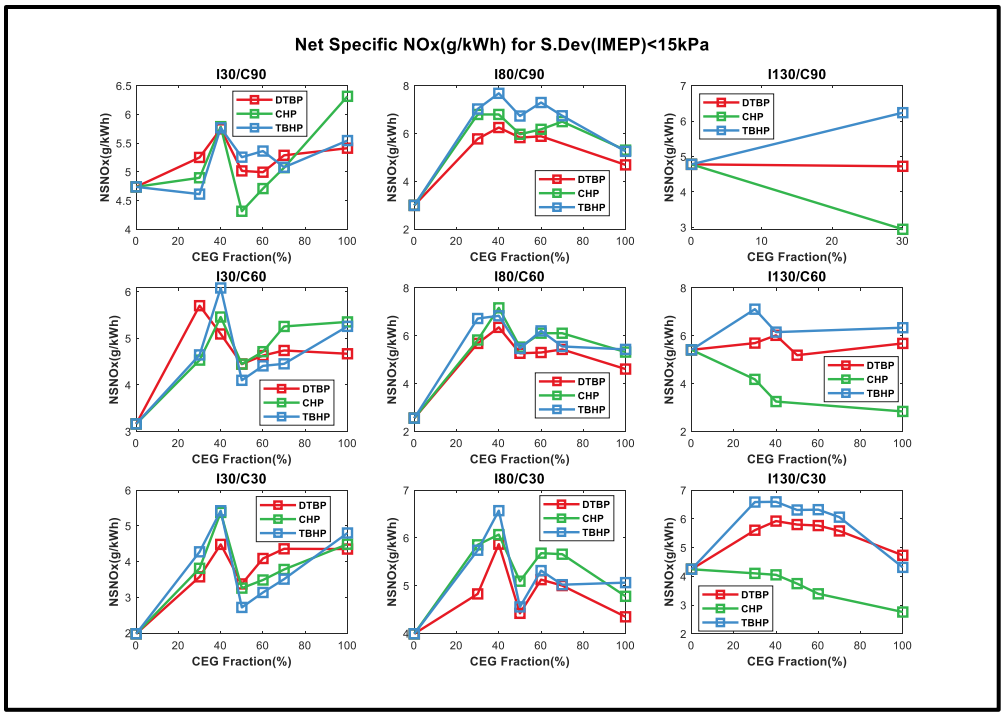

Figure 6-29: NO_X emissions of all three CEGs tested at stability limited manifold pressures.

The ability of the organic peroxide, namely DTBP to impact auto-ignition propensity through the reduction in ignition delay to a greater extent compared to the hydroperoxides can be attributed to the differences in the mechanisms for bond dissociation. Whereas the bond dissociation for the organic peroxide to form alkyl radicals is largely homolytic as shown reaction 6-1, it can be theorized that the dissociation for the hydroperoxides is more heterolytic in nature. Heterolytic bond dissociation energy is known to be considerably higher than homolytic bond dissociation energy and this could be the reason for the greater affinity of the DTBP blend to auto-ignite compared to the hydroperoxide blends. A comparison of the initial dissociation reactions is shown below:

DTBP: $(CH_3)_3COOC(CH_3)_3 \rightarrow (CH_3)_3CO\bullet + (CH_3)_3CO\bullet$ **(6-9)**

CHP: $C_6H_5(CH_3)_2COOH \rightarrow C_6H_5(CH_3)_2CO^+ + OH^-$ **(6-10)**

TBHP: $(CH_3)_3COOH \rightarrow (CH_3)_3CO^+ + OH^-$ **(6-11)**

6.4 Summary and Conclusions

Three sets of experiments were conducted with a focus on low load GCI testing. The issue of reduced combustion stability was addressed by testing using cetane enhanced gasoline which was found to make GCI operation more robust compared to baseline gasoline. The difference in performance of the fuels is more pronounced at low temperatures since the low temperatures inhibits gasoline auto-ignition. The findings of the experimental studies are summarized below:

1. The observations from the stratification study were consistent with the observations of Curran et al. [61]. Heavy fuel stratification injection strategies are preferred for GCI operation at low load.
2. Heavy fuel stratification led to greater control of combustion phasing and higher combustion efficiency. However, the high combustion efficiency did contribute to greater NO_X formation and the higher level of stratification led to greater soot formation compared to low stratification injection strategies.
3. A comparison of gasoline and DTBP blended CEG (2%) as potential single fuels for GCI operation at low loads demonstrated the benefits of CEG. Parasitic losses were reduced which makes CEG a more practically applicable fuel for GCI combustion.
4. In addition to reduced manifold pressure requirements, DTBP blended CEG fuel demonstrated higher thermal efficiency and combustion efficiency than baseline gasoline.
5. After confirming the potential of CEG to overcome the challenge of GCI operation at low loads and cold temperatures, a novel dual fuel injector was installed on the engine.
6. It was concluded from the single fuel testing results, that ideal GCI operation could be achieved by switching fuels from CEG to baseline gasoline as the engine got warm after

a cold start. Moreover, the fact that current state of the art reactors can only formulate a small quantity of CEG in a couple hours necessitated the installation of hardware that could optimize CEG consumption.

7. The tests with the dual fuel injector demonstrated the potential of reaping the benefits of CEG operation while consuming less CEG fuel compared to the single fuel tests.

8. Moreover, a comparison of different peroxide compounds showed that the DTBP blend performed better than the CHP and TBHP blends at low temperatures in terms of thermal and combustion efficiency. It was hypothesized that this was due to the lower bond dissociation energy of the organic peroxide compared to the hydroperoxides to form alkyl radicals which promote auto-ignition.

9. These results are consistent with the data from the CID which showed that the DTBP blend has a lower ignition delay compared to the hydroperoxide blends.

While previous studies in the literature have shown the benefits of reactivity-controlled compression ignition [100,173,174], the high reactivity fuel in those studies is a separately formulated fuel. This separately formulated fuel of higher reactivity is either diesel or low octane rated gasoline such as naphtha. The study presented in this chapter is novel because it suggests using the same fuel for both fuel supplies and follows up on previous work that has demonstrated formulating the high reactivity fuel from the more abundantly available low reactivity fuel. This presents an opportunity for a more practical application of RCCI as it would not have to involve the end user to fill up two separate fuels. Moreover, this is the first study that focuses on potentially solving the issue of combustion robustness of GCI combustion at low loads and low temperatures. It can be concluded from this study that using a combination of gasoline and

peroxide blended cetane enhanced gasoline is a more practical way to implement GCI operation in light duty applications.

Chapter 7
Summary and Recommendations for Future Work

7.1 Summary of dissertation

This dissertation has addressed the drawbacks of current generation downsized gasoline engines operating on both spark ignited and compression ignited strategies. Experiments were conducted on both engine platforms to demonstrate potential solutions. The conclusions from these experiments are summarized below.

In Chapter 4, Miller cycle operation was successfully implemented on a model year 2020 Ford Dragon engine. Benchmarking studies of current vehicles show that Miller cycle implementation on gasoline engines is largely restricted to naturally aspirated engines since the large geometry of the engine compensates for the low volumetric efficiency of Miller cycle. Some similar studies have shown that Miller cycle implementation on downsized boosted engines is restricted to light loads and throttled conditions since the current generation turbochargers cannot meet the excess boost pressure demand required for Miller cycle at high loads. This study is the first known study that successfully implements Miller cycle on a downsized boosted engine at high loads across all engine speeds. The unique implementation of Miller cycle at high loads has resulted in lower fuel consumption and lower NO_X emissions compared to the baseline.

In Chapter 5, the knock-soot correlation was studied on a production multi-cylinder engine. Three independent studies were conducted at knock limited conditions. Miller cycle demonstrated the ability to advance knock limited combustion phasing. A comparison of direct and port injections verified the benefit of direct injection strategies at knock limited conditions. This is the first known report of the demonstration of the knock-soot correlation on a production multi-cylinder gasoline direct injection engine. Moreover, a comparison of fuels of different octane ratings confirmed that high-octane rated fuels led to lower particulate emissions at knock limited conditions due to the lower knock propensity. This suggests that Miller cycle can be combined with direct injection of high-octane rated fuels at knock limited conditions to reap the benefits of low knock propensity and low particulate emissions. This result provides an important insight for engine calibrators and future engine designers for implementing concepts such as octane-on-demand.

In Chapter 6, the drawbacks of low combustion stability and combustion efficiency are addressed by the formulation of higher cetane rated gasoline fuel which is doped with organic peroxides. The highest reduction in parasitic losses is achieved at low temperatures. This is the first known report of the benefits of peroxide blended gasoline at light loads and low temperatures. Moreover, the implementation of a prototype dual fuel injector allows the implementation of a cetane-on-demand concept. Combining this concept with the concept of on-board formulation of high cetane rated fuel from the more readily available low cetane rated gasoline fuel is a novel approach.

The suggested strategies in these three chapters can be leveraged to expand the current bounds of gasoline engine powertrain efficiency. Leveraging novel hardware and fuel chemistry as was done in this thesis has the potential for greatly impacting the performance of gasoline

engines in light duty vehicle applications whether that be on a spark ignited or compression ignited platform.

7.2 Recommendations for future work

7.2.1 Chapter 4: Miller cycle implementation on a current generation GDI engine

Even though our application of Miller cycle on the engine was limited to using the existing camshafts and the VCT phasors, there is a clear trend in improvement of fuel efficiency and engine out NO_X and CO emissions. With more time and resources, investing in actual Miller camshafts, which would not have the intake valve opening coupled with the intake valve closing timings, would enable broader and deeper optimization. Moreover, further optimization efforts would help narrow down the best injection strategies for a Miller engine. This would solve the issue of excess soot and UHC emissions as has been proven from the limited data that was available with alternate injection timings. In addition, as seen from a comparison of spark timing and CA50, there is potential for further improvement since the spark timings could not be overridden to take advantage of the lower in cylinder temperature with the implementation of Miller cycle. The current spark tables on Ford's ECU (engine control unit) are on the basis of intake manifold pressure rather than engine torque. As a result, the CA50 and spark timings with our Miller engine are delayed compared to the baseline engine (since we use more boost for the same engine torque).

Alternate ideas that would result in higher engine thermal efficiency are the implementation of:

a. A cooled low pressure exhaust gas recirculation loop
b. Octane On demand using high octane rated fuel leveraging either set of injectors.
c. Combined FNT+WG actuation to reduce pumping losses

It would be interesting to see how much the thermal efficiency of the engine could be improved by implementing these concepts. Moreover, comparisons of turbo lag would be beneficial to quantify benefits in terms of faster response.

Baseline Engine with FGT **Miller Engine with VGT**

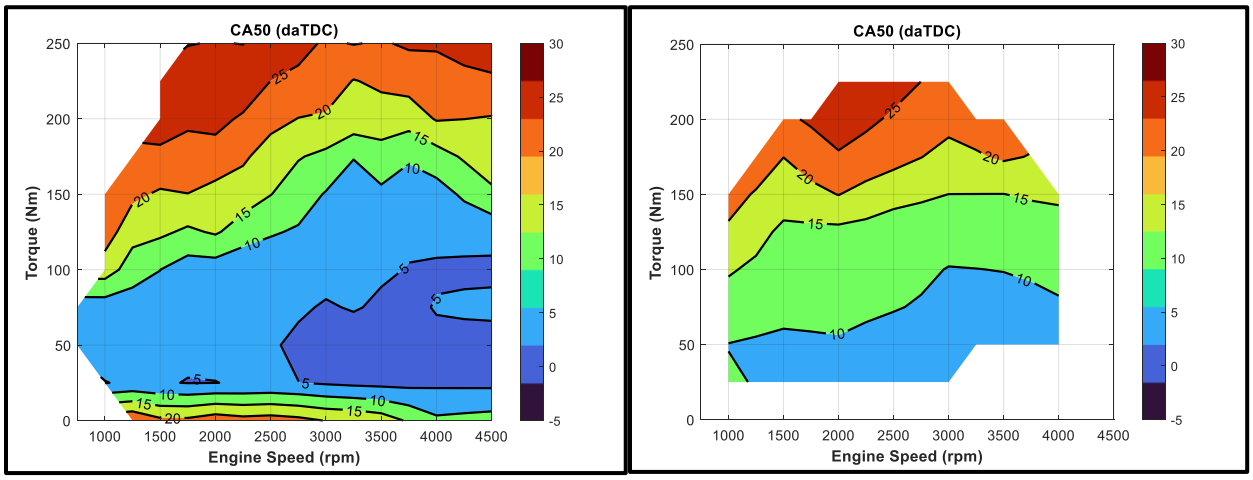

(a) (b)

Figure 7-1: Comparison of CA50 of (a) baseline engine vs. (b) Miller engine.

Baseline Engine with FGT **Miller Engine with VGT**

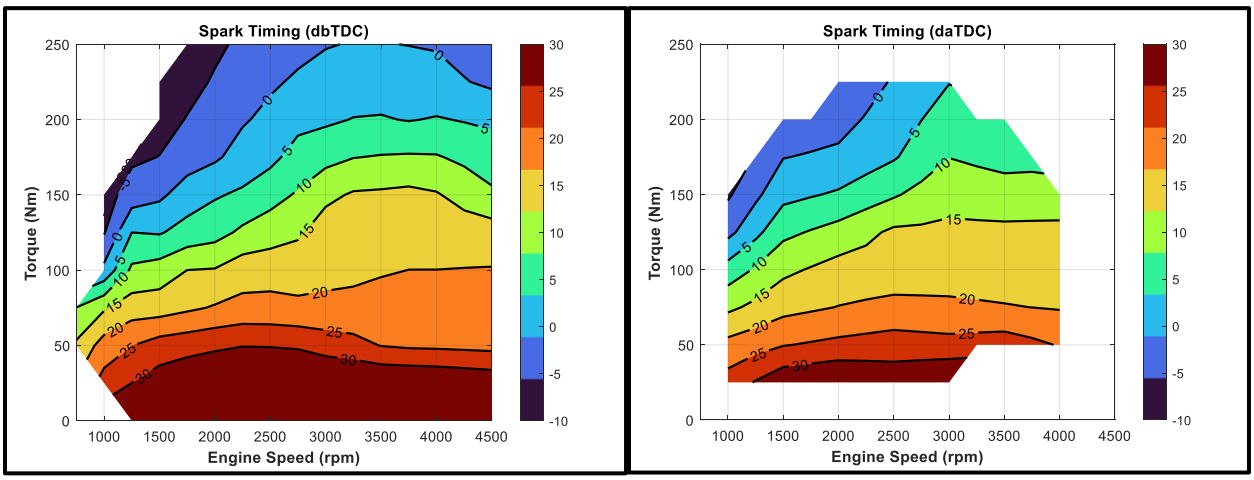

(a) (b)

Figure 7-2: Comparison of spark timing of (a) baseline engine vs. (b) Miller engine.

7.2.2 Chapter 5: Strategies for reducing knock propensity and particulate emissions

The knock-soot correlation could be further understood with some follow up experiments involving changing the chemistry of the engine oil and collecting thermophoretic samples from the engine exhaust. Studying the thermophoretic samples under a TEM (transmission electron microscope) could potentially provide further insight into whether the particulate matter formed during knock occurrence is largely from oil particles or from fuel rich pockets instead. If certain chemical markers are found that are a result of changing the oil chemistry then that could tell us that the engine oil theory is the more likelier theory out of those discussed in this chapter and Han's work [30].

The set of two injectors on this particular engine platform could be leveraged to further investigate the effect of using separate fuels for each set of injectors. An Octane on Demand strategy could be employed using the high octane Sunoco fuels with the DI injectors at knock limited conditions. A low octane fuel could be used with the PFI injectors since the PFI injectors are calibrated to fuel only at mid to low loads where the injector is not knock limited. Also as shown in one of the studies, the direct injection is a preferred strategy at high loads that are knock limited. However, one must also keep in mind that with the DI injectors not operational for most of the engine map, the tips of the injector holes continue to be exposed to high in cylinder temperatures which could potentially lead to damaged injectors. Taking this into account, it might be desirable to use the high octane fuel with the port injectors rather than the direct injectors. This would allow the advancement of combustion phasing to maximum brake torque timing while minimizing the consumption of high octane fuel which will reduce the frequency of refilling the high octane fuel tank. The benefits of operating at maximum brake torque timing include lower fuel consumption and thus lower CO_2 emissions. Moreover, as this

chapter confirmed, preventing knocking prevents the associated high concentrations of accumulation mode particulate matter. This could potentially reduce expense on particulate filters and their regeneration frequencies. Reduced regeneration frequencies will lead to reduced fuel consumption and more efficient operation.

The separate fuels approach can also be used in conjunction with additional hardware which would not require the user to refill two separate fuel tanks. Researchers at Honda R&D have developed on board fuel separation systems that produces high concentration of Ethanol fuel from pump E10 gasoline fuel [190]. The study showed improvement of fuel economy as well as lower knock propensity using separate fuels approach. Honda R&D researchers have also explored the possibility of on demand octane boost by aerobic oxidation of gasoline using NHPI (N-hydroxypthalimide) and cobalt catalysts [191]. Both these technologies have the potential to reduce upstream costs of blending higher octane fuels that would also need to be refilled by the vehicle driver.

The two set of injectors could also be used for water injection strategies to advance knock limit spark timing. Researchers have shown benefits of water injection are comparable to the use of cooled exhaust gas recirculation in effecting the working charge temperature [192]. Advancing knock limit using water injection will lead to more efficient engine operation and lower soot emissions as confirmed in Chapter 5.

7.2.3 Chapter 6: On-demand reactivity enhancement for practical implementation of GCI

The installation of the dual fuel injector and demonstration on the single cylinder engine showed potential for enhanced GCI performance by switching between fuels based on in-cylinder conditions. The next step towards practical implementation of GCI on a light-duty

platform would be to install such hardware on a multi-cylinder GCI engine. Once installed, the engine could be mapped to determine which locations on the speed-load map would require the injection of cetane enhanced gasoline. Furthermore, control algorithms could be installed in the engine control unit which would command cetane enhance gasoline injection based on feedback from lambda sensor in the exhaust. The lambda sensor can indicate when the engine is operating with low combustion efficiency.

After steady state mapping, transient test cycles could be run on the engine to quantify the consumption of cetane enhanced gasoline under simulated real world driving conditions. This is similar to the work of Roberts et al. [91] except for the fact that this would be a real transient cycle rather than a simulated one. This could then help the design team of the batch or flow reactor to accordingly design the size of the reactor such that enough quantities of peroxide containing cetane enhanced gasoline could be formulated.

To further justify the investment in hardware such as the QuantLogic adaptive dual fuel injector, it would be interesting to see the results of a cost benefit analysis that compares the performance of the dual fuel injector to two separate lower cost direct injectors or a combination of direct and port injectors.

7.3 Closing statement

While electrified powertrain architectures among light duty vehicles are growing at a rapid pace especially in the North American and European markets, energy outlook reports that are published annually predict gasoline powered internal combustion engines will continue to remain in some capacity in future production vehicles [1].

The investigation of Miller cycle on a current generation engine showed the potential to increase fuel economy and reduce NO_X emissions that will help meet future stringent carbon-di-oxide and criteria pollutant emissions standards. With hybrid powertrain architectures becoming popular among light duty vehicles, implementing Miller cycle on the engine working in conjunction with the battery of a full hybrid or a mild hybrid presents opportunities for further improvement. Switching to high-octane fuels at knock-limited conditions reduces both knock propensity as well as indirectly reduces particulate emissions based on the knock-soot correlation. Each cycle of engine knocking avoided ensures less particles emitted out the engine. Practical implementation of gasoline compression ignition for light duty vehicles and potentially replacing light-duty diesel engines can be realized by switching to high cetane gasoline at light loads.

This work demonstrated great promise of the suggested strategies to improve future light duty gasoline fueled engines. Allocation of resources by future engine manufacturers to implement these strategies in production vehicles can maximize the benefits while simultaneously addressing any drawbacks.

Appendices

A. MATLAB code for post processing Dragon Data

```
%%  DragonDataProcessing.m
%
%   BMTS Dragon Data processing
%   This is a master script containing all of the calculation steps for the
%   Dragon engine data (currently being used for the BMTS project)
%
%   Author: Kaustav Bhadra (kaustav@umich.edu)
%   Copyright 2021-2022 University of Michigan
%%  ***PROCESSING EXPERIMENTAL DATA***

%% Create the struct object that will contain the relevant data
Dragon = createstruct;
%%  Reading the txt file with all the relevant data exported via AVL concerto

Dragon.Data.Filename = '21_0406_BL_Hooks_1506.xlsx';

%%  Import the engine info into the struct object

Dragon = importEngineInfo(Dragon);
%% %%  Import the fuel info into the struct object

Dragon = importFuelInfo(Dragon);
%% Rearranging the scalar data from txt export for masterTable in Excel
spreadsheet
%Rearranging scalar data from txt export.

Dragon = importScalarData(Dragon);
%% Calculations based on Cylinder Pressure
Data(P,HRR,iEGR,Tgas,MFB,CALocations)
Dragon = importVectorData(Dragon);

%% Output Table for Spreadsheet
[Data_Table,CylP_Table,AHRR_Table,HRR_Table,TGas_Table,CALoc_Table,CALoc_Tabl
e2]= masterTable_Old(Dragon);

%% Enter the name of the mat file to which you want to save the data
%Preferably enter the date in the file name
save 21_0406_BL_Hooks_1506.mat; %Remember to change this name so as not to
overwrite the data
```

B. Uncertainty Analysis

The error bars denoting 95% confidence intervals on select plots in the dissertation was calculated using a couple different methods. Errors in cylinder pressure and fuel flow measurements used to determine brake specific fuel consumption (BSFC) were calculated using the zeroth-, first-, and Nth-order uncertainty analysis outlined by Moffat [193].

Emissions data, both gaseous emissions and particulate emissions as well as particle size distributions, had their 95% confidence interval calculated utilizing the standard error formula for a two- tailed distribution:

$$95\%\ CI = x \pm t\frac{\sigma}{\sqrt{n}}$$

where x is the mean value, σ is the standard deviation, n is the number of samples, and t is the t-score value for 95% confidence corresponding to n samples according to the t-distribution tables.

Degrees of freedom	Significance level					
	20% (0.20)	10% (0.10)	5% (0.05)	2% (0.02)	1% (0.01)	0.1% (0.001)
1	3.078	6.314	12.706	31.821	63.657	636.619
2	1.886	2.920	4.303	6.965	9.925	31.598
3	1.638	2.353	3.182	4.541	5.841	12.941
4	1.533	2.132	2.776	3.747	4.604	8.610
5	1.476	2.015	2.571	3.365	4.032	6.859
6	1.440	1.943	2.447	3.143	3.707	5.959
7	1.415	1.895	2.365	2.998	3.499	5.405
8	1.397	1.860	2.306	2.896	3.355	5.041
9	1.383	1.833	2.262	2.821	3.250	4.781
10	1.372	1.812	2.228	2.764	3.169	4.587
11	1.363	1.796	2.201	2.718	3.106	4.437
12	1.356	1.782	2.179	2.681	3.055	4.318
13	1.350	1.771	2.160	2.650	3.012	4.221
14	1.345	1.761	2.145	2.624	2.977	4.140
15	1.341	1.753	2.131	2.602	2.947	4.073
16	1.337	1.746	2.120	2.583	2.921	4.015
17	1.333	1.740	2.110	2.567	2.898	3.965
18	1.330	1.734	2.101	2.552	2.878	3.922
19	1.328	1.729	2.093	2.539	2.861	3.883
20	1.325	1.725	2.086	2.528	2.845	3.850
21	1.323	1.721	2.080	2.518	2.831	3.819
22	1.321	1.717	2.074	2.508	2.819	3.792
23	1.319	1.714	2.069	2.500	2.807	3.767
24	1.318	1.711	2.064	2.492	2.797	3.745
25	1.316	1.708	2.060	2.485	2.787	3.725
26	1.315	1.706	2.056	2.479	2.779	3.707
27	1.314	1.703	2.052	2.473	2.771	3.690
28	1.313	1.701	2.048	2.467	2.763	3.674
29	1.311	1.699	2.043	2.462	2.756	3.659
30	1.310	1.697	2.042	2.457	2.750	3.646
40	1.303	1.684	2.021	2.423	2.704	3.551
60	1.296	1.671	2.000	2.390	2.660	3.460
120	1.289	1.658	1.980	2.158	2.617	3.373
∞	1.282	1.645	1.960	2.326	2.576	3.291

Figure A 1: T-distribution table.

C. GT Power validation

The GT Power model used for the simulation efforts in Chapter 4 was validated against engine data obtained from the Ford Dragon engine after the installation of the BMTS floating nozzle turbocharger. Some plots depicting the iterative efforts to validate the simulation data against the engine data are shown below:

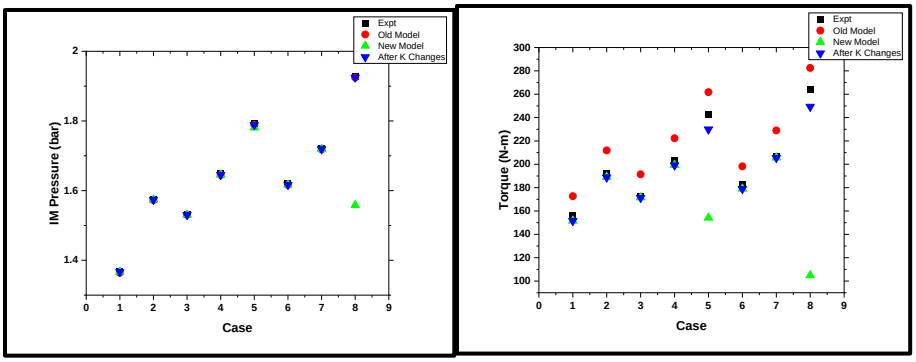

(a)

(b)

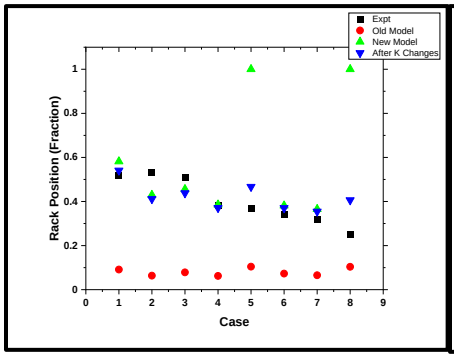

(c)

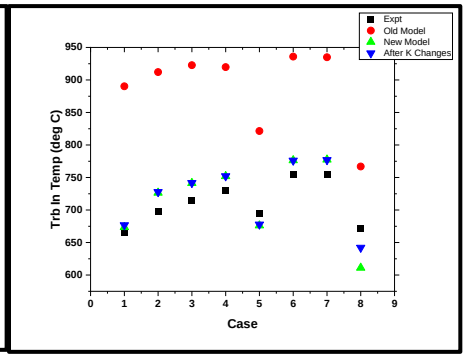

(d)

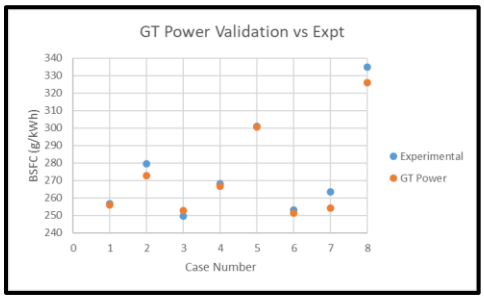

(e)

Figure A 2: Validation of GT Power model (a) Manifold pressure (b) Torque (c) Rack position (d) Turbine in temperature (e) Brake specific fuel consumption.

D. Injection Strategy Experimental Data (low load GCI stratification study)

The results of the effect of varying stratification levels on the performance and emissions of a GCI engine at low load are shown below:

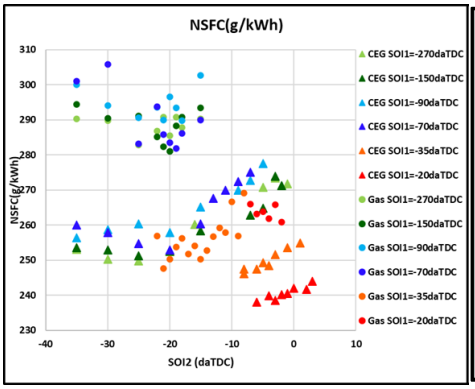

(a)

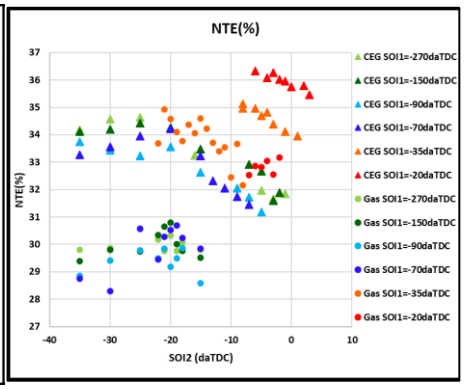

(b)

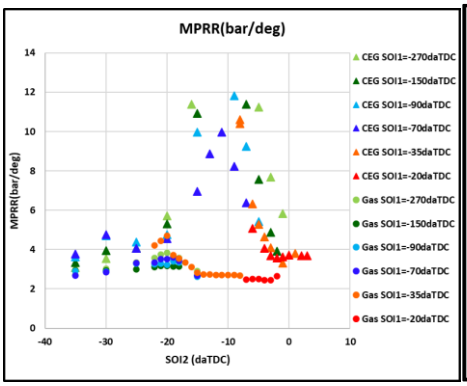

(c)

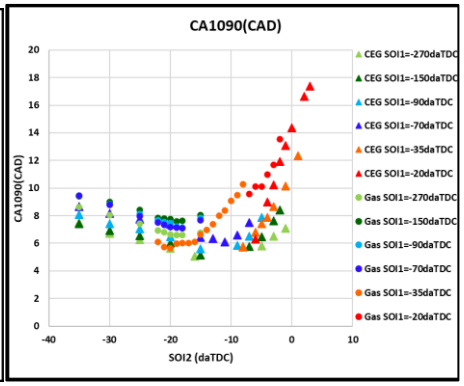

(d)

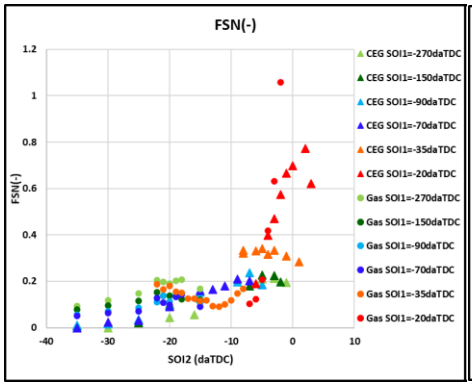

(e)

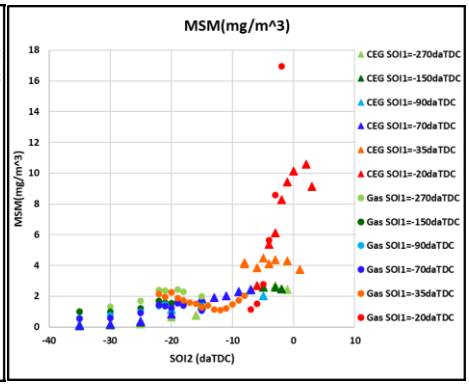

(f)

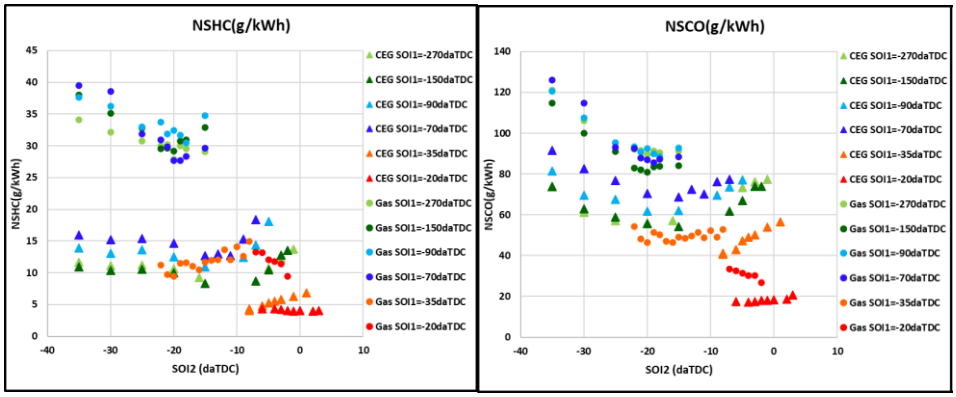

(g) (h)

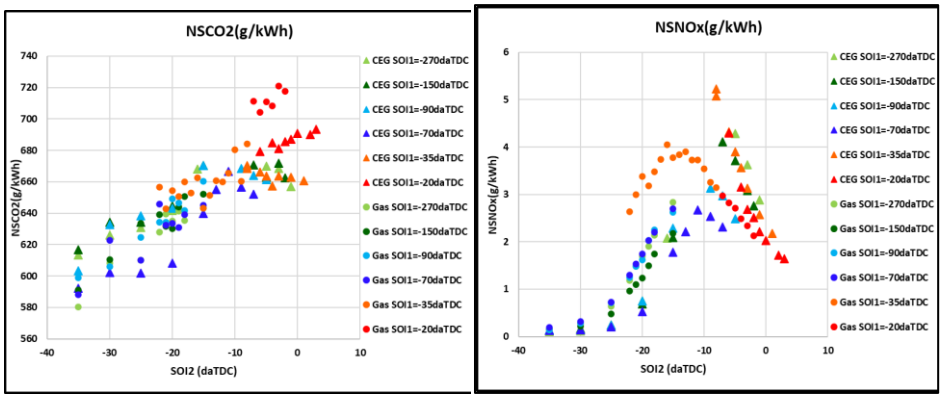

(i) (j)

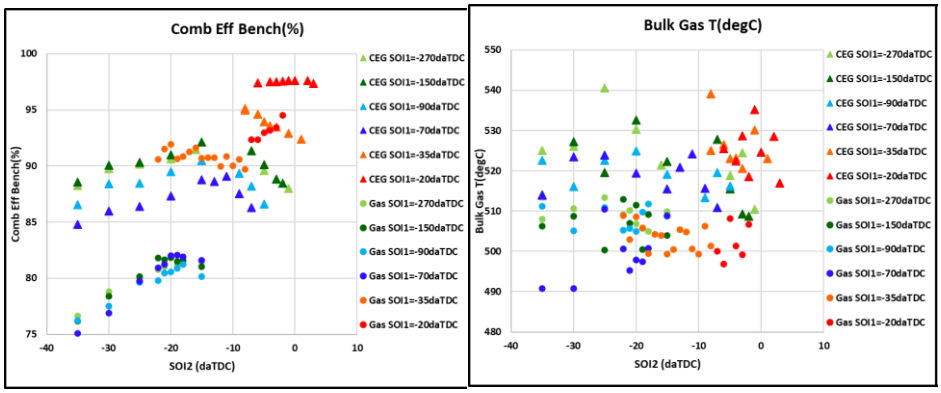

(k) (l)

Figure A 3: Results of varying levels of stratification at light loads on a gasoline compression ignition engine.

(a) Net specific fuel consumption (b) Net indicated thermal efficiency (c) Maximum pressure rise rate (d) CA1090 (e) Filter smoke number (f) Particulate mass measured by the microsoot meter (g) Net specific unburnt hydrocarbon emissions (h) Net specific carbon monoxide emissions (i) Net specific carbon dioxide emissions (j) Net specific NO_X emissions (k) Combustion efficiency (l) Bulk gas temperature

Bibliography

1. Energy Information Association, U.S., “Annual Energy Outlook,” 2022.
2. Energy Information Association, U.S., “International Energy Outlook,” 2021.
3. Reitz, R.D., Ogawa, H., Payri, R., Fansler, T., Kokjohn, S., Moriyoshi, Y., Agarwal, A.K., Arcoumanis, D., Assanis, D., Bae, C., Boulouchos, K., Canakci, M., Curran, S., Denbratt, I., Gavaises, M., Guenthner, M., Hasse, C., Huang, Z., Ishiyama, T., Johansson, B., Johnson, T. V., Kalghatgi, G., Koike, M., Kong, S.C., Leipertz, A., Miles, P., Novella, R., Onorati, A., Richter, M., et al., “IJER editorial: The future of the internal combustion engine,” *Int. J. Engine Res.* 21(1):3–10, 2020, doi:10.1177/1468087419877990.
4. Kalghatgi, G., Is it really the end of internal combustion engines and petroleum in transport?, *Appl. Energy* 225:965–974, 2018, doi:10.1016/j.apenergy.2018.05.076.
5. Kalghatgi, G., Development of Fuel/Engine Systems—The Way Forward to Sustainable Transport, *Engineering* 5(3):510–518, 2019, doi:10.1016/j.eng.2019.01.009.
6. Kalghatgi, G.T., “Developments in internal combustion engines and implications for combustion science and future transport fuels,” *Proc. Combust. Inst.* 35(1):101–115, 2015, doi:10.1016/j.proci.2014.10.002.
7. Chu, S. and Majumdar, A., “Opportunities and challenges for a sustainable energy future,” *Nature* 488(7411):294–303, 2012, doi:10.1038/nature11475.
8. Heywood, J.B., “Internal Combustion Engine Fundamentals,” 1988.
9. https://cartreatments.com/how-internal-combustion-engine-works/.
10. Allan T.Kirkpatrick, “Internal Combustion Engines: Applied Thermosciences,” ISBN 9781118533314, 1986.
11. Han, D., Han, S.K., Han, B.H., and Kim, W.T., “Development of 2.0L turbocharged DISI engine for downsizing application,” *SAE Tech. Pap.* (724), 2007, doi:10.4271/2007-01-0259.
12. Ito, N., Ohta, T., Kono, R., Arikawa, S., and Matsumoto, T., “Development of a 4-cylinder gasoline engine with a variable flow turbo-charger,” *SAE Tech. Pap.* (724), 2007, doi:10.4271/2007-01-0263.
13. Conway, G., Robertson, D., Chadwell, C., McDonald, J., Kargul, J., Barba, D., and Stuhldreher, M., “Evaluation of Emerging Technologies on a 1.6 L Turbocharged GDI Engine,” *SAE Tech. Pap.* 2018-April:1–15, 2018, doi:10.4271/2018-01-1423.
14. Isenstadt, A., German, J., Dorobantu, M., Boggs, D., and Watson, T., “Downsized, boosted gasoline engines,” *Internaltional Counc. Clean Transp.* (October 2016):23, 2016.
15. Fraser, N., Blaxill, H., Lumsden, G., and Bassett, M., “Challenges for increased efficiency

through gasoline engine downsizing," *SAE Tech. Pap.* 2(1):991–1008, 2009, doi:10.4271/2009-01-1053.
16. Wada, Y., Nakano, K., Mochizuki, K., and Hata, R., "Development of a New 1.5L I4 Turbocharged Gasoline Direct Injection Engine," *SAE Technical Papers*, SAE International, 2016, doi:10.4271/2016-01-1020.
17. Patil, C., Varade, S., and Wadkar, S., "A Review of Engine Downsizing and its Effects," *Int. J. Curr. Eng. Technol. IJCET INPRESSO Spec. Issue* 7(7):2277–4106, 2017.
18. Hancock, D., Fraser, N., Jeremy, M., Sykes, R., and Blaxill, H., "A new 3 cylinder 1.2l advanced downsizing technology demonstrator engine," *SAE Tech. Pap.* 2008(724):776–790, 2008, doi:10.4271/2008-01-0611.
19. Lee, W., Schubert, E., Li, Y., Li, S., Bobba, D., and Sarlioglu, B., "Overview of Electric Turbocharger and Supercharger for Downsized Internal Combustion Engines," *IEEE Trans. Transp. Electrif.* 3(1):36–47, 2017, doi:10.1109/TTE.2016.2620172.
20. Tang, H., Pennycott, A., Akehurst, S., and Brace, C.J., "A review of the application of variable geometry turbines to the downsized gasoline engine," *Int. J. Engine Res.* 16(6):810–825, 2015, doi:10.1177/1468087414552289.
21. Gabriel, H., Jacob, S., Münkel, U., Rodenhäuser, H., and Schmalzl, H.-P., "The turbocharger with variable turbine geometry for gasoline engines," *MTZ Worldw.* 68(2):7–10, 2007, doi:10.1007/BF03226804.
22. Wang, L.S. and Yang, S., "Turbo-Cool turbocharging system for spark ignition engines," *Proc. Inst. Mech. Eng. Part D J. Automob. Eng.* 220(8):1163–1175, 2006, doi:10.1243/09544070JAUTO172.
23. Uchida, H., "Transient performance prediction for turbocharging systems incorporating variable-geometry turbochargers," *R&D Rev. Toyota CRDL* 41(3):22–28, 2006.
24. Capobianco, M. and Gambarotta, A., "Variable geometry and waste-gated automotive turbochargers: Measurements and comparison of turbine performance," *J. Eng. Gas Turbines Power* 114(3):553–560, 1992, doi:10.1115/1.2906624.
25. Andersen, J., Karlsson, E., and Gawell, A., "Variable turbine geometry on SI engines," *SAE Tech. Pap.* 2006(724):776–790, 2006, doi:10.4271/2006-01-0020.
26. Arnold, S., Groskreutz, M., Shahed, S.M., and Slupski, K., "Advanced variable geometry turbocharger for diesel engine applications," *SAE Tech. Pap.* (724), 2002, doi:10.4271/2002-01-0161.
27. Bernard, L., Ferrari, A., Micelli, D., Perotto, A., Rinolfi, R., and Vattaneo, F., "Electro-hydraulic valve control with multiair technology," *MTZ Worldw.* 70(12):4–10, 2009, doi:10.1007/BF03226988.
28. Luttermann, C., Schünemann, E., and Klauer, N., "Enhanced VALVETRONIC technology for meeting SULEV emission requirements," *SAE Tech. Pap.* 2006(724), 2006, doi:10.4271/2006-01-0849.
29. Hu, B., Yang, J., Li, J., Li, S., and Bai, H., "Intelligent control strategy for transient response of a variable geometry turbocharger system based on deep reinforcement learning," *Processes* 7(9), 2019, doi:10.3390/pr7090601.
30. Han, T., "Strategies to Improve Efficiency and Emissions in Spark Ignition Engines," 2019.
31. Szybist, J.P., Busch, S., McCormick, R.L., Pihl, J.A., Splitter, D.A., Ratcliff, M.A., Kolodziej, C.P., Storey, J.M.E., Moses-DeBusk, M., Vuilleumier, D., Sjöberg, M., Sluder, C.S., Rockstroh, T., and Miles, P., "What fuel properties enable higher thermal efficiency

in spark-ignited engines?," *Prog. Energy Combust. Sci.* 82:100876, 2021, doi:10.1016/j.pecs.2020.100876.
32. Merola, S.S., Tornatore, C., and Irimescu, A., "Cycle-resolved visualization of pre-ignition and abnormal combustion phenomena in a GDI engine," *Energy Convers. Manag.* 127:380–391, 2016, doi:10.1016/j.enconman.2016.09.035.
33. Schießl, R. and Maas, U., "Analysis of endgas temperature fluctuations in an SI engine by laser-induced fluorescence," *Combust. Flame* 133(1–2):19–27, 2003, doi:10.1016/S0010-2180(02)00538-2.
34. Vuilleumier, D., Huan, X., Casey, T., and Sjöberg, M., "Uncertainty Assessment of Octane Index Framework for Stoichiometric Knock Limits of Co-Optima Gasoline Fuel Blends," *SAE Int. J. Fuels Lubr.* 11(3):247–270, 2018, doi:10.4271/04-11-03-0014.
35. Fouts, L.A., Fioroni, G.M., Christensen, E.D., Ratcliff, M.A., McCormick, R.L., Zigler, B.T., Sluder, S., Szybist, J.P., Dec, J.E., Miles, P.C., Ciatti, S., Bays, J.T., Pitz, W., and Mehl, M., "Co-Optimization of Fuels & Engines: Properties of Co-Optima Core Research Gasolines. Technical Report NREL/TP-5400-71341," (August), 2018.
36. Stansfield, P.A., Bisordi, A., OudeNijeweme, D., Williams, J., Gold, M., and Ali, R., "The Performance of a Modern Vehicle on a Variety of Alcohol-Gasoline Fuel Blends," *SAE Int. J. Fuels Lubr.* 5(2):813–822, 2012, doi:10.4271/2012-01-1272.
37. Han, T., Lavoie, G., Wooldridge, M., and Boehman, A., "Dual Fuel Injection (DI + PFI) for Knock and EGR Dilution Limit Extension in a Boosted SI Engine," *SAE Tech. Pap.* 2018-Septe:1–14, 2018, doi:10.4271/2018-01-1735.
38. Singh, R., Burch, T., Lavoie, G., Wooldridge, M., and Fatouraie, M., "Effects of Fuel Injection Events of Ethanol and Gasoline Blends on Boosted Direct-Injection Engine Performance," *SAE Tech. Pap.* 2017-Octob, 2017, doi:10.4271/2017-01-2238.
39. Wang, Z., Liu, H., Long, Y., Wang, J., and He, X., "Comparative study on alcohols-gasoline and gasoline-alcohols dual-fuel spark ignition (DFSI) combustion for high load extension and high fuel efficiency," *Energy* 82:395–405, 2015, doi:10.1016/j.energy.2015.01.049.
40. Szybist, J.P., Youngquist, A.D., Barone, T.L., Storey, J.M., Moore, W.R., Foster, M., and Confer, K., "Ethanol blends and engine operating strategy effects on light-duty spark-ignition engine particle emissions," *Energy and Fuels* 25(11):4977–4985, 2011, doi:10.1021/ef201127y.
41. Singh, R., "Enabling Ethanol Use as a Renewable Transportation Fuel : A Micro- and Macro-scale Perspective," 2019.
42. Vuilleumier, D. and Sjöberg, M., "Significance of RON, MON, and LTHR for Knock Limits of Compositionally Dissimilar Gasoline Fuels in a DISI Engine," *SAE Int. J. Engines* 10(3):938–950, 2017, doi:10.4271/2017-01-0662.
43. Cooper, A., Harrington, A., Bassett, M., Reader, S., and Bunce, M., "Application of the Passive MAHLE Jet Ignition System and Synergies with Miller Cycle and Exhaust Gas Recirculation," *SAE Technical Papers*, SAE International, 2020, doi:10.4271/2020-01-0283.
44. Caton, J.A., "A comparison of lean operation and exhaust gas recirculation: Thermodynamic reasons for the increases of efficiency," *SAE Tech. Pap.* 2, 2013, doi:10.4271/2013-01-0266.
45. Caton, J.A., "A thermodynamic comparison of external and internal exhaust gas dilution for high-efficiency internal combustion engines," *Int. J. Engine Res.* 16(8):935–955, 2015,

doi:10.1177/1468087414560593.
46. Siokos, K., Koli, R., Prucka, R., Schwanke, J., and Miersch, J., "Assessment of Cooled Low Pressure EGR in a Turbocharged Direct Injection Gasoline Engine," *SAE Int. J. Engines* 8(4):1535–1543, 2015, doi:10.4271/2015-01-1253.
47. Kargul, J., Stuhldreher, M., Barba, D., Schenk, C., Bohac, S., McDonald, J., Dekraker, P., and Alden, J., "Benchmarking a 2018 Toyota Camry 2.5-liter atkinson cycle engine with cooled-EGR," *SAE Technical Papers*, SAE International, 2019, doi:10.4271/2019-01-0249.
48. Nazari, S., Stefanopoulou, A., Kiwan, R., and Tsourapas, V., "A coordinated boost control in a twincharged spark ignition engine with high external dilution," *ASME 2016 Dyn. Syst. Control Conf. DSCC 2016* 2:1–8, 2016, doi:10.1115/DSCC2016-9691.
49. Szybist, J.P., Wagnon, S.W., Splitter, D., Pitz, W.J., and Mehl, M., "The Reduced Effectiveness of EGR to Mitigate Knock at High Loads in Boosted SI Engines," *SAE Int. J. Engines* 10(5), 2017, doi:10.4271/2017-24-0061.
50. Szybist, J.P. and West, B.H., "The Impact of Low Octane Hydrocarbon Blending Streams on the Knock Limit of 'E85,'" *SAE Int. J. Fuels Lubr.* 6(1):44–54, 2013, doi:10.4271/2013-01-0888.
51. Mikalsen, R., Wang, Y.D., and Roskilly, A.P., "A comparison of Miller and Otto cycle natural gas engines for small scale CHP applications," *Appl. Energy* 86(6):922–927, 2009, doi:10.1016/j.apenergy.2008.09.021.
52. Li, T., Gao, Y., Wang, J., and Chen, Z., "The Miller cycle effects on improvement of fuel economy in a highly boosted, high compression ratio, direct-injection gasoline engine: EIVC vs. LIVC," *Energy Convers. Manag.* 79:59–65, 2014, doi:10.1016/j.enconman.2013.12.022.
53. Aramco Technical Seminar, NUMERICAL MODELING AND ANALYSIS OF SOOT FORMATION IN GDI ENGINES.
54. https://www.visualcapitalist.com/wp-content/uploads/2020/10/relative-size-of-particles-infographic.html.
55. Eastwood, P., "Particulate Emissions from Vehicles," John Wiley & Sons, Ltd.: Hoboken, NJ, USA., 2008.
56. Kwon, H.S., Ryu, M.H., and Carlsten, C., "Ultrafine particles: unique physicochemical properties relevant to health and disease," *Exp. Mol. Med.* 52(3):318–328, 2020, doi:10.1038/s12276-020-0405-1.
57. Raza, M., Chen, L., Leach, F., and Ding, S., "A Review of particulate number (PN) emissions from gasoline direct injection (gdi) engines and their control techniques," *Energies* 11(6), 2018, doi:10.3390/en11061417.
58. Sonntag, D.B., Bailey, C.R., Fulper, C.R., and Baldauf, R.W., "Contribution of lubricating oil to particulate matter emissions from light-duty gasoline vehicles in Kansas City," *Environ. Sci. Technol.* 46(7):4191–4199, 2012, doi:10.1021/es203747f.
59. Violi, A., D'Anna, A., and D'Alessio, A., "Modeling of particulate formation in combustion and pyrolysis," *Chem. Eng. Sci.* 54(15–16):3433–3442, 1999, doi:10.1016/S0009-2509(98)00460-6.
60. Dec, J.E., "A Conceptual Model of DI Diesel Combustion Based on Laser-Sheet Imaging*."
61. Curran, S., Szybist, J., Kaul, B., Easter, J., and Sluder, S., "Fuel Stratification Effects on Gasoline Compression Ignition with a Regular-Grade Gasoline on a Single-Cylinder

Medium-Duty Diesel Engine at Low Load," *SAE Technical Papers*, SAE International, 2021, doi:10.4271/2021-01-1173.
62. Alriksson, M. and Denbratt, I., "Low temperature combustion in a heavy duty diesel engine using high levels of EGR," *SAE Tech. Pap.* 2006(724), 2006, doi:10.4271/2006-01-0075.
63. Feng, H., Zheng, Z., Yao, M., Cheng, G., Wang, M., and Wang, X., "Effects of exhaust gas recirculation on low temperature combustion using wide distillation range diesel," *Energy* 51:291–296, 2013, doi:10.1016/j.energy.2012.12.023.
64. Maiboom, A., Tauzia, X., Hétet, J.F., Cormerais, M., Tounsi, M., Jaine, T., and Blanchin, S., "Various effects of EGR on combustion and emissions on an automotive di diesel engine: Numerical and experimental study," *SAE Tech. Pap.*, 2007, doi:10.4271/2007-01-1834.
65. Sarangi, A.K., McTaggart-Cowan, G.P., and Garner, C.P., "The effects of intake pressure on high EGR low temperature diesel engine combustion," *SAE Tech. Pap.* (X), 2010, doi:10.4271/2010-01-2145.
66. Zhu, H., Bohac, S. V., Nakashima, K., Hagen, L.M., Huang, Z., and Assanis, D.N., "Effect of biodiesel and ethanol on load limits of high-efficiency premixed low-temperature combustion in a diesel engine," *Fuel* 106(x):773–778, 2013, doi:10.1016/j.fuel.2012.10.073.
67. Krishnasamy, A., Gupta, S.K., and Reitz, R.D., "Prospective fuels for diesel low temperature combustion engine applications: A critical review," *Int. J. Engine Res.* 22(7):2071–2106, 2021, doi:10.1177/1468087420960857.
68. Lilik, G.K. and Boehman, A.L., "Advanced diesel combustion of a high cetane number fuel with low hydrocarbon and carbon monoxide emissions," *Energy and Fuels* 25(4):1444–1456, 2011, doi:10.1021/ef101653h.
69. Tanaka, S., Ayala, F., Keck, J.C., and Heywood, J.B., "Two-stage ignition in HCCI combustion and HCCI control by fuels and additives," 2003.
70. Kalghatgi, G.T., Auto-Ignition Quality of Practical Fuels and Implications for Fuel Requirements of Future SI and HCCI Engines, 2005, doi:10.4271/2005-01-0239.
71. Hyvönen, J., Haraldsson, G., and Johansson, B., "Supercharging HCCI to extend the operating range in a multi-cylinder VCR-HCCI engine," *SAE Tech. Pap.* 2003(724), 2003, doi:10.4271/2003-01-3214.
72. Olsson, J.O., Tunestål, P., and Johansson, B., "Boosting for high load HCCI," *SAE Tech. Pap.* 2004(724), 2004, doi:10.4271/2004-01-0940.
73. Sjöberg, M. and Dec, J.E., "Comparing late-cycle autoignition stability for single- and two-stage ignition fuels in HCCI engines," *Proc. Combust. Inst.* 31 II:2895–2902, 2007, doi:10.1016/j.proci.2006.08.010.
74. Janecek, D., Rothamer, D., and Ghandhi, J., "Investigation of cetane number and octane number correlation under homogenous-charge compression-ignition engine operation," *Proc. Combust. Inst.* 36(3):3651–3657, 2017, doi:10.1016/j.proci.2016.08.015.
75. Dempsey, A.B., Curran, S.J., and Wagner, R.M., A perspective on the range of gasoline compression ignition combustion strategies for high engine efficiency and low NOx and soot emissions: Effects of in-cylinder fuel stratification, *Int. J. Engine Res.* 17(8):897–917, 2016, doi:10.1177/1468087415621805.
76. Borgqvist, P., Tunestal, P., and Johansson, B., "Comparison of negative valve overlap (NVO) and rebreathing valve strategies on a gasoline PPC engine at low load and idle

operating conditions," *SAE Int. J. Engines* 6(1):366–378, 2013, doi:10.4271/2013-01-0902.
77. Scott Curran, Vitaly Prikhodko, Kukwon Cho, Charles Sluder, James Parks and Robert Wagner, S.K. and R.R., "In-Cylinder Fuel Blending of Gasoline/Diesel for Improved Efficiency and Lowest Possible Emissions on a Multi-Cylinder Light-Duty Diesel Engine."
78. Kalghatgi, G.T., Solutions, G., Risberg, P., and Ångström, H.-E., "Partially Pre-Mixed Auto-Ignition of Gasoline to Attain Low Smoke and Low NOx at High Load in a Compression Ignition Engine and Comparison with a Diesel Fuel," 2007.
79. Chang, J., Kalghatgi, G., Amer, A., and Viollet, Y., "Enabling high efficiency direct injection engine with naphtha fuel through partially premixed charge compression ignition combustion," *SAE Technical Papers*, SAE International, 2012, doi:10.4271/2012-01-0677.
80. Dec, J.E., Yang, Y., Dernotte, J., and Ji, C., "Effects of Gasoline Reactivity and Ethanol Content on Boosted, Premixed and Partially Stratified Low-Temperature Gasoline Combustion (LTGC)," *SAE Int. J. Engines* 8(3):935–955, 2015, doi:10.4271/2015-01-0813.
81. Zhang, Y., Kumar, P., Traver, M., and Cleary, D., "Conventional and Low Temperature Combustion Using Naphtha Fuels in a Multi-Cylinder Heavy-Duty Diesel Engine," *SAE Int. J. Engines* 9(2):1021–1035, 2016, doi:10.4271/2016-01-0764.
82. Zhang, Y., Sommers, S., Pei, Y., Kumar, P., Voice, A., Traver, M., and Cleary, D., "Mixing-Controlled Combustion of Conventional and Higher Reactivity Gasolines in a Multi-Cylinder Heavy-Duty Compression Ignition Engine," *SAE Technical Papers*, SAE International, 2017, doi:10.4271/2017-01-0696.
83. Cho, K., Zhao, L., Ameen, M., Zhang, Y., Pei, Y., Moore, W., and Sellnau, M., "Understanding fuel stratification effects on partially premixed compression ignition (PPCI) combustion and emissions behaviors," *SAE Technical Papers*, SAE International, 2019, doi:10.4271/2019-01-1145.
84. Sellnau, M., Sinnamon, J., Hoyer, K., and Husted, H., "Gasoline Direct Injection Compression Ignition (GDCI) - Diesel-like Efficiency with Low CO2 Emissions," *SAE Int. J. Engines* 4(1):2010–2022, 2011, doi:10.4271/2011-01-1386.
85. Sellnau, M.C., Sinnamon, J., Hoyer, K., and Husted, H., "Full-Time Gasoline Direct-Injection Compression Ignition (GDCI) for High Efficiency and Low NOx and PM," *SAE Int. J. Engines* 5(2):300–314, 2012, doi:10.4271/2012-01-0384.
86. Kolodziej, C., Kodavasal, J., Ciatti, S., Som, S., Shidore, N., and Delhom, J., "Achieving Stable Engine Operation of Gasoline Compression Ignition Using 87 AKI Gasoline Down to Idle," *SAE Technical Papers*, SAE International, 2015, doi:10.4271/2015-01-0832.
87. Sellnau, M., Moore, W., Sinnamon, J., Hoyer, K., Foster, M., and Husted, H., "GDCI Multi-Cylinder Engine for High Fuel Efficiency and Low Emissions," *SAE Int. J. Engines* 8(2):775–790, 2015, doi:10.4271/2015-01-0834.
88. Kolodziej, C.P., Sellnau, M., Cho, K., and Cleary, D., "Operation of a Gasoline Direct Injection Compression Ignition Engine on Naphtha and E10 Gasoline Fuels," *SAE Int. J. Engines* 9(2):979–1001, 2016, doi:10.4271/2016-01-0759.
89. Cho, K., Latimer, E., Lorey, M., Cleary, D.J., and Sellnau, M., "Gasoline Fuels Assessment for Delphi's Second Generation Gasoline Direct-Injection Compression Ignition (GDCI) Multi-Cylinder Engine," *SAE Int. J. Engines* 10(4):1430–1442, 2017,

doi:10.4271/2017-01-0743.
90. Zhang, Y., Kumar, P., Pei, Y., Traver, M., and Cleary, D., "An Experimental and Computational Investigation of Gasoline Compression Ignition Using Conventional and Higher Reactivity Gasolines in a Multi-Cylinder Heavy-Duty Diesel Engine," *SAE Technical Papers*, SAE International, 2018, doi:10.4271/2018-01-0226.
91. Roberts, J., Kokjohn, S., Hou, D., and Huang, Y., "Performance of Gasoline Compression Ignition (GCI) with On-Demand Reactivity Enhancement over Simulated Drive Cycles," *SAE Technical Papers*, SAE International, 2018, doi:10.4271/2018-01-0255.
92. Kalghatgi, G.T., Risberg, P., and Ångström, H.E., "Partially pre-mixed auto-ignition of gasoline to attain low smoke and low NOx at high load in a compression ignition engine and comparison with a diesel fuel," *SAE Technical Papers*, SAE International, 2007, doi:10.4271/2007-01-0006.
93. Kalghatgi, G., Hildingsson, L., and Johansson, B., "Low NOx and low smoke operation of a diesel engine using gasolinelike fuels," *J. Eng. Gas Turbines Power* 132(9):1–9, 2010, doi:10.1115/1.4000602.
94. Zhang, Y. and Sellnau, M., "A Computational Investigation of PPCI-Diffusion Combustion Strategy at Full Load in a Light-Duty GCI Engine," *SAE Technical Papers*, SAE International, 2021, doi:10.4271/2021-01-0514.
95. Cheng, S., Goldsborough, S.S., Wagnon, S.W., Whitesides, R., McNenly, M., Pitz, W.J., Lopez-Pintor, D., and Dec, J.E., "Replicating HCCI-like autoignition behavior: What gasoline surrogate fidelity is needed?," *Appl. Energy Combust. Sci.* 12(May):100091, 2022, doi:10.1016/j.jaecs.2022.100091.
96. Sellnau, M., Foster, M., Hoyer, K., Moore, W., Sinnamon, J., and Husted, H., "Development of a Gasoline Direct Injection Compression Ignition (GDCI) Engine," *SAE Int. J. Engines* 7(2):835–851, 2014, doi:10.4271/2014-01-1300.
97. Sellnau, M., Foster, M., Moore, W., Sinnamon, J., Hoyer, K., and Klemm, W., "Second Generation GDCI Multi-Cylinder Engine for High Fuel Efficiency and US Tier 3 Emissions," *SAE Int. J. Engines* 9(2):1002–1020, 2016, doi:10.4271/2016-01-0760.
98. Sellnau, M., Hoyer, K., Moore, W., Foster, M., Sinnamon, J., and Klemm, W., "Advancement of GDCI Engine Technology for US 2025 CAFE and Tier 3 Emissions," *SAE Tech. Pap.* 2018-April:1–16, 2018, doi:10.4271/2018-01-0901.
99. Sellnau, M., Foster, M., Moore, W., Sinnamon, J., Hoyer, K., and Klemm, W., "Pathway to 50% brake thermal efficiency using gasoline direct injection compression ignition," *SAE Tech. Pap.* 2019-April(April):1581–1603, 2019, doi:10.4271/2019-01-1154.
100. Martin, J. and Boehman, A., "Mapping the combustion modes of a dual-fuel compression ignition engine," *Int. J. Engine Res.* 23(9):1453–1474, 2022, doi:10.1177/14680874211018376.
101. Ortiz-Soto, E.A., Lavoie, G.A., Martz, J.B., Wooldridge, M.S., and Assanis, D.N., "Enhanced heat release analysis for advanced multi-mode combustion engine experiments," *Appl. Energy* 136:465–479, 2014, doi:10.1016/j.apenergy.2014.09.038.
102. Kalghatgi, G. and Johansson, B., "Gasoline compression ignition approach to efficient, clean and affordable future engines," *Proc. Inst. Mech. Eng. Part D J. Automob. Eng.* 232(1):118–138, 2018, doi:10.1177/0954407017694275.
103. Shahlari, A.J. and Ghandhi, J.B., "A comparison of engine knock metrics," *SAE Technical Papers*, SAE International, 2012, doi:10.4271/2012-32-0007.
104. Zhen, X., Wang, Y., Xu, S., Zhu, Y., Tao, C., Xu, T., and Song, M., "The engine knock

analysis - An overview," *Appl. Energy* 92:628–636, 2012, doi:10.1016/j.apenergy.2011.11.079.
105. Rockstroh, T., Kolodziej, C.P., Jespersen, M.C., Goldsborough, S.S., and Wallner, T., "Insights into Engine Knock: Comparison of Knock Metrics across Ranges of Intake Temperature and Pressure in the CFR Engine," *SAE Int. J. Fuels Lubr.* 11(4):545–561, 2018, doi:10.4271/2018-01-0210.
106. Martins, J.J.G., Uzuneanu, K., Ribeiro, B.S., and Jasasky, O., "Thermodynamic analysis of an over-expanded engine," *SAE Tech. Pap.* (724), 2004, doi:10.4271/2004-01-0617.
107. Al-Sarkhi, A., Jaber, J.O., and Probert, S.D., "Efficiency of a Miller engine," *Appl. Energy* 83(4):343–351, 2006, doi:10.1016/j.apenergy.2005.04.003.
108. Zhao, Y. and Chen, J., "Performance analysis of an irreversible Miller heat engine and its optimum criteria," *Appl. Therm. Eng.* 27(11–12):2051–2058, 2007, doi:10.1016/j.applthermaleng.2006.12.002.
109. Ribeiro, B. and Martins, J., "Direct comparison of an engine working under Otto, Miller and diesel cycles: Thermodynamic analysis and real engine performance," *SAE Tech. Pap.* (724), 2007, doi:10.4271/2007-01-0261.
110. Wang, Y., Lin, L., Roskilly, A.P., Zeng, S., Huang, J., He, Y., Huang, X., Huang, H., Wei, H., Li, S., and Yang, J., "An analytic study of applying Miller cycle to reduce NOx emission from petrol engine," *Appl. Therm. Eng.* 27(11–12):1779–1789, 2007, doi:10.1016/j.applthermaleng.2007.01.013.
111. Wang, Y., Lin, L., Zeng, S., Huang, J., Roskilly, A.P., He, Y., Huang, X., and Li, S., "Application of the Miller cycle to reduce NOx emissions from petrol engines," *Appl. Energy* 85(6):463–474, 2008, doi:10.1016/j.apenergy.2007.10.009.
112. Wei, H., Yu, J., and Zhou, L., "Improvement of engine performance with high compression ratio based on knock suppression using Miller cycle with boost pressure and split injection," *Front. Energy* 13(4):691–706, 2019, doi:10.1007/s11708-019-0621-3.
113. Bozza, F., Bellis, V. De, Gimelli, A., and Muccillo, M., "Strategies for Improving Fuel Consumption at Part-Load in a Downsized Turbocharged SI Engine: a Comparative Study," *SAE Int. J. Engines* 7(1):60–71, 2014, doi:10.4271/2014-01-1064.
114. Luisi, S., Doria, V., Stroppiana, A., Millo, F., and Mirzaeian, M., "Experimental Investigation on Early and Late Intake Valve Closures for Knock Mitigation through Miller Cycle in a Downsized Turbocharged Engine," *SAE Tech. Pap.* 2015-April(April), 2015, doi:10.4271/2015-01-0760.
115. Wei, H., Shao, A., Hua, J., Zhou, L., and Feng, D., "Effects of applying a Miller cycle with split injection on engine performance and knock resistance in a downsized gasoline engine," *Fuel* 214(June 2017):98–107, 2018, doi:10.1016/j.fuel.2017.11.006.
116. Shen, K., Xu, Z., Chen, H., and Zhang, Z., "Investigation on the EGR effect to further improve fuel economy and emissions effect of Miller cycle turbocharged engine," *Energy* 215, 2021, doi:10.1016/j.energy.2020.119116.
117. Al-Hasan, N., Beer, J., Ehrhard, J., Lorenz, T., and Stump, L., "Charging Technologies for CO2 Optimization by Millerization," *SAE Tech. Pap.* 2015-April(April), 2015, doi:10.4271/2015-01-1250.
118. Ellies, B., Schenk, C., and Dekraker, P., "Benchmarking and Hardware-in-the-Loop Operation of a 2014 MAZDA SkyActiv 2.0L 13:1 Compression Ratio Engine," *SAE Tech. Pap.*, 2016, doi:10.4271/2016-01-1007.
119. Stuhldreher, M., Kargul, J., Barba, D., McDonald, J., Bohac, S., Dekraker, P., and

Moskalik, A., “Benchmarking a 2016 Honda Civic 1.5-Liter L15B7 Turbocharged Engine and Evaluating the Future Efficiency Potential of Turbocharged Engines,” *SAE Int. J. Engines* 11(6):1273–1305, 2018, doi:10.4271/2018-01-0319.
120. Roper, E., Wang, Y., and Zhang, Z., “Numerical Investigation of the Application of Miller Cycle and Low-Carbon Fuels to Increase Diesel Engine Efficiency and Reduce Emissions,” *Energies* 15(5), 2022, doi:10.3390/en15051783.
121. Deng, B., Li, Q., Chen, Y., Li, M., Liu, A., Ran, J., Xu, Y., Liu, X., Fu, J., and Feng, R., “The effect of air/fuel ratio on the CO and NOx emissions for a twin-spark motorcycle gasoline engine under wide range of operating conditions,” *Energy* 169:1202–1213, 2019, doi:10.1016/j.energy.2018.12.113.
122. Leach, F., Chapman, E., Jetter, J.J., Rubino, L., Christensen, E.D., John, P.C. St., Fioroni, G.M., and McCormick, R.L., “A Review and Perspective on Particulate Matter Indices Linking Fuel Composition to Particulate Emissions from Gasoline Engines,” *SAE Int. J. Fuels Lubr.* 15(1), 2021, doi:10.4271/04-15-01-0001.
123. Pirjola, L., Karjalainen, P., Heikkilä, J., Saari, S., Tzamkiozis, T., Ntziachristos, L., Kulmala, K., Keskinen, J., and Rönkkö, T., “Effects of fresh lubricant oils on particle emissions emitted by a modern gasoline direct injection passenger car,” *Environ. Sci. Technol.* 49(6):3644–3652, 2015, doi:10.1021/es505109u.
124. Joshi, A., “Review of Vehicle Engine Efficiency and Emissions,” *SAE Tech. Pap.* 2020-April(April):734–761, 2020, doi:10.4271/2020-01-0352.
125. Giechaskiel, B., Joshi, A., Ntziachristos, L., and Dilara, P., “European regulatory framework and particulate matter emissions of gasoline light-duty vehicles: A review,” *Catalysts* 9(7), 2019, doi:10.3390/catal9070586.
126. Frenklach, M., “Reaction mechanism of soot formation in flames,” *Phys. Chem. Chem. Phys.* 4(11):2028–2037, 2002, doi:10.1039/b110045a.
127. Michelsen, H.A., Colket, M.B., Bengtsson, P.E., D’Anna, A., Desgroux, P., Haynes, B.S., Miller, J.H., Nathan, G.J., Pitsch, H., and Wang, H., “A review of terminology used to describe soot formation and evolution under combustion and pyrolytic conditions,” *ACS Nano* 14(10):12470–12490, 2020, doi:10.1021/acsnano.0c06226.
128. Bockhorn, H., “Ultrafine particles from combustion sources: Approaches to what we want to know,” *Philos. Trans. R. Soc. A Math. Phys. Eng. Sci.* 358(1775):2659–2672, 2000, doi:10.1098/rsta.2000.0675.
129. Frenklach, M., Clary, D.W., Yuan, T., Gardiner, W.C., and Stein, S.E., “Mechanism of Soot Formation in Acetylene-Oxygen Mixtures,” ISBN 0010220860, 1986, doi:10.1080/00102208608923927.
130. Frenklach, M., Clary, D.W., Gardiner, W.C., and Stein, S.E., “Effect of fuel structure on pathways to soot,” *Symp. Combust.* 21(1):1067–1076, 1988, doi:10.1016/S0082-0784(88)80337-0.
131. Frenklach, M., Clary, D.W., Gardiner, W.C., and Stein, S.E., “Detailed kinetic modeling of soot formation in shock-tube pyrolysis of acetylene,” *Symp. Combust.* 20(1):887–901, 1985, doi:10.1016/S0082-0784(85)80578-6.
132. Frenklach, M., Yuan, T., and Ramachandra, M.K., “Soot Formation in Binary Hydrocarbon Mixtures,” *Energy and Fuels* 2(4):462–480, 1988, doi:10.1021/ef00010a013.
133. Frenklach, M. and Warnatz, J., “Detailed Modeling of PAH Profiles in a Sooting Low-Pressure Acetylene Flame,” *Combust. Sci. Technol.* 51(4–6):265–283, 1987,

doi:10.1080/00102208708960325.
134. Frenklach, M. and Wang, H., “Detailed modeling of soot particle nucleation and growth,” *Symp. Combust.* 23(1):1559–1566, 1991, doi:10.1016/S0082-0784(06)80426-1.
135. Wang, H. and Frenklach, M., “A detailed kinetic modeling study of aromatics formation in laminar premixed acetylene and ethylene flames,” *Combust. Flame* 110(1–2):173–221, 1997, doi:10.1016/S0010-2180(97)00068-0.
136. Wang, H., Du, D.X., Sung, C.J., and Law, C.K., “Experiments and numerical simulation on soot formation in opposed-jet ethylene diffusion flames,” *Symp. Combust.* 26(2):2359–2368, 1996, doi:10.1016/S0082-0784(96)80065-8.
137. Ohlwein, S., Kappeler, R., Kutlar Joss, M., Künzli, N., and Hoffmann, B., “Health effects of ultrafine particles: a systematic literature review update of epidemiological evidence,” *Int. J. Public Health* 64(4):547–559, 2019, doi:10.1007/s00038-019-01202-7.
138. Liu, C., Chen, R., Sera, F., Vicedo-Cabrera, A.M., Guo, Y., Tong, S., Coelho, M.S.Z.S., Saldiva, P.H.N., Lavigne, E., Matus, P., Valdes Ortega, N., Osorio Garcia, S., Pascal, M., Stafoggia, M., Scortichini, M., Hashizume, M., Honda, Y., Hurtado-Díaz, M., Cruz, J., Nunes, B., Teixeira, J.P., Kim, H., Tobias, A., Íñiguez, C., Forsberg, B., Åström, C., Ragettli, M.S., Guo, Y.-L., Chen, B.-Y., et al., “Ambient Particulate Air Pollution and Daily Mortality in 652 Cities,” *N. Engl. J. Med.* 381(8):705–715, 2019, doi:10.1056/nejmoa1817364.
139. Powell, T.R., Szybist, J.P., Dal Forno Chuahy, F., Curran, S.J., Mengwasser, J., Aradi, A., and Cracknell, R., “Octane Index Applicability over the Pressure-Temperature Domain,” *Energies* 14(3):607, 2021, doi:10.3390/en14030607.
140. Szybist, J.P. and Splitter, D.A., “Pressure and temperature effects on fuels with varying octane sensitivity at high load in SI engines,” *Combust. Flame* 177:49–66, 2017, doi:10.1016/j.combustflame.2016.12.002.
141. Mittal, V., Heywood, J.B., and Green, W.H., “The underlying physics and chemistry behind fuel sensitivity,” *SAE Tech. Pap.* 3(1):256–265, 2010, doi:10.4271/2010-01-0617.
142. Perceau, M., Guibert, P., Guilain, S., Segretain, F., Redlinger, T., Université, S., and Jean, I., “Why can Miller cycle improve the overall efficiency of gasoline engines ?,” (September):1–20, 2020.
143. Stuhldreher, M., Schenk, C., Brakora, J., Hawkins, D., Moskalik, A., and Dekraker, P., “Downsized Boosted Engine Benchmarking and Results,” *SAE Tech. Pap.* 2015-April(April), 2015, doi:10.4271/2015-01-1266.
144. Bahreini, R., Xue, J., Johnson, K., Durbin, T., Quiros, D., Hu, S., Huai, T., Ayala, A., and Jung, H., “Characterizing emissions and optical properties of particulate matter from PFI and GDI light-duty gasoline vehicles,” *J. Aerosol Sci.* 90:144–153, 2015, doi:10.1016/j.jaerosci.2015.08.011.
145. Chen, L., Liang, Z., Zhang, X., and Shuai, S., “Characterizing particulate matter emissions from GDI and PFI vehicles under transient and cold start conditions,” *Fuel* 189:131–140, 2017, doi:10.1016/j.fuel.2016.10.055.
146. Fu, H., Wang, Y., Li, X., and Shuai, S.J., “Impacts of Cold-Start and Gasoline RON on Particulate Emission from Vehicles Powered by GDI and PFI Engines,” *SAE Tech. Pap.* 2014-Octob, 2014, doi:10.4271/2014-01-2836.
147. He, X., Ratcliff, M.A., and Zigler, B.T., “Effects of gasoline direct injection engine operating parameters on particle number emissions,” *Energy and Fuels* 26(4):2014–2027, 2012, doi:10.1021/ef201917p.

148. Aikawa, K., Sakurai, T., and Jetter, J.J., "Development of a predictive model for gasoline vehicle particulate matter emissions," *SAE Tech. Pap.* 3(2):610–622, 2010, doi:10.4271/2010-01-2115.
149. Aikawa, K. and Jetter, J.J., "Impact of gasoline composition on particulate matter emissions from a direct-injection gasoline engine: Applicability of the particulate matter index," *Int. J. Engine Res.* 15(3):298–306, 2014, doi:10.1177/1468087413481216.
150. Barrientos, E.J., Lapuerta, M., and Boehman, A.L., "Group additivity in soot formation for the example of C-5 oxygenated hydrocarbon fuels," *Combust. Flame* 160(8):1484–1498, 2013, doi:10.1016/j.combustflame.2013.02.024.
151. Barrientos, E.J., Anderson, J.E., Maricq, M.M., and Boehman, A.L., "Particulate matter indices using fuel smoke point for vehicle emissions with gasoline, ethanol blends, and butanol blends," *Combust. Flame* 167:308–319, 2016, doi:10.1016/j.combustflame.2016.01.034.
152. Kellerer, H., Müller, A., Bauer, H.J., and Wittig, S., "Soot formation in a shock tube under elevated pressure conditions," *Combust. Sci. Technol.* 113–114:67–80, 1996, doi:10.1080/00102209608935488.
153. Kellerer, H., Koch, R., and Wittig, S., "Measurements of the growth and coagulation of soot particles in a high- pressure shock tube," *Combust. Flame* 120(1–2):188–199, 2000, doi:10.1016/S0010-2180(99)00067-X.
154. Kahandawala, M.S.P., Graham, J.L., and Sidhu, S.S., "Particulate emission from combustion of diesel and Fischer-Tropsch fuels: A shock tube study," *Energy and Fuels* 18(2):289–295, 2004, doi:10.1021/ef0340108.
155. Alexiou, A. and Williams, A., "Soot formation in shock-tube pyrolysis of toluene-n-heptane and toluene-iso-octane mixtures," *Fuel* 74(2):153–158, 1995, doi:10.1016/0016-2361(95)92648-P.
156. Agafonov, G.L., Smirnov, V.N., and Vlasov, P.A., "Shock tube and modeling study of soot formation during the pyrolysis and oxidation of a number of aliphatic and aromatic hydrocarbons," *Proc. Combust. Inst.* 33(1):625–632, 2011, doi:10.1016/j.proci.2010.07.089.
157. Kahandawala, M.S.P., Graham, J.L., and Sidhu, S.S., "Impact of lubricating oil on particulates formed during combustion of diesel fuel - A shock tube study," *Fuel* 83(13):1829–1835, 2004, doi:10.1016/j.fuel.2004.02.016.
158. Hong, Z., Davidson, D.F., Vasu, S.S., and Hanson, R.K., "The effect of oxygenates on soot formation in rich heptane mixtures: A shock tube study," *Fuel* 88(10):1901–1906, 2009, doi:10.1016/j.fuel.2009.04.013.
159. Zhao, L., Ameen, M., Pei, Y., Zhang, Y., Kumar, P., Tzanetakis, T., and Traver, M., "Numerical Evaluation of Gasoline Compression Ignition at Cold Conditions in a Heavy-Duty Diesel Engine," *SAE Technical Papers*, SAE International, 2020, doi:10.4271/2020-01-0778.
160. Zhao, L., Zhang, Y., Pei, Y., Zhang, A., Traver, M., and Ameen, M., "Numerical Evaluation of Spark Assisted Cold Idle Operation in a Heavy-Duty Gasoline Compression Ignition Engine," *SAE Technical Papers*, SAE International, 2021, doi:10.4271/2021-01-0410.
161. Cung, K.D., Ciatti, S.A., Tanov, S., and Andersson, Ö., "Low-Temperature Combustion of High Octane Fuels in a Gasoline Compression Ignition Engine," *Front. Mech. Eng.* 3(December):1–14, 2017, doi:10.3389/fmech.2017.00022.

162. Voice, A.K., Kumar, P., and Zhang, Y., “Effect of Fuel Reactivity on Ignitability and Combustion Phasing in a Heavy-Duty Engine Simulation for Mixing-Controlled and Partially Premixed Combustion,” *J. Eng. Gas Turbines Power* 140(4), 2018, doi:10.1115/1.4038015.
163. Algunaibet, I.M., Voice, A.K., Kalghatgi, G.T., and Babiker, H., “Flammability and volatility attributes of binary mixtures of some practical multi-component fuels,” *Fuel* 172:273–283, 2016, doi:10.1016/j.fuel.2016.01.023.
164. Zhang, Y., Voice, A., Tzanetakis, T., Traver, M., and Cleary, D., “An Evaluation of Combustion and Emissions Performance with Low Cetane Naphtha Fuels in a Multicylinder Heavy-Duty Diesel Engine,” *J. Eng. Gas Turbines Power* 138(10):1–10, 2016, doi:10.1115/1.4032879.
165. Zhang, Y., Voice, A., Pei, Y., Traver, M., and Cleary, D., “A Computational Investigation of Fuel Chemical and Physical Properties Effects on Gasoline Compression Ignition in a Heavy-Duty Diesel Engine,” *J. Sol. Energy Eng. Trans. ASME* 140(10):1–10, 2018, doi:10.1115/1.4040010.
166. Christensen, M., Hultqvist, A., and Johansson, B., “Demonstrating the multi fuel capability of a homogeneous charge compression ignition engine with variable compression ratio,” *SAE Tech. Pap.* 108:2099–2113, 1999, doi:10.4271/1999-01-3679.
167. Manente, V., Johansson, B., and Cannella, W., “Gasoline partially premixed combustion, the future of internal combustion engines?,” *Int. J. Engine Res.* 12(3):194–208, 2011, doi:10.1177/1468087411402441.
168. Hildingsson, L., Kalghatgi, G., Tait, N., Johansson, B., and Harrison, A., “Fuel octane effects in the partially premixed combustion regime in compression ignition engines,” *SAE Tech. Pap.* (January 2015), 2009, doi:10.4271/2009-01-2648.
169. Manente, V., Johansson, B., Tunestal, P., and Cannella, W., “Effects of different type of gasoline fuels on heavy duty partially premixed combustion,” *SAE Int. J. Engines* 2(2):71–88, 2010, doi:10.4271/2009-01-2668.
170. Rockstroh, T., Fridlyand, A., Ciatti, S., Cannella, W., and Goldsborough, S.S., “Autoignition behavior of a full boiling-range gasoline: Observations in RCM and GCI engine environments,” *Combust. Flame* 209:239–255, 2019, doi:10.1016/j.combustflame.2019.07.013.
171. Al-Abdullah, M.H., Kalghatgi, G.T., and Babiker, H., “Flash points and volatility characteristics of gasoline/diesel blends,” *Fuel* 153:67–69, 2015, doi:10.1016/j.fuel.2015.02.070.
172. Roberts, J., Chuahy, F.D.F., Kokjohn, S.L., and Roy, S., “Isolation of the parametric effects of pre-blended fuel on low load gasoline compression ignition (GCI),” *Fuel* 237:522–535, 2019, doi:10.1016/j.fuel.2018.09.150.
173. Reitz, R.D. and Duraisamy, G., Review of high efficiency and clean reactivity controlled compression ignition (RCCI) combustion in internal combustion engines, *Prog. Energy Combust. Sci.* 46:12–71, 2015, doi:10.1016/j.pecs.2014.05.003.
174. Agarwal, A.K., Singh, A.P., García, A., and Monsalve-Serrano, J., “Challenges and Opportunities for Application of Reactivity-Controlled Compression Ignition Combustion in Commercially Viable Transport Engines,” *Prog. Energy Combust. Sci.* 93(July):101028, 2022, doi:10.1016/j.pecs.2022.101028.
175. Hanson, R., Kokjohn, S., Splitter, D., and Reitz, R., “Fuel Effects on Reactivity Controlled Compression Ignition (RCCI) Combustion at Low Load,” *SAE Int. J. Engines*

4(1):394–411, 2011, doi:10.4271/2011-01-0361.
176. DelVescovo, D., Wang, H., Wissink, M., and Reitz, R.D., "Isobutanol as Both Low Reactivity and High Reactivity Fuels with Addition of Di-Tert Butyl Peroxide (DTBP) in RCCI Combustion," *SAE Int. J. Fuels Lubr.* 8(2):329–343, 2015, doi:10.4271/2015-01-0839.
177. Benajes, J., García, A., Monsalve-Serrano, J., and Lago Sari, R., "Fuel consumption and engine-out emissions estimations of a light-duty engine running in dual-mode RCCI/CDC with different fuels and driving cycles," *Energy* 157:19–30, 2018, doi:10.1016/j.energy.2018.05.144.
178. Olmeda, P., García, A., Monsalve-Serrano, J., and Lago Sari, R., "Experimental investigation on RCCI heat transfer in a light-duty diesel engine with different fuels: Comparison versus conventional diesel combustion," *Appl. Therm. Eng.* 144(August):424–436, 2018, doi:10.1016/j.applthermaleng.2018.08.082.
179. Schwab, S.D., Guinther, G.H., Henly, T.J., and Miller, K.T., "The effects of 2-ethylhexyl nitrate and di-tertiary-butyl peroxide on the exhaust emissions from a heavy-duty diesel engine," *SAE Tech. Pap.* (724), 1999, doi:10.4271/1999-01-1478.
180. Chinitz, W., Cresci, D., Tsai, C.Y., and Aradi, A.A., "Theoretical and wind tunnel experimental studies of diesel ignition and ignition-enhancing additives," *SAE Tech. Pap.* (412), 1996, doi:10.4271/961162.
181. Lee, D., Goto, S., Honma, H., Wakao, Y., and Mori, M., "Chemical Kinetic Study of a Cetane Number Enhancing Additive for an LPG DI Diesel Engine," 2000.
182. Eng, J.A., Leppard, W.R., and Sloane, T.M., "The effect of di-tertiary butyl peroxide (DTBP) addition to gasoline on HCCI combustion," *SAE Tech. Pap.* 2003(724), 2003, doi:10.4271/2003-01-3170.
183. Derek Splitter, R.R. and R.H., "High Efficiency, Low Emissions RCCI Combustion by Use of a Fuel Additive Derek," 2010.
184. Al-Taher, M.M., Kalamaras, C., Alqahtani, M.A., and Alomar, F.S., "Aerobic oxidation of hydrocarbons using N-hydroxyphthalimide (NHPI) catalysts for cetane enhancement," *Fuel* 324(PB):124563, 2022, doi:10.1016/j.fuel.2022.124563.
185. Hashimoto, K., Ikeda, M., Arai, M., and Tamura, M., "Cetane number improvement of diesel fuel by autoxidation," *Energy and Fuels* 10(6):1147–1149, 1996, doi:10.1021/ef960090m.
186. Hou, D., "US 2014/0373806 A1," 2014.
187. Splitter, D., Reitz, R., and Hanson, R., "High efficiency, low emissions RCCI combustion by use of a fuel additive," *SAE Technical Papers*, SAE International: 742–756, 2010, doi:10.4271/2010-01-2167.
188. Wang, H., DelVescovo, D., Reitz, R.D., and Yao, M., "Numerical Study of RCCI and HCCI Combustion Processes Using Gasoline, Diesel, iso-Butanol and DTBP Cetane Improver," *SAE Int. J. Engines* 8(2):831–845, 2015, doi:10.4271/2015-01-0850.
189. Curran, H.J., Pitz, W.J., Westbrook, C.K., Callahan, C. V., and Dryer, F.L., "Oxidation of automotive primary reference fuels at elevated pressures," *Symp. Combust.* 27(1):379–387, 1998, doi:10.1016/S0082-0784(98)80426-8.
190. Kuzuoka, K., Kurotani, T., Chishima, H., and Kudo, H., "Study of High-Compression-Ratio Engine Combined with an Ethanol-Gasoline Fuel Separation System," *SAE Int. J. Engines* 7(4):1773–1780, 2014, doi:10.4271/2014-01-2614.
191. Hashimoto, K., Kudo, T., Sato, T., Takase, I., Suzuki, T., and Nakano, T., "On Demand

Octane Number Enhancement Technology by Aerobic Oxidation," *SAE Technical Papers*, SAE International, 2016, doi:10.4271/2016-01-2167.
192. Cordier, M., Lecompte, M., Malbec, L.M., Reveille, B., Servant, C., Souidi, F., and Torcolini, N., "Water injection to improve direct injection spark ignition engine efficiency," *SAE Tech. Pap.* 2019-April(April):1–15, 2019, doi:10.4271/2019-01-1139.
193. Moffat, R.J., "Describing the uncertainties in experimental results," *Exp. Therm. Fluid Sci.* 1(1):3–17, 1988, doi:10.1016/0894-1777(88)90043-X.